2022

DEFINING THE ENDMEMBER SYSTEM OF US SOILS AND QUANTIFYING RELATIONSHIPS, AND A HYPERSPECTRAL APPROACH TO THE ALTERATION STRENGTH INDEX

Rachel Rulison
Michigan Technological University, rmhether@mtu.edu

DEFINING THE ENDMEMBER SYSTEM OF US SOILS AND QUANTIFYING RELATIONSHIPS, AND A HYPERSPECTRAL APPROACH TO THE ALTERATION STRENGTH INDEX

By

Rachel M. Hetherington

A DISSERTATION

Submitted in partial fulfillment of the requirements for the degree of

DOCTOR OF PHILOSOPHY

In Geology

MICHIGAN TECHNOLOGICAL UNIVERSITY

2022

This dissertation has been approved in partial fulfillment of the requirements for the Degree of DOCTOR OF PHILOSOPHY in Geology.

Department of Geological and Mining Engineering and Sciences

Dissertation Advisor:	*Dr. Chad Deering*
Committee Member:	*Dr. Simon Carn*
Committee Member:	*Dr. Snehamoy Chatterjee*
Committee Member:	*Ryan Williams*
Department Chair:	*Dr. Aleksey Smirnov*

Table of Contents

List of Figures

List of Tables

Acknowledgements

I'd like to acknowledge my advisor and thank my committee members for their feedback.

Thank you to the Corescan team for their data and related communications, and to Dr. Joesph Moore at the University of Utah for providing the Telaga Bodas core samples for my research.

My appreciation goes out to Henrique (Kiko) de Melo e Silva, Rob Fritz, and Bob Barron for their support and assistance with lab work and equipment. A special thanks to Cabot Savidge of New England Research for providing training and immense support for the BenchLab 7000 EX permeameter, and thanks to Dr. Thomas Oommen and Dr. Stan Vitton for their assistance with equipment for lab testing.

My biggest appreciation is for my husband, family, and friends for their unconditional support and encouragement throughout this journey.

Abstract

Soils form a complex part of the environment, providing important functions in systems such as food production, groundwater movement, and ecosystem health. There have been numerous studies on soil geochemistry and the origin of elements within soils, but few studies into quantifying the relationships between elements and geographical data on a national scale. Using geochemical data obtained by the USGS, the surficial soils of the US were defined by a 13-endmember system using Polytopic Vector Analysis and mapped in GIS. Correlation matrices provided Pearson's correlation coefficients for elements in the Top 5 cm soil profile, the A horizon, and the C horizon. The Top 5 cm element concentrations were also correlated with the endmembers, and geographical data for land cover, soil order, and soil pH. The quantification of these relationships supported many of the spatial patterns shown in maps and provided insight into other relationships, especially where correlation is weaker.

The high spectral resolution of hyperspectral imagery has provided revolutionary advancements in many fields, including mineral identification. Hyperspectral core data from the company Corescan allowed for quantifiable mineral proportions for core sections from Karaha Telaga-Bodas, in Indonesia, and Lake City Caldera, in Colorado. The Alteration Strength Index (ASI) is a value based on mineral parameters that correlate to rock strength. The incorporation of hyperspectral data in the ASI aimed to improve the accuracy of the mineralogical parameters and provide more reliable strength data which in turn would reduce the need for time-consuming lab testing. Results showed that for the Telaga Bodas and Lake City samples, the ASI was not able to provide rock strength estimates within a reasonable range, and calibration of mineralogical parameters may be needed for samples with low ASI values. Though hyperspectral data may be a valuable tool in this venture, other issues with the current ASI would need to be resolved.

1 Defining the Endmember System of US Soils and Quantifying Relationships

1.1 Introduction

Soil is both a complex and important constituent of the environment, the properties of which form from, and therefore reflect, the interactions between the lithosphere, biosphere, hydrosphere, and atmosphere (Chesworth, 2007; Rowell, 2014). Soil plays a key part in many systems, such as food production, ecosystem health, exchange of essential nutrients, and groundwater movement and storage (Smith et al., 2013; Woodruff et al., 2015). It also provides an avenue for bioaccumulation, therefore affecting human and animal health as elements and chemicals in soils can be ingested, absorbed, or inhaled (Wilson et al., 2008; Smith et al., 2013; Smith et al., 2013).

Geochemical analyses are necessary for soil characterisation, ecological evaluation, and determining and assessing soil processes, health, and quality. This understanding is the basis needed in order to determine and understand the impact and influence of anthropogenic activities on soil properties (Wilson et al., 2008).

In order to recognise and quantify chemical changes in soils and other aspects of the near-surface environment, whether they are sourced naturally or anthropogenically, is it vital to both define and understand the variability, abundance, and spatial distribution of chemical elements at the present (Smith et al., 2012).

Studies on soil geochemistry have been conducted worldwide, however, few large scale, continental studies exist. Only a handful of datasets exist for national-scale geochemical data for the U.S. (Smith et al., 2013). The first of these large-scale studies was carried out by Hansford Shacklette of the USGS, with sampling carried out for the conterminous U.S. between 1961 and 1975. Sites were selected to represent unaltered, or only slightly altered, soils and can therefore be regarded as the background range of elements in soils (Shacklette & Boerngen, 1984; Smith et al., 2013). The most recent study is The North American Soil Geochemical Landscapes Project, which was started in 2002 and is ongoing (Smith et al., 2013). The goals of the project are to: "(1) develop a continental-scale design and protocols for generating soil geochemical and mineralogical data; (2) provide baseline soil geochemical and mineralogical data that are useful for a wide range of applications and disciplines; (3) interpret the resulting geochemical and mineralogical patterns in terms of processes acting at the broad scale of the project; and (4) establish an archive of soil samples for future investigators" (Smith et al., 2013). For this project, over 4800 samples were taken in the contiguous U.S. (Figure 1) between the years 2007 and 2010, and sites were selected by random design but ensured to avoid obvious polluted sites. At each location, samples were taken from the top 5 cm, the A-horizon, and the C-horizon (Smith et al., 2013; Smith et al., 2013). Mineralogical and geochemical analyses of the samples were completed in 2013 (Smith et al., 2013). Interactive geochemical and mineralogical maps from this data and interpretations of their concentrations and distribution can be found on the USGS Publications Warehouse (https://pubs.usgs.gov/sir/2017/5118/index.html).

The data collected from projects like this has allowed for many studies into regional- and national-scale correlation between the mineralogical and geochemical content of soils and influencing factors such as parent lithology, climate, soil type, and age, among many others. However, it seems little has been done in relation to quantifying and assessing the correlation between elements in the soil on a national scale.

The purpose of this research is to determine the number and composition of the endmembers which can define the surficial soil system in the U.S. and provide quantitative analyses between elements and endmembers, in addition to their relation with other nation-wide datasets. Quantitative analyses on this scale could increase knowledge on the relationships between element distribution and behaviour in U.S soils.

Figure 1. Locations of the 4857 soil samples taken by the USGS.

1.2 Methods

1.2.1 Source Data and GIS

The datasets analyzed for this study were collected by the USGS and are available through their Online Publications Directory (https://pubs.usgs.gov/sir/2017/5118/index.html). Samples were collected from three soil horizons: Top 5, A horizon, and C horizon. The surficial soil samples for the study were taken from the top 5 cm (depth 0-5 cm, "Top 5") and analyzed for concentrations of 44 elements: Ag, Al, As, Ba, Be, Bi, Ca, Cd, Ce, Co, Cr, Cs, Cu, Fe, Ga, Hg, In, K, La, Li, Mg, Mn, Mo, Na, Nb, Ni, P, Pb, Rb, S, Sb, Sc, Se,

Sn, Sr, Te, Th, Ti, Tl, U, V, W, Y, and Zn. The A horizon is the uppermost mineral horizon, containing little to none of the original rock structure and formed at the surface or just below the organic-dominated O horizon (USDA, 2017). Samples collected from the A horizon ranged in depth from 0-80 cm (Smith et al., 2013). The C horizon is the lowest soil horizon, lying just above hard bedrock, and displays little evidence of soil forming processes (USDA, 2017). Soil from the C horizon tends to be partially weathered parent material and samples ranged to a depth of 167 cm (Smith et al., 2013). The same 44 elements were analyzed for the A and C horizons as for the Top 5 horizon, with an addition three for carbon (total carbon, organic carbon, and inorganic carbon). There were also 26 minerals analyzed for the A and C horizons: quartz, potassium feldspar, plagioclase, total feldspar, 14A clays, 10A clays, kaolinite, total clays, gibbsite, calcite, dolomite, aragonite, total carbonates, analcime, heulandite, total zeolites, gypsum, talc, hornblende, serpentine, hematite, geothite, pyroxene, pyrite, other, and amorphous.

Samples with no data in each soil horizon were removed, resulting in a total of 4841 samples for the Top 5 soils layer, 4813 samples for the A horizon, and 4780 samples for the C horizon. Note that the samples with no data were still listed in the raw files as data had been collected at those sample locations in one or more of the soil horizons. To ensure consistency for our statistical analysis all data was converted into ppm, and, for the creation of the maps, all values below detection limit were replaced with zeros to avoid fictitious numbers.

This data was then imported into ArcGIS and converted to raster files for the mapping and multivariate interpolation of the major and trace elements. Concentration maps were created for each element in each of the three datasets: 44 maps for the Top 5, 47 for the A horizon, and 47 for the C horizon, with an additional 26 for mineral data in the A horizon, and 26 for the mineral data in the C horizon. The Band Collection Statistics tool was used to quantitatively analyze the geochemical raster datasets and calculate a correlation matrix. The output tables were then exported into Excel.

Data for bedrock geology, land cover, soil types, soil pH, mine locations, and superfund sites were also downloaded and imported into ArcGIS for analysis in relation to mineral and geochemical concentrations in each of the three soil horizons. Geology data was obtained from the USGS Mineral Resources Data (https://mrdata.usgs.gov/geology/state/), and land cover data was from the NLCD 2011. The source for the soil type data came from UC Davis, and the soil pH map was created from this data. Mine location data came from the USGS Mineral Resources Data System (MRDS), and the superfund sites from the EPA. Each GIS layer, including the geochemical, mineral, and end-member maps, was projected into USA_Continuous_Lambert_Conformal_Conic Coordinate System. All raster files (land cover, soil types, soil pH, geochemical, mineral, and end-member maps) were created using Inverse Distance Weighting (IDW) and resampled using bilinear interpolation for a smoother image. The cell size for all raster files, except for soil order and pH, was 222 km^2. The soil classification and pH maps had a raster size of 0.64 km^2 which provided more detailed maps due to the data being discrete as opposite to continuous.

1.2.2 Polytopic Vector Analysis

Polytopic Vector Analysis (PVA) is a multivariate statistical technique for analyzing collections of samples that are mixtures and is used to determine the following components of the mixing system: 1) the number of end-members, 2) the composition of each end-member, and 3) the relative proportions of each end-member in each sample. An advantage of PVA is that it does not require a priori knowledge of these parameters to do this (Ehrlich, 2007).

PVA was used on the Top 5 dataset. In preparing the data file for PVA, elements with ≥ 5% unusable data, which includes those with no values and values below detection limit, were removed from the dataset. These elements were Ag, Cd, Cs, Hg, In, S, Se, Te, and Tl, leaving a total of 35 analytes to be included in the PVA analysis. Elements with values below detection limit were removed prior to analysis leaving a total of 4526 samples.

The first PVA module, VSPACE, determines the number of end-members. Klovan/Miesch Coefficient of Determination (KMCD) values are calculated for each variable based on the ratio between the variance of a specific variable and the back-calculated equivalent. KMCD values of 0.5 and above are considered to be able to support a k end-member solution, with 0.7 providing strong support and 0.9 very strong support. Low KMCD values (< 0.5) imply that a variable will likely contribute little-to-nothing to the analysis (Ehrlich, 2007). Based on the KMCD values for the Top 5 dataset, 19 elements had reached a coefficient of 0.5 or above by end-member 8, and 22 elements by end-member 15. Due to the likelihood that some samples could have high concentrations of certain elements, no outlier samples were considered to be erroneous, and all data was kept in the analysis.

The second, PVA, module calculates the end-member compositions and relative proportions in each sample but requires the number of end-members to be specified. The PVA module was run several times, each with a different number of end-members specified. The only run to terminate having reached a satisfactory result, meaning that the program converged to the extent specified in the PVA procedures options, was for a 13 end-member solution. The output file displays the extreme raw samples from the dataset, the composition of the end-members, and the mixing proportions of each end-member in each sample. The mixing proportions were taken from the final iteration of the program.

The mixing proportions data for the amount of end-member in each sample was imported into ArcGIS and raster maps were created for each of the 13 end-members. As with the element raster files, the Band Collection Statistics tool was used to quantitatively analyze the end-member and geochemical raster datasets and calculate a correlation matrix. The output tables were then exported into Excel.

1.3 Results

1.3.1 PVA

Table 1 displays the PVA endmember compositions for a 13 end-member solution after the eighth and final iteration for the Top 5 soil samples. Although there were traces of other elements present in many of the end-members, those only present below 1% were removed from the table. Several of the remaining elements also have less than 1% presence in some end-members but were kept because they had more than 1% in one or more end-members. Table 2 lists the extreme samples and the mixing proportions, which are the relative amounts of the end-member in each sample. The end-member with the highest amount in each sample is highlighted. Some cells show a negative mixing proportion. This indicates that some samples lie outside of the polytope, however the values are close to zero and within the defined allowable limit for negative values for acceptable convergence. The locations of the 13 extreme samples are shown in Figure 2.

Table 1. End-member compositions. Red cells display major components (>25%), orange display intermediate (10-25%), and yellow display minor components (1-10%).

	EM1	EM2	EM3	EM4	EM5	EM6	EM7	EM8	EM9	EM10	EM11	EM12	EM13
Al	99.974	-	13.758	-	16.810	-	-	58.385	60.322	29.555	39.978	75.106	-
Ba	-	-	0.258	-	-	-	-	-	-	8.854	-	2.394	-
Ca	-	99.893	-	-	-	-	38.519	-	-	-	-	-	-
Ce	-	-	-	-	0.407	-	0.001	0.161	0.006	0.114	-	2.188	-
Fe	-	-	-	-	-	99.426	-	-	21.416	29.750	19.562	9.480	0.166
K	-	-	85.672	1.286	9.626	-	-	-	-	27.522	-	-	1.628
La	-	-	-	-	0.180	-	0.009	0.044	0.009	0.083	0.024	1.051	-
Mg	-	-	-	-	-	-	10.891	-	0.940	-	-	-	97.566
Mn	-	-	-	-	-	-	0.086	35.887	-	-	-	-	-
Na	-	-	-	97.608	-	-	47.069	-	-	-	-	-	-
P	-	-	-	-	0.504	-	-	4.161	0.001	-	37.005	-	-
Sr	-	0.107	-	1.079	-	-	1.066	-	-	1.223	0.388	-	0.100
Ti	-	-	-	-	71.742	-	-	-	15.839	2.022	-	7.372	-
Zn	-	-	-	-	-	0.168	0.533	0.413	-	0.153	1.491	0.031	-

Table 2. Extreme samples and mixing proportions. Highlighted cells show the highest end-member amount for each sample.

Extreme Samples	**End-member Mixing Proportions**												
	EM1	EM2	EM3	EM4	EM5	EM6	EM7	EM8	EM9	EM10	EM11	EM12	EM13
AL5408	0.596	-0.003	0.051	-0.010	0.025	0.225	0.024	0.000	0.053	0.011	0.009	0.013	0.008
FL48	0.043	0.908	-0.006	0.002	0.002	0.020	0.007	-0.001	0.005	0.007	0.004	0.002	0.008
CO8427	0.303	0.014	0.471	0.021	0.025	0.023	0.012	0.005	0.009	0.069	0.008	0.029	0.011
NV1871	0.236	0.127	0.094	0.293	0.011	0.095	0.022	0.006	0.030	0.033	0.009	0.005	0.040
VA5020	0.227	0.007	0.052	-0.012	0.297	0.216	0.041	0.014	0.052	0.039	0.039	0.019	0.009
LA11852	0.143	0.000	0.015	-0.009	0.014	0.696	0.024	0.032	0.035	0.024	0.006	0.014	0.006
CA8143	0.224	0.181	0.087	0.130	0.013	0.057	0.165	0.007	0.020	0.032	0.008	-0.005	0.082
PA6396	0.203	0.019	0.118	0.031	0.049	0.146	0.029	0.246	0.056	0.056	0.026	0.015	0.005
CA3871	0.251	0.159	0.023	0.076	-0.009	0.210	0.002	0.012	0.177	0.003	0.004	-0.003	0.094
MT9582	0.219	0.028	0.055	0.037	-0.001	0.202	0.025	0.022	0.036	0.301	0.014	0.017	0.046
FL480	0.247	0.081	-0.005	0.003	0.029	0.232	0.015	0.006	0.050	0.029	0.256	0.032	0.026
GA2208	0.228	0.011	0.033	-0.001	0.064	0.190	0.009	0.032	0.036	0.055	0.027	0.263	0.054
NV11887	0.038	0.250	0.013	0.083	0.004	0.000	0.037	-0.006	0.001	0.020	0.016	-0.001	0.545

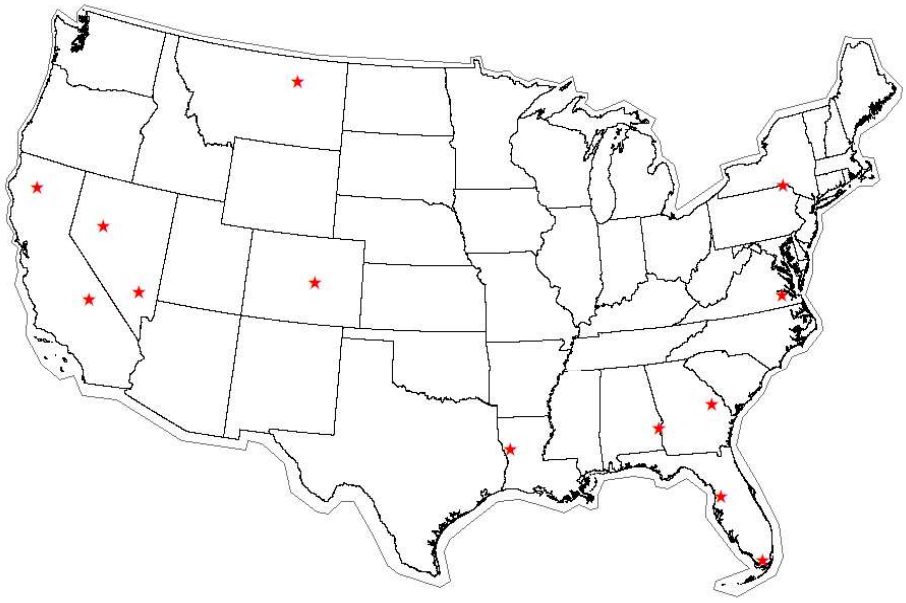

Figure 2. The red stars represent the locations of the 13 extreme samples.

1.3.2 Correlation Matrices

There are 18 EM-EM and EM-element pairs with a correlation coefficient ≥ 0.5, including those with negative correlations. This breaks down to four pairs with a correlation coefficient of 0.8 and above, two pairs with a correlation of 0.7-0.8, two pairs with a correlation of 0.6-0.7, and 10 pairs with a correlation of 0.5-0.6. The end-member pairs for each coefficient category are shown in Table 3.

Table 3. End-member correlation coefficients.

≥ 0.8	≥ 0.7	≥ 0.6	≥ 0.5	
EM2 - Ca	EM6 - EM9	EM4 - Ba	EM4 - K	EM2 - EM9 (-ve)
EM4 - Na	EM1 - Ca (-ve)	EM8 - Mn	EM4 - Al	EM9 - Sc
EM13 - Mg			EM4 - EM7	EM4 - Ga
EM1 - EM2 (-ve)			EM5 - K (-ve)	EM5 - Rb
			EM4 - Sr	EM2- EM6

The correlation matrix for the elements analyzed in the Top 5 cm shows there are 67 pairs with a correlation coefficient of 0.7 and above. This breaks down to 19 pairs with a correlation of 0.9-1, 14 pairs with a correlation of 0.8-0.9, and 34 pairs with a correlation of 0.7-0.8 (Table 4).

Table 4. Correlation coefficients for Top 5 element pairs.

≥ 0.9		≥ 0.8		≥ 0.7			
Al - Ga	Hg - Te	Al - Fe	La - Y	Al - Ba	Be - Nb	Ce - Y	Nb - Y
Bi - Hg	Hg - W	Al - Sc	Pb - W	Al - Be	Be - Rb	Co - Ti	Rb - Th
Bi - Pb	Hg - Zn	Ce - Th	Rb - Tl	Al - Na	Be - Tl	Ga - Na	Sc - Ti
Bi - Te	K - Rb	Co - Fe	W - Zn	Al - V	Be - Y	Ga - Sc	Ti - V
Bi - W	Pb - Te	Co - Sc		Ba - Ga	Bi - Cd	Ga - V	
Bi - Zn	Pb - Zn	Co - V		Ba - K	Cd - Hg	Ga - Y	
Ce - La	Sc - V	Fe - Ga		Be - Ce	Cd - Pb	K - Tl	
Cr - Ni	Te - W	Fe - Ti		Be - Ga	Cd - Te	La - Nb	
Fe - Sc	Te - Zn	Fe - V		Be - K	Cd - Zn	La - Rb	
Hg - Pb		La - Th		Be - La	Ce - Nb	Na - Sr	

Table 5. Correlation coefficients for A Horizon (black), and C Horizon (blue) mineral pairs.

≥ 0.9		≥ 0.8	≥ 0.7	
Plag – Tot-fs	Plag – Tot-fs	Quartz – Al (-ve)	Quartz – Plag (-ve)	Total-fs – Ba
Plag – Na	Plag – Na	Quartz – Ga (-ve)	Quartz – Tot_fs (-ve)	Total-fs – Ga
Tot-fs – Na	Tot-fs – Na	10A-clays – Tot-clays	Quartz – Amorphous (-ve)	Total-fs – K
Calcite – Tot-carb	Calcite – Tot-carb	Heulandite – Tot-zeolites	Quartz – Fe (-ve)	Talc – Ni
Calcite – C-inorg	Calcite – Ca	Talc – Cr	Quartz – Na (-ve)	Quartz – Amorphous (-ve)
Calcite – Ca	Tot-carb – C-inorg	Calcite – C-inorg	Quartz – Sc (-ve)	K-fs – Tot-fs
Tot-carb – C-inorg	Tot-carb - Ca		K-fs – Tot-fs	K-fs – K

Tot-carb – Ca	Heulandite – Tot-zeolites		K-fs – K	10A-clays – Tot-clays
Gypsum – S	Gypsum – S		Plag – Al	Kaolinite – Tot-clays
C-tot – C-org	C-inorg – Ca		Plag – Ga	C-tot – C-org
C-inorg - Ca			Total-fs - Al	

Table 5 shows the correlation coefficients for mineral pairs in the A and C Horizons. The A Horizon has 11 pairs with a correlation of 0.9-1, five pairs with a correlation of 0.8-0.9, and 15 pairs with a correlation of 0.7-0.8. The C Horizon has 10, one, and six pairs with coefficients of 0.9-1, 0.8-0.9, and 0.7-0.8 respectively. All correlation coefficients involving quartz are negative. The correlation matrix for elements in the A Horizon show there are 44 element pairs with a correlation coefficient of 0.7 or above; eight pairs with a correlation of 0.9-1, 12 pairs with a correlation of 0.8-0.9, and 24 pairs with a correlation of 0.7-0.8 (Table 6).

Table 6. Correlation coefficients for element pairs in the A Horizon.

≥ 0.9	**≥ 0.8**		**≥ 0.7**		
Al – Ga	Al – Fe	Fe – Ga	Al – Ba	Be – Ga	Ga – V
Bi – Te	Al – Sc	Fe – Ti	Al – Be	Be – K	Ga – Y
Ce – La	Ba – K	Ga - Sc	Al – Na	Be – La	La – Rb
Cr – Ni	Be – Rb	La - Th	Al – V	Be – Nb	La – Y
Fe – Sc	Ce – Th		As – Sb	Be – Y	Nb – Y
Fe – V	Co – Fe		Ba – Ga	Ce – Y	Rb – Th
K – Rb	Co – Sc		Ba – Na	Co – Ti	Sc – Ti
Sc - V	Co – V		Be – Ce	Ga – Na	Ti – V

The correlation matrix for elements in the C Horizon show there are 28 element pairs with a correlation coefficient of 0.7 or above; four pairs with a correlation of 0.9-1, 10 pairs with a correlation of 0.8-0.9, and 14 pairs with a correlation of 0.7-0.8 (Table 7). The full correlation matrices for each of the soil horizons can be found in Appendix A1.

Table 7. Correlation coefficients for element pairs in the C Horizon.

≥ 0.9	≥ 0.8		≥ 0.7		
Al – Ga	Al – Fe	K – Rb	Al – Ti	Ce – Th	Ga – Sc
Ce – La	Al – Sc	La – Th	Al – V	Co – Sc	La – Y
Cr – Ni	Co – Fe	Rb – Tl	Al – Zn	Co - V	Rb – Th
Fe – Sc	Fe – Ti	Sc – Ti	Be – Ga	Fe – Ga	Ti - V
	Fe – V	Sc – V	Be – Rb	Fe – Zn	

Figure 3 displays the correlation coefficients for mineral pairs in the A and C horizons where at least one of the horizons has a coefficient of 0.7 or higher for each pair. Quartz pairs have negative correlations. The quartz dilution effect is the displacement of minerals and materials where quartz content is high and explains these negative relationships (Bern, 2009). Fourteen of the 32 mineral-mineral and mineral-element pairs display a difference between the A and C Horizon coefficients of >0.1: C_tot-C_org, 10A_clays- tot_clays, Talc- Cr, Talc-Ni, Plag-Al, Plag-Ga, Tot_fs-Al, Tot_fs-Ga, Tot_fs-Ba, Kaol-Tot_clays, Quartz-Sc, Quartz-Fe, Quartz-Ga, and Quartz-Al. For most of these pairs, correlation is higher in the A Horizon, the exception being kaolinite and total clays which has stronger correlation in the C Horizon.

Figures 4, 5, and 6 show a comparison of correlation coefficients for all three soil horizons for element pairs where the coefficient in at least one soil horizon is 0.9-1, 0.8-0.9, and 0.7-0.8 respectively. In Figure 4, seven of the 20 element pairs show identical correlation in all three soil horizons. The remainder show clear separation, where they all have high correlation in the surface soils, but much lower correlation in the A Horizon, and even lower correlation in the C Horizon. All of the pairs which demonstrate a correlation decrease with increasing depth involve the elements Pb, Zn, Bi, Hg, W, and Te. A likely explanation could be the anthropogenic impact of heavy metals in the environment as opposed to a geological source where C horizon concentrations and relationships would also be high.

The correlation coefficients in Figure 5 are all similar in each soil horizon, with only two pairs showing much lower correlation in both the A and C horizons (Pb-W and W-Zn), and two other pairs showing a lesser difference in either the A or C Horizon (Rb-Tl and Ba-K). Figure 6 shows more variation, however there are five pairs which show a greater difference between the Top 5 correlation and the correlation in the A and C Horizons. These five pairs all involve Cd paired with Te, Zn, Bi, Hg, and Pb. Unlike with the other graphs, Figure 6 also shows several pairs where the A and C horizons display much higher correlation than the Top 5 (Al-Zn, Fe-Zn, Be-Nb, and Be-La).

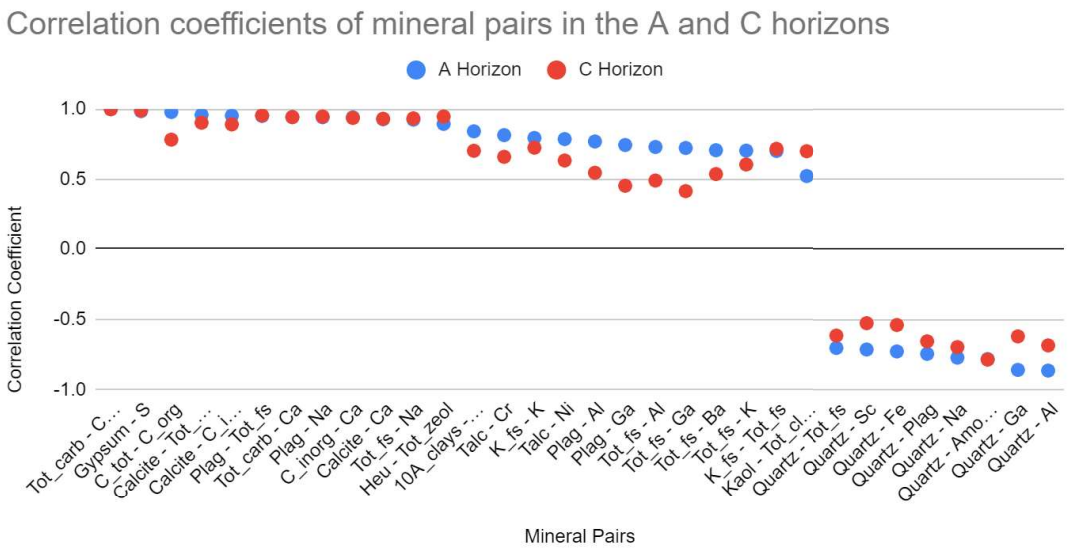

Figure 3. Graph comparing correlation coefficients for mineral pairs in the A and C horizons. Note that quartz pairs are negative.

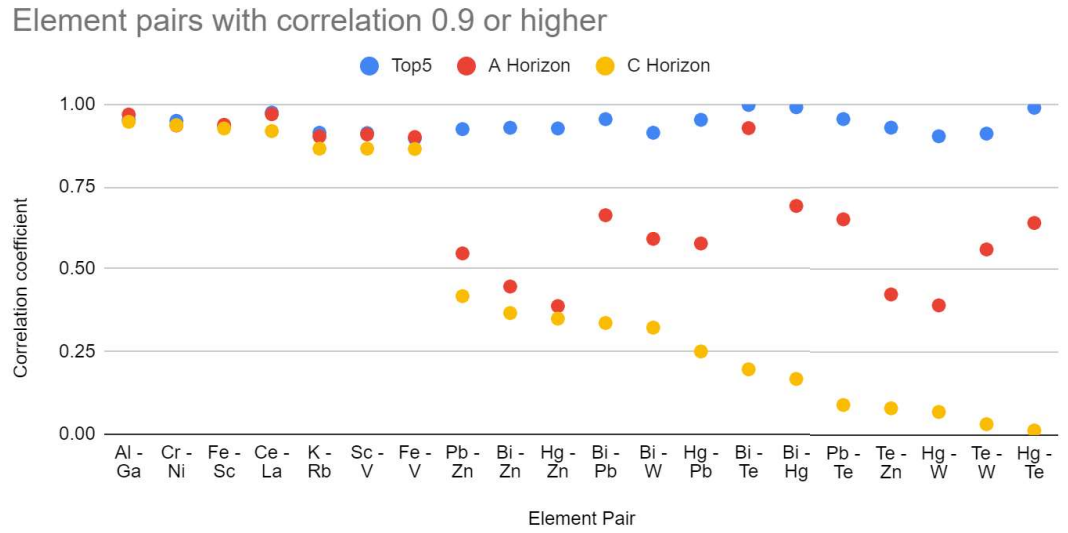

Figure 4. Graph comparing correlation coefficients for element pairs where at least one horizon has a coefficient of 0.9 or higher.

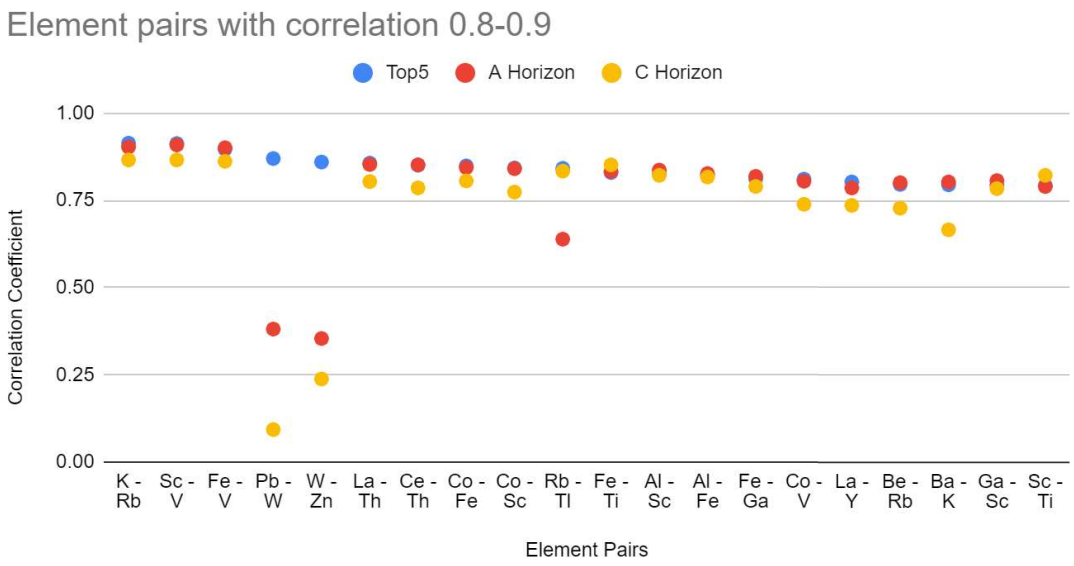

Figure 5. Graph comparing correlation coefficients for element pairs where at least one horizon has a coefficient of 0.8-0.9.

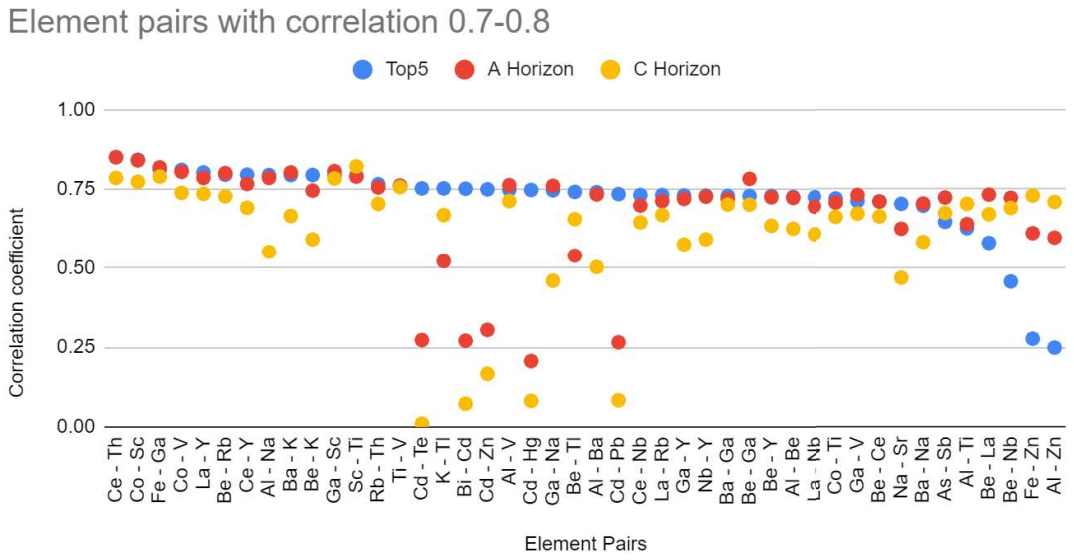

Figure 6. Graph comparing correlation coefficients for element pairs where at least one horizon has a coefficient of 0.7-0.8.

1.3.3 Endmember Maps

Figures 7-19 show each of the 13 end-member maps. Each legend represents the proportion of the end-member present in the samples. End-member 1 has widespread distribution across the US, comprising roughly a third of most samples. The highest amounts are in the southeastern states of Georgia, South Carolina, and West Virginia, and the lowest amounts in Florida, Texas, and Utah. End-member 2 has generally low proportions across the US but high amounts in Florida, Texas, and Utah where end-member 1 has its lowest amounts. End-members 3-13 have low proportions throughout most areas, with the majority of these end-members not comprising more than 25% of any sample. The exceptions are end-members 3, 6 and 13 which comprise up to 45%, 65%, and 55% of a sample respectively. Western and Upper Michigan has the highest proportions of end-member 3 with slightly lower amounts in and around the central and mid-western states. The lowest amounts are in the Pacific Northwest, the southeast, and parts of Texas. End-member 4 has a few high points in the western states and is lowest across the Atlantic coastal plains. The highest proportions of end-member 5 are on the eastern coast of Virginia and North Carolina. The rest of the US has very little variation. End-member 6 is highest in northwestern Oregon and eastern Texas into western Louisiana. The highest amounts of end-member 7 are located in Montana, California, and on the border between New York and Pennsylvania, though even these points are very low. End-member 8 is also low, with highest proportions in Pennsylvania and into lower New York. End-member 9 is highest in northern California, and end-member 10 in Montana and Louisiana. The highest proportions of end-members 11, 12, and 13 are located in western-central Florida, eastern Georgia, and southern Nevada respectively.

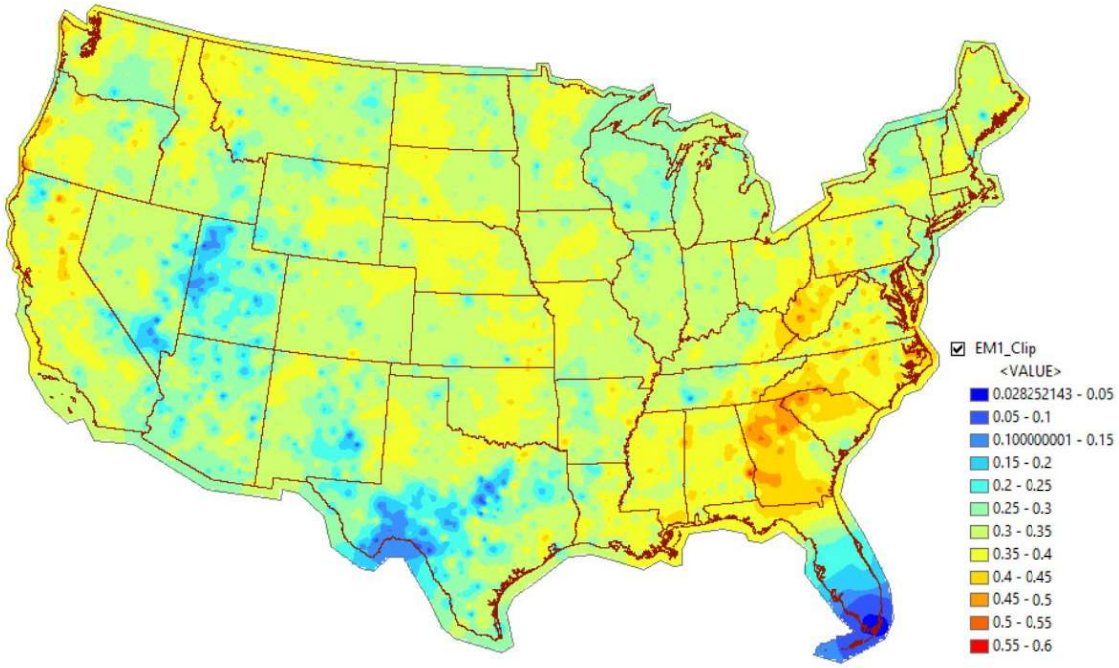

Figure 7. Endmember 1 distribution.

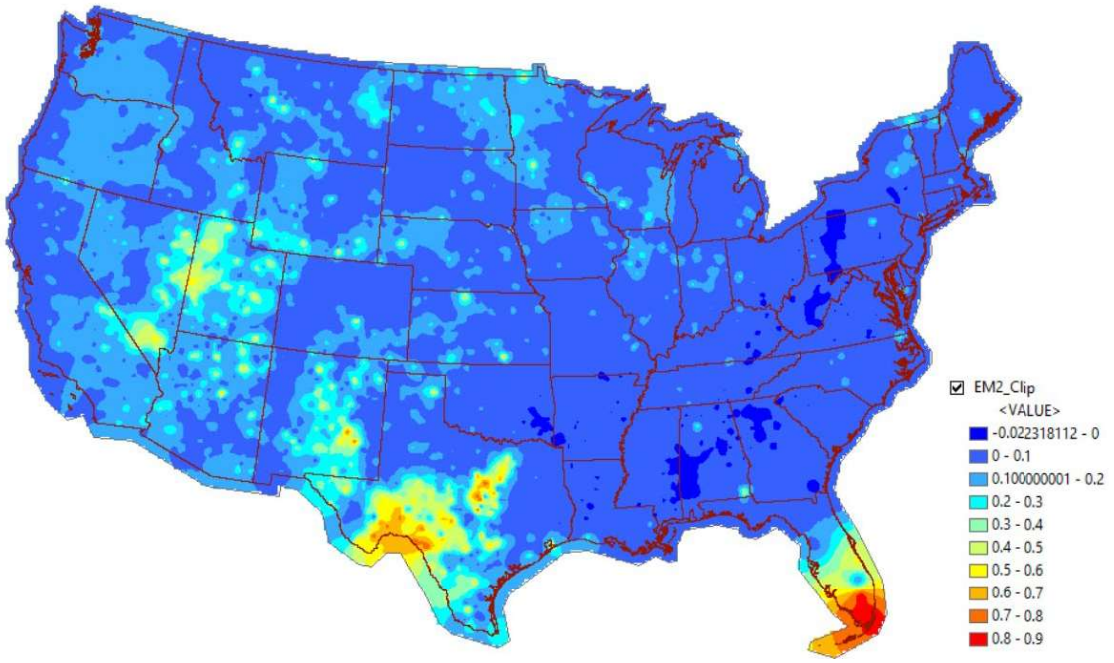

Figure 8. Endmember 2 distribution.

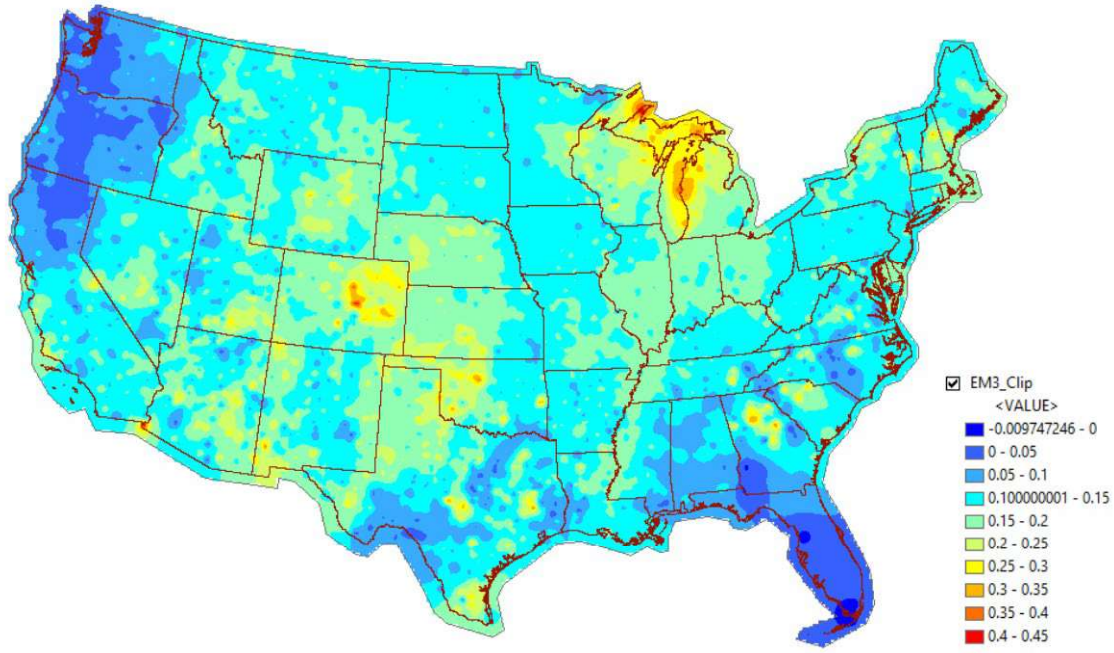

Figure 9. Endmember 3 distribution.

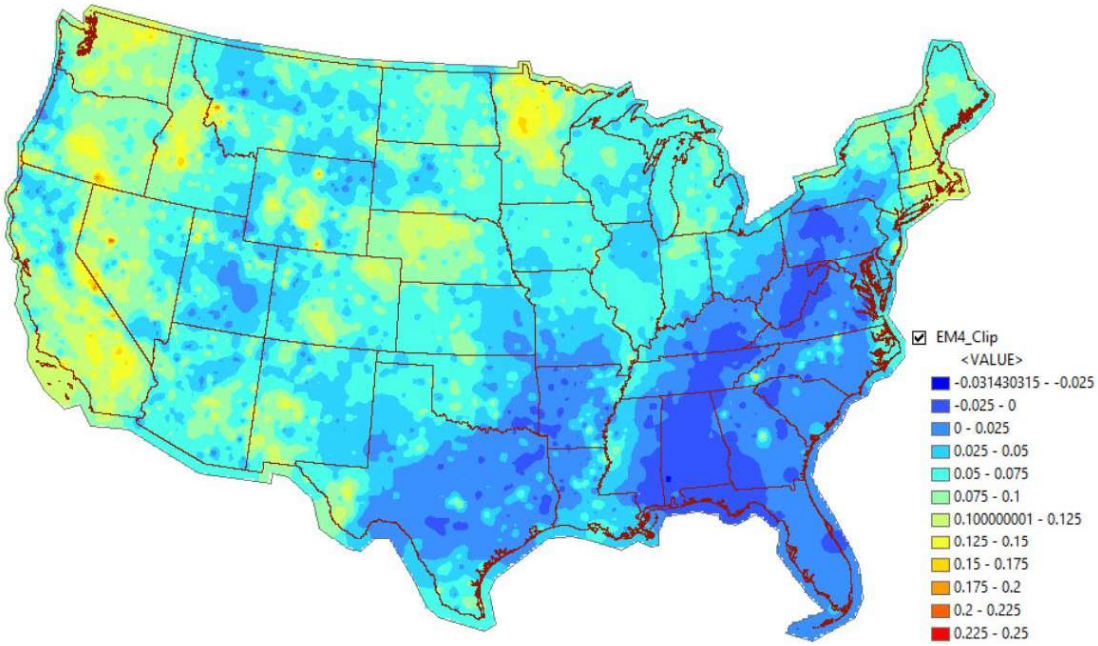

Figure 10. Endmember 4 distribution.

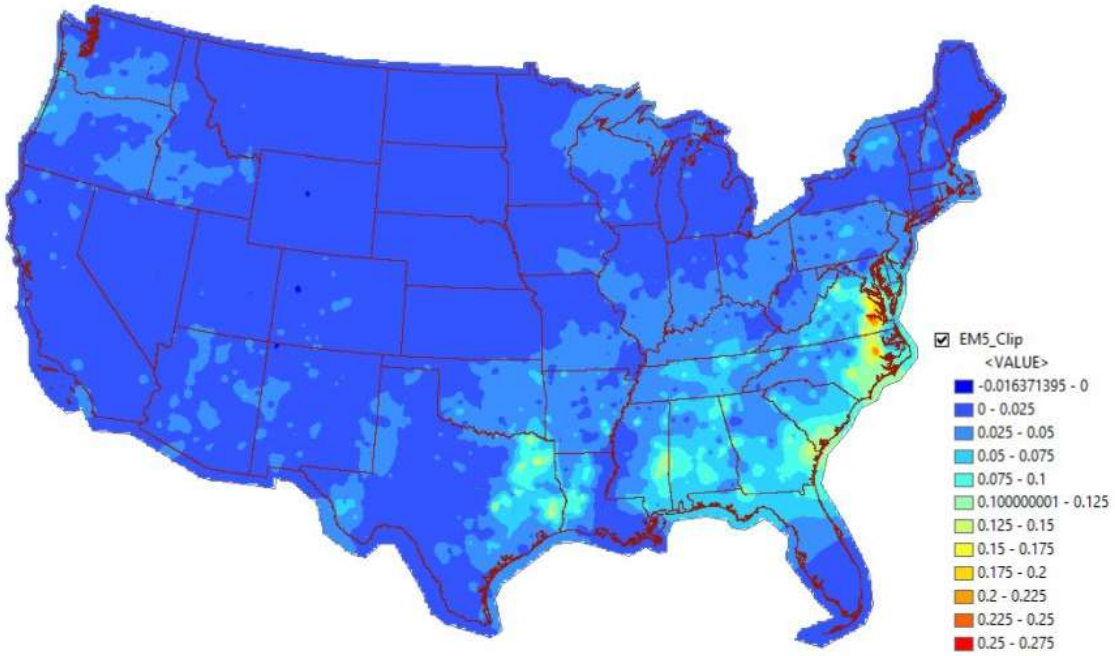

Figure 11. Endmember 5 distribution.

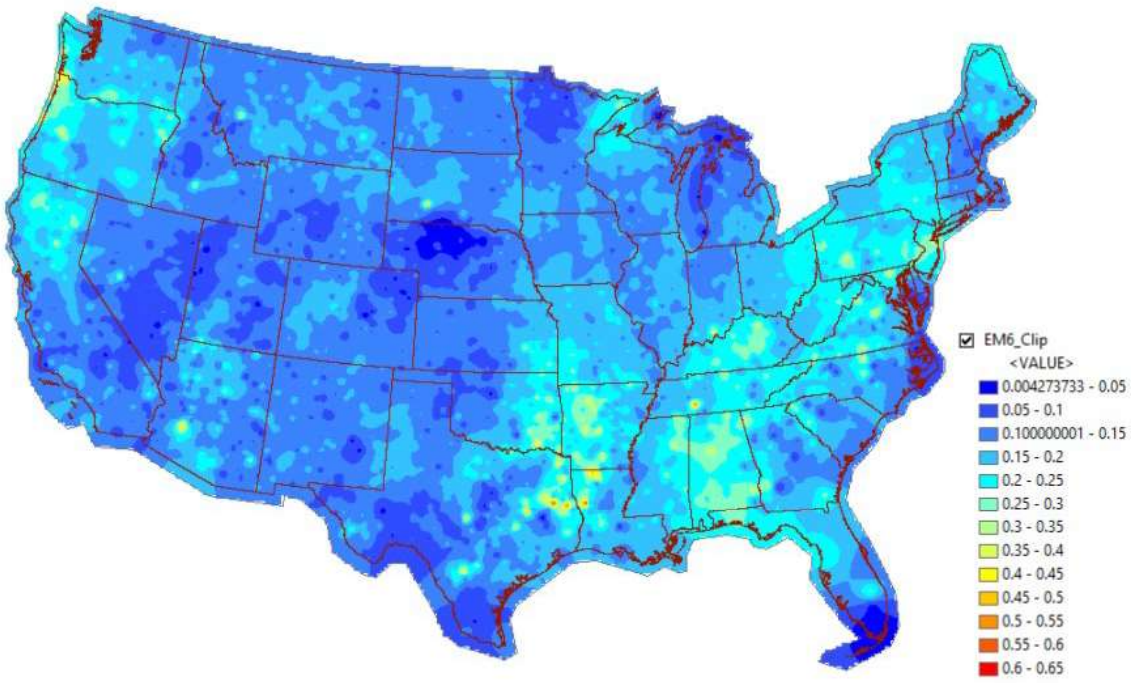

Figure 12. Endmember 6 distribution.

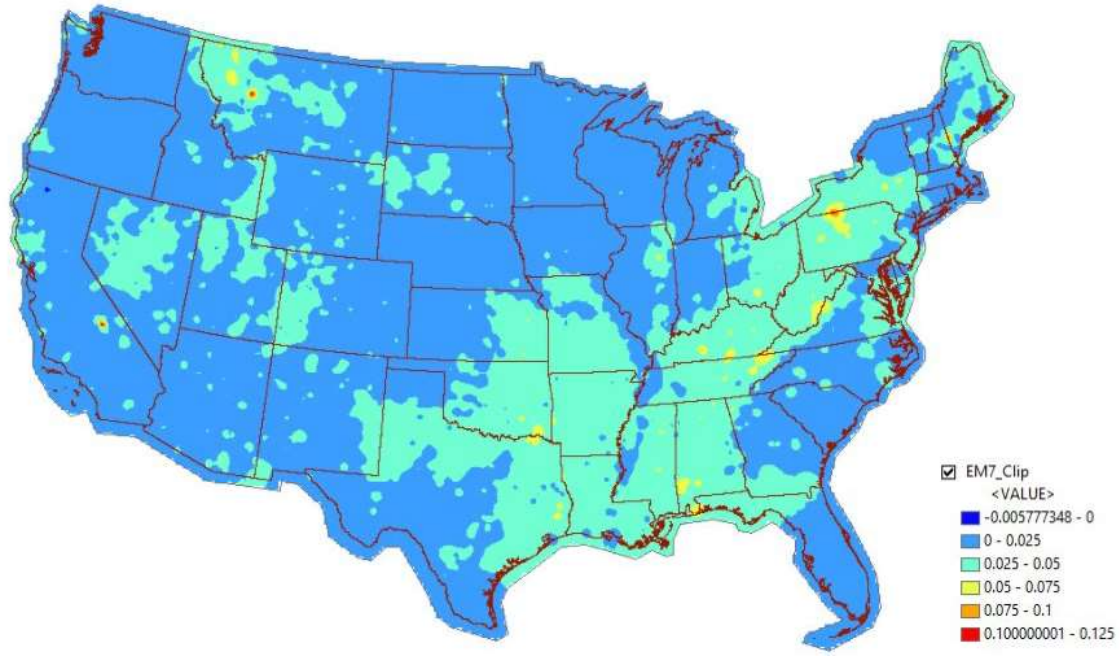

Figure 13. Endmember 7 distribution.

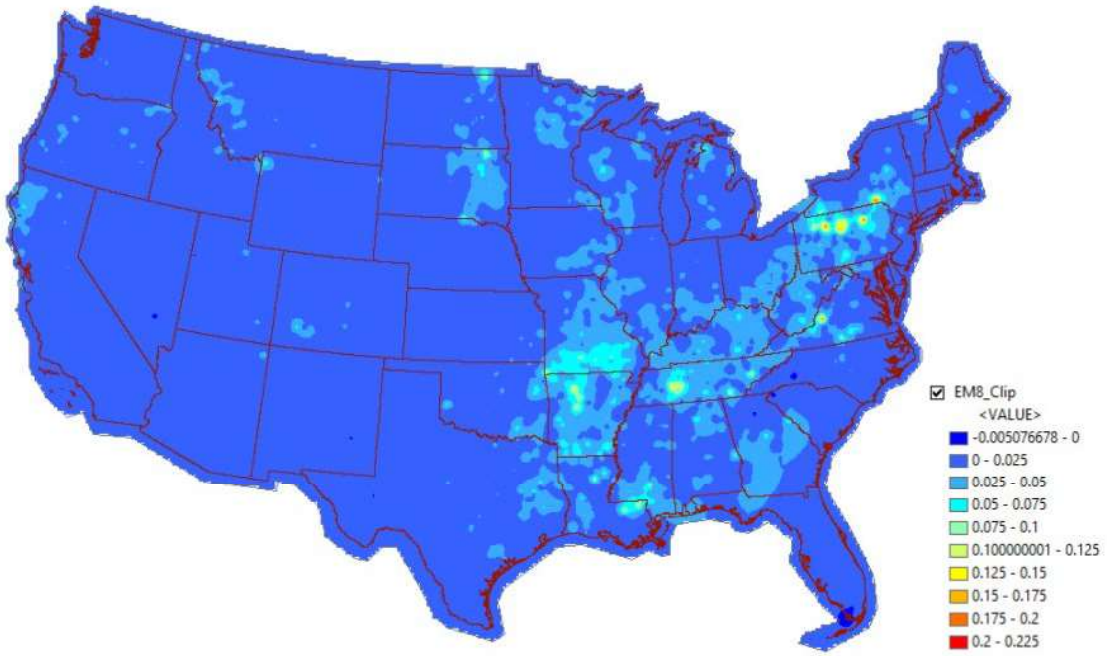

Figure 14. Endmember 8 distribution.

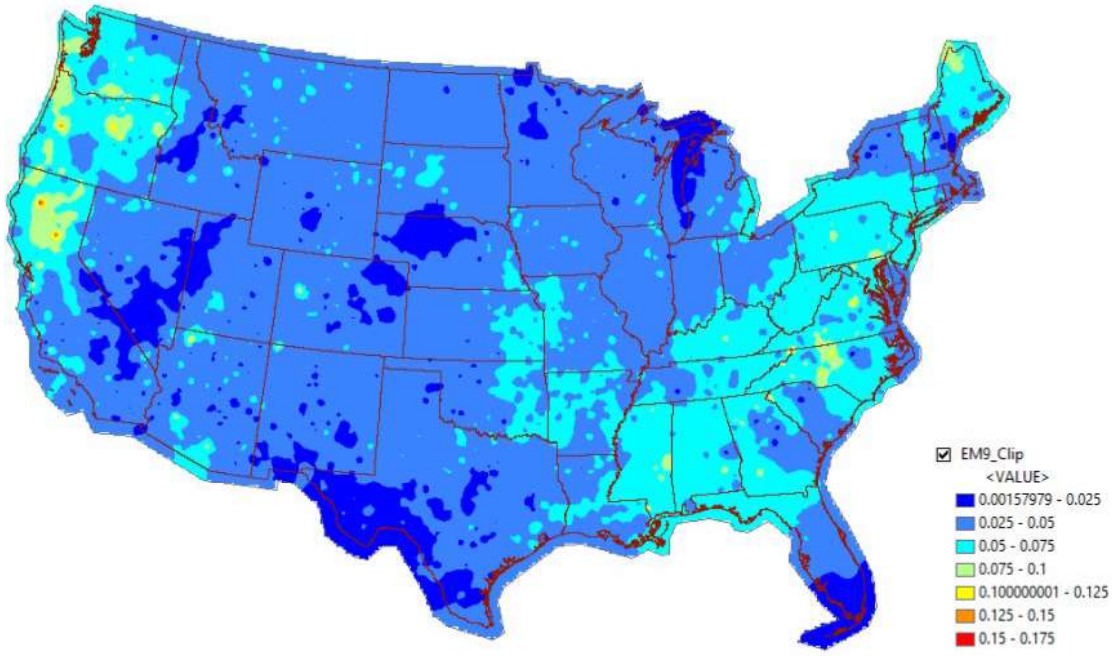

Figure 15. Endmember 9 distribution.

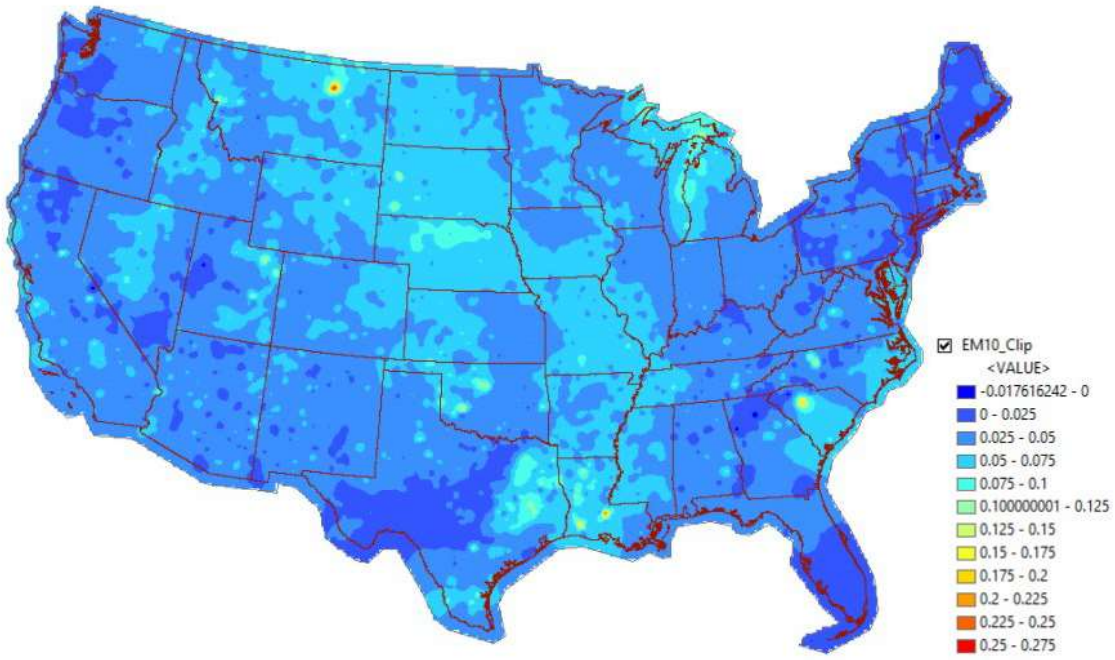

Figure 16. Endmember 10 distribution.

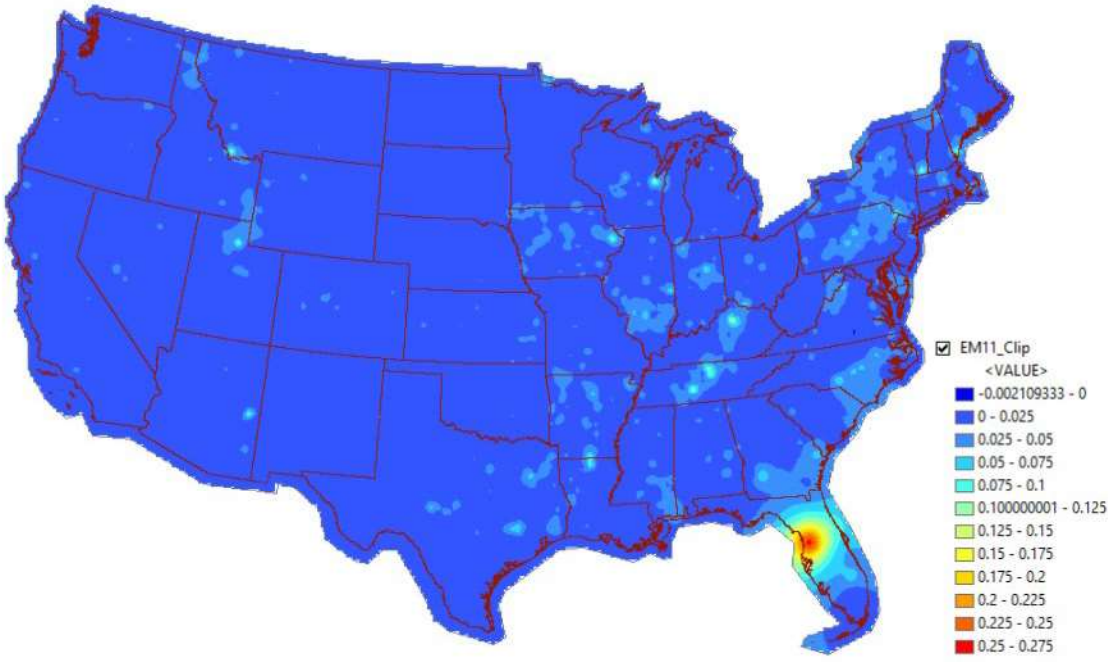

Figure 17. Endmember 11 distribution.

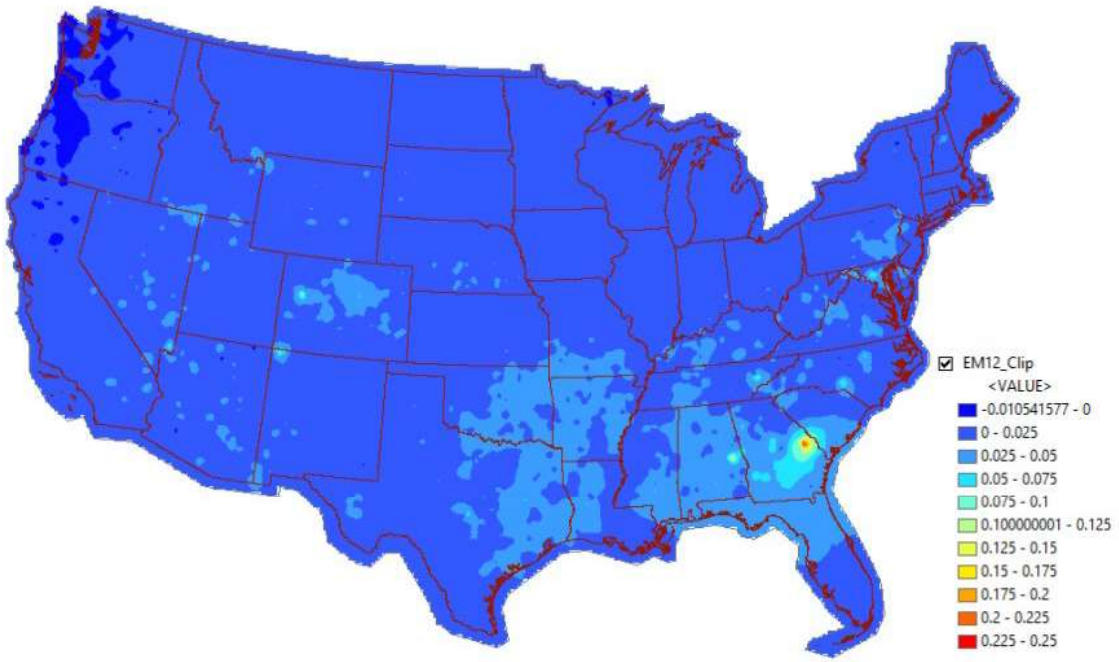

Figure 18. Endmember 12 distribution.

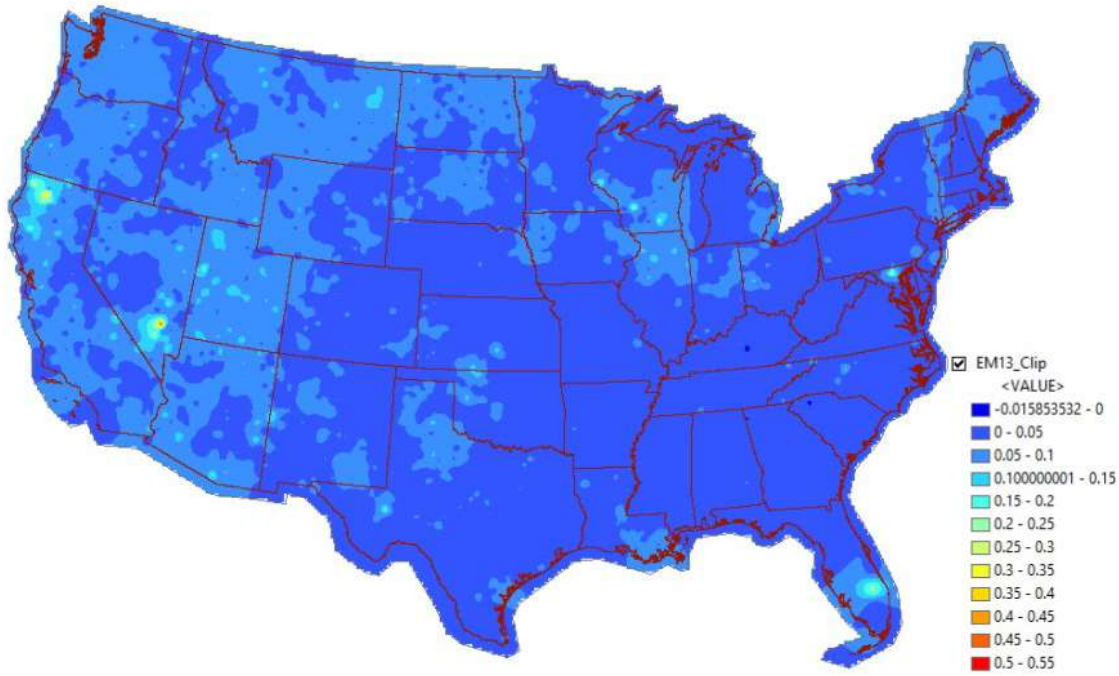

Figure 19. Endmember 13 distribution.

The high negative correlation coefficient in Table 3 between EM1 and EM2 is clearly supported visually in figures 7 and 8, where Figure 8 is the opposite of Figure 7. The high EM1 concentrations correlate well with the low EM2 concentrations. The high correlation between EM6 and EM9 can also be seen in figures 12 and 15. Though less detailed due to the fewer categories representing the low amounts of EM9, the concentration map shows areas of higher and lower concentrations which align with those in Figure 12.

1.3.4 Geochemical Maps

Figures 20-30 show the element maps in the Top 5 Horizon which correlate with one or more of the end-member maps. These elements are Ca, Na, Mg, Ba, Mn, K, Al, Sr, Sc, Ga, and Rb. The highest concentrations of Ca are found in southern Florida and central-southwestern Texas, as seen in Figure 20. Moderate concentrations are shown in western Utah and eastern and southern Nevada.

The geochemical map for Na shows the highest concentrations in the western and southwestern states, inset from the coast. Moderate Na concentrations are seen in some central and northeastern states, with the Atlantic coastal plains having the lowest concentrations (Figure 21). Figure 22 displays the geochemical concentration map for Mg which has areas of high concentration in northern California and southern Nevada. Other smaller areas of high concentration are mainly found in surrounding states, such as Arizona, Montana, Oregon, and Utah. Concentrations of Ba are highest in Montana, with Idaho, Nevada and southern California displaying large areas of high levels also (Figure 23). Manganese displays elevated concentrations in the Pacific Northwest and in a V-shape starting in eastern North Dakota, down to Missouri and Tennessee, and up along the Appalachians to New York (Figure 24). Figure 25 displays high concentrations of K in a C-shape, in the southwestern U.S., from Colorado, up through Wyoming and Idaho, down through Nevada and the lower half of California, and along southern Arizona and through southwestern New Mexico and ending in southwestern Texas. These areas of high concentration surround low concentrations in Utah and northern Arizona. The geochemical map for Al (Figure 26) shows high concentrations along the west coast, in Washington, Oregon, Idaho, California, and Nevada, with the highest primarily in Oregon and northern California. The concentrations of Sr (Figure 27) show a similar pattern to that of Na, though to a lesser extent. The highest concentrations of Sr can be found in the western and southwestern states, as well as in southern Florida. Concentrations of Sc are highest in the Pacific Northwest (Washington, Oregon, and northern California) and Arizona (Figure 28). The concentration map of Ga (Figure 29) is identical to that of Al, and Rb (Figure 30) is similar to that of K.

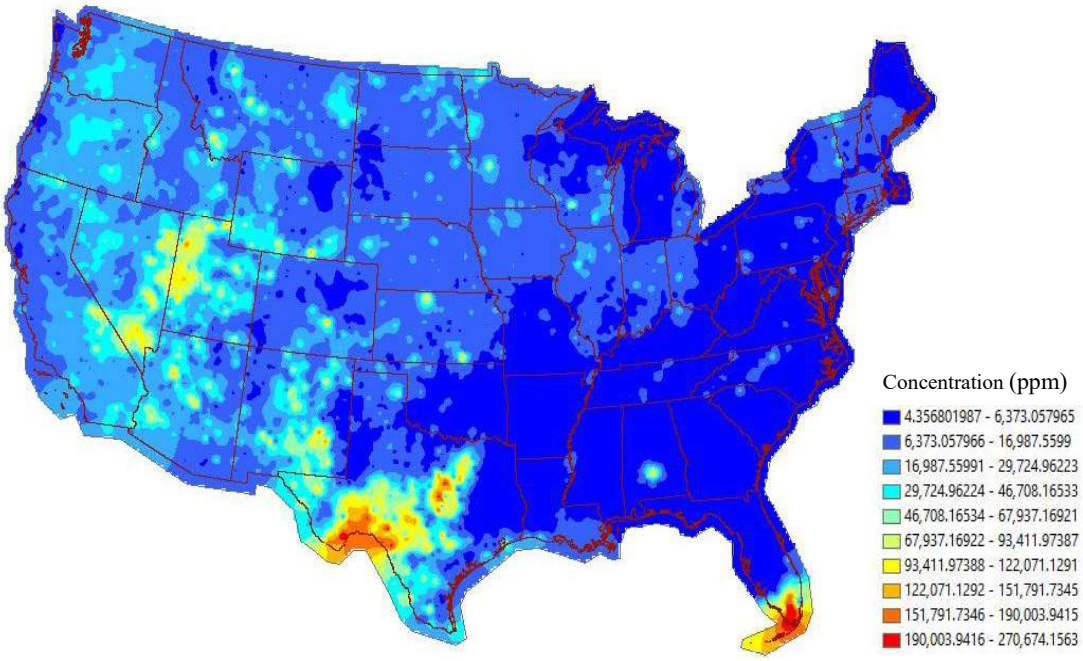

Figure 20. Geochemical concentration map for Ca. Red indicates high concentration, blue indicates low concentration. The highest Ca concentrations are in southern Florida and central-southwestern Texas.

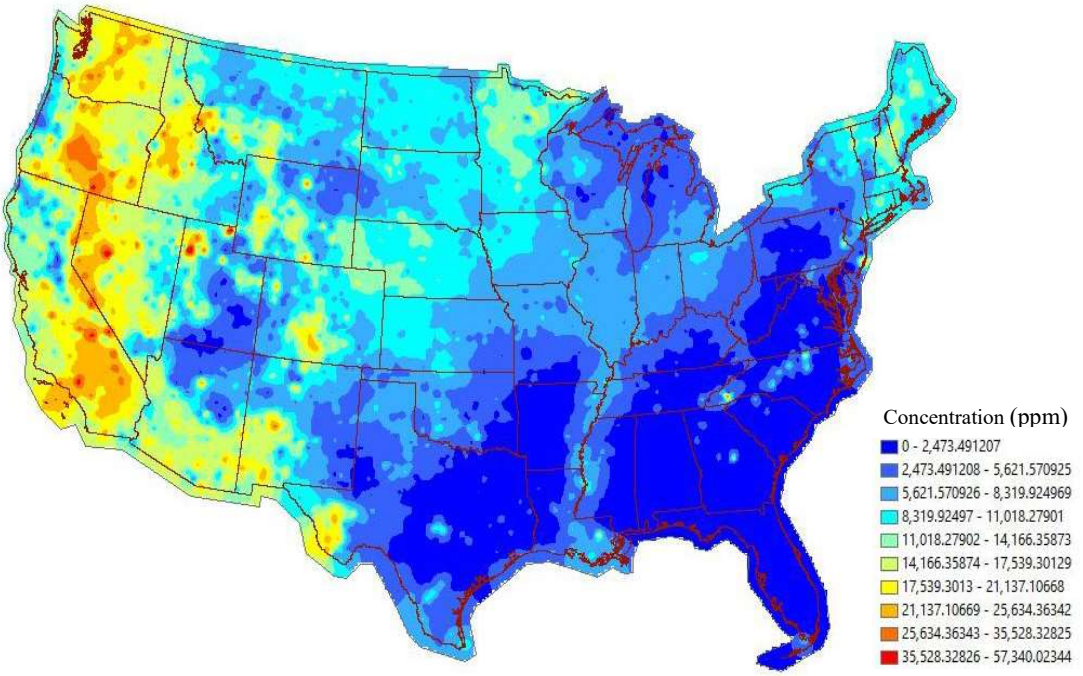

Figure 21. Geochemical concentration map for Na. High concentrations (red) are found in the western and southwestern states.

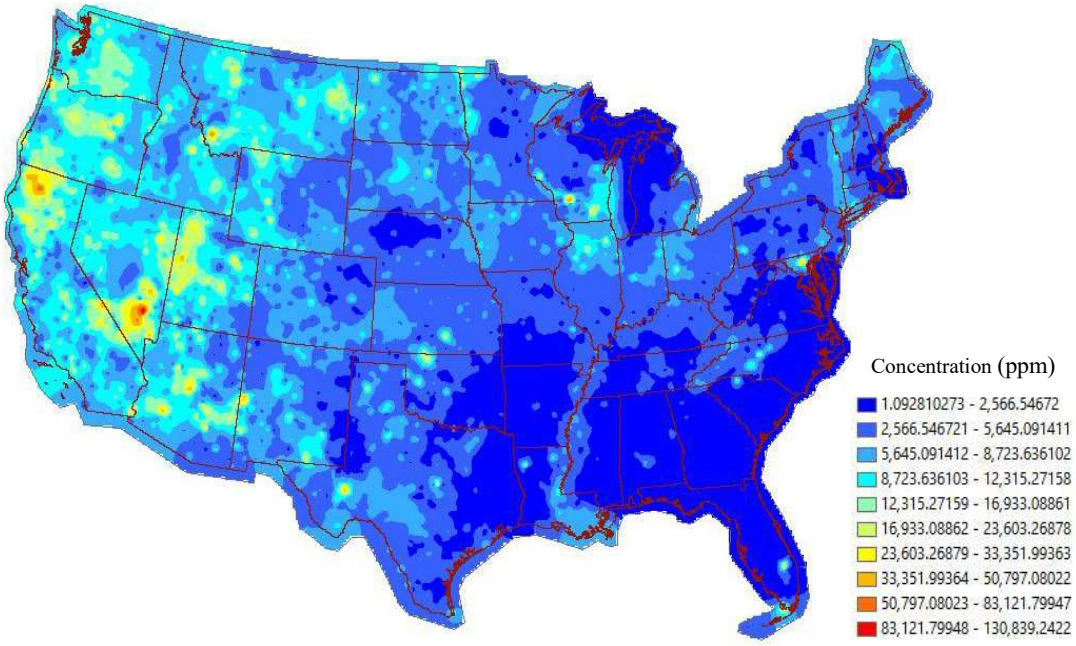

Figure 22. Geochemical concentration map for Mg. Areas of high concentrations are found in northern California and southern Nevada.

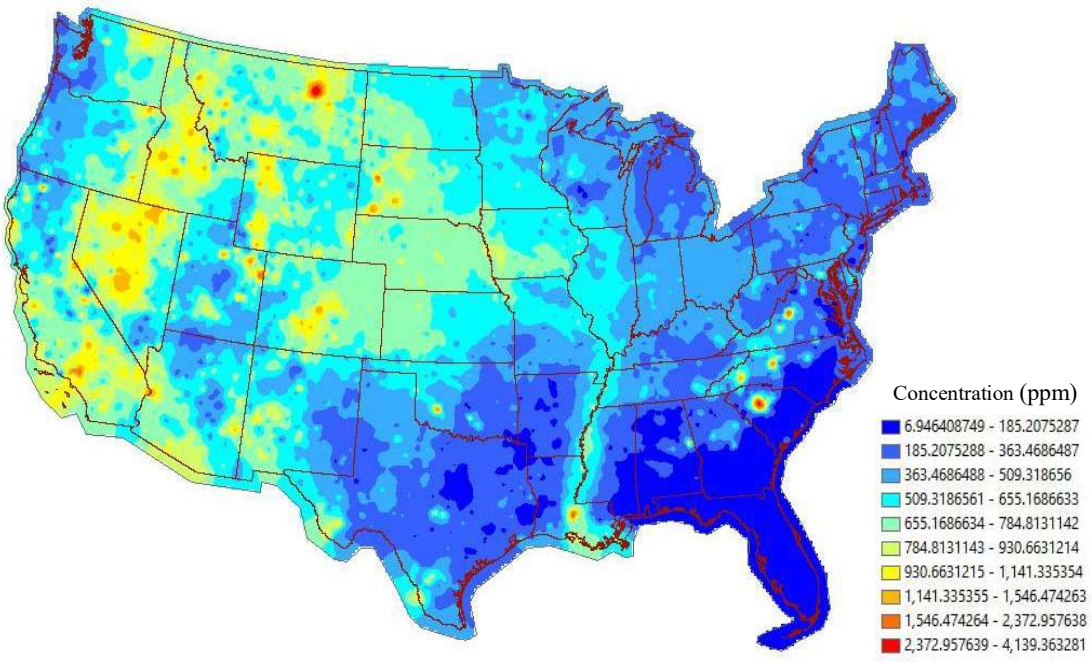

Figure 23. Geochemical concentration map for Ba. The highest concentration is found in northern Montana, with high concentration areas through Idaho, Nevada and into southern California.

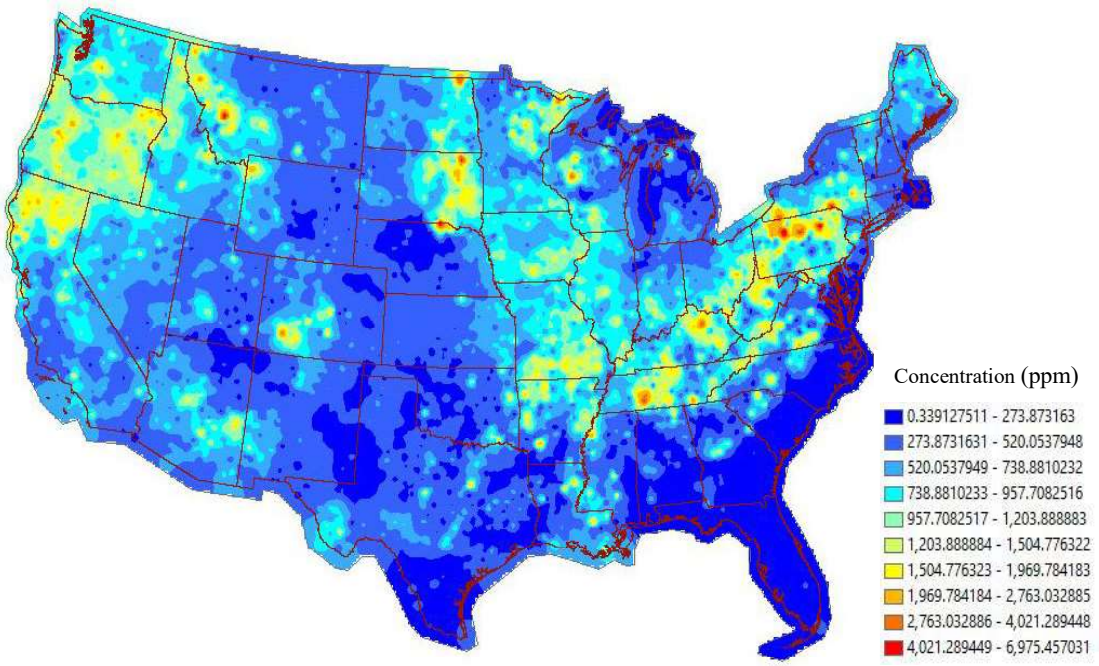

Figure 24. Geochemical concentration map for Mn. Highest concentrations are found in the northeast, Midwest, and northwest.

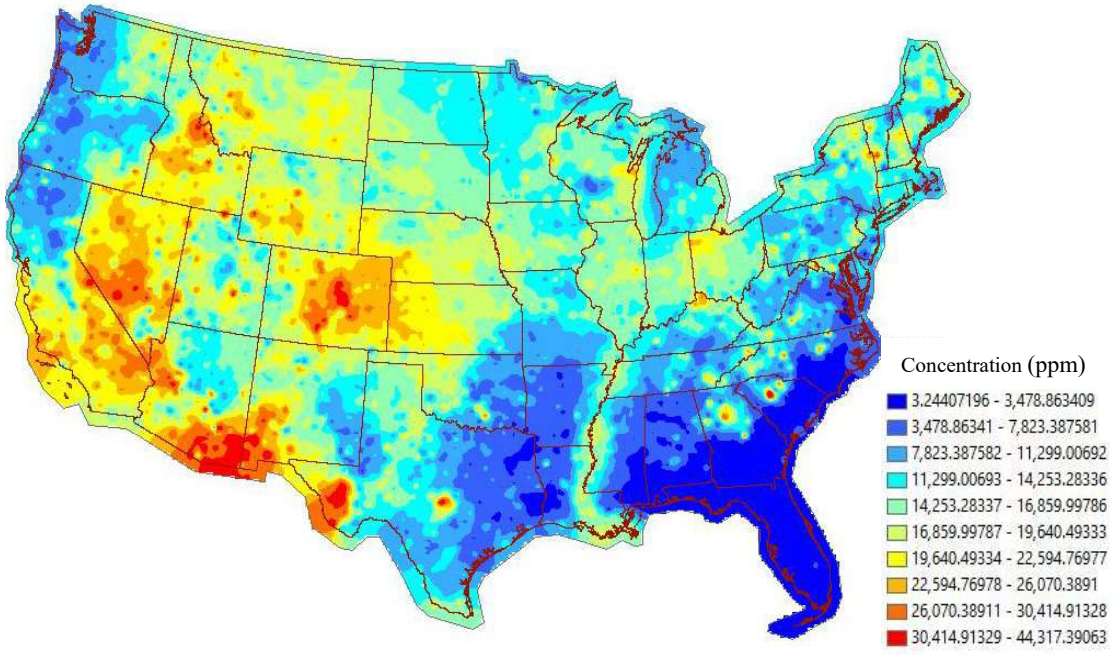

Figure 25. Geochemical concentration map for K. Areas of high concentration form a C-shape in the southwestern states, from Colorado, up to Idaho, down through Nevada and southern California, and along southern Arizona and New Mexico, and into Texas.

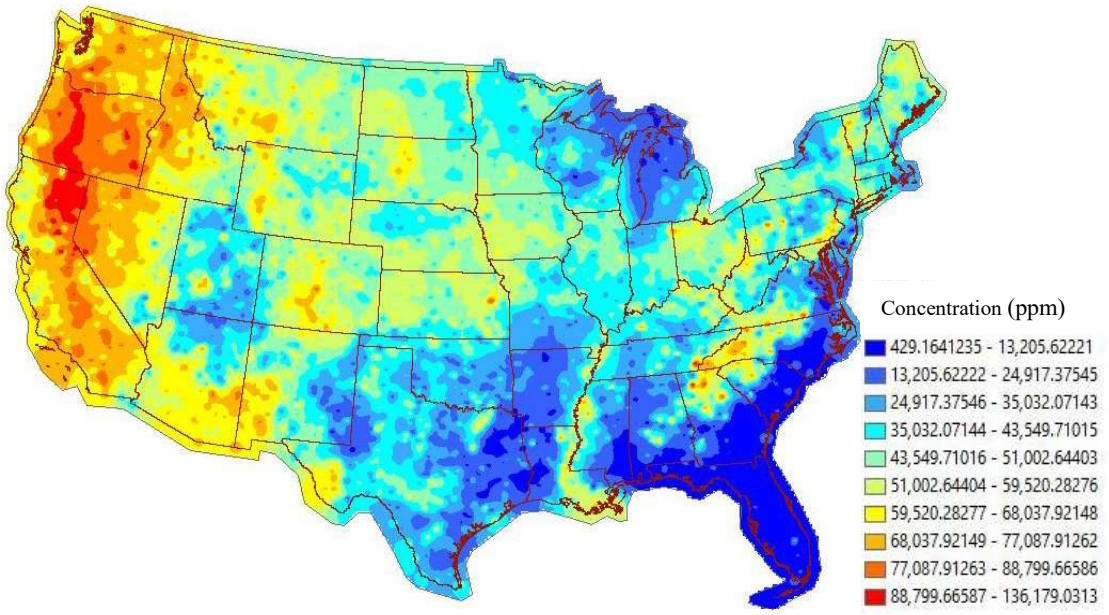

Figure 26. Geochemical concentration map for Al. High concentration are found along the west coast, primarily in Oregon and northern California.

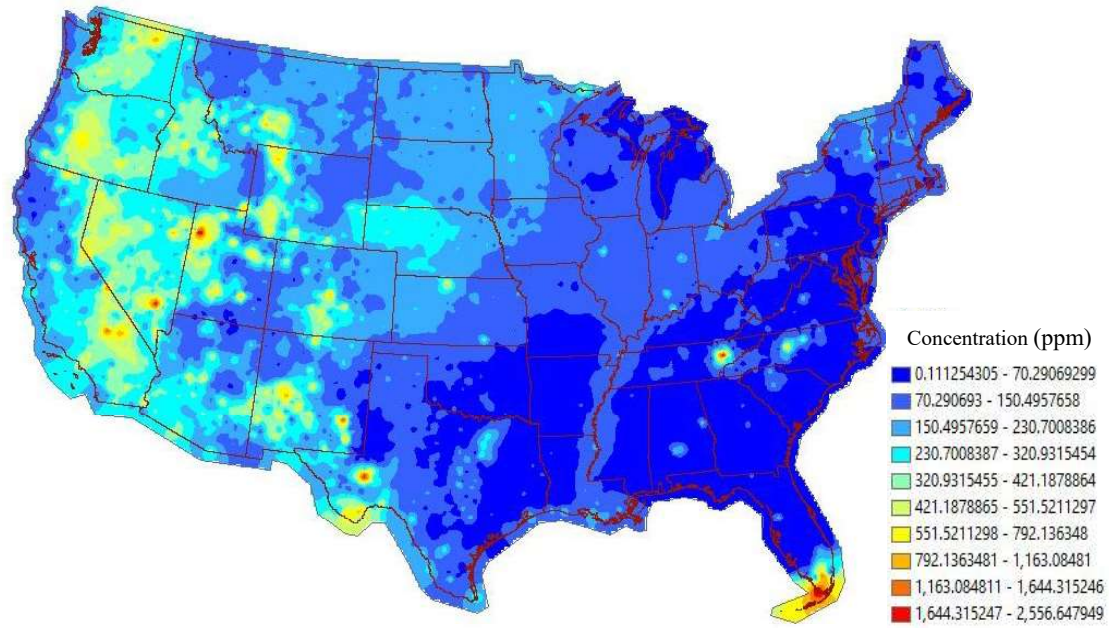

Figure 27. Geochemical concentration map for Sr. High concentrations are found in southern Florida, and western and southwestern states.

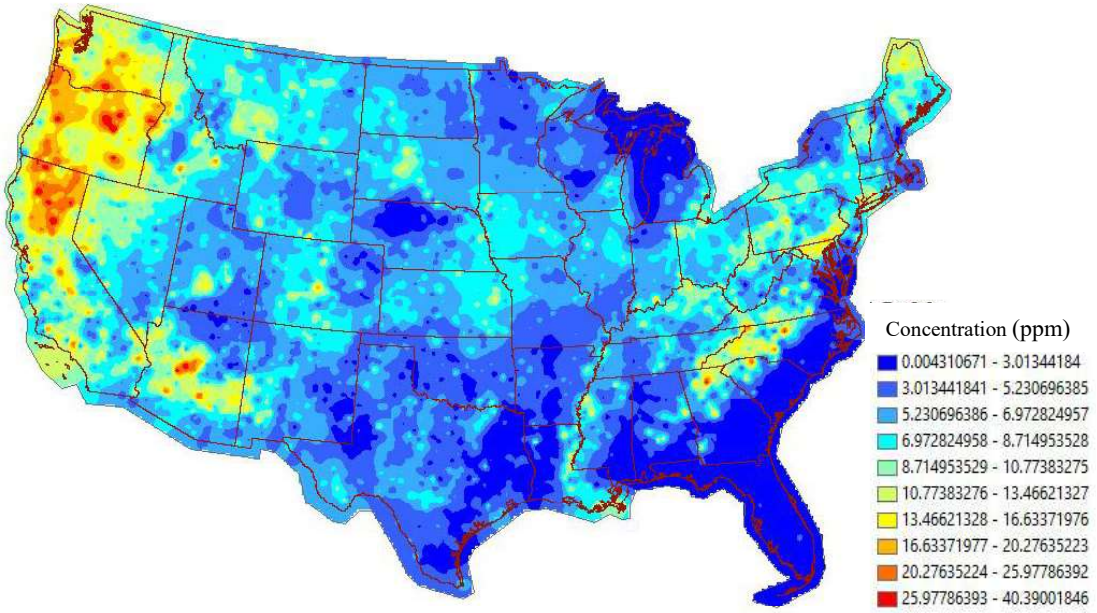

Figure 28. Geochemical concentration map for Sc. High concentrations are found in the Pacific Northwest, with high concentrations also in Arizona.

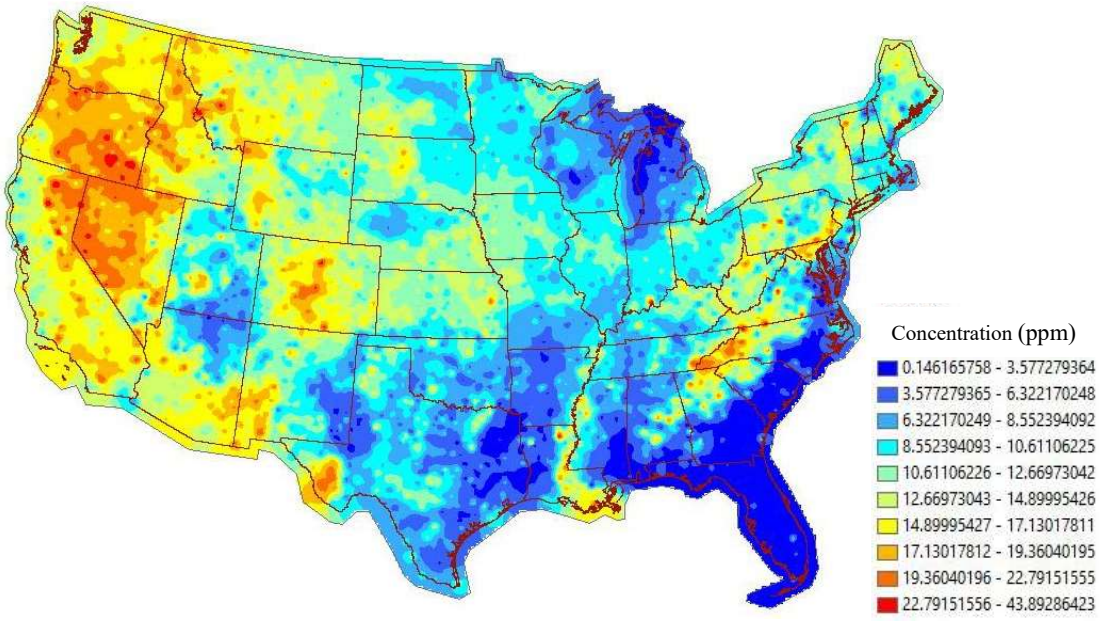

Figure 29. Geochemical concentration map of Ga. Highest concentrations are found in the western states, and distribution is identical to that of Al.

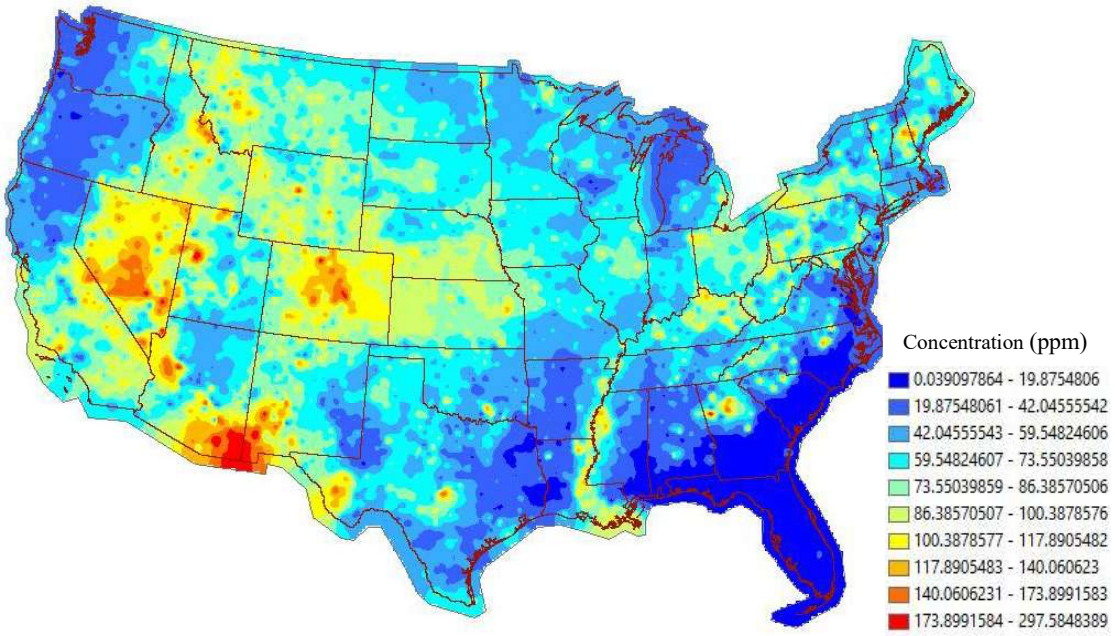

Figure 30. Geochemical concentration map of Rb. Highest concentrations form a C-shape in the southwestern states, similar to the concentration distribution of K.

The high positive correlation coefficients for EM2-Ca, EM4-Na, and EM13-Mg are clearly supported by the concentration maps, as expected (Figure 31). As shown in Table 1, EM2 is composed of 99.9% Ca, EM4 is composed of 97.6% Na, and EM13 is composed of 97.6% Mg, so the concentration maps should be relatively identical to the EM maps. Differences are due to the legend and scale differences in concentrations and relative proportions. The strong negative correlation between EM1 and Ca is identical to that of EM1-EM2, as EM2 is primarily Ca in composition (Figure 32).

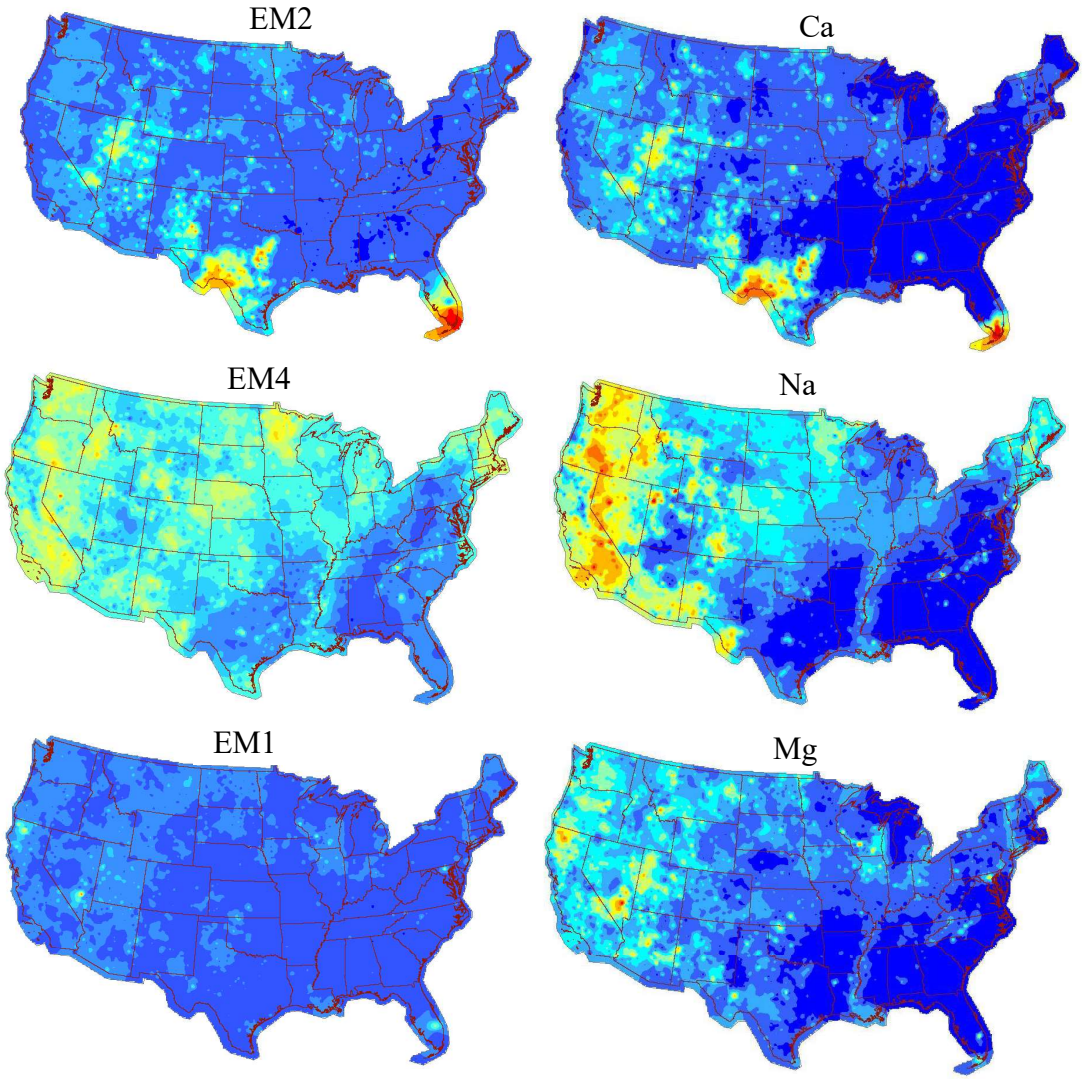

Figure 31. EM and element maps for high correlation pairs.

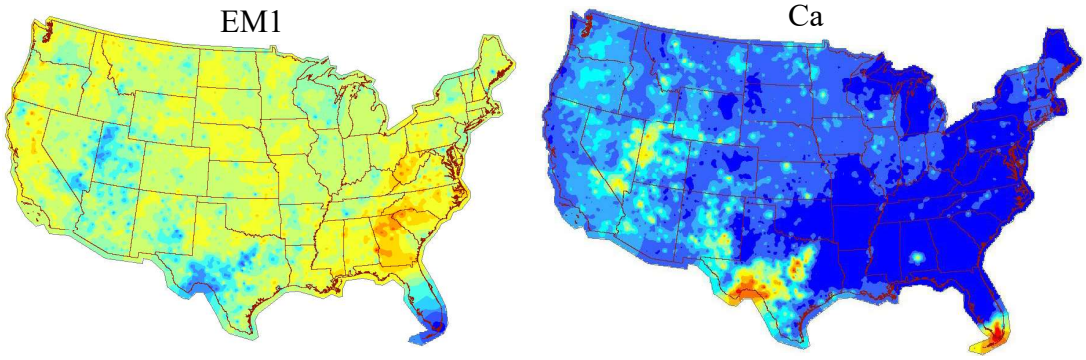

Figure 32. Strong negative correlation between EM1 and Ca maps.

1.3.5 GIS Map Layers

Figures 33-38 display the data for the other GIS layers created for comparison with the soil geochemical data. The geological map (Figure 33) shows basement geology and was used to identify the geological unit for each of the extreme sample locations. This information was used to determine whether the PVA compositions of these extreme samples are plausible. The mining locations data (Figure 34) is used to identify any locations where elements are mined, or have been mined, and correlate with the geochemical concentration maps. This is the same for the Superfund sites, where the data is used to determine if they influence any of the surrounding soil compositions (Figure 35). Land Cover data (Figure 36), soil classification (Figure 37), and soil pH data (Figure 38) are used to identify any patterns in the spatial distribution of elements.

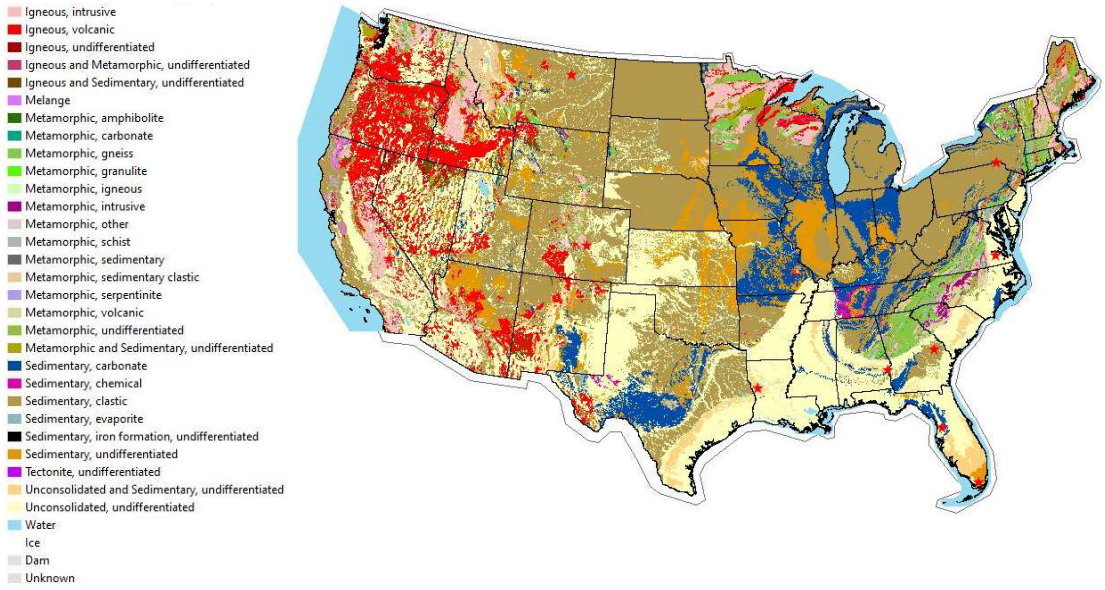

Figure 33. Geological map of the US showing basement geological units.

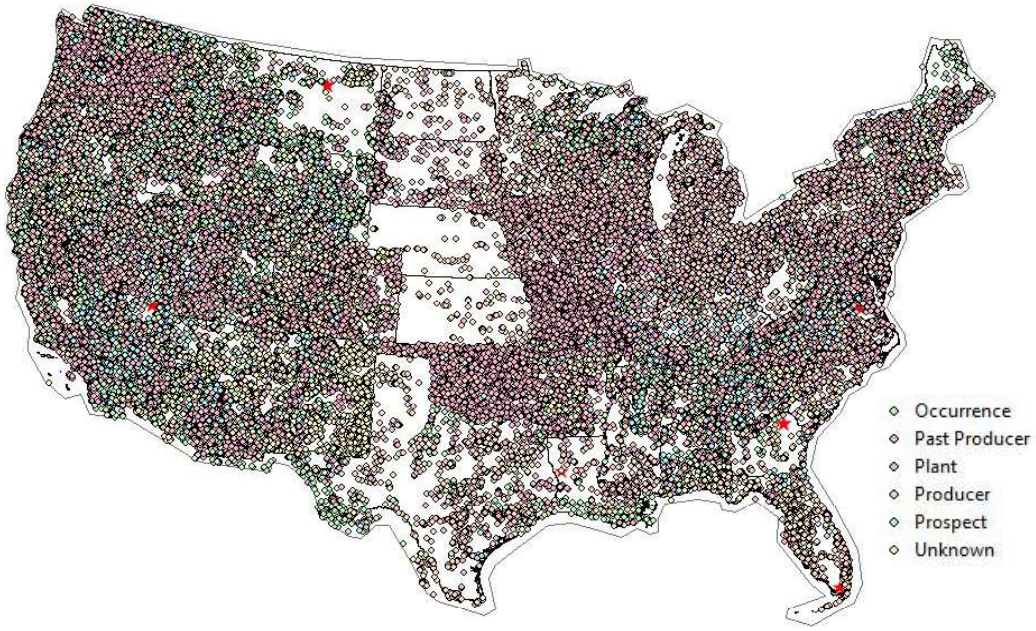

Figure 35. All past, current, and prospective mining locations across the continuous U.S.

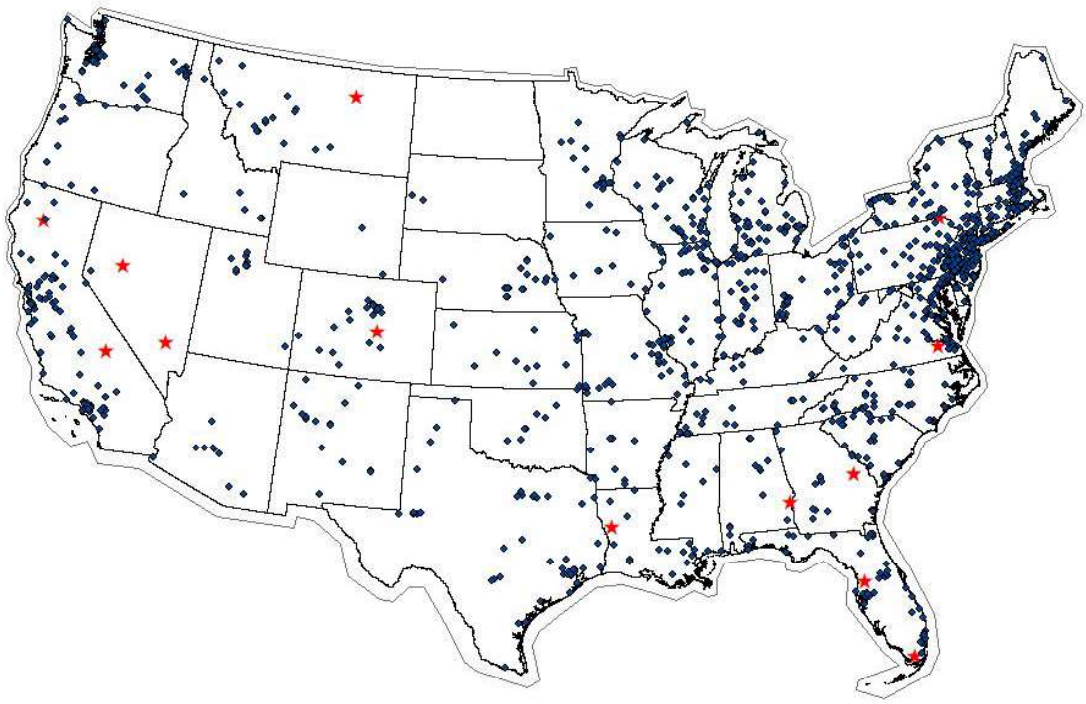

Figure 34. U.S. Superfund sites. Red stars show the locations of the extreme EM samples.

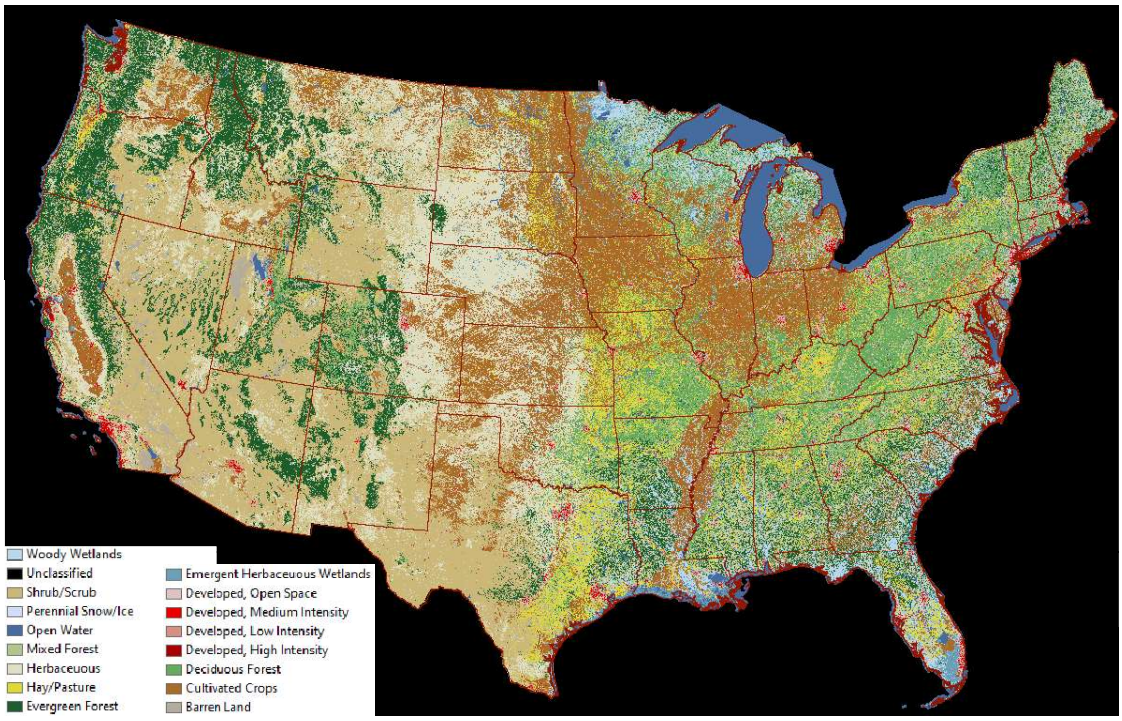

Figure 36. NLCD 2011 Land Cover.

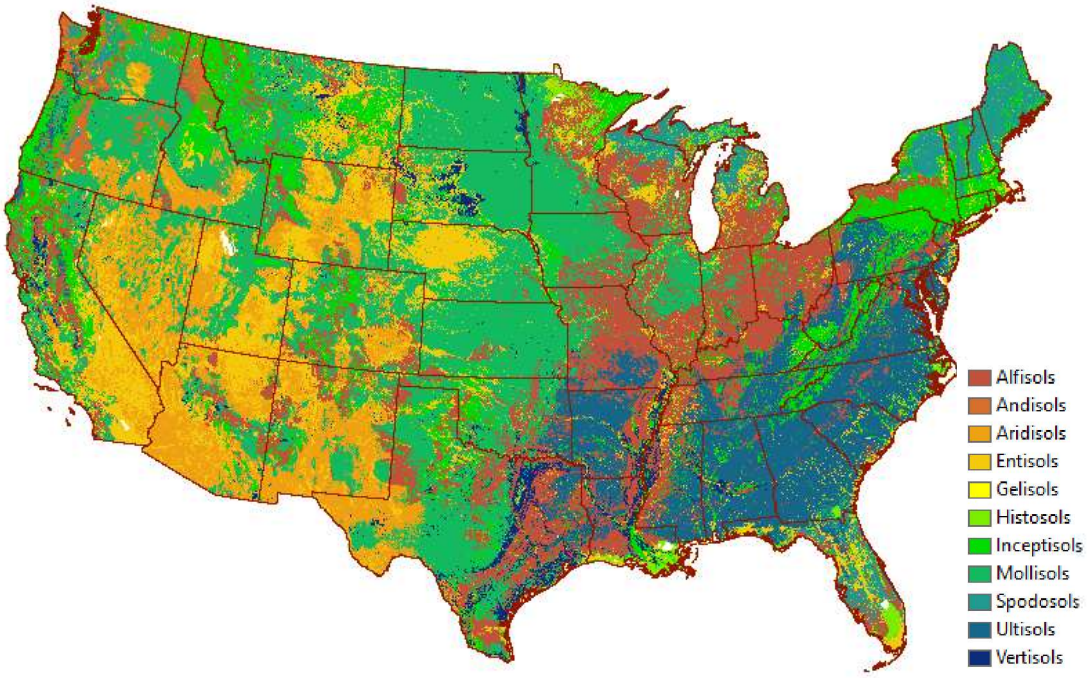

Figure 37. Soil classification map of the contiguous U.S.

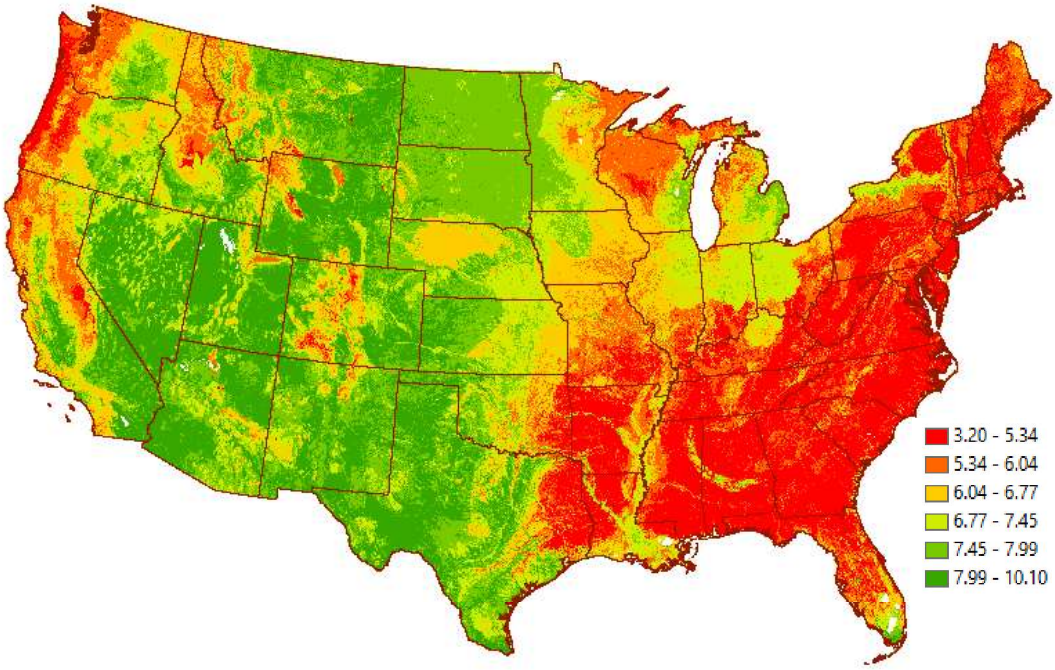

Figure 38. Soil pH map of the contiguous U.S.

1.3.6 Layer Comparisons

1.3.6.1 Geology

The geological units for the 13 extreme endmember samples were looked at to determine whether the endmember compositions make sense at each location. The data for each unit composition is found on the mineral resources site by the USGS. It should be noted that the endmember compositions and extreme samples were based on element concentrations in the Top 5 horizon, and the geological unit would be more closely represented by the C horizon.

Sample AL5408 is located within the high terrace deposits in eastern Alabama and is represented by ~0.6 EM1 and ~0.2 EM6 which equate to a composition of approximately 60% aluminium and 20% iron. The geological units of the high terrace deposits include ferruginous sand, silt, and clay, meaning high levels of aluminium and iron are expected. The geochemical maps for these elements however do not show high concentrations in this area, but instead further north, at the southern end of the Appalachian Mountains. As the maps are interpolated images, the high point concentration is not reflected; in the Top 5 horizon, sample location AL5408 has an Al concentration of ~81,000 ppm and Fe concentration of ~32,000 ppm, whereas the state average for those elements is ~22,000 ppm and 13,000 ppm respectively. The C horizon concentrations are much lower at this sample point: 5000 ppm for Al and 3000 ppm for Fe, where state averages are ~49,000

ppm and 26,000 ppm respectively, and A horizon concentrations are lower. This would imply transportation from other areas which accumulate in the surficial soils.

Sample ID FL48 is in southern Florida and is composed of ~0.9 EM2 which means a composition of 90% calcium. The geological unit at this location is the Miami Limestone, which is consistent with the endmember composition and the element concentration maps in each of the three soil horizons. In the Top 5 horizon, Ca concentration is over 300,000 ppm, where the state average based on available samples is ~26,000 ppm. In the C horizon, Ca concentration is 247,000 ppm and the state average is ~27,000 ppm. This shows that FL48 has a consistent amount of calcium across the three soil horizons and is well above the state average.

Sample CO8427 in central Colorado is represented by ~0.47 EM3 and ~0.3 EM1, equating to ~57% Al and ~43% K. The geological unit is the Denver Fm or lower part of the Dawson Arkose which is composed of shale, arkose, and mudstone, with high potassium feldspar content. The geochemical maps for aluminium in each horizon show moderate concentrations as there are other areas with much higher concentrations, however, potassium has very high concentrations around this sample site across all three horizons, as do the mineral maps for potassium feldspar. The potassium concentration in the Top 5 horizon is ~40,000 ppm and aluminium concentration at 40,000 ppm. The Colorado state average for potassium is ~23,000 ppm and for aluminium is ~53,000 ppm. The sample site and state average concentrations are similar for both elements in the A horizon and there is no data for that location in the C horizon. Available data is consistent with a geological source to the endmember composition.

Sample NV1871 in western Nevada and is composed of ~0.3 EM4 and ~0.24 EM1 which is a composition of ~30% Na and ~25% Al. The geological unit is alluvium composed of detrital meaning unweathered sand, gravel, and plagioclase feldspar could be the source of the endmember composition. The geochemical maps for Na are consistent across the soil horizons, all showing high concentrations. Aluminium displays higher concentration in the Top 5 horizon and moderate concentrations in the C horizon. The mineral map for plagioclase feldspar displays high concentrations at this location. In the Top 5 horizon, concentrations of Al and Na at the sample location are ~62,000 ppm and ~64,000 ppm respectively, and the state average for Nevada is ~66,000 ppm and ~16,000 ppm for Al and Na respectively, showing that the EM sample has lower than average Al, but much higher-than-average Na. In the C horizon, the point concentration for Al is ~78,000 ppm, which is higher than the state average of ~65,000 ppm, and for Na the point concentration is 14,500 ppm, which is lower than the state average of ~15,000 ppm. This implies a strong geological source, especially for Al, but transportation and accumulation of Na in the topsoil to reach the concentrations measured at the sample site.

Sample VA5020 in eastern Virginia is represented by a more diverse composition: ~0.3 EM5, ~0.2 EM1, and ~0.2 EM6, meaning a composition of ~27% Al, ~23% Fe, ~17% Ti, and ~2% K. VA5020 is within the Bacons Castle Formation which is composed of unconsolidated detrital of gravel, sand, silt, and clay. The element concentrations in the Top 5 horizon at this site are ~7400 ppm Al, ~5000 ppm Fe, ~2000 ppm K, and ~5000 ppm

Ti where the average concentrations for the state are ~37,000 ppm Al, ~20,000 ppm Fe, ~9000 ppm K, and ~4000 ppm Ti. Titanium is the only element with higher concentrations at the sample location than the state average concentration. In the C horizon, the sample location concentrations are ~31,000 ppm Al, ~17,000 ppm Fe, ~1000 ppm K, and ~5000 ppm Ti. As with the Top 5 horizon, Ti is the only element with concentrations in the sample that is similar to the state average. The other elements have much higher average concentrations. This suggests a consistency between the sample and EM composition and the geological composition of the area.

LA11852 is in the western part of the Louisiana and is composed of ~0.7 EM6, which is represented by ~70% Fe. This is located within the Cook Mountain Formation composed of clay, marl, and banded-iron formations, therefore having a higher iron content in the local geology. The geochemical maps display high concentrations of Fe in in the sample area, and much lower concentrations throughout the rest of the state in all horizons. In the Top 5 horizon, Fe concentrations are ~85,000 ppm compared to the state average of ~17,000 ppm and in the C horizon, concentrations are ~120,000 ppm compared to the state average of ~25,000 ppm, suggesting a strong geological component to the soil Fe content.

CA8143 is in central California and has low endmember proportions: ~0.22 EM1 and ~0.17 EM7 which means a composition of ~22% Al, ~9% Na, ~8% Ca, and ~2% Mg. The sample location is with the Quaternary alluvium and marine deposits which consist of unconsolidated detrital (alluvial, terrace and lacustrine). The geochemical maps show high concentrations of Al and Na at this location, and moderately low concentrations of Mg and Ca across all three horizons. In the Top 5 horizon, the concentrations of the sample are ~59,000 ppm Al, ~56,000 ppm Ca, ~18,000 ppm Mg, and ~46,000 ppm Na compared to the state average of ~72,000 ppm Al, ~22,000 ppm Ca, ~11,000 ppm Mg, and ~17,000 ppm Na. In the C horizon, point concentrations for Al and Mg (~73,000 ppm Al and ~13,000 ppm Mg) are close to the state average of ~78,000 ppm Al and ~13,000 ppm Mg. The point concentrations for Ca and Na are much higher than the state average: ~57,000 ppm Ca, and ~30,000 ppm Na compared to ~25,000 ppm Ca, and ~17,000 ppm Na. The relative different between the C horizon concentrations and the topsoil indicates the endmember for surficial soils is consistent with the local geology.

Sample PA6369 is located in northwestern Pennsylvania in the Catskill geological formation which is composed of sandstone, mudstones, and siltstone. The sample endmember proportions are ~0.25 EM8 and ~0.2 EM1 (~32% Al, ~9% Mn, and ~1% P). The geochemical maps show low Al concentrations, moderate P, and high Mn in the Top 5 horizon and lower concentrations in the C horizon. Top 5 concentrations of Al, Mn, and P are ~26,000 ppm, ~5700 ppm, and ~1100 ppm respectively compared to the state average of ~44,000 ppm, ~1300 ppm and ~900 ppm. In the C horizon, state average and sample concentrations for Al are both ~58,000 ppm while Mn and P concentrations are both ~1000 ppm in the sample, compared to the state average of ~800 ppm and ~500 ppm respectively. Aluminium concentrations are much higher in the C horizon than in the topsoil, Mn concentrations are lower, and P concentrations are similar, indicating that the phosphorus isn't transported after weathering of the bedrock.

CA3871 is located in northern California in the Paleozoic metavolcanics rocks consisting of mafic and felsic volcanics as well as sedimentary mudstones, conglomerates, and sandstones. The endmember proportions are ~0.25 EM1, ~0.2 EM6, and ~0.118 EM9 giving a composition of ~39% Al, ~27% Fe, and ~1% Ti which is consistent with bedrock geology. The geochemical maps display high Al and Fe concentrations around this sample and moderate Ti concentrations in each of the soil horizons. Aluminium has a concentration of ~72,000 ppm in the Top 5 horizon which is identical to the state average concentration, and over 100,000 ppm in the C horizon, which is much higher than the average of ~78,000 ppm. Iron has a Top 5 concentration of ~53,000 ppm and a C horizon concentration of ~76,000 ppm. State average concentrations are ~34,000 ppm for the Top 5 and ~39,000 ppm for the C horizon. Titanium concentrations very similar across the horizons and to the state average (~4000 ppm), with the Top 5 sample containing closer to 3000 ppm.

Sample MT9582 endmember proportions are ~0.3 EM10, ~0.2 EM1, and ~0.2 EM6, relating to ~30% Al, ~30 Fe, ~6% K, and ~2% Ba. The geological unit for this sample is the Bearpaw Formation, composed of shale and bentonite. Geochemical maps show Al, Fe, and K to be moderate across the horizons but Ba has high concentrations in the Top 5 and low in the C horizon. The state average concentration for the Top 5 and C horizons are identical (~56-59,000 ppm Al, ~25,000 ppm Fe, ~18,000 ppm K, and ~800 ppm Ba). The sample concentrations in the topsoil are identical to the averages for Al and K but much higher for Fe and Ba (~55,000 ppm and ~5000 ppm respectively). In the C horizon, Al has a concentration of ~74,000 ppm, Fe ~44,000 ppm, K ~23,000 ppm, and Ba ~800 ppm. The difference in the amount of Ba between the topsoil and the C horizon suggests Ba-rich material was transported and accumulated in this area providing the source for this component of EM10.

FL480 is located in western Florida and is part of the Hawthorn Group which is comprised of detrital (sand and clay) and incidental phosphorite. This accounts for the endmember proportions of ~0.25 EM11, ~0.25 EM1, and ~0.25 EM6 which relates to a composition of ~35% Al, ~30% Fe, and ~9% P. The geochemical maps display low Al and Fe content in all horizons, but high P content. Sample concentrations are much higher than the state averages. Concentrations in the Top 5 are ~18,000 ppm Al, ~14,000 ppm Fe, ~4000 ppm P, and in the C horizon ~ 35,000 ppm Al, ~12,000 ppm Fe, and ~4000 ppm P. The average concentrations in Florida are ~5000 ppm Al, ~2000 ppm Fe, and ~400 ppm P for the Top 5 and ~9000 ppm Al, ~4000 ppm Fe, and ~400 ppm P.

GA2208 is composed of Neogene sandstones and claystones in eastern Georgia. The sample contains ~0.26 EM12 and ~0.23 EM1 with an element composition of ~43% Al, ~2% Fe, and ~2% Ti. The geochemical maps do not reflect high concentrations in the Top 5 horizon but higher concentrations in the C horizon. The Top 5 has a sample composition of ~6000 ppm Al, ~3000 ppm Fe, and ~1000 ppm Ti compared to the state average of ~24,000 ppm Al, 11,000 ppm Fe, and ~2000 ppm Ti. The C horizon sample composition is ~63,000 ppm Al, ~29,000 ppm Fe, and ~2000 ppm Ti which supports a geological source to the soil sample composition. The C horizon averages are ~57,000 ppm Al, ~25,000 ppm Fe, and ~3000 ppm Ti.

Sample NV11887 in southern Nevada is composed of ~0.55 EM13 and ~0.25 EM2 which represents ~50% Mg and ~25% Ca. The geological unit for the sample is undifferentiated alluvium composed of detrital. Geochemical maps show moderate to high concentrations of Mg and Ca in each horizon as well as dolomite, accounting for the Mg and Ca in the soil samples. Magnesium concentrations at this site in the Top 5 are 136,000 ppm and Ca ~63,000 ppm. In the C horizon Mg has a concentration of ~74,000 and Ca 130,000 ppm. Local geology accounts for these high concentrations. The average Mg concentration in Nevada is ~12,000 ppm in the Top 5 and ~13,000 ppm in the C horizon. Calcium has an average concentration of ~35,000 ppm and ~53,000 ppm in the Top 5 and C horizon respectively.

1.3.6.2 Superfund Sites

When collecting soil sample data, the USGS were careful to avoid obviously contaminated sites, and to obtain samples away from roadsides. A total of 1309 NPL (National Priorities List) Superfund sites were plotted using GIS. Using the proximity tool in ArcMap, there are 56 sample locations within 5 km of an NPL superfund site, and five sample locations within 2 km of a superfund site, so highly contaminated areas were avoided.

Element concentrations at each of the superfund sites were extrapolated from the geochemical raster files. Given that the concentration scale varies from element to element, the concentration category, as opposed to amounts in ppm, was used to assess which areas have high concentrations of elements. Table (8) shows the number of superfund sites which have concentrations in the red and orange legend categories (1st and 2nd highest) for each element, and what the threshold concentration for that element is.

Table 8. Number of Superfund sites with element concentrations in the orange and red categories.

Element	**No. of Superfund sites in top 2 conc. categories**	**Lower conc. Limit (ppm)**
Al	31	77,087.91
Ag	1	2.74
Ca	1	151,791.73
Ce	2	152.13
Fe	3	59,891.43
Ga	19	19.36
K	15	26,070.39
La	3	77.35
Mn	2	2763.03
Na	2	25,634.36
P	2	3084.52
Rb	6	140.06

Sc	8	20.28
Sn	2	38.57
Sr	1	1163.08
Ti	2	11,054.09
V	1	241.34
Y	2	51.52

Of particular interest are those which have high concentrations in discrete points and are not widespread or abundant in the geochemical maps: Sn and Ag. The two NPL sites located in a high Sn concentration zone are in southwestern California. Tin has localized high concentrations in the Top 5 and A horizons but very low concentrations in the C horizon (~1 ppm compared to ~50 ppm in the A horizon). Of the numerous mining locations which include tin in the element list, none of them are located within the high concentration areas where the Superfund sites are. The nearest mine is ~70 km away, and the nearest sample is CA4535, ~4 km away. This suggests that the concentrations of Sn could be linked to the contamination produced by the Operating Industries, Inc. Landfill which has the highest Sn amounts of the NPL sites. Most other Superfund sites with similarly high Sn concentrations are in this area and may be the product of interpolation from the few sample points in proximity.

The second element of interest is silver. The Bonita Peak Mining District NPL site has an interpolated Ag concentration of 3.46 ppm and the California Gulch NPL site has a concentration of 2.5 ppm. The nearest sample location to each is CO2715 (~18 km away) and CO4315 (~4 km away) respectively. Both site locations show high silver concentrations in the Top 5 and A horizons, but only the site NPL site shows high concentrations in the C horizon also. The high amounts of silver in the soil and the contamination of these areas can be explained by the mining activity which left heavy metals in the soil and groundwater. This region is inundated with mines, past and present, which list silver as one of the elements mined.

1.3.6.3 Mining

There are over 250,000 mines mapped in the GIS mining layer including past producers and present producers. The publication data of the data used was 2005 which is a couple of years prior to the collection of the soil samples, and some records were updated in 2016. Every geochemical map shows mining locations within the highest concentration category (red), though there may be fewer of them due to the effects of interpolation and the density of mining points in comparison to sample points.

The elements of primary interest in relation to mining activities are those which contribute to endmembers. This is because these elements were in the extreme sample compositions defining those endmembers. Table 9 shows how many of the mines list the elements comprising portions of the endmember compositions. As the table shows, there are

hundreds-to-thousands of mining locations covering each element. Some high concentrations in the topsoil may be accumulated products from mining operations.

Table 9. Number of mines listed for each element comprising endmember compositions.

Element	No. of mines with element in code list
Al	1929
Ba	3593
Ca	736
Fe	18,805
K	1411
Mg	734
Mn	8205
Na	715
P	561
REE	1015
Sr	180
Ti	1359
Zn	20,803

1.3.6.4 Land Cover, Soil Order and Soil pH

Correlation with the three additional raster layers (land cover, soil order and soil pH) shows there is moderate positive correlation between the land cover type and the pH (correlation coefficient of 0.43). The average pH for each land cover type is displayed in Table 10. The data shows that, on average, barren land is more alkali and developed land is more acidic. There was no correlation between land cover and element concentrations, or land cover and soil order.

Table 10. Average pH based on land cover type.

Land Cover Category	Average pH
Barren	8.06
Developed	5.64
Forested Upland	5.87
Herbaceous Upland	7.37
Non-Natural Woody	6.78
Planted/Cultivated	6.70
Shrubland	7.93

The average soil pH for each soil order is presented in Table 11. There was weak negative correlation between soil order and pH (-0.25). Most soils range from a pH of 3.5 to 10,

with drier areas having a higher range than wetter areas (Queensland Gov, 2016). A pH value below 6.5 represents acidic soil, 6.5-7.5 is neutral, and over 7.5 represents alkaline soil. As shown in the table, aridisols are the most alkali with an average pH of 8.12 and Ultisols are the most acidic with an average pH of 5.05. According to the Queensland Government site (2016), a pH below 5.5 is considered strongly acidic, which encompasses Ultisols and Spodosols, and could be caused by factors such as aluminium or manganese toxicity, or calcium or magnesium deficiency. As seen in the geochemical maps, the Atlantic coastal plains, primary to these acidic soil orders, have very low concentrations of magnesium and calcium. Table 12 shows the elements that have a correlation coefficient >0.3 with soil pH. Calcium, magnesium, and aluminium all have moderate positive correlation with pH. Soil pH was the only layer to have any correlation, with eight elements showing moderate positive correlation with pH. There was no correlation between soil order and element concentrations.

Table 11. Average pH based on soil order.

Soil Order	**Average pH**
Alfisols	6.47
Andisols	6.04
Aridisols	8.12
Entisols	7.38
Histosols	6.59
Inceptisols	6.31
Mollisols	7.40
Spodosols	5.43
Ultisols	5.05
Vertisols	7.37

Table 12. Correlation coefficients for elements with >0.3 correlation with soil pH.

Element	**Correlation Coefficient**
Potassium	0.52
Barium	0.43
Rubidium	0.40
Strontium	0.40
Calcium	0.40
Sodium	0.37
Magnesium	0.36
Aluminium	0.31

1.4 Discussion

1.4.1 Endmembers

Endmember soil sample compositions were compared with geological units and descriptions obtained from the USGS Mineral Resources Online Spatial Data Geological Maps (https://mrdata.usgs.gov/geology/state/map-us.html#home) and with the GIS element and endmember maps created in this research. Each endmember composition was assessed to determine its validity.

As shown in Table 2, endmember sample NV11887 is composed of ~0.55 EM13 and ~0.25 EM2, corresponding to ~50% Mg and ~25% Ca. The geological unit for this location is detrital (undifferentiated alluvium) and the element and mineral maps show presence of dolomite and high concentrations of Mg and Ca, which is consistent with the weathering of dolomite and the endmember composition for this sample. The geological unit for sample NV1871 is also undifferentiated alluvium, and the sample contains ~0.3 EM4 and ~0.24 EM1 equating to ~30% Na and ~25% Al, which could lead to high concentrations of plagioclase feldspar in the soil detrital. The element maps for surficial soils, and mineral maps for lower soil horizons, show a high concentration of aluminium, sodium, and plagioclase feldspar in the vicinity of this sample location. Sample FL48 has a composition of ~0.9 EM2, representing ~90% Ca. The geological unit for this area is the Miami Limestone, which is consistent with the high concentrations of Ca in the element map. Sample FL480 has a composition of ~0.25 EM11, ~0.25 EM1, and ~0.2 EM6, which represents ~35% Al, ~30% Fe, and ~9% P. The geological unit for this sample location is the Hawthorn Group, Undifferentiated, and is composed of detrital, sand and clay, and incidental phosphorus. The presence of Al, Fe, and P at this location is consistent with the weathering of local geological units, however, only the element map for P shows a high concentration in this area. Aluminium and iron concentrations are low, yet slightly higher than the surroundings. CO8427 contains ~0.47 EM3 and ~0.3 EM1 which equates to ~36.5% Al and ~40% K and is consistent with the weathering of shale, arkose, and mudstone, which comprise the underlying geological unit of the Denver Fm or lower part of Dawson Arkose. The concentration in the mineral map for K-feldspar is high in this area, as are the element concentrations of Al and K. Sample LA11852 is ~0.7 EM6 which represents ~70% Fe. The geological unit for this location is the Cook Mountain Formation, composed of clay, ironstone, and marl, which includes iron, and incidental banded iron-formations. There is also high iron concentration in the element maps for this location. AL5408 has ~0.6 EM1 and ~0.2 EM6, representing ~60% Al and ~20% Fe, consistent with weathering of geological units of the High Terrace Deposits, including ferruginous sand and clay. Weathering of clay and silica could lead to high Al and Fe content in the surrounding soil. The Al and Fe element maps show low to moderate concentrations in this region. Sample VA5020 represents ~0.3 EM5, ~0.2 EM1, and ~0.2 EM6, which corresponds to ~27% Al, ~23% Fe, ~17% Ti, and ~2% K. This location is part of the Bacons Castle Formation, composed of unconsolidated gravel, sand, silt and clay. The element maps show a higher concentration of Ti around this location, but low concentrations of Al, Fe, and K. High Ti content in this endmember is consistent with high abundances of Ti in Virginia. Sample CA8143 contains ~0.2 EM7, which equates to ~9.5%

Na, ~8% Ca, and ~2% Mg. The geological unit for this location is Quaternary alluvium and marine deposits, composed of unconsolidated detrital. Element maps show elevated Ca, Mg, and Na in the vicinity. CA3871 is located in Paleozoic metavolcanic rocks, unit 1 (Eastern Klamath Mountains), and comprises ~0.25 EM1, ~0.2 EM6, and ~0.18 EM9, representing ~38.5% Al, ~27% Fe, and ~1.5% Ti. Weathering of metavolcanic flows, breccia, and tuff would result in higher concentrations of Al, Fe, and Ti, which is also consistent with elements maps showing high concentrations of Al and Fe and elevated Ti in the region. PA6369 is ~0.25 EM8 and ~0.2 EM1, equating to ~32% Al, ~9% Mn, and ~1% P, and is part of the Catskill Formation. This formation includes sandstone, siltstone, mudstone, and shale. Element maps show high concentrations of Mn, elevated concentrations of P in the area, and low to moderate Al concentration in the area. Sample MT9582 contains ~0.3 EM10, ~0.2 EM1, and ~0.2 EM6 representing ~30% Al, ~30% Fe, ~6% K, and ~2% Ba. The sample location belongs to the Bearpaw Formation which is composed of shale and minor claystone. Element maps show a high concentration of Ba around the sample location and moderate concentrations of Al, Fe, and K. Sample GA2208 contains ~0.26 EM12 and ~0.23 EM1, representing ~43% Al, ~2% Fe, and ~2% Ti. It is part of the Neogene undifferentiated geological unit which is composed of Coastal Plain sedimentary rocks, mainly sandstone and claystone. The composition is consistent with weathering of the geological units. All of these elements display low concentrations in the element maps.

These 13 endmembers define the U.S. surficial soil system. In defining a system as large and heterogeneous as the U.S. surficial soils, it is expected that there will be several endmembers in play, therefore, with an input composed of 35 analytes, a 13-endmember solution is a reasonable outcome. Endmembers 9 and 12 have identical compositions, and endmember 7 is not present in any extreme sample in proportions greater than 0.17, therefore it may be possible to define the system in 11 endmembers instead of 13. However, changing the number of endmembers would change the polygon defining the system and so the endmember locations and proportions would also change. Therefore, reducing the number of endmembers may not capture the system as well as a 13-endmember solution.

1.4.2 Spatial Correlation

Quantitative correlation reduces speculation and subjectivity in analysis. Qualitative data alone, such as the maps created, can be misleading. Visual patterns are highly influenced by the choice of the type and number of unit breaks in the legends. Qualitative data is useful for visualisation and identification of high and low concentration areas, whereas quantitative data is helpful where patterns appear different visually but not quantitatively. A combination of both qualitative and quantitative is beneficial for identifying behavioural patterns.

The spatial distribution of minerals and elements analysed displayed three prominent patterns: West Coast, Pacific Northwest, and Southwest C-shape. The West Coast category consists of aluminium and gallium for each of the three soil horizons, with the C-horizon also displaying a strong presence in the Appalachian piedmont. Quartz has the inverse

concentration distribution to aluminium and gallium, with the lowest concentrations along the west coast and the highest concentrations along the Atlantic coastal plains. This is consistent with the correlation coefficient of 0.95-0.97 for Al-Ga across all three soil horizons and quartz having a negative correlation with Al and Ga with coefficients of -0.62 to -0.68 in the C horizon and -0.86 in the A horizon.

The Pacific Northwest region contains high concentrations of iron, scandium, vanadium, titanium, and cobalt in each of the soil horizons, in addition to high concentrations of pyroxene. These maps also all have high concentrations in Arizona. Iron has elevated concentrations in northeastern Minnesota, with the Top 5 and A-horizon also having elevated concentrations in southwestern Texas and scattered throughout the Appalachians. The C-horizon displays a much stronger iron presence in the Appalachians. For scandium, higher concentrations can be found in northern Maine and the Appalachian piedmont region for the Top 5 horizon, scattered through the Appalachians for the A-horizon, and stronger in the Appalachian piedmont for the C-horizon. Titanium displays higher concentrations in the Appalachian piedmont regions, northeastern Minnesota, and southwestern Texas for all three soil horizons. The C-horizon for vanadium displays high concentrations in Kentucky and Virginia, and all three soils horizons for cobalt show high concentrations in Maryland. The amorphous mineral category has the highest concentration in the Pacific Northwest but is present in high concentrations throughout the western states. The lowest concentrations are in Michigan, Wisconsin, and the Atlantic coastal plains. The correlation coefficients of these elements are consistent across all three soil horizons with the coefficients between element pairs in the Top 5 and A horizons being identical (range of 0.72 for Co-Ti to 0.93 for Fe-Sc) and slightly lower in the C horizon (range of 0.66 for Co-Ti to 0.93 for Fe-Sc). The correlation of each element in this group with pyroxene is also consistent across the A and C horizons with a range of 0.42 to 0.52 in the A horizon and 0.44 to 0.55 in the C horizon. Titanium has the highest correlation.

Several elements display high concentrations in a C-shape, in the southwestern U.S., from Colorado, up through Wyoming and Idaho, down through Nevada and the lower half of California, and along southern Arizona and through southwesthern New Mexico and ending in southwestern Texas. These areas of high concentration surround low concentrations in Utah and northern Arizona. These elements include potassium, rubidium, thorium, cerium, lanthanum, niobium, beryllium, barium, thallium, and yttrium, and the mineral, K-feldspar. In addition to the prominent C-shape in each map for each horizon, potassium in the C-horizon also shows high concentrations in the Appalachians and in the Great Lakes states. Rubidium and thorium in the C-horizon both have areas of high concentrations in the Appalachians, with thorium being concentrated more in the piedmont region. All three horizons for cerium and lanthanum display elevated concentrations in the Appalachians. Niobium displays high concentrations in the Appalachian piedmont as well as in Washington and Oregon, but has low concentrations in Wyoming, breaking the C-shape typically seen in the other maps. Yttrium also has low concentrations in Wyoming. Yttrium displays an area of high concentration in Maryland with the Top 5 and A-horizon extending through southeastern Pennsylvania and into northern New Jersey. Beryllium is elevated in New Hampshire and lower Maine with some high points in the lower Appalachians in the C-horizon. Barium displays an expanded C-shape, which includes

higher concentrations in Montana and South Dakota. Thallium shows an extension through the central U.S. states of Kansas and Missouri, with high concentrations also in Ohio. The C-horizon also has a high concentration in Kentucky. K-feldspar has elevated concentrations in northern New York, New Hampshire, southern Maine, Michigan, Wisconsin, and Minnesota. Correlation coefficients are consistent with the spatial distribution of these elements and are within a consistent range across the soil horizons for the most part, with the C horizon generally having weaker correlation coefficients than the Top 5. Notable exceptions include Ce-K and Ce-Rb. Ce-K has a coefficient of 0.98 in the Top 5 horizon and 0.59 and 0.46 in the A and C horizons respectively. Ce-Rb has a coefficient of 0.69 in the Top 5, 0.67 in the A horizon, and 0.92 in the C horizon. Correlations with K-feldspar are higher in the A horizon than the C horizon but still generally low for most of the elements. K and Rb are the only elements in the C horizon with a coefficient above 0.5 with the addition of Ba in the A horizon.

1.4.3 Quantitative Correlation

When compared with the correlation coefficients obtained for soils samples in the FOREGS European study (FOREGS. 2005), those of the US soils are generally in agreement. The reference to subsoils in the FOREGS data relates to the C horizon and the topsoil covers depths 0-25 cm which relates to the Top 5 and A horizons. The categories for strong and good correlation are >0.6 and >0.4 respectively. Where the vast majority of US soil element relationships and correlation coefficients are consistent with those in the European soils, several elements stand out as being very dissimilar, mainly Ag, Cd, Cs, Cu, In, Mo, S, Te, and U. Silver displays no good correlations and only one weak correlation with Mo in the US subsoil as opposed to the numerous good and weak relationships in the FOREGS data. In contrast, there are several topsoil correlations that are strong in US soils and not in European soils, as well as a difference in the elements those correlations are with. Similarly, Cd has no relationships in the US subsoil and several strong correlations in the Top 5 of the topsoil whereas the European soils display several relationships with good to weak correlation in both the subsoil and topsoil. Cesium lacks any strong correlations in the US soils but many of the element relationships are similar, which is identical to Cu correlations also. Indium has much fewer and weaker correlations and relationships in US souls and is inconsistent with the relationship with most other elements. In the European data, however, In displays numerous strong and good correlations. US Mo relationships show little consistency with European data, with more good pairings and with higher correlation coefficients. Though sulphur in the European soils has few and weak correlations with other elements, in US soils the relationship with Sr in the subsoil is the only one to have a coefficient above 0.3, and there are no correlations in the topsoil. Tellurium shows very little similarity, both with the European soils and between horizons, with US soil data showing a strong Cu relationship in the subsoil and several strong relationships in the topsoil, especially the Top 5 horizon. Most correlations involving U are similar, however, the US topsoils do not include the same stronger element correlations seen in the European soils. In addition to these elements that are mostly inconsistent with the FOREGS data, one of the major recurring differences is the correlation of Zn. Zinc has a strong correlation with heavy metals in the topsoil (Top 5) however disagrees with many of the European patterns, with Zn tending to have lower

correlations in the topsoil for other elements. The US soil data also shows more but weaker relationships in the C horizon and fewer but stronger relationships in the Top 5.

Comparison of element correlation in surficial soils obtained from the Three Gorges Reservoir in China (Wu et al., 2021) and the Huangpi district in Wuhan, China (Tadesse et al., 2018), show very little similarities to the US for the comparable trace elements and metals studied. Where correlation coefficients for the US data were above 0.5 for select element pairs, approximately half were weaker than those in the Chinese soil studies and half were stronger. Those that were stronger include all combination pairs of Cd, Hg, Pb, and Zn. The correlation for As-Hg was also stronger in the US data. The only pairings to be roughly equal in strength were Co-Fe and Co-Ni (Tadesse et al., 2018).

1.4.4 GIS Layers

In relation to the soil pH, the FOREGS data (2005) describes good positive correlation between pH and calcium (~0.5) and good negative correlation between pH and sodium (~ -0.4) and barium (~ -0.3). The correlation in US soils is slightly weaker for Ca (0.4) but for Na is positive, with a correlation of 0.37 and Ba 0.43 which is the opposite relationship to that in the European soils. Maps of the European soil data show that areas of higher pH (more alkaline) correlate more with lower Na content, whereas the US maps show acidic soil regions to have low Na content. The negative Ba and Na relationships with pH have been attributed to feldspar-rich regions coinciding with climate-related acidity (Foregs, 2005). Areas of higher rainfall have higher acidity due to leaching of elements such as Na, and soils in dry regions are more alkaline (Rengel, 2011). When compared with Wu et al., (2021), of the corresponding elements, all had a weaker correlation with pH and, though also true for Ca and Mg, these were the only elements in the US soils data to have a correlation >0.3. In Tadesse et al., (2018) there was no significant correlation between the elements analysed and the pH of the soils.

The Soil Taxonomy of the US (Soil Survey Staff, 1999) describes the characteristics of each soil order and sub-orders, including the pH at various soil depths (Table). For the samples in this study, the average pH for each order is generally higher, (i.e. less acidic) than the general soil taxonomy pH values, with the exception of Alfisols and Vertisols which show a lower pH and Ultisols which are the same as the taxonomy characterisation.

Table 13. Soil pH for soil orders from the Soil Taxonomy Soil Survey, 1999.

Soil Order	**Depth (cm)**	**pH**
Alfisols	0-13	7.7
Andisols	0-4	5.6
Aridisols	0-33	7.8
Entisols	0-13	5.8
Histosols	No data table	-
Inceptisols	0-10	5.6
Mollisols	0-18	6.3

Spodosols	0-3	4.3
Ultisols	0-12	5.1
Vertisols	0-14	7.6

As shown in Figures 37 and 38, Ultisols, Inceptisols, and Spodosols are the most acidic soils, Alfisols are neutral, and Mollisols and Aridisols are the most alkaline. Rengel (2011) states that approximately 66% of the world's acidic soils are among the Ultisols, Entisols, and Oxisols orders. Oxisols are not present in the contiguous US (Soil Survey, 1999) so are not part of this US dataset. Relating to the land cover type, Figure 36 shows that shrubland covers a large portion of the alkaline areas, forested regions are more acidic, and cultivated areas are more neutral in pH. Most acidic soils are related to forested areas (Rengel, 2011).

1.5 Conclusion

The surficial soils of the Contiguous US can be defined by a 13-endmember system with each endmember composition in an extreme endmember sample location. Most endmembers were present in low amounts nationwide and could be attributed to the underlying parent materials. The majority of endmembers showed good or strong correlation with other endmembers and elements in the Top 5 horizon. A combination of qualitative and quantitative data describes the relationships between elements, endmembers, and geographical data, providing insight into the behavior and patterns of soils in the US. Correlation coefficient data for topsoil and subsoil are generally in agreement with those in other regions and tend to be consistent with the visual representations. Due to the influence of factors such as legend units and categories for the maps, the use of coefficients by way of correlation matrices provides quantitative data for analyses, which is more reliable than qualitative data alone.

2 A Hyperspectral Approach to the Alteration Strength Index

2.1 Introduction

2.1.1 Telaga Bodas

Telaga Bodas is an acid lake within the Karaha-Telaga Bodas geothermal field of Galunggung Volcano, located in West Java, Indonesia, approximately 140 miles southeast of Jakarta (Figures 39a and 39b). The area is an active, volcano-hosted, vapour-dominated geothermal system (Moore et al., 2008). Several studies have conducted petrological analyses of rocks from drill cores to determine the hydrothermal evolution of the system during its lifetime. The Karaha-Telaga Bodas geothermal field lies beneath the Kawah Galunggung crater at Galunngung Volcano, and extends northwards underneath the volcanic ridge. Galunggung Volcano is composed of three geologic formations: the Old Galunggung Formation (ash-flow, air fall, lahar deposits, and lava flows), the Tasikmalaya Formation (debris avalanche, lahar, and pyroclastic deposits), and the Cibanjaran Formation (ash-flow, air fall and lahar deposits since the 1822 eruption, and lava flows). Lava flows and volcanics from Galunggung Volcano and exposed dykes in crater walls range from basalt to basaltic andesite in composition, with older flows and pyroclastic deposits having a compositional range from andesite to dacite. The geothermal reservoir primarily formed in pervasively altered pyroclastic deposits. There are also local occurrences of thin tuffaceous sandstone and mudstone layers interbedded with the volcanics (Moore et al., 2008). During the mid- to -late- 1990's, 29 wells were drilled at the Karaha-Telaga Bodas geothermal area, by Karaha-Bodas Co. LLC, to a maximum depth of 3 km. Numerous studies have focused on the Karaha-Telaga Bodas geothermal system, its magmatic evolution and faulting, through analysis of various cores taken from the wells (Nemčok et al., 2001; Moore et al., 2002; Moore et al., 2004; Nemčok et al., 2004; Moore et al., 2008; Moore, 2012). The geothermal system at Karaha-Telaga Bodas formed within the last 6000 years (Nemčok et al., 2004; Moore et al., 2008). Analysis of core hole (wells drilled to extract continuous rock) samples led to the identification of four main assemblages: 1) an initial, high temperature, liquid dominated system, divided into three main zones; an upper zone of argillic alteration (characterised by clay minerals, zeolites, and carbonates), an intermediate zone of propylitic alteration (chlorite, epidote, and actinolite), and a lower zone of high temperature biotite (biotite and tourmaline), 2) the development of a vapour-dominated system, involving the deposition of amorphous silica, chalcedony, quartz, and rare bladed calcite, 3) anhydrite, calcite and wairakite deposition due to a decrease in pressure, and 4) precipitates of NaCl, KCl and FeCl in areas which have boiled dry, implying a high temperature, vapour-dominated zone (Moore et al., 2002; Moore et al., 2004; Nemčok et al., 2004; Moore et al., 2008; Moore, 2012). The propylitic zone is defined by the appearance of epidote, and the biotite zone by the appearance of biotite. Moore et al., (2008) used petrological analyses of hydrothermal mineral assemblage evolution to create a model of evolution for volcano-hosted, vapour-dominated geothermal systems based on the analysis of samples from Karaha-Telaga Bodas. The T-2 and K-33 coreholes were two of several thermal gradient and deep production wells drilled by Karaha Bodas Co. The coreholes are located between the

thermal features of the Telaga Bodas acid lake and Kawah Karaha towards the north of the ridge (Figure 39c) (Moore et al., 2008).

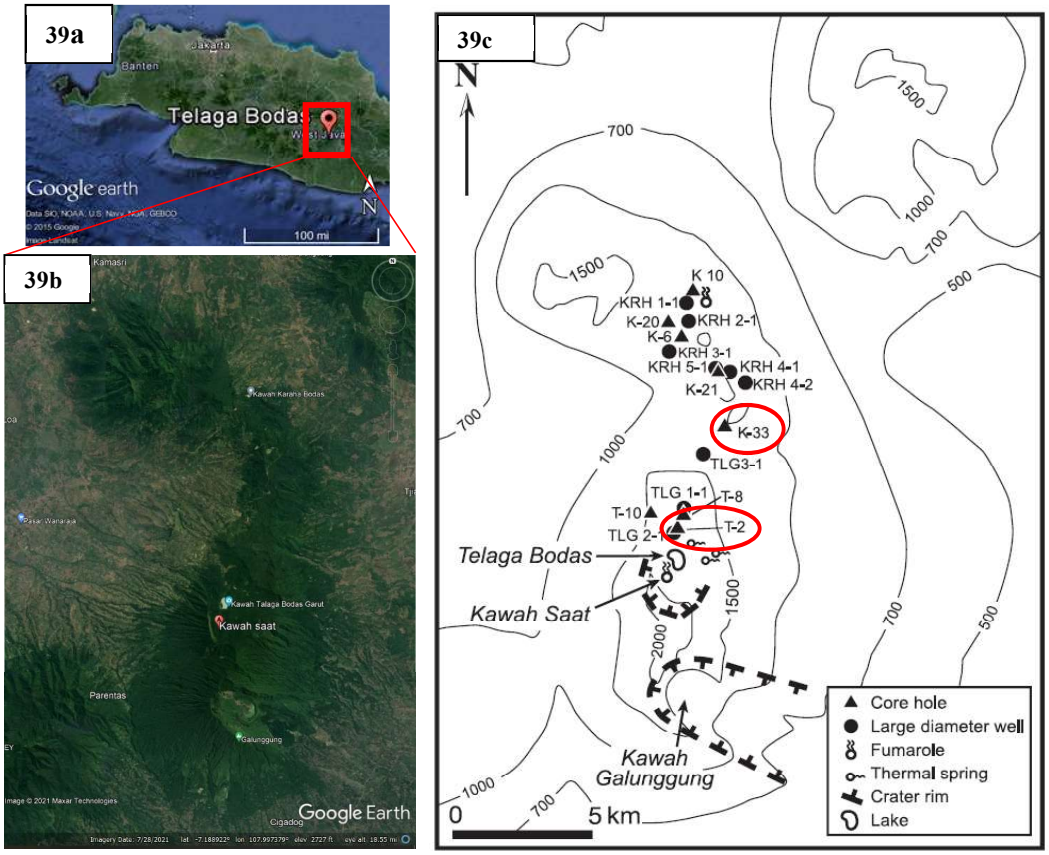

Figure 39. (a) Location of Telaga Bodas in West Java, Indonesia; (b) The Galunggung Volcanic Complex (Images from Google Earth), and (c) Map of Telaga Bodas and areas of study. Modified from Moore et al., (2008). Red circles highlight the location of the T-2 and K-33 coreholes used in this study.

2.1.2 Lake City

Lake City Caldera is part of the San Juan Volcanic Field (SJVF) in southwestern Colorado, and at ~22.9 Ma is the youngest caldera in the system (Kennedy et al., 2012; Kennedy et al., 2015; Garden et al., 2017; Garden et al., 2020). Lake City Caldera lies within the much larger Uncompahgre Caldera (Figure 40), and formed during the eruption of the Sunshine Peak Tuff (Lipman et al., 1973). The caldera has a granitic basement of Precambrian age (Garden, 2017), overlain by intermediate lavas and breccias, and ash-flow and lava sequences of Oligocene age, followed by Miocene bimodal volcanics (Lipman et al., 1973). The Lake City and Uncompahgre calderas each have fossil hydrothermal systems. The hydrothermal mineral assemblages formed during the Oligocene and Miocene periods (Sanford, 1992).

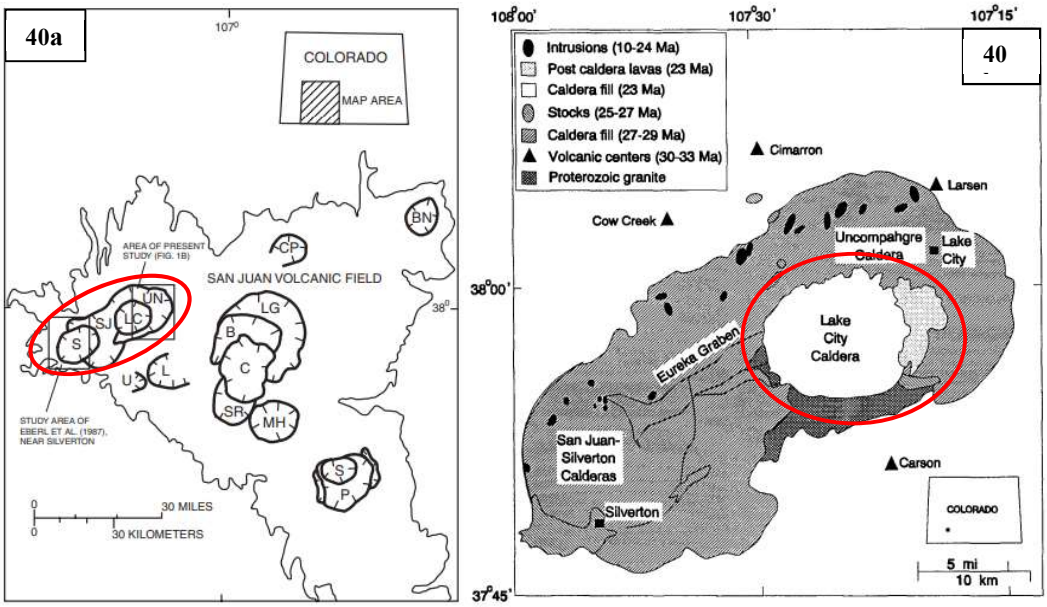

Figure 40. (a) Map of the San Juan Volcanic Field in Colorado, modified from Bove et al., (2002). The red oval encompasses the area shown in 40b. LC represents the location of the Lake City Caldera; (b) Map of the general geology of the Lake City and Uncompahgre calderas, modified from Sanford (1992). The red circle encompasses the Lake City Caldera.

2.1.3 Hyperspectral Data

Hyperspectral imaging has high spectral resolution, hence it can obtain more detail in the resulting spectra than lower spectral resolution due to a higher number of bands of very narrow intervals. For example, the Airborne Visible/IR Imaging Spectrometer (AVIRIS) is an airborne hyperspectral instrument which records radiance data in 224 bands (0.4-2.5 μm), with sampling intervals of ≤ 10 nm (Figure 41) (Sabins, 1999; Hellman & Ramsey, 2004). In comparison, the Landsat 7 Enhanced Thematic Mapper satellite records data in only 8 bands (0.45-2.35 μm), therefore, having a much higher sampling interval (~ 200 nm) (Sabins, 1999). With respect to geological applications, the amount of detail obtained from hyperspectral scanners enables the identification of specific minerals in an area. This is due to the similarities and differences in the detail and position of reflectance and absorption features which can be seen between the recorded spectra and those from a spectral library, which provides reference spectra for over 2400 materials (both man-made and natural) (Nasa, 2016). Calvin and Pace (2016) used a field spectroradiometer to map alteration minerals in geothermal drill cores and recommended the use of spectral logging in order to identify locations for further geochemical analyses with the aim of reducing the time spent preparing samples in the lab. In light of this, with the use of hyperspectral imagery obtained through companies such as Corescan, mineral identification and dispersion may be more quickly and easily obtained.

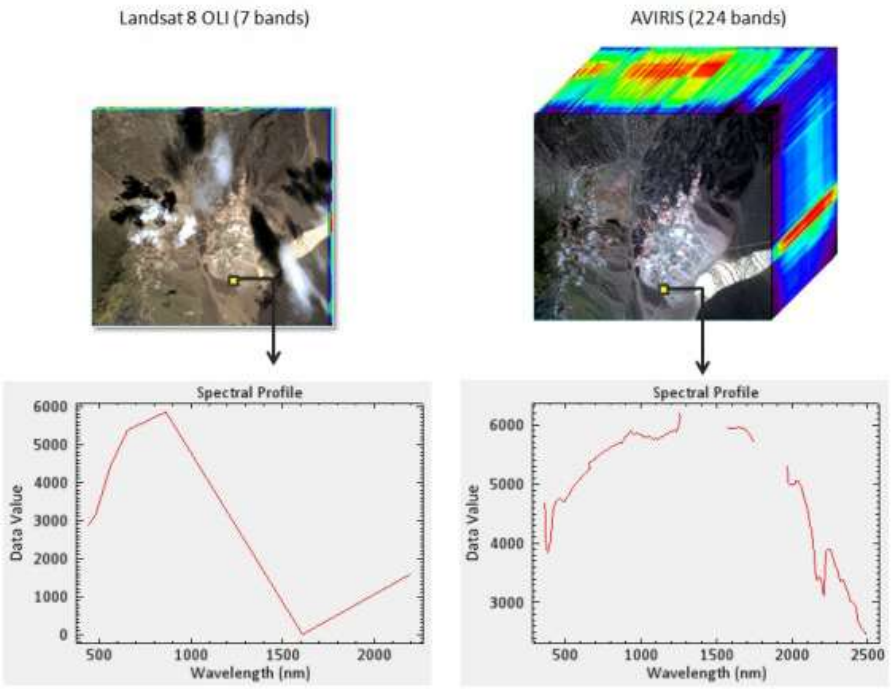

Figure 41. Comparison of spectral data obtained from AVIRIS and Landsat 8 OLI imagery. Image from ENVI Tutorial, 2015.

2.1.4 Core Imaging

Corescan is a hyperspectral imaging company in Australia which scans rock cores and provides high spectral and spatial resolution imagery of core mineralogy and geochemistry (Corescan, 2017). The scanned core images are displayed on Coreshed, which is the digital storage area of Corescan. This system provides several categories for core viewing, including mineralogy, geotechnical imagery, and core imagery, which includes core photography, true colour (natural colour) spectral imagery, false colour (non-natural colour) spectral imagery and the core profile. Using Coreshed, different minerals can be selected and displayed for each core, as well as the overall mineralogy for spatial representation of the minerals and for comparison (Figure 42). The colour displayed in the individual mineral maps represent the quality of mineral matching, with red representing higher match and blue representing lower match (i.e. close to the threshold of what to include as a match). The threshold is no lower than a 92% match between the spectral signature detected in the pixel and the project spectral library. Black represents no match. This is determined by the minerals detected in each 0.5 x 0.5 mm pixel. Each pixel may contain multiple minerals, so the overall mineral classification maps display the mineral which is given priority in each pixel. Priority is determined with mineral decision-tree organisation based on rules set by the spectral geologist, and project goals (Martini et al., 2017).

The imagery displayed on Coreshed can be compared, in terms of mineral occurrence and depths of occurrence, with mineralogical descriptions and images from petrology studies carried out on Karaha-Telaga Bodas cores (Nemčok et al., 2001; Moore et al., 2002; Moore et al., 2004; Nemčok et al., 2004; Moore et al., 2008; Moore, 2012). Similarities and differences between the available data could allow for a comparison of hyperspectral imaging and petrological imaging to determine if hyperspectral scanning of minerals is beneficial in the identification of target minerals. Corescan also provides a spreadsheet of data for the calculated percentages of each mineral present in each length of core as well as the wavelength at which certain minerals display a specific absorption feature.

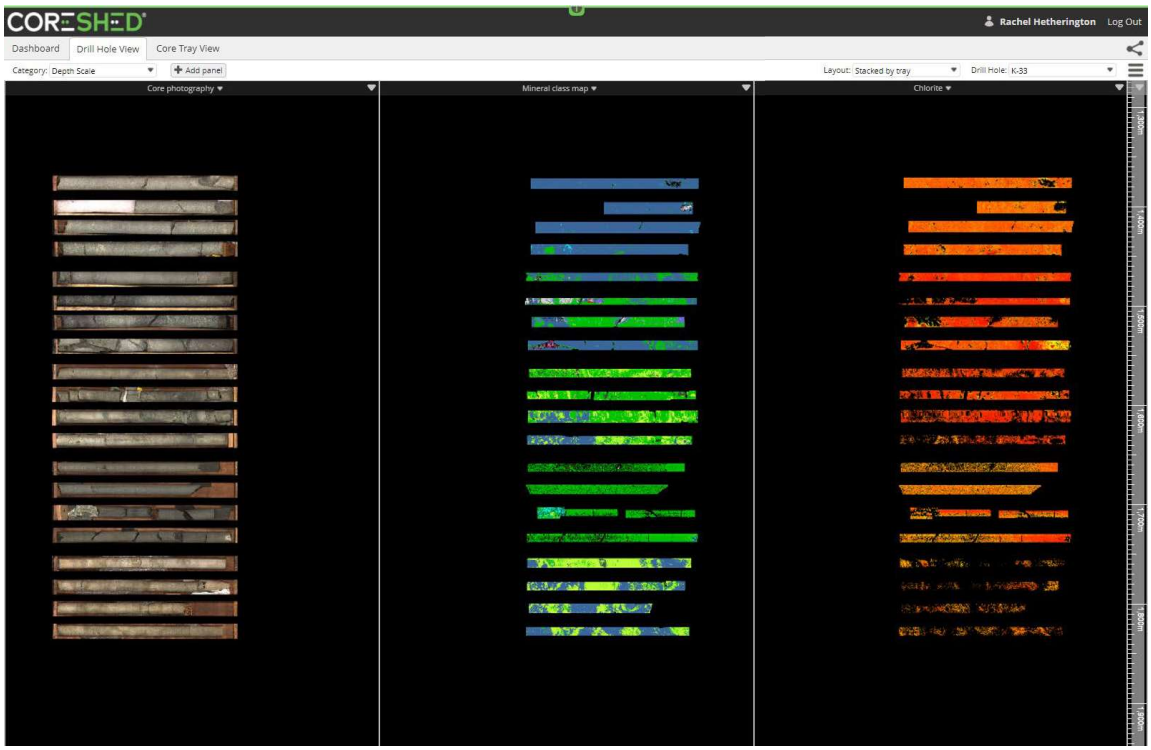

Figure 42. Corescan's Drill Hole View of the K-33 core sections on Coreshed. Each section of core is scanned and displayed in a tray. The first panel displays the core photography, the second panel displays the overall mineral class map, and the third panel displays chlorite occurrence. The mineral class map displays the primary mineral in each pixel: blue represents white mica, green represents chlorite, and yellow represents epidote. Chlorite occurrence shows every pixel where chlorite was detected and the degree of matching, where red is the highest match and yellow is the lowest match in this example. Black pixels mean no match.

2.1.5 Alteration Strength Index

The Alteration Strength Index (ASI), developed by Wyering et al., (2015), is a calculated value which correlates with uniaxial compressive strength (UCS), and can, therefore, be

used to estimate rock strength. The ASI equation was devised to be a tool used in the field to rapidly assess and estimate the strength of hydrothermally altered rocks based on mineralogical and physical properties. The ASI is calculated using an equation which takes into consideration parameters which have the most influence on rock strength: primary mineralogy (Pm), secondary mineralogy (Sm), alteration index (AI), porosity (Φ), and fracture index (Snf) (Eq. 1). The equation has been developed such that the parameters which have the most influence on rock strength (i.e. primary and secondary mineralogy) are weighted more heavily.

$$ASI = (Pm * (1 - AI) + Sm * AI) * \left(\Phi^{-0.03}\right) * (1 - \left(\frac{\text{Snf}}{25}\right)) \quad \text{(Eq. 1)}$$

Primary mineralogy (Pm) refers to the minerals associated with the original lithology and is a representative value based on the hardness and relative proportion of each mineral present. Each primary mineral identified is assigned a category and representative percentage based on abundance in thin section (Table 14). Secondary mineralogy (Sm) refers to the minerals associated with alteration and is also a representative value based on the hardness and relative proportion of each mineral present. The main difference is that the categories for secondary mineralogy are also ranked to account for multiple minerals in each category due to the abundance of alteration minerals which could be present (Table 15). The Pm and Sm values are calculated by multiplying the representative percentage by hardness index for each mineral, then summing those values.

Table 14. Semi-quantitative categories and representative percentages for primary mineralogy. From Wyering et al., 2015.

Category	**Representative Percentage**
Abundant (A)	50
Common (C)	25
Minor (M)	10
Rare (R)	5

Table 15. Semi-quantitative categories and representative percentages for secondary mineralogy. From Wyering et al., 2015.

Rank	**1**	**2**	**3**	**4**	**5**	**6**	**7**	**8**	**9**	**10**	**11**
Representative percentages of secondary minerals											
Abundant (A)	50										
Common (C)	45	40	35	30	25						
Minor (M)		20	17.5	15	12.5	10	7.5	5			
Rare (R)			5	4.5	4	3.5	3	2.5	2	1.5	1

Table 16. Moh's Hardness and assigned Hardness Index. From Wyering et al., 2015.

Moh's Hardness Scale	Hardness Index
>7	2.1
7-6	1.7
6-4.5	1.3
4.5-3	0.9
3-2	0.5
<2	0.1

To account for the influence of mineral hardness, Wyering et al., (2015) assigned a Hardness Index value based on Moh's hardness (Table 16). Minerals with Moh's hardness >5 are considered hard and assigned a Hardness Index value >1, and those with Moh's hardness <5 are considered soft and assigned a Hardness Index value <1. A mineral with a Hardness Index value >1 is considered to strengthen a rock whereas a value <1 is considered to weaken the rock.

The Alteration Index (AI) is a measure of relative proportions of primary and secondary mineralogy in a rock, (i.e. how much of the rock has been altered from the original lithology), and is assigned a value between 0 and 1, with 0 representing no alteration from the primary mineralogy, and 1 representing complete alteration to secondary mineralogy.

The Fracture Index (Snf) accounts for the fact that rocks tend to fail along pre-existing planes of weakness. The values increase with severity of the fractures present as the presence of larger fractures weakens the rock more than smaller fractures (Table 17).

Table 17. Assigned fracture value based on fractures seen in the rock and in thin section. From Wyering et al., 2015.

Fracture Value (Snf)	Fracture Type	Fracture Size
0	No fractures	-
1	Microfractures seen in thin section	Narrow fractures in thin section
2	Small fracture – closed	1 fracture < 1 mm in width, < 10 mm in length, closed
3	Small fracture – open	1 fracture < 1 mm in width, < 10 mm in length, open
4	Large fracture – closed	1 fracture > 1 mm in width, > 10 mm in length, closed
5	Large fracture – open	1 fracture > 1 mm in width, > 10 mm in length, open
6	Multiple large fractures – closed/open	2 or more fractures > 1 mm in width, > 10 mm in length

Equation 2 can be used to calculate the UCS from the ASI which can then determine rock strength.

$$UCS = 7 * 10^{-8} * ASI^{4.3661} \qquad \text{(Eq. 2)}$$

The Modified Alteration Strength Index (mASI) (Wyering et al., 2015; 2017) is the same as the ASI but excludes porosity, for use when porosity cannot be determined, such as with drill cuttings. Although the mASI values calculated still correlate with UCS, the accuracy is reduced in comparison to the ASI.

2.1.6 Hyperspectral-Alteration Strength Index

The Alteration Strength Index is a good tool for strength approximation, however, it has limitations. The Pm and Sm categories are subjective which can lead to inconsistencies and variation, and they have a maximum representative percentage of 50, not accounting for samples composed primarily of one main mineral. In the case of Pm, there are large intervals between categories which can lead to vast under- or over-estimation in representative percentages.

The Hardness Index categories (Table 16) are not scaled equally so some categories cover a Moh's hardness range of 1 and other 1.5. However, the main issue arises with overlapping categories. For example, magnetite has a hardness range of 5.5-6.5 which could be assigned a hardness index of either 1.3 or 1.7. This is the same for minerals with a hardness on the limit of the range, such as calcite. A hardness of 3 could be assigned a hardness index of either 0.5 or 0.9 as it belongs to both categories. When multiplying the representative mineral percentages by the hardness index, inaccuracies and uncertainties in the resulting Pm, Sm, and AI values will produce inaccurate results.

The fracture index accounts for seven classifications of fractures, as shown in Table 17, with the main measurements for consideration being whether or not the fractures are < 1mm wide and < 10 mm in length, or >1 mm wide and >10 mm in length. There are no categories for fractures which are <1 mm wide and > 10 mm in length or >1 mm wide and < 10 mm in length.

The use of the hyperspectral data from Corescan will reduce inaccuracies in the Pm and Sm values by providing actual mineral abundances throughout each section of scanned core. These percentages will be used instead of the representative percentages from Wyering et al., (2015). For example, if hyperspectral data determined a mineral accounted for 66% of a sample, then 66 would be multiplied by the assigned hardness index for that mineral instead of the representative amount of 50 assigned to the most abundant Pm and Sm mineral (Tables 14 and 15). This would provide more accurate Pm and Sm values, and thereby creating the H-ASI from the ASI.

2.2 Methods

2.2.1 Core Imaging

The scanned images on Coreshed were used to visualize and assess core mineralogy and abundance. Individual minerals, as well as overall core mineralogy, can be displayed to show the abundance and distribution of minerals in each tray. Corescan imaged five sections of Karaha Telaga-Bodas cores from holes T-2 and K-33, each section approximately 3 m long, covering various depths (Table 18). Each of the five sections was split across four trays, the tray number appended with _00, _01, _02, or _03 for identification and associated depths. The Lake City Caldera samples were hand samples as opposed to lengths of core. They were displayed and imaged in trays, however, their identification was based on their individual sample ID rather than tray ID and depth.

Table 18. Tray ID and respective depths of each section of cores T-2 and K-33 from Telaga Bodas.

Core	**T-2**					**K-33**				
Tray Number	0076	0079	0117	0118	0156	0191	0192	0364	0393	0423
Depth (m)	577.3 - 580.1	586.0 - 588.6	693.2 - 695.9	695.9 - 698.8	802.6 - 805.5	1273 - 1276	1276 - 1278	1751 - 1754	1832 - 1835	1916 - 1919

Mineral logs were obtained from Corescan where the total pixels and mineral abundance in those pixels were calculated over short spatial intervals for the length of the Telaga Bodas cores and the Lake City hand samples. Using this data, the average mineral abundance over the length of the core samples used in this study (or original bulk sample in the case of Lake City samples) were calculated. For example, sample K33_0393_1834 was taken from a depth of 1834 m. It could be 1834.1 m or 1834.9 m as it was not specified. The specific depth could be at the beginning, middle, or end of the 5 cm long sample cored for this research. Therefore, the mineral abundances for each interval length potentially encompassing the sample depth, as documented by personnel at Corescan, were averaged to obtain the average mineral abundances. This provided the modal mineral percentages for each sample which were then used for the calculations of Pm, Sm, and AI in the ASI equation.

2.2.2 Sample Preparation

Samples for this study were chosen based on their availability of hyperspectral imaging data via Corescan and the ability to cut sections from the original cores and rocks without damaging them. Subsequent core samples needed to be approximately 1 x 2 inch in size, ensuring a diameter:height ratio of 1:2. Once cored, all samples were cut to a length of ~ 2

inches and smoothed using a grinder to ensure the ends of the cores were flat. Some ends of the cores had been chipped during preparation so were as flat and smooth as possible. Each sample had a diameter of 23 mm and a length of 49-51 mm.

There were 30 samples used in this study, from the two different geographical locations. Thirteen core samples were from the Karaha-Telaga Bodas geothermal field. Of these 13 samples, three were from the T-2 corehole which had a total depth of 1383 m, and nine were from the K-33 corehole which had a total depth of 2018 m (Moore et al., 2008). The reason for so few samples from the T-2 well is due to the difficulty in taking smaller cores in the lab. Many were brittle and disintegrated during the coring process, leaving only three viable samples. Seventeen core samples were taken from hand specimens from Lake City Caldera.

2.2.3 Permeability

Permeability testing was carried out on a BenchLab 7000 EX Velocity and Permeability Measurement System floor model from New England Research, Inc. (NER) (Figure 43). The 1-inch permeameter coreholder was specifically used to measure low permeability in the range of ~ 5 nD to 5 µD (NER 2016). Water was used as the pore fluid for all tests. The top end-cap of the coreholder contains the pressure source and the bottom end-cap contains the pressure transducer where the pressure response is measured (Figure 44) (NER 2016). The same pressure conditions were used for all samples for consistency; confining pressure (Pc) was set to 2.5 MPa, and pore pressure (PP2) was set to 0.7 MPa, which were a little above the base settings of 2.0 MPa and 0.4 MPa respectively. These values were chosen so the amplitude of the pressure pulse, which was set to 1.0 for all tests, did not extend past zero on the lower end and Pc on the upper end. The internal pressure of the sample (PPint) needed to equilibrate with PP2 before a permeability capture could be run in order to test the response, so higher Pc and PP2 values would take longer to reach and longer to equilibrate due to the low permeability of the samples. For each permeability capture, the source was PP2, the response measured was PPint, and the transient was set to "multipulse", meaning the pressure increases 0.5 above PP2, and 0.5 below PP2 for the total amplitude of 1.0. Frequency was the only variable. This controlled the length of time of the capture and is calculated as shown in Equation 3.

$$Time\ (hrs) = \left(\frac{1}{freq}\right) * 2.5\ \div 60\ \div 60 \qquad \text{(Eq.3)}$$

Frequency was determined on a trial-and-error basis and adjusted based on the results. A bad response and high errors indicate that either a higher or lower frequency is needed for higher quality results. The frequency was adjusted and permeability was recaptured until more reliable results were obtained.

Figure 43. The BenchLab 7000 EX from NER.

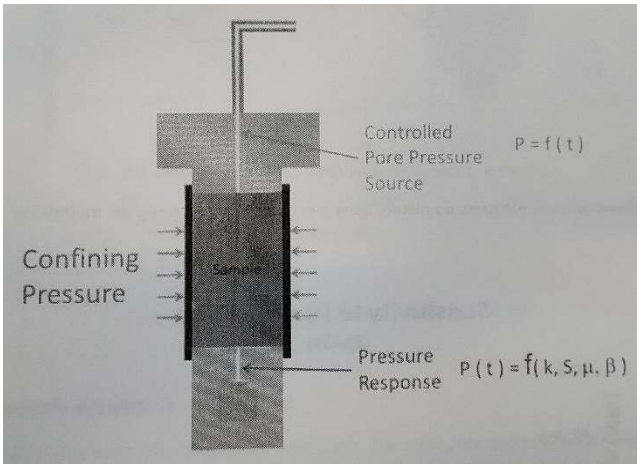

Figure 44. Diagram of the low permeability end-caps. Image from NER.

2.2.4 Porosity

2.2.4.1 Wax Immersion Method

Porosity testing followed the wax immersion method and procedures described by Crawford (2013). The samples were oven dried for a period of 24 hours at 110°C, then left to cool to room temperature. They were then placed in a freezer bag to prevent moisture in the samples. Each sample was dry weighed, coated in a layer of paraffin wax (heated to ~135°F), weighed again, then placed in a basket immersed in a bucket of room temperature water (~22°C, specific gravity of 1) suspended from below the scales, and weighed again (Figure 45). The scale was accurate to 0.01 g.

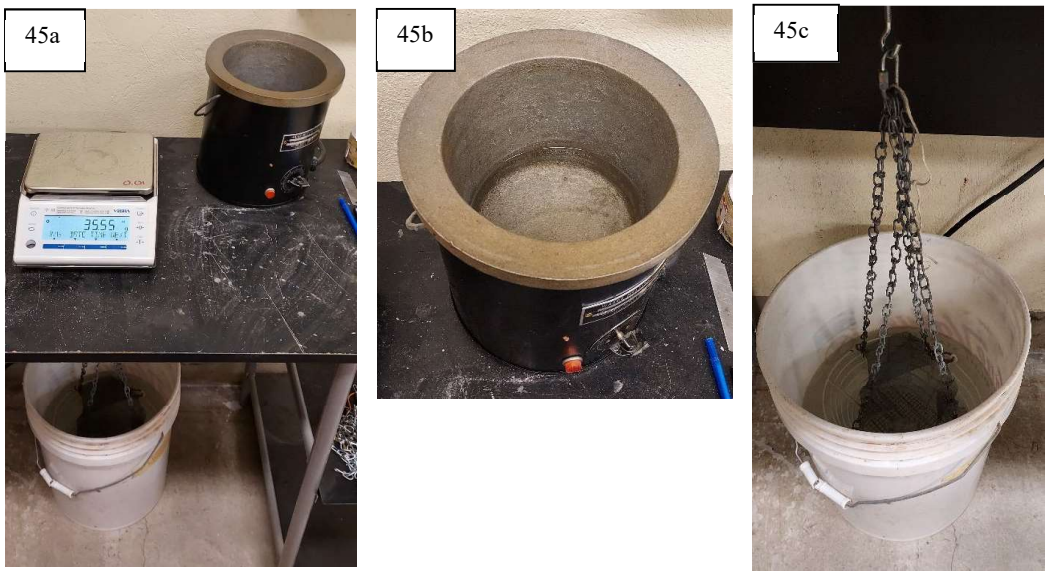

Figure 45. Wax Immersion Method equipment. a) scale, wax bucket, and water bucket with suspended basket; b) wax bucket; c) bucket of water with basket suspended below scales.

The volume of the sample was determined by first calculating the total volume of the sample, including the wax coating (V_{SW}), where P is the weight of the wax-coated sample (g), and S_{WAX}) is the suspended weight of the wax-coated sample (g) (Equation 4).

$$V_{SW} = P - S_{WAX} \qquad \text{(Eq.4)}$$

The volume of the wax coating (V_{WAX}) was calculated second, where P is the weight of the wax-coated sample (g), W is the weight of the dried sample (g), and K_{WAX} is the density of the wax (g/cm3) (Equation 5).

$$V_{WAX} = \frac{P-W}{K_{WAX}} \qquad \text{(Eq. 5)}$$

The volume of the sample (V) (cm3) is the difference between the volume of the sample with wax and the wax coating (Equation 6).

$$V = V_{SW} - V_{WAX} \qquad \text{(Eq.6)}$$

The bulk density of the sample (G_B) (g/cm3) was calculated by dividing the dry weight of the sample (W) by the sample volume (V) (Equation 7).

$$G_B = \frac{W}{V} \qquad \text{(Eq.7)}$$

2.2.4.2 Helium Pycnometry

Helium pycnometry was used to determine the particle density of the samples. Due to problems with the intended pycnometer, an alternate pycnometer had to be used that had a much smaller sample chamber, so the core samples were unable to be used to for pycnometry. Instead, smaller samples were taken from the original rocks which the core samples came from. Approximately four small samples were taken for each rock sample. They were cut using a diamond-edged rock saw, labelled, and dried in an oven for ~24 hours at 110°C. A few samples were too small for accurate readings in the pycnometer, and some needed to be manually sanded down to size as they were too big to fit in the sample cup. Overall, 118 samples were tested.

The AccuPyc 1330 Pycnometer (Figure 46) measures the pressure change of helium in a calibrated volume to determine density and volume of the sample. Each sample was weighed, in grams, using a Mettler pm400 closed chamber scale (Figure 9), to three decimal places. The sample was placed in the pycnometer sample cup, the Sample ID and weight was entered, and the analysis started. The pycnometer did three purges (for air and moisture removal from the inside of the chamber) and five iterations (runs) to collect the data, reporting the average density and the standard deviation at the end of the cycle. The average density for each of the samples was used as the particle density value (G_P) to calculate porosity (ϕ) (Equation 8).

$$\phi = \left(1 - \left(\frac{G_B}{G_P}\right)\right) * 100 \qquad \text{(Eq.8)}$$

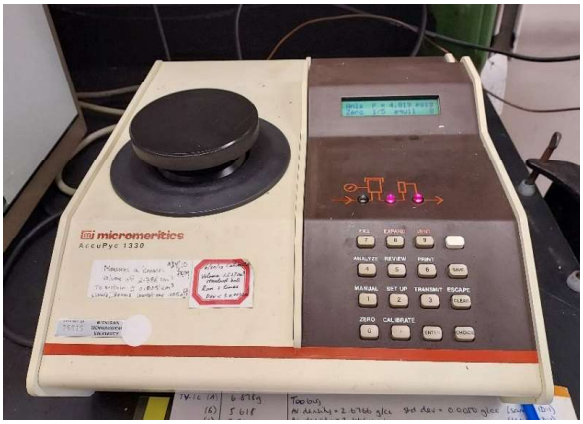

Figure 46. AccuPyc 1330 Helium Pycnometer.

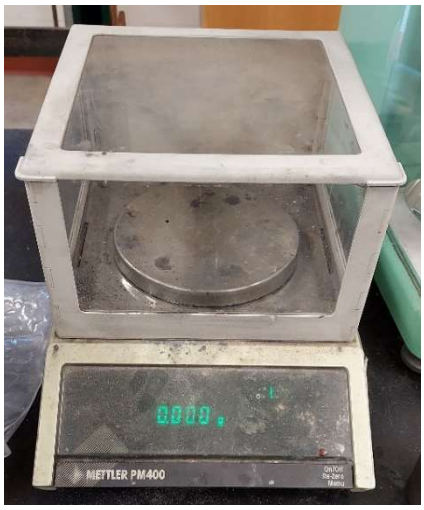

Figure 47. Mettler PM400 scales.

2.2.5 UCS Testing

Uniaxial Compressive Strength testing was carried out using a Controls Uniaxial and Triaxial Test System model A32Z10 with a compression device compliant to ASTM D7012 test methods (Figure 48). The test type selected was “Uniaxial Compressive Core: ASTM D7012”, specimen type “Core”. For each sample, the test date was entered along with the Specimen ID, Certificate Number (self-selected ID for which I used the Specimen ID), and sample dimensions in inches. The loading rate was adjusted based on visible sample fractures and rock type to try to cause failure within 15 minutes.

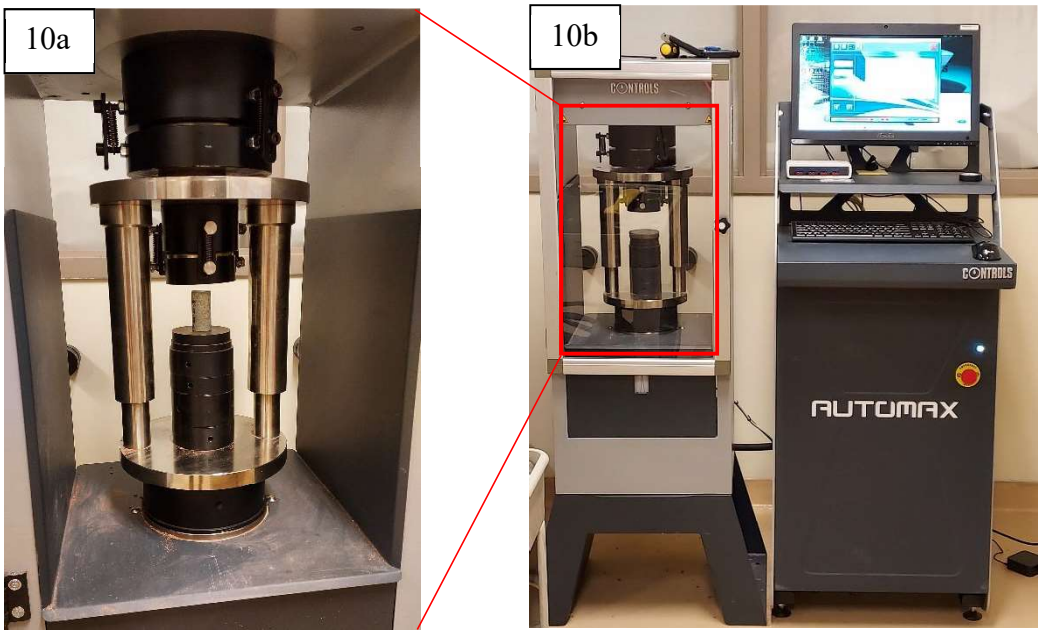

Figure 48. a) The compression device for b) the Controls Uniaxial and Triaxial Test System.

2.3 Results

2.3.1 Corescan and Alteration Mineralogy

The purpose of using mineral data from Corescan was to determine whether or not hyperspectral data can improve the accuracy of the modal mineral percentages in samples to improve the Pm, Sm, and AI estimations in the ASI equation, and to determine how significant the differences are between the ASI representative values and the calculated H-ASI values.

All Telaga Bodas (TB) and Lake City (LC) samples had undergone varying degrees of alteration. The mineral maps on Coreshed provide visualisation of the mineralogy of each sample. For easier visualisation, the overall mineral classification maps are presented in this section, as opposed to each individual mineral map for each sample, and the calculated modal proportions of the main minerals present are given. The modal percentage data for each sample from Corescan are provided in Appendix B1.

2.3.1.1 Telaga Bodas Samples

Figure 49 shows the Corescan colour legend for the mineral classification map for the Telaga Bodas samples. The following thirteen sample images show the minerals given priority for each pixel in the classification map, as displayed by the representative colour for that mineral.

Figure 49. Colour legend for the Telaga Bodas mineral classification map.

1. K33_0191_00 (1275-1276 m)

Sample K33_0191_00 (Figure 50) displays white mica as the primary mineral throughout this section of core, however, individual mineral maps show that chlorite is equally abundant across the same area. Individual maps also show an abundance of gypsum throughout, a moderate abundance of epidote and minor amounts of alunogen, carbonate, dickite, kaolinite, magnetite, and prehnite. Some pixels can also be classified as simply aspectral, which means there were no diagnostic features in the wavelength range used. Aspectral mineralogy is usually either quartz or feldspar. The modal amounts of each mineral present are 40% white mica, 38% chlorite, and 17% gypsum. Mineralogy is indicative of phyllic and propylitic alteration.

Figure 50. Mineral classification map for sample K33_0191_00. Depth 1275-1276 m. The primary minerals in this section of core are white mica and chlorite. White mica is displayed as the prominent mineral in this map.

2. K33_0191_03 (1273-1274 m)

As with the previous sample, sample K33_0191_03 (Figure 51) has an equal abundance of white mica and chlorite; though white mica is displayed as the primary mineral in the classification map, with visible areas of chlorite and carbonate. Individual mineral maps show moderate amounts of epidote and gypsum, as well as minor aspectral, magnetite, and prehnite. The calculated modal proportions show an almost 50/50 split between the main minerals: 48% white mica and 48% chlorite. As with sample K33_0191_00, mineralogy indicates phyllic and propylitic alteration.

Figure 51. Mineral classification map for sample K33_0191_03. Depth 1273-1274 m. The primary minerals in this section of core are white mica and chlorite. White mica is displayed as the prominent mineral in this map.

3. K33_0192_1276m (Tray 02/03)

The upper of the two core lengths below covers the depth interval between 1276-1277 m and the lower covers only 1276 m (Figure 52). The mineral class map shows that the upper image (Tray 02) is predominantly chlorite, whereas the lower image (Tray 03) is predominantly white mica. Individual mineral maps display chlorite as abundant in both trays and white mica is abundant the whole length of Tray 03, but only at the end and middle of Tray 02. Gypsum is abundant in Tray 03 and moderate in Tray 02, whereas beidellite is abundant in Tray 02 and low-moderate in Tray 03. Epidote has low-moderate amounts in both trays. Aspectral minerals are moderate in Tray 02 and sparse in Tray 03, alunite is moderate in Tray 03 and very sparse in Tray 2, and carbonate in sparse in Tray 02 and very sparse in Tray 03. Kaolinite, montmorillonite, and prehnite are sparse in both trays. Zeolites are very sparse in Tray 02. Modal proportions for the sample are calculated to be 46% chlorite, 23% white mica, 18% beidellite, and 9% gypsum. The mineralogy described here is indicative of propylitic alteration with a lesser degree of phyllic alteration.

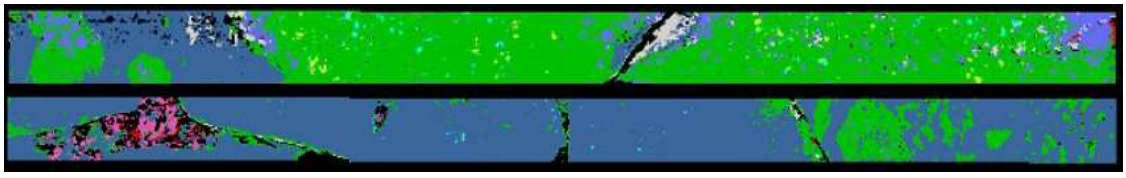

Figure 52. Mineral classification map for sample K33_0192_1276m. The 1 m depth for 1276 m is covered over two trays (02 and 03). The upper tray (02) displays chlorite as the primary mineral, and the lower tray (03) displays white mica as the primary mineral.

4. K33_0192_1277.75m (Tray 01)

Sample K33_0192-1277.75m is from Tray 0192_01 (Figure 15) which appears much more heterogeneous in the mineral class map than the previous samples. As seen in the class map, the primary mineral is chlorite, covering most of the core length. White mica is also a prominent mineral, though not as widespread as chlorite. Though clearer in the individual maps, aspectral, beidellite, and magnetite are abundant in the first half of the core. Carbonate and epidote are present in moderately low amounts, with epidote mostly in the second half of the core section. Gypsum, kaolinite, montmorillonite, and prehnite are sparse. The modal proportions for the section of the tray this sample came from are 56% chlorite and 33% white mica. The mineralogy of this sample demonstrates phyllic and propylitic alteration.

Figure 53. Mineral classification map for sample K33_0192_1277.75m. The primary minerals in this section of core are chlorite and white mica, however the class map shows more mineral variation than the previous sample class maps.

5. K33_0364_1752 m (Tray 01/02)

The depth of sample K33_0364_1752m (Figure 54) is from one of the two sections below, which cover 1751-1753 m. As displayed in the class map, individual mineral maps show that chlorite is abundant throughout the upper and lower core sections, with white mica only being abundant in the first half of the lower core section. Individual maps show that epidote is abundant throughout both cores, more so than is shown in the overall class maps. Prehnite has a moderate abundance in the upper core and is sparse in the lower core, whereas gypsum is barely present in the upper core but moderate-sparse in the lower core. Aspectral also has moderate amounts throughout. Carbonate and magnetite are present in minor amounts, and montmorillonite and wairakite have minor amounts in the lower core only. Alunogen has a very minor presence in the lower core. Modal proportions for the sample are calculated to be 68% chlorite, 23% epidote, and 8% prehnite. The abundance of chlorite and epidote indicates intensive propylitic alteration.

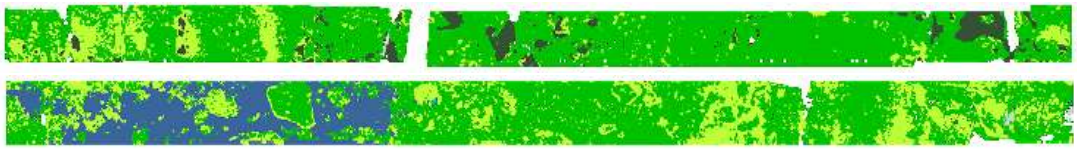

Figure 54. Mineral classification map for sample K33_0364_1752m. This depth is covered across two trays. The primary minerals in this section of core are chlorite and epidote. Chlorite is displayed as the prominent mineral in both trays in this map.

6. K33_0364_1753 m (Tray 00/01)

Sample K33_0364_1753m (Figure 55) has a depth which is covered by two core sections. One of these sections is the same as for the previous sample (K33_0364_1752m), so descriptions of mineralogy for this sample will only cover the upper core section below. Individual maps display an abundance of chlorite and epidote covering the length of the core section. Prehnite has a moderate abundance, and aspectral is abundant in the second half of the core section. Carbonate, gypsum, magnetite, and montmorillonite are present in minor amounts. Wairakite is present in a small amount also. The modal proportions for this sample are identical to the previous sample: 56% chlorite, 32% epidote, and 6% prehnite. As above, chlorite and epidote indicate intensive propylitic alteration.

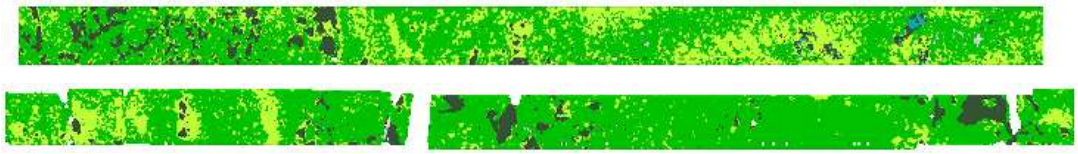

Figure 55. Mineral classification map for sample K33_0364_1753m. This depth is covered across two trays. The primary minerals in this section of core are chlorite and epidote. Chlorite is displayed as the prominent mineral in both trays in this map.

7. K33_0393_1833.2m (Tray 02/03)

This sample is either from Tray 02 (top image) or Tray 03 (bottom image) (Figure 56). The mineral class map shows chlorite as the primary mineral with high concentrations of carbonate at the beginning of Tray 02 and the end of Tray 03. Individual mineral maps display an abundance of chlorite throughout both trays and carbonate in moderate amounts in Tray 02 and sparse amounts in Tray 03. Wairakite is present in low-moderate amounts in Tray 02 and is sparse in Tray 03. Epidote is low-moderate in both trays. Montmorillonite and prehnite are sparse in both trays with aspectral being sparse in Tray 03 and very sparse in Tray 02. Beidellite is sparse in Tray 02. The calculated modal proportions for this sample are 84% chlorite and 14% unclassified. The abundance of chlorite indicates pervasive propylitic alteration.

Figure 56. Mineral classification map for sample K33_0393_1833.2m. This depth is from one of the two trays displayed. Chlorite is the primary mineral and main mineral displayed in the class map. Unclassified minerals are relatively high in this sample.

8. K33_0393_1834 m (Tray 00/01/02)

Sample K33_0393_1834m (Figure 57) has a depth whose range is covered by three core sections. Individual mineral maps show that, as displayed in the class map, chlorite is the only abundant mineral present. Carbonate is abundant only in the first part of the lowest core section, otherwise is in minor amounts in each core section. Prehnite, magnetite, and aspectral have minor quantities, and though epidote has minor concentrations overall, it has a moderate amount in the first part of the lowest core section. Montmorillonite and wairakite are present in moderate amounts only in the first part of the lowest core section, and beidellite has minor amounts in the same area. Alunogen is sparse in the upper and middle core sections. Modal mineral proportions for the sample are calculated to be 67% chlorite and 32% unclassified. These three sections of core underwent propylitic alteration.

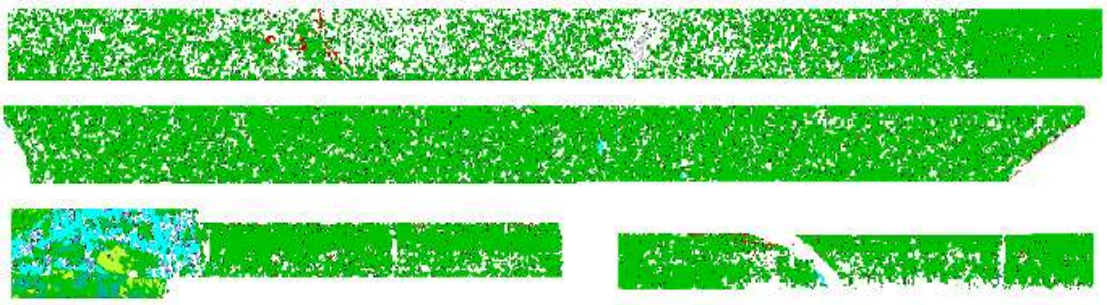

Figure 57. Mineral classification map for sample K33_0393_1834m. This depth is from one of the three trays displayed. Chlorite is the primary mineral and main mineral displayed in the class map. Unclassified minerals are relatively high in this sample.

9. K33_0423_1916.3 m (Tray 03)

Sample K33_0423_1916.3m primarily displays white mica and epidote on the class map (Figure 58). Individual maps show that epidote is the most abundant mineral, followed by white mica, then chlorite. Aspectral is present in moderate amounts, while gypsum, montmorillonite, prehnite, and wairakite are present in minor amounts. Beidellite and carbonate are sparse. Modal proportions for the sample are 49% white mica, 29% epidote, and 21% chlorite. Mineralogy is indicative of phyllic and propylitic alteration, with propylitic alteration being the most pervasive.

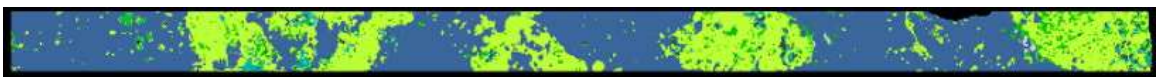

Figure 58. Mineral classification map for sample K33_0423_1916.3m. The primary minerals are epidote and white mica as reflected in the class map for this sample.

10. K33_0423_1919 m (Tray 00)

Mineralogy of K33_0423_1919m (Figure 21) is identical to that of K33_0423_1916m. Epidote is the primary mineral present, with an abundance of chlorite also. White mica is abundant only at either end of the core section. Aspectral, prehnite, and wairakite have moderate concentrations, and gypsum and montmorillonite have minor concentrations. Beidellite is sparse. Modal proportions are calculated to be 69% epidote, 22% white mica, and 8% chlorite. As with the previous sample, alteration type is phyllic and propylitic, with propylitic alteration being the most pervasive.

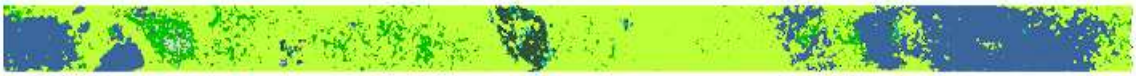

Figure 59. Mineral classification map for sample K33_0423_1919m. The primary mineral is epidote as reflected in the class map for this sample.

11. T2_0156_03 (802.6 – 803.3 m)

Sample T2_0156_03 (Figure 60) displays primarily chlorite and white mica in the class map. Individual maps show that chlorite is the most abundant mineral present, followed by white mica. Beidellite and montmorillonite are also abundant through the length of the core section, though in lesser amounts than chlorite and white mica. Apsectral, epidote, gypsum, kaolinite, and wairakite are all present in minor amounts. The modal proportions of the sample are 73% chlorite, 15% white mica, 5% montmorillonite, and 4% beidellite. The mineralogy of this section indicates phyllic, propylitic, and argillic alteration, with propylitic being the most pervasive type.

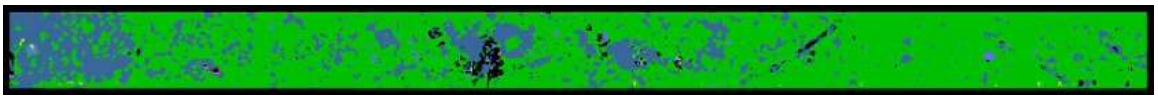

Figure 60. Mineral classification map for sample T2_0156_03. Depth covers 802.6 – 803.3 m. The primary mineral in this section of core is chlorite as displayed in the class map.

12. T2_0117_00 (695.2 - 695.9m)

The class map for sample T2_0117_00 shows a mix of chlorite, beidellite, and aspectral (Figure 61). Individual mineral maps show an abundance of beidellite, chlorite, and aspectral throughout the length of the tray. There are low-moderate amounts of wairakite and white mica, while alunogen, gypsum, and kaolinite are sparse. Carbonate is very sparse. The modal proportions for this sample are 51% beidellite, 25% chlorite, and 20% aspectral. Mineralogy is indicative of argillic alteration and a lesser degree of propylitic alteration.

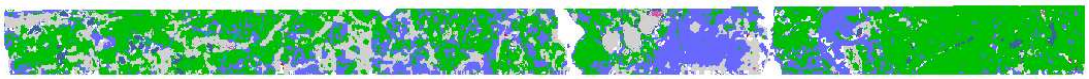

Figure 61. Mineral classification map for sample T2_0117_00. Depth covers 695.2 - 695.9 m. The primary mineral in the section of core is beidellite, however, chlorite is prominent in the mineral class map.

13. T2_0117_03 (693.2 – 693.9m)

Sample T2_0117_03 (Figure 62) is similar to T2_0117_00. The overall class map shows a high abundance of chlorite, aspectral, and beidellite, with areas of gypsum and carbonate. Individual mineral maps also show low amounts of montmorillonite. Kaolinite, wairakite, and white mica are sparse, and alunogen is very sparse. The calculated modal proportions are 50% beidellite, 24% chlorite, and 19% aspectral. As with sample 0117_00, mineralogy is indicative of argillic alteration and a lesser degree of propylitic alteration.

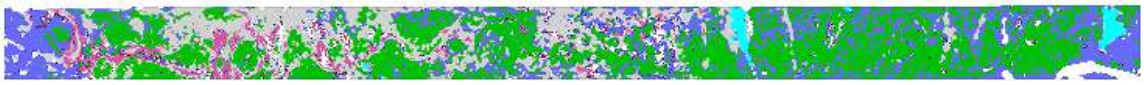

Figure 62. Mineral classification map for sample T2_0117_03. Depth covers 693.2 - 693.9 m. The primary mineral is beidellite however the class map is more heterogenous.

2.3.1.2 Lake City Samples

The Lake City samples used in this research include breccia (B), granite (G), tuff (T), dacite lava (DLA), and vein (V) rock types from various locations in and around the LC caldera. Figure 63 shows the mineral class map colour index provided by Corescan for the LC samples.

Figure 63. Colour legend for the Lake City mineral classification map.

1. LCB090314-1b

Breccia sample LCB090314-1b is fairly homogenous (Figure 64), the primary classification being aspectral with minor white mica (sericite). Individual mineral maps show there is also a minor presence of chlorite and amethyst. The modal mineral proportions of the sample are 94% aspectral and 6% white mica. The lack of alteration minerals indicates this sample has only minor phyllic alteration as shown by the presence of sericite.

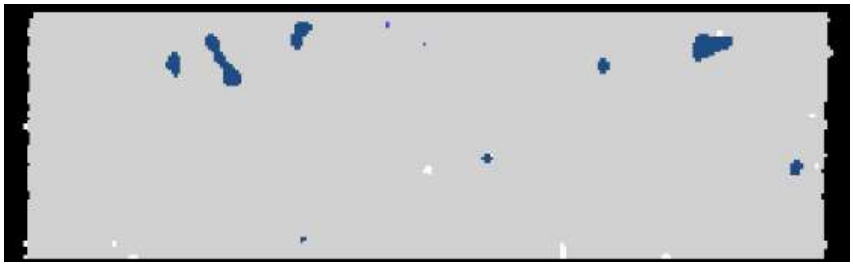

Figure 64. Mineral classification map for sample LCB090314_1b. The primary classification in this sample is aspectral.

2. LCB090314-5

Breccia sample LCB090314-5 is primarily sericite, with a high abundance of a silica-clay mix and a chlorite-white mica mix (Figure 65). There is also aspectral and chlorite present, with a minor amount of carbonate. Individual mineral maps also show minor amounts of montmorillonite and tourmaline. Modal proportions of the sample are 69% white mica, 14% iron oxide, 8% chlorite, 6% silica/quartz, and 2% aspectral. Mineralogy of this sample is indicative of phyllic alteration with a lesser degree of propylitic alteration.

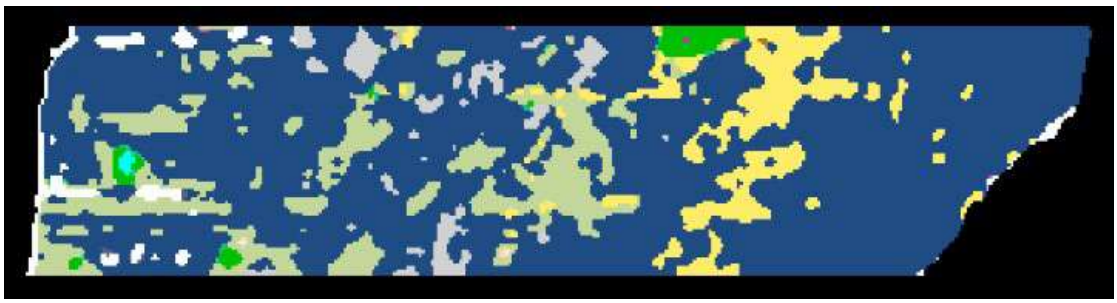

Figure 65. Mineral classification map for sample LCB090314-5. The primary mineral in this sample is white mica.

3. LCB091414-2

Like sample LCB090314-1b, Breccia sample LCB091414-2 (Figure 28) is primarily aspectral with some white mica. Carbonate is present in minor amounts, with lesser amounts of chlorite-white mica mix and chlorite. Individual mineral maps show aspectral is abundant, while white mica is present in moderate amounts. Maps also show minor amounts of amethyst, epidote, and silica. Modal proportions are calculated to be 74% aspectral and 24% white mica. Due to the primary aspectral mineralogy with lesser alteration mineralogy, this sample shows weak phyllic alteration.

Figure 66. Mineral classification map for sample LCB091414-2. The primary mineral in this sample is aspectral.

4. LCDLA082913-1

Sample LCDLA082913-1 is from dacitic lava and is fairly homogenous (Figure 67). The bulk of the sample is montmorillonite with minor occurrences of jarosite. The modal proportions are 96% montmorillonite and 3% iron oxide. This sample displays argillic alteration as shown by the almost exclusive presence of montmorillonite.

Figure 67. Mineral classification map for sample LCDLA082913-1. The primary mineral in this sample is montmorillonite.

5. LCDLA082913-2

Sample LCDLA08913-2 (Figure 68) is identical to LCDLA082913-1; montmorillonite is the primary mineral present with minor amounts of jarosite. Individual mineral maps also show minor amounts of white mica. The calculated modal proportions are 90% montmorillonite, 6% iron oxide, and 4% jarosite. As with the previous sample, this sample also underwent argillic alteration.

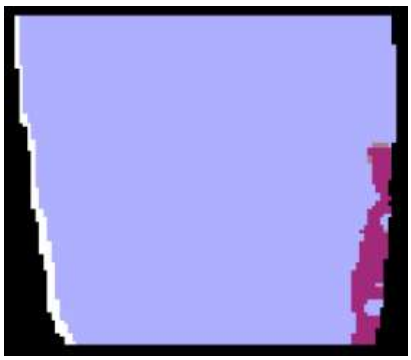

Figure 68. Mineral classification map for sample LCDLA082913-2. The primary mineral in this sample is montmorillonite.

6. LCG090714-2c

Granite sample LCG090714-2c has a primary mineralogy of white mica with some chlorite-white mica mix, aspectral, and minor amounts of chlorite, montmorillonite, and silica-clay mix (Figure 69). The modal proportions for this sample are 89% white mica, 6% montmorillonite, 2% aspectral, and 2% chlorite. The mineralogy is indicative of intensive phyllic alteration with minor amounts of propylitic and argillic alteration.

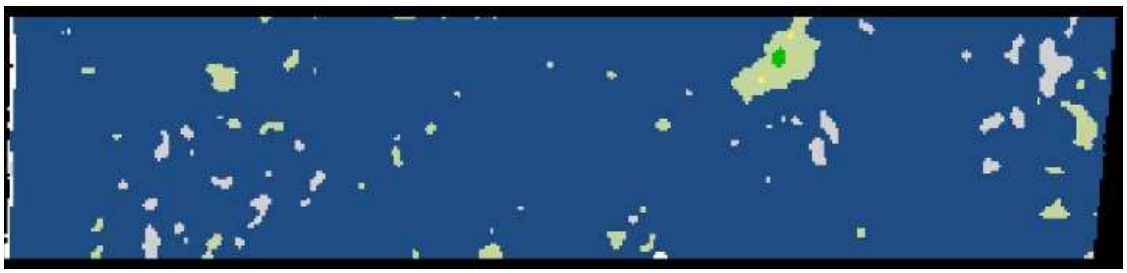

Figure 69. Mineral classification map for sample LCG090714-2c. The primary mineral in this sample is white mica.

7. LCG090714-3a

Granite sample LCG090714-3a is composed mainly of white mica with high amounts of a silica-clay mix (Figure 70). There is also some silica with minor amounts of montmorillonite and aspectral minerals. Individual mineral maps also show a very minor amount of jarosite. Modal proportions are 53% white mica, 32% iron oxide, 11% silica/quartz, and 4% montmorillonite. The dominance of white mica in this sample indicates phyllic alteration, with a minor degree of argillic alteration.

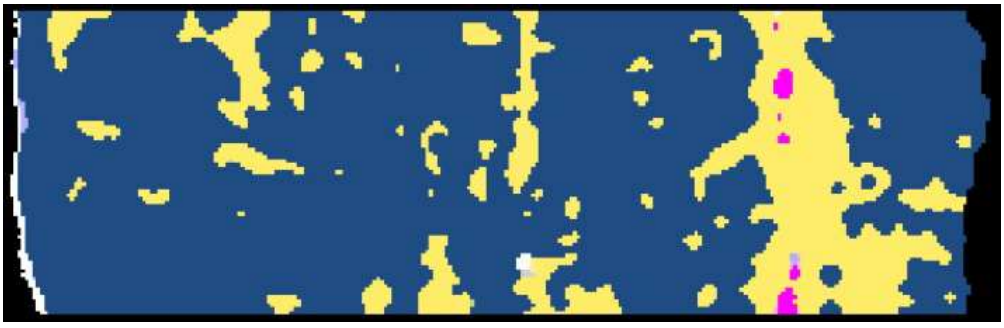

Figure 70. Mineral classification map for sample LCG090714-3a. The primary mineral in this sample is white mica.

8. LCG090714-3b

Granite sample LCG090714-3b is primarily white mica with a white mica-chlorite mix (Figure 71). There are lesser amounts of chlorite, silica-clay mix, kaolinite, and montmorillonite present, with aspectral and silica seen additionally in the individual mineral map. The modal proportions for this sample are 75% white mica, 13% chlorite, 8% iron oxide, and 4% montmorillonite. This mineralogy shows the sample went through phyllic alteration and displays lesser degrees of propylitic and argillic alteration.

Figure 71. Mineral classification map for sample LCG090714-3b. The primary mineral in this sample is white mica.

9. LCG091314-1b

Granite sample LCG091314-1b (Figure 34) has a primary mineralogy of white mica with a silica-clay mix and minor aspectral. Individual mineral maps show white mica as the primary mineral, an abundance of silica, some montmorillonite, and a minor amount of epidote in the sample. Modal proportions are calculated to be 45% white mica, 40% iron oxide, and 14% silica/quartz. The abundance of white mica is indicative of phyllic alteration.

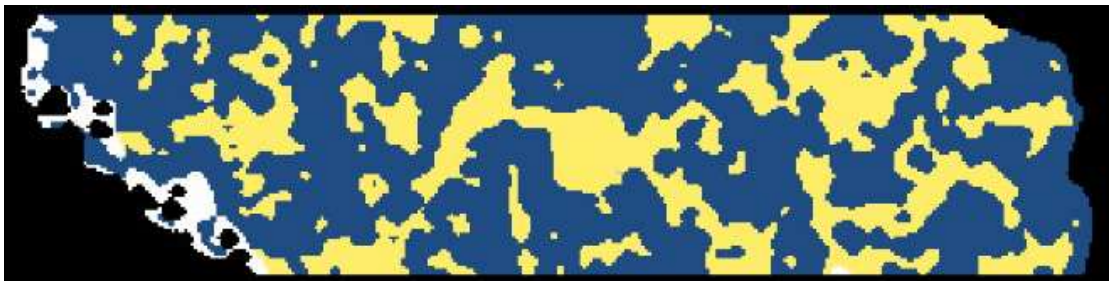

Figure 72. Mineral classification map for sample LCG091314-1b. The primary mineral in this sample is white mica.

10. LCT091014-1a

Tuff sample LCT091014-1a is primarily white mica with aspectral (Figure 73). There are minor amounts of chlorite-white mica mix, carbonate, chlorite, and silica-clay mix.

Individual mineral maps also show the presence of minor amounts of montmorillonite. The modal proportions for this sample are 82% white mica, 11% aspectral, and 4% iron oxide. This sample displays extensive phyllic alteration.

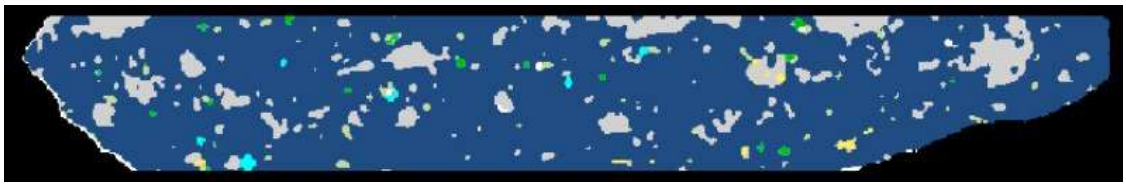

Figure 73. Mineral classification map for sample LCT091014-1a. The primary mineral in this sample is white mica.

11. LCT091014-1b

Unlike LCT091014-1a, tuff sample LCT091014-1b appears primarily aspectral with lesser amounts of white mica (Figure 74). However, individual mineral maps display an almost equal abundance of white mica and aspectral. They also show a minor amount of montmorillonite. The high sericite content is indicative of phyllic alteration. There were no modal percentages provided for this sample so approximations were made for calculations in later sections. These approximations include 49% white mica, 46% aspectral, 3% iron oxide, and 2% silica/quartz. The basis for these decisions can be found in Appendix B2.

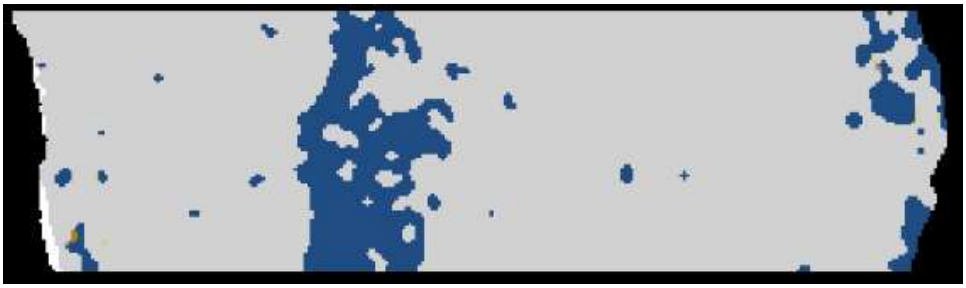

Figure 74. Mineral classification map for sample LCT091014-1b.

12. LCT091514-3

The class map for LCT09154-3 shows a primary presence of aspectral, with some white mica, and minor amounts of montmorillionite, kaolinite, and silica/clay (Figure 75). Individual maps also show sparse amounts of dickite. The modal proportions for this sample are 84% aspectral, 10% white mica, 4% montmorillonite, and 2% silica/quartz. The mineralogy is indicative of weak phyllic, and very weak argillic alteration.

Figure 75. Mineral classification map for sample LCT091514-3. The primary mineral in this sample is aspectral.

13. LCTBV071714-5a

The tuff breccia vein sample LCTBV071714-5a is mainly aspectral with a high amount of silica-clay mix and white mica (Figure 76). Jarosite is also present as well as a minor amount of carbonate and silica. Individual mineral maps display a high abundance of aspectral and silica. White mica is present in lesser amounts as well as montmorillonite and a minor amount of fluorite. Modal proportions for this sample are more varied than most of the previous samples: 35% aspectral, 31% silica/quartz, 22% white mica, 6% montmorillonite, 5% iron oxide, and 1% jarosite. This sample shows weak phyllic alteration.

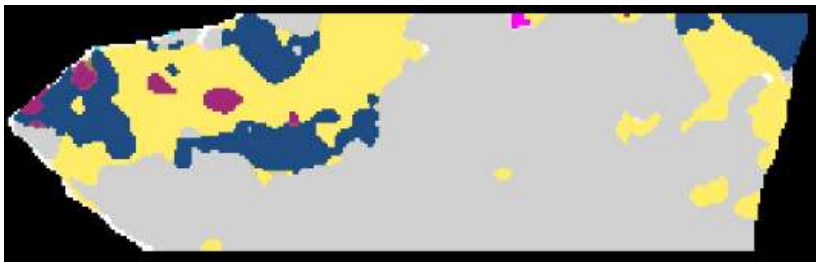

Figure 76. Mineral classification map for sample LCTBV071714-5a. This sample contains almost equal proportions of aspectral and silica/quartz.

14. LCTV090314-4a

Tuff vein sample LCTV090314-4a is abundant in dickite, silica-clay mix, aspectral, and white mica with minor amounts of silica and jarosite (Figure 77). Individual mineral maps also display an abundance of dickite, aspectral, silica, and white mica. They also show minors amounts of epidote and montmorillonite. The calculated modal proportions for this sample are 29% silica/quartz, 21% dickite, 18% white mica, 17% aspectral, and 15% iron oxide. The presence of dickite is indicative of advanced argillic alteration.

Figure 77. Mineral classification map for sample LCTV090314-4a. Silica/quartz, dickite, white mica, and aspectral are all present in similar amounts.

15. LCTV091014-1c

Tuff vein sample LCTV091014-1c is abundant in silica-clay mix, aspectral, and sericite, with a minor amount of silica (Figure 40). Individual maps show an abundance of silica, aspectral, and white mica, and also some montmorillonite. Modal proportions are 31% silica/quartz, 26% white mica, 24% iron oxide, 14% aspectral, and 5% montmorillonite. Alteration mineralogy indicates moderate phyllic alteration, with some weak argillic alteration.

Figure 78. Mineral classification map for sample LCTV091014-1c. Silica/quartz and white mica are the primary minerals in this sample.

16. LCTV091014-1d

Tuff vein sample LCTV091014-1d is abundant in silica-clay mix, with sericite and aspectral, with minor silica (Figure 41). Individual maps show silica as the most abundant mineral, followed by white mica. Individual maps also show presence of montmorillonite and minor jarosite. The modal proportions for this sample are calculated to be 33% silica/quartz, 31% white mica, 17% iron oxide, 10% aspectral, and 9% montmorillonite,

which is very similar to the composition of sample LCTV091014-1c. Mineralogy shows this sample underwent phyllic alteration with some weak argillic alteration also.

Figure 79. Mineral classification map for sample LCTV091014-1d. Silica/quartz and white mica are the primary minerals in this sample.

The largest discrepancies between the representative percentages from the ASI and the hyperspectral percentages for the H-ASI are for the ASI "Abundant" categories, whether Pm or Sm. (Appendices B3 and B4) The representative percentages from the ASI max out at 50%, whereas some samples contain >70% of one mineral. These samples include two TB samples, where the ASI percentage and H-ASI percentage has a difference of 23-33% composition (i.e. ASI composition of 50% and H-ASI composition of 73-83%), and eight LC samples, where the difference is 24-46% (i.e. ASI composition of 50% and H-ASI composition of 74-96%).

The modal mineral percentages obtained through hyperspectral imaging are used in place of the representative percentages assigned in the ASI. These H-ASI values therefore more accurately represent actual sample compositions, meaning they are able to provide closer estimates of Pm, Sm, and AI, in turn reducing the subjectivity.

2.3.2 ASI Parameters

2.3.2.1 Pm, Sm, and AI

The primary and secondary mineralogy (Pm and Sm) values for each sample were calculated by multiplying the modal percentage (i.e. abundance), as determined by Corescan imaging, by the mineral hardness index for each mineral present in amounts which, rounded up, were equal to or greater than 1%. The values for those minerals associated with primary mineralogy were then summed together to determine Pm, and those associated with secondary mineralogy were summed together for Sm. The Alteration Index (AI) was calculated by summing the modal percentages of secondary minerals present in each sample and dividing by 100. The results for the Telaga Bodas samples are presented in Table 19 and those for the Lake City samples in Table 20. Modal percentages

for sample LCT091014-1b were estimated by comparing the Corescan hyperspectral images for this sample to the images of other samples, as mentioned previously.

Table 19. Pm, Sm, and AI values for the Telaga Bodas samples.

Sample	Pm	Sm	AI
K33_0191_00	1.02	33.4	0.96
K33_0191_03	0	31.38	0.99
K33_0192_1276	3.06	32.48	0.96
K33_0192_1277.75	3.4	33.14	0.92
K33_0364_1752	1.36	86.84	0.99
K33_0364_1753	9.35	92.24	0.94
K33_0393_1833.2	0	44.91	0.86
K33_0393_1834	1.7	34.61	0.67
K33_0423_1916.3	0	63.72	0.99
K33_0423_1919	1.53	123.11	0.99
T2_0156_03	0	29.15	0.99
T2_0117_00	33.49	18.41	0.77
T2_0117_03	32.3	19.14	0.78

Results for the Telaga Bodas samples show very low Pm values, with the exception of the 0117 samples, where the Pm is higher than the Sm. The 0117 samples have high percentages classified as aspectral, which is assumed to contribute to primary mineralogy. As expected, the AI for these samples is therefore lower than for the samples where Sm is higher than Pm. The exception is sample K33_0393_1834, where Sm is higher than Pm but the AI is low at 0.67. This is because 31.6% of the sample has been categorized as unclassified, and therefore has neither been attributed to Pm or to Sm. This high percentage of unclassified mineralogy causes a large margin of error for this sample.

Table 20. Pm, Sm, and AI values for the Lake City samples.

Sample	Pm	Sm	AI
LCB090314-1b	159.8	0.57	0.06
LCB090314-5	3.74	48.24	0.98
LCB091414-2	125.97	3.25	0.25
LCDLA082913-1	0	15.39	1
LCDLA082913-2	0	22.71	1
LCG090714-2c	4.08	10.71	0.98

LCG090714-3a	0	84.47	1
LCG090714-3b	0	28.9	1
LCG091314-1b	0	102.04	1
LCT091014-1a	18.87	17.57	0.89
LCT091014-1b*	78.2	13.99	0.54
LCT091514-3 (1)**	142.63	5.38	0.16
LCT091514-3 (2)**	142.63	5.38	0.16
LCTBV071714-5a	59.33	76.87	0.65
LCTV090314-4a	28.22	89.57	0.83
LCTV091014-1c	23.12	108.89	0.87
LCTV091014-1d	16.49	102.19	0.90

*Modal percentage data for this sample are estimates based on other samples.

**Two samples were taken from LCT091514-3, however, because they are from the same sample, their Pm, Sm, and AI values will be the same due to the Corescan mineralogy data having been obtained from the bulk rock.

Results for the Lake City samples show more variation in Pm, Sm, and AI than the TB samples. Given the quartz veining and alteration at Lake City Caldera (Garden et al., 2020), the modal percentages for quartz/silica have been attributed to secondary mineralogy and so contribute towards the calculation of Sm and AI.

The samples with the largest difference between the ASI and H-ASI modal mineral percentages are the same samples which have the largest differences between the ASI and H-ASI Pm and Sm values. The largest difference is for minerals with a hardness index greater than 0.1. For the samples where the mineral with the largest abundance difference is assigned a hardness index of 0.1, the difference in the resulting Pm or Sm values are small. This difference is greater for minerals with a hardness index of 0.5 and higher. Among the Telaga Bodas samples, K33_0423_1919 has the largest difference, with an ASI Sm value of 90.75 and a H-ASI Sm value of 123.11, a difference of 32.36. For the Lake City samples, LCB090314-1b has the largest difference, with an ASI Pm value of 85 and a H-ASI value of 159.8, a difference of 74.8 (Appendix B4).

2.3.2.2 Fracture Index

The fracture index was determined based on visual inspection of the 1x2 inch core samples, and not the bulk rock (Appendix B5). None of the ASI Snf categories accurately described the fractures seen in the core samples, so the closest category was used for the ASI calculations. Results for the Telaga Bodas samples are presented in Table 21 and results for the Lake City samples are presented in Table 22. None of the samples had large (>1 mm wide) fractures, so based on the Fracture Index descriptions put forth by Wyering et

al., (2015), none of the TB or LC samples were assigned a Snf value of 4 or higher, with the exception of the two LC samples with cavities.

Table 21. Fracture Index for the Telaga Bodas samples.

Sample	Snf	Description
K33_0191_00	2	Several possible hairline fractures, <1 mm wide, > 10 mm long, closed
K33_0191_03	2	Several possible hairline fractures, < 1mm wide, one > 10 mm long, closed
K33_0192_1276	2	Possible hairline fractures, <1 mm wide, > 10 mm long, closed
K33_0192_1277.75	0	No fractures visible.
K33_0364_1752	3	1 small fracture, <1 mm wide, <10 mm long, open. Some veining at one end, closed.
K33_0364_1753	2	1 possible small fracture at end of sample, closed. Less clear than other samples.
K33_0393_1833.2	0	No fractures visible.
K33_0393_1834	3	1 fracture on end of sample, surficial, <1 mm wide, ~19mm long, open
K33_0423_1916.3	0	No fractures visible.
K33_0423_1919	0	No fractures visible.
T2_0156_03	2	Possible hairline fracture, <1 mm wide, > 10 mm long. Less clear than sample K33_0191_03
T2_0117_00	0	No fractures visible. Veining, closed.
T2_0117_03	3	1 long fracture, <1 mm wide, >10 mm long, possible open (fine). Veining, closed. Damaged ends of core.

Table 22. Fracture Index for the Lake City samples.

Sample	Snf	Description
LCB090314-1b	3	1 long, open fracture, <1 mm wide, almost full length of sample.
LCB090314-5	3	Several fractures, <1 mm wide, >10 mm long, open or partially open. 1 groove, 2 mm wide, 9 mm long. Several Closed fractures.
LCB091414-2	3	2 fractures, <1 mm wide, >10 mm long, open. Possible other hairline fractures, closed.
LCDLA082913-1	0	No fractures visible.
LCDLA082913-2	0	No fractures visible.

LCG090714-2c	2	1 possible hairline fracture at end of sample, <1mm wide, >10 mm long, closed. Possible slight veining.
LCG090714-3a	2	Several possible closed fractures or veins, 1 partially open fracture, <1mm wide, >10mm long. A couple of veins ~1mm wide.
LCG090714-3b	3	2 partially open fractures, <1mm wide, >10mm long. Several veins.
LCG091314-1b	3	Partially open fractures, several hairline fractures, <1mm wide, >10 mm long, closed.
LCT091014-1a	0	No fractures visible.
LCT091014-1b	0	No fractures visible. Surficial line on one end
LCT091514-3 (1)	2	Possible, fine, hairline fractures, <1mm wide, closed.
LCT091514-3 (2)	0	No fractures visible. Possible slight veining, surficial line on one end
LCTBV071714-5a	2	1 fracture, <1mm wide, >10 mm long, closed. Several possible thin veins.
LCTV090314-4a	4	Several interconnected fractures and veins, <1mm wide, >10 mm long. Several small cavities.
LCTV091014-1c	2	Several long, <1mm wide, >10 mm long, fractures, closed.
LCTV091014-1d	4	Fractures, closed and partially open, <=1mm wide, >10 mm long. Large cavity, smaller cavities.

Given the inaccuracies in the current Snf for the samples used in this study, the actual impact of the fractures is likely greater than currently predicted using the ASI Snf categories. A revised Fracture Index will be assessed in a later section to determine the impact on the resulting ASI and UCS values.

2.3.3 Permeability

Permeability measurements were taken to determine whether or not a correlation exists between ASI parameters and the UCS, and the permeability of the variably altered samples used in this study, and if permeability can improve the use of the ASI equation.

The permeability and storage porosity results for the Telaga Bodas samples are provided in Table 23, along with alteration type and dominant mineralogy discussed in previous sections. A permeability result could not be obtained for sample K33_0192_1276. The PPint did not change when the sample was loaded into the BenchLab chamber, meaning the sample was unresponsive and a test could not be run. Results for the rest of the TB samples range from 1.73e-07 mD to 1.99e-04 mD. All graphs for Telaga Bodas samples are provided in Appendix B6.

Table 23. Permeability, storage porosity, and alteration mineralogy for the Telaga Bodas samples.

Sample	Permeability (mD)	Storage Porosity (%)	Alteration Type(s)	Dominant mineral(s)
K33_0191_00	7.58e-06	0.421	Phyllic, propylitic	Chlorite, white mica
K33_0191_03	5.61e-06	0.210	Phyllic, propylitic	Chlorite, white mica
K33_0192_1276*	N.D.	N.D.	Propylitic, phyllic	Chlorite
K33_0192_1277.75	7.93e-07	0.087	Phyllic, propylitic	Chlorite
K33_0364_1752	1.99e-04	0.731	Propylitic	Chlorite
K33_0364_1753	9.82e-05	0.248	Propylitic	Chlorite
K33_0393_1833.2	1.73e-07	0.312	Propylitic	Chlorite
K33_0393_1834	1.58e-04	0.205	Propylitic	Chlorite
K33_0423_1916.3	1.84e-06	0.090	Phyllic, propylitic	Epidote, white mica
K33_0423_1919	7.54e-06	0.790	Propylitic, phyllic	Epidote
T2_0156_03	2.72e-06	0.127	Phyllic, propylitic, argillic	Chlorite
T2_0117_00	1.3e-05	0.168	Argillic, propylitic	Beidellite
T2_0117_03	2.75e-07	0.119	Argillic, propylitic	Beidellite

* N.D. = No Data.

All but one of the Telaga Bodas permeability samples graphs (Appendix B6) show that good, clean results were obtained from the permeameter. An example of a good, reliable result is shown in Figure 80. The first plot shows the time history of the Pore Pressure Source. The second plot shows the response (blue line), the response function with maximum and minimum storage estimates (teal and green lines), and the best fit to the collected data (red line). The red line should be close to the real data (blue line). The third plot shows the amplitude ratio of the source/response versus the frequency. Ideally, the A-ratio should reach between 0.4 and 0.8. Most of the Telaga Bodas results fall within or close to this range. The fourth plot shows permeability against storage porosity and should be linear. The last plot shows how well the permeability and storage porosity pair fits the actual data. The lower the error, the better the fit. A strong minimum point shows a well constrained capture. While some curves are stronger than others, all but one sample displays a curve and minimum point. Sample K33_0393_1834 doesn't have the same level of accuracy in the results. The third and fifth plots deviate from the expected trend and actual data, however, the response function (second plot) is still good, and plot four isn't too far off the trend. Though this sample doesn't have the highest permeability recorded for the Telaga Bodas samples, it does consistently appear as an outlier in graphs in subsequent sections.

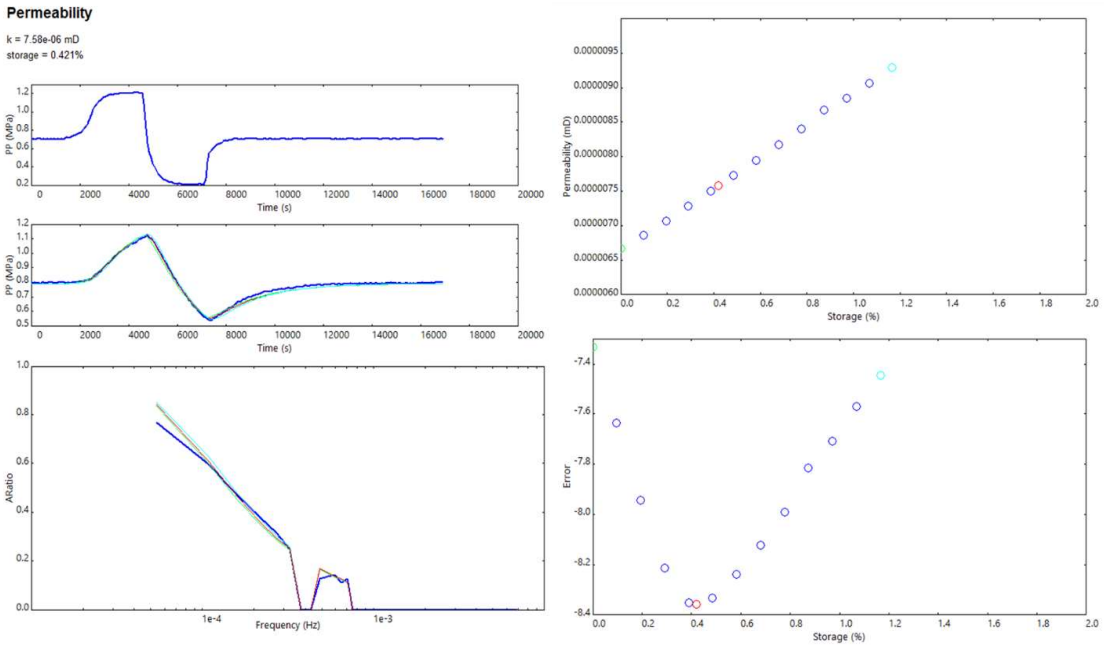

Figure 80. Example of the BenchLab permeability results graph. These results are for sample K33_0191_00 and show well constrained data.

Figure 81 shows a graph of the permeability results for the Telaga Bodas samples. Three of the 12 samples have higher permeability than the rest. The two with the highest permeability values are the same as those with some of the highest assigned fracture index values from the Telaga samples. A closer look at the lower nine samples is shown in Figure 82.

The two 0117 samples have identical mineral percentages, yet a relatively large difference in permeability, which is likely attributed to the difference in the fracture index. The other samples all have greater differences in mineral percentages and different fracture indexes for samples taken from the same core sections, which would all contribute to the differences in permeability for similar samples.

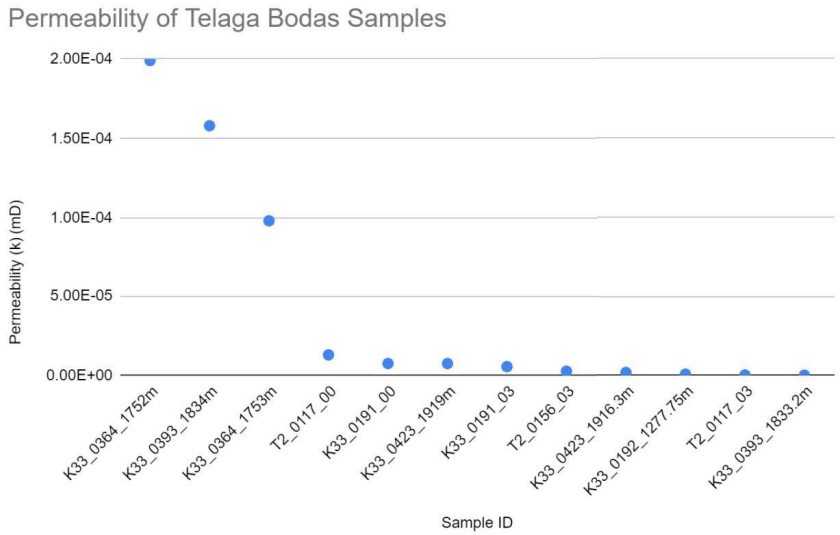

Figure 81. Permeability graph for Telaga Bodas samples.

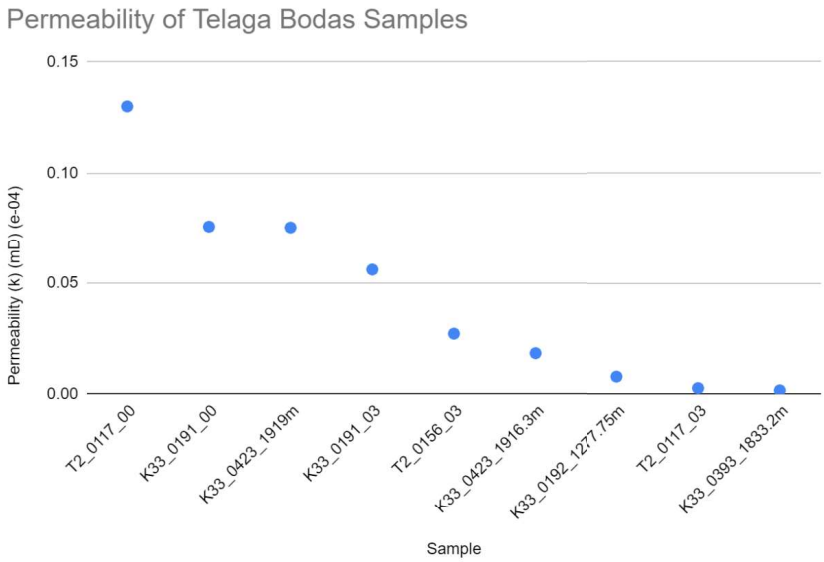

Figure 82. A closer look at the Telaga Bodas samples with lower permeability.

A comparison of the permeability data with the percentage of soft minerals in a sample (Hardness Index < 1) provides a correlation coefficient of -0.33 for the Telaga Bodas samples (Figure 83A). Figure 83B shows the sample results after removing the three outliers and has a correlation coefficient of -0.22. The coefficients show there is a weak negative correlation between permeability and the percentage of soft minerals.

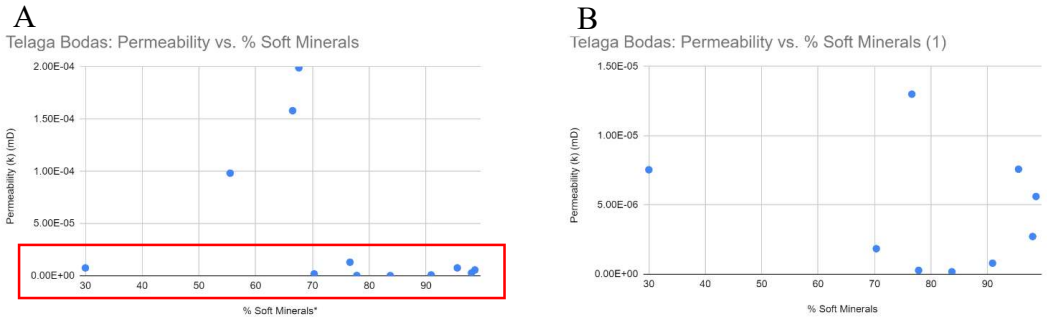

Figure 83. A. Graph showing the relationship between permeability and the percentage of soft minerals in a sample for the Telaga Bodas samples. Though the graph shows no apparent correlation between the two parameters, the correlation coefficient is -0.33 (weak negative). B. A close-up of the lower permeability samples as outlined by the red box in figure A. The correlation coefficient for the subset of samples is -0.22.

Table 24 displays the permeability results, storage porosity, and alteration mineralogy for the Lake City samples. Permeability ranges from 1.36e-07 mD to 1.04e-04 mD. All graphs for Lake City samples are provided in Appendix B6. The graphs show more inconsistent results than the Telaga Bodas samples, with more graphs displaying a less than ideal fit for several of the plots. While some have partially good data, there are a couple of samples where well-fitting data could not be obtained. However, on the whole, most of the plots were clean and provide reliable data. Figure 84 shows a graph of the permeability results for the Lake City samples. Two samples have a higher permeability than the rest. There appears to be no obvious similarities between the samples with higher permeability values. Figures 85 and 86 show a closer look at the permeabilities and relative values for the lower permeability samples. There doesn't appear to be any identifiable pattern between ASI values, Snf, or mineral proportions for the samples showing similar permeability values.

Table 24. Permeability, storage porosity, and alteration mineralogy for the Lake City samples.

Sample	**Permeability (mD)**	**Storage Porosity (%)**	**Alteration Type(s)**	**Dominant mineral(s)**
LCB090314-1b	1.66e-06	0.000	Weak phyllic	Aspectral

LCB090314-5	1.76e-05	0.211	Phyllic, propylitic	White mica
LCB091414-2	4.28e-07	0.046	Weak phyllic	Aspectral
LCDLA082913-1	2.57e-06	0.490	Argillic	Montmorillonite
LCDLA082913-2	1.61e-06	1.204	Argillic	Montmorillonite
LCG090714-2c	9.66e-07	0.363	Phyllic, argillic, propylitic	White mica
LCG090714-3a	6.78e-05	0.187	Phyllic, argillic	White mica
LCG090714-3b	4.14e-07	0.510	Phyllic, propylitic, argillic	White mica
LCG091314-1b	5.98e-06	0.287	Phyllic	White mica
LCT091014-1a	2.89e-07	0.182	Phyllic	White mica
LCT091014-1b	1.43e-06	0.199	Phyllic	White mica
LCT091514-3 (1)	1.36e-07	0.295	Phyllic, propylitic, argillic	Aspectral
LCT091514-3 (2)	4.21e-07	0.943	Phyllic, propylitic, argillic	Aspectral
LCTBV071714-5a	2.59e-07	0.120	Weak phyllic	Aspectral, silica
LCTV090314-4a	9.96e-07	0.199	Advanced argillic	Silica, dickite, white mica
LCTV091014-1c	1.04e-04	0.188	Phyllic, argillic	Silica, white mica
LCTV091014-1d	5.63e-06	0.590	Phyllic, argillic	Silica, white mica

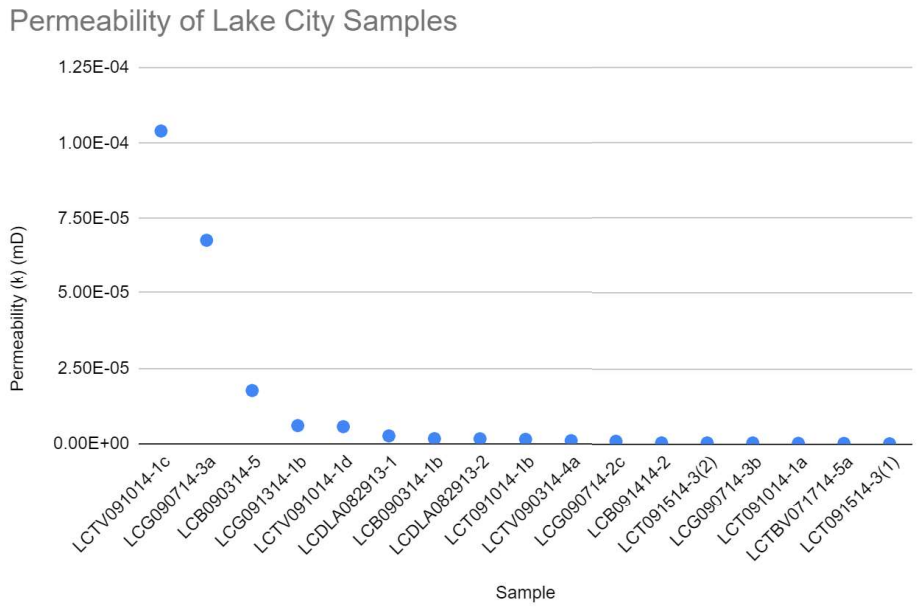

Figure 84. Permeability graph for Lake City samples.

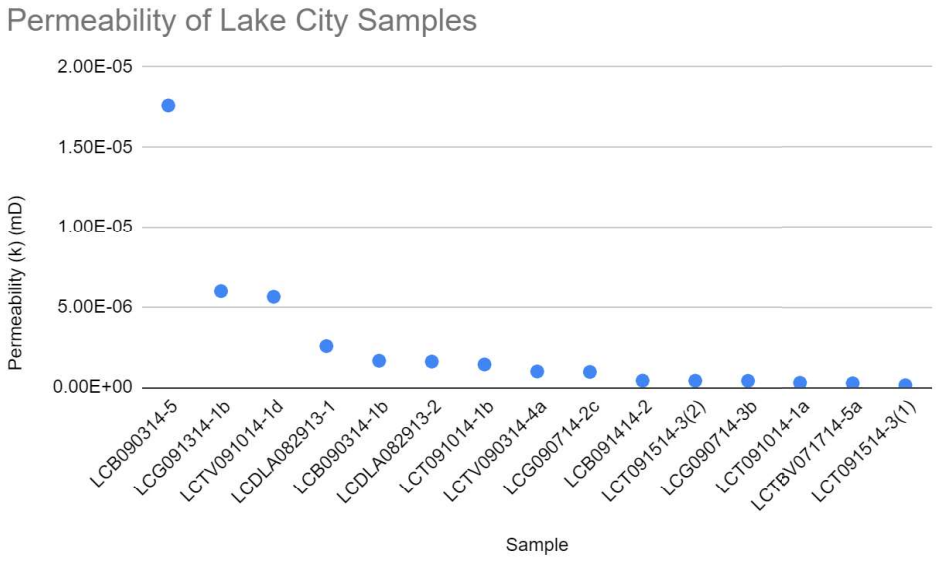

Figure 85. Permeability graph for Lake City samples without the two highest samples.

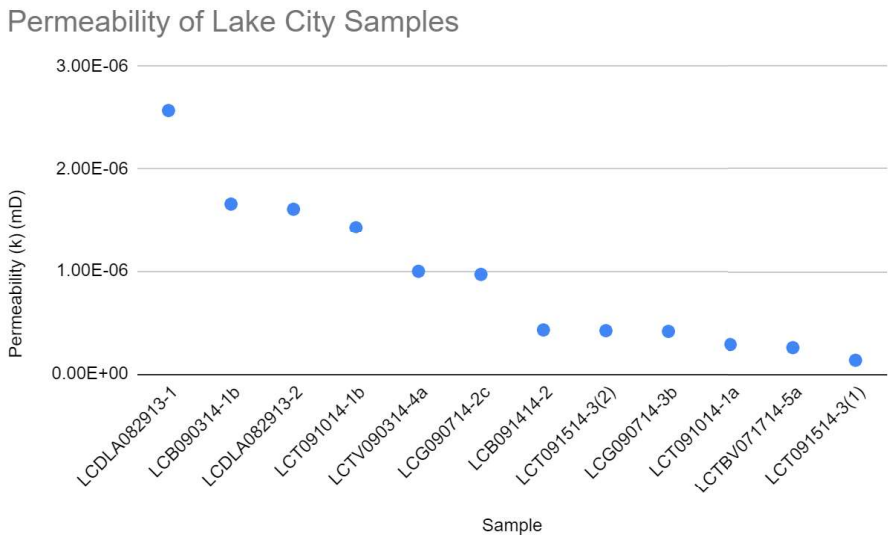

Figure 86. Permeability graph for Lake City samples, without the highest five samples.

A comparison of the Lake City permeability data with the percentage of soft minerals present in a sample also shows no correlation, even after removing the three outliers from the dataset (Figures 87). The Lake City samples have a correlation coefficient of -0.1 (Figure 87A) and for the subset of samples after removing the three outliers, the correlation coefficient is 0.1 (Figure 87B), reflecting no correlation between permeability and the percentage of soft minerals in a sample. When all Telaga Bodas and Lake City data is combined, there is no correlation (-0.04) between the two parameters.

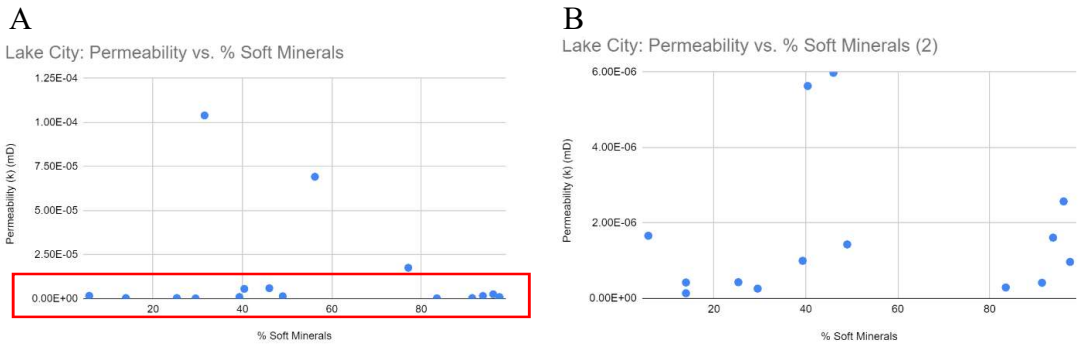

Figure 87. A. Graph showing the relationship between permeability and the percentage of soft minerals in a sample for the Lake City samples. As shown in the graph, there appears to be no correlation between the two parameters. B. A close-up of the lower permeability samples as outlined by the red box in Figure A. There is still no apparent correlation shown.

2.3.4 Porosity

Porosity is a key parameter of the ASI equation and is not impacted by the H-ASI changes to the mineral parameters. However, as noted previously, porosity data was obtained from smaller samples of each rock and not from the core samples themselves due to instrument restrictions. The particle density for each sample is the average of the particle density of the sub-samples. The largest range between particle density measurements of the sub-samples was 0.18 g/cm3, and only four of the 29 samples (Note: LCT091514-3 had two core samples) had a range of ≥ 0.1 g/cm3. This shows that there was very little variation between different pieces of the samples, even where the sub-samples were visually varied (e.g. breccias), hence can be taken to be reliable substitutes for the actual core samples. Data for the Telaga Bodas and Lake City porosity tests and sub-samples for can be found in Appendix B7.

Porosity results for the Telaga Bodas samples are presented in Table 25, and in Table 26 for the Lake City samples. Porosity ranges from 4.31% to 18.09% and from 2.06% to 21.54% for the Telaga Bodas and Lake City samples respectively. From the Telaga dataset, the three T2 samples have identical porosities, as do the two 0393 samples. Though the rest of the samples have a larger difference in porosity for samples from the same tray, the range of porosity is small overall. The same can be said for the Lake City samples; the range of porosity is small for similar samples, with the dacite samples (DLA) having noticeably larger porosity.

Table 25. Porosity results for Telaga Bodas samples.

Sample	**Dry Weight (W) (g)**	**Volume (V) (cm^3)**	**Particle Density (G_P) (g/cm^3)**	**Bulk Density (G_B) (g/cm^3)**	**Porosity (%)**
K33_0191_00	52.26	21.89	2.8567	2.39	16.42
K33_0191_03	51.31	20.84	2.8224	2.46	12.77
K33_0192_1276	55.92	22.21	2.7304	2.52	7.78
K33_0192_1277.75	53.14	22.29	2.7819	2.38	14.31
K33_0364_1752	55.71	21.21	2.9518	2.63	11.00
K33_0364_1753	52.66	21.42	3.0018	2.46	18.09
K33_0393_1833.2	59.60	22.19	2.8074	2.69	4.31
K33_0393_1834	59.23	21.85	2.8434	2.71	4.67
K33_0423_1916.3	56.24	21.64	2.9191	2.60	10.95
K33_0423_1919	52.86	21.91	2.8382	2.41	15.00
T2_0156_03	54.98	22.00	2.7270	2.50	8.37
T2_0117_00	57.87	22.09	2.8518	2.62	8.15
T2_0117_03	56.56	21.28	2.9107	2.66	8.69

Table 26. Porosity results for Lake City samples.

Sample	Dry Weight (W) (g)	Volume (V) (cm^3)	Particle Density (G_P) (g/cm^3)	Bulk Density (G_B) (g/cm^3)	Porosity (%)
LCB090314-1b	57.98	21.72	2.7866	2.67	4.21
LCB090314-5	55.43	21.49	2.6890	2.58	4.07
LCB091414-2	55.96	21.74	2.7911	2.57	7.79
LCDLA082913-1	41.79	21.41	2.4882	1.95	21.54
LCDLA082913-2	42.71	20.52	2.5645	2.08	18.85
LCG090714-2c	56.22	22.34	2.6723	2.52	5.84
LCG090714-3a	53.28	21.48	2.6832	2.48	7.54
LCG090714-3b	55.55	20.99	2.7022	2.65	2.06
LCG091314-1b	54.52	21.37	2.6414	2.55	4.84
LCT091014-1a	51.20	21.34	2.7136	2.40	11.60
LCT091014-1b	51.69	21.84	2.6580	2.37	10.94
LCT091514-3 (1)	53.50	22.17	2.5911	2.41	6.85
LCT091514-3 (2)	52.65	21.61	2.5911	2.44	5.97
LCTBV071714-5a	55.76	21.85	2.6737	2.55	4.54
LCTV090314-4a	54.99	21.54	2.6756	2.55	4.57
LCTV091014-1c	55.08	21.37	2.6715	2.58	3.54
LCTV091014-1d	54.54	22.02	2.6987	2.48	8.22

There is no correlation between permeability and porosity for the Telaga Bodas samples; the correlation coefficient is -0.08 (Figure 88A). When the three outlier samples are removed, the correlation coefficient increases to 0.27, showing weak positive correlation (Figure 88B). When the outlying sample from Figure 88B is removed, the correlation coefficient increases to 0.73, showing strong positive correlation between the two parameters. However, this removed a third of the data points from the original results.

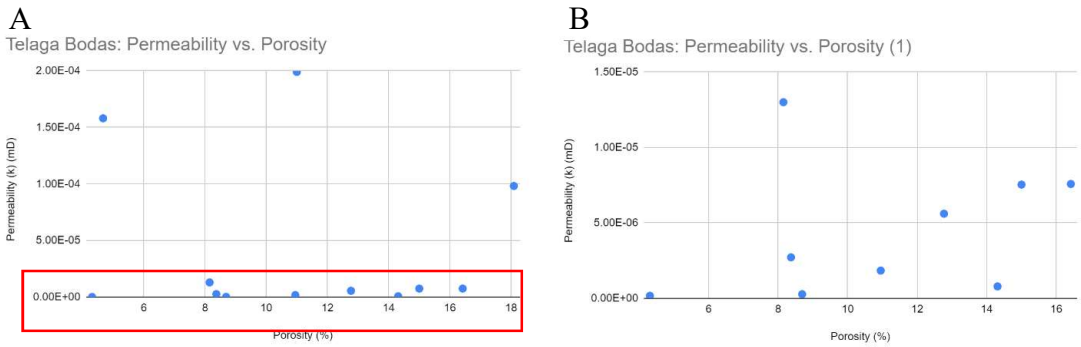

Figure 88. A. Graph showing the relationship between permeability and porosity for the Telaga Bodas samples. As shown in the graph, there is no correlation between the two parameters (correlation coefficient of -0.08). B. A close-up of the lower permeability samples (outlined by the red box) after removing the three outliers increases the correlation coefficient to 0.27.

For the Lake City samples, the correlation coefficient between permeability and porosity is -0.21 (Figure 89A). There is very little change in coefficient after removing the three samples with the highest permeability. After removing the two outliers in Figure 89B, the correlation coefficient increases to 0.66, showing moderate to strong positive correlation, however, this is a loss of a quarter of the sample data.

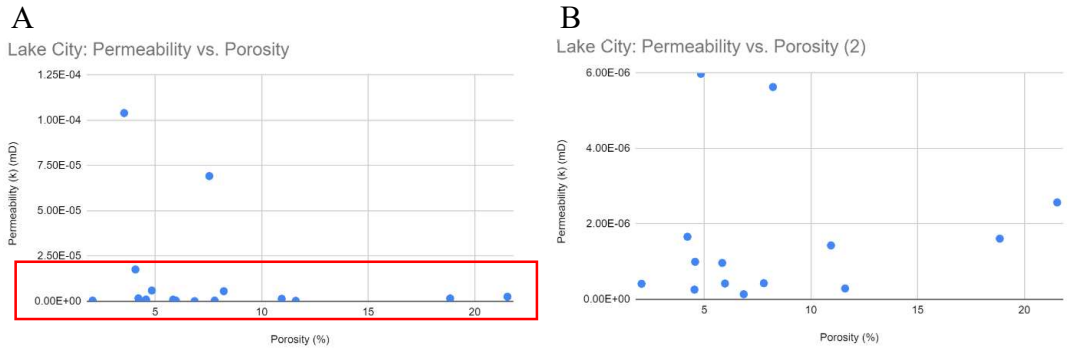

Figure 89. A. Graph showing the relationship between permeability and porosity for the Lake City samples. The correlation coefficient is -0.21, showing weak negative correlation between the two parameters. B. A close-up of the lower permeability samples (outlined by the red box) after removing the two samples with the highest permeability. The correlation coefficient is 0.1.

Overall there is no correlation at all between porosity and permeability when all Telaga Bodas and Lake City samples data are combined. By removing the four outliers from TB and the five from LC, the coefficient between the two parameters is 0.54 (moderate positive correlation). This is not very strong for losing a third of the data points.

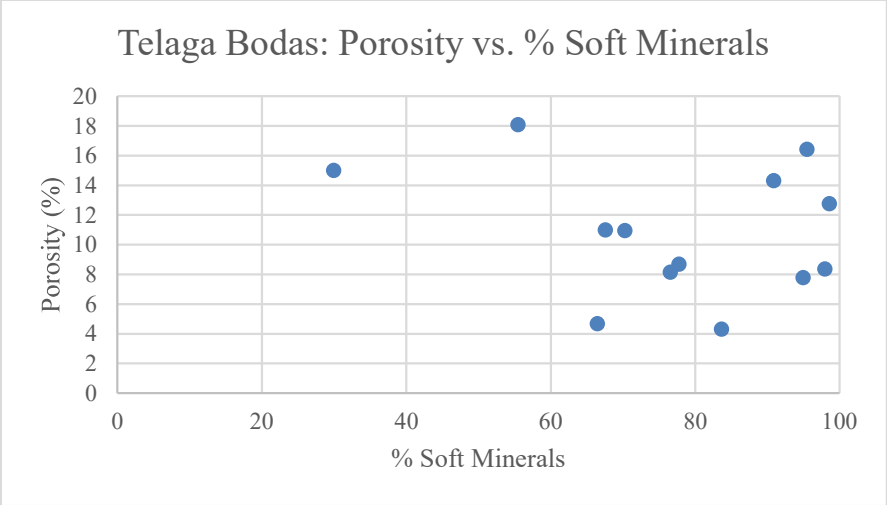

Figure 90. Graph showing the relationship between the percentage of soft minerals and porosity for the Telaga Bodas samples. The correlation coefficient is -0.24, showing weak negative correlation between the two parameters.

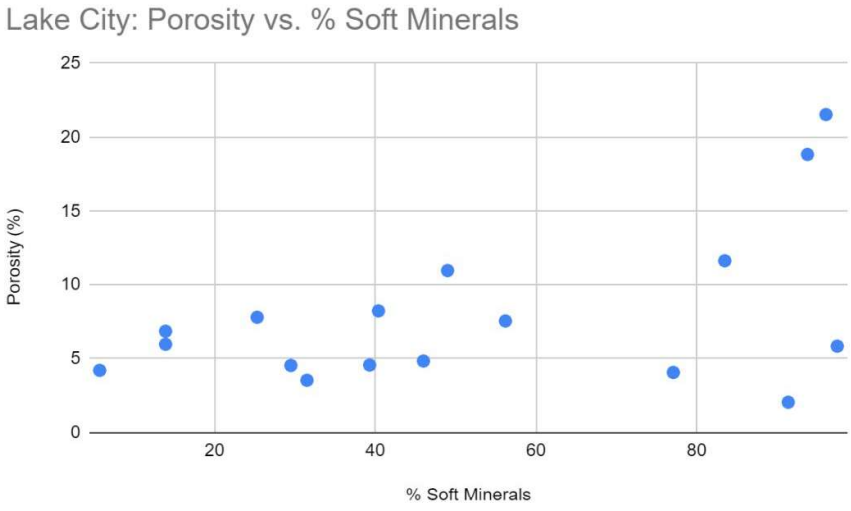

Figure 91. Graph showing the relationship between the percentage of soft minerals and porosity for the Lake City samples. The correlation coefficient is 0.47, showing moderate positive correlation between the two parameters.

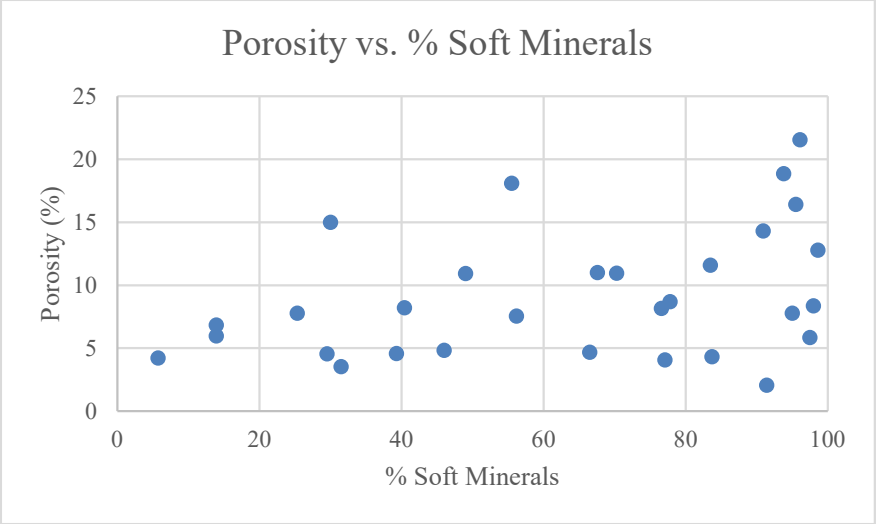

Figure 92. Graph showing the relationship between the percentage of soft minerals and porosity for all samples. The correlation coefficient is 0.36, showing moderate positive correlation between the two parameters overall.

Plots of porosity against the percentage of soft minerals shows a weak negative correlation for the Telaga Bodas samples, with a correlation coefficient of -0.24 (Figure 90). The correlation coefficient for the Lake City samples is 0.47, showing moderate positive correlation (Figure 91). With all data combined, the correlation coefficient between porosity and the percentage of soft minerals is 0.36, showing a moderate positive correlation between the two parameters (Figure 92).

2.3.5 H-ASI and Predicted UCS

The H-ASI values and predicted UCS were calculated using equations 1 and 2. The results for the Telaga Bodas samples are given in Table 27, and the results for the Lake City samples are in Table 28. As shown, the predicted UCS is unrealistically low for many of the samples. Wyering et al., (2015) state "Our dataset does not include samples with ASI values below 60, however rocks with such low ASI could be encountered, for example if samples have extremely high porosity. According to Fig. 4 and Eq. (2), however, the strength would be so low as to barely be classified as rocks." Half of the Telaga Bodas and Lake City samples have a H-ASI value below 60 and have low porosity, so based on the author's work, these samples should barely classify as rock. As the Telaga Bodas and Lake City samples are rocks, it highlights issues with the ASI and UCS equations and their ability to encompass the range of hydrothermally altered samples found in nature. This suggests some level of calibration may be required for samples with low H-ASI values.

Table 27. H-ASI and predicted UCS for Telaga Bodas samples using Equation 2.

Sample	H-ASI	Predicted UCS (MPa)
K33_0191_00	27.27	0.13

K33_0191_03	26.59	0.12
K33_0192_1276	26.98	0.12
K33_0192_1277.75	28.35	0.15
K33_0364_1752	70.27	8.1
K33_0364_1753	73.33	9.75
K33_0393_1833.2	36.75	0.48
K33_0393_1834	20.04	0.03
K33_0423_1916.3	58.59	3.66
K33_0423_1919	112.05	62.08
T2_0156_03	34.2	0.35
T2_0117_00	20.5	0.04
T2_0117_03	18.19	0.02

Table 28. H-ASI and predicted UCS for Lake City samples using Equation 2.

Sample	**H-ASI**	**Predicted UCS (MPa)**
LCB090314-1b	127.04	107.42
LCB090314-5	39.80	0.68
LCB091414-2	78.54	13.16
LCDLA082913-1	13.97	0.01
LCDLA082913-2	20.77	0.04
LCG090714-2c	9.20	0.00
LCG090714-3a	73.07	9.60
LCG090714-3b	24.84	0.09
LCG091314-1b	85.65	19.21
LCT091014-1a	16.46	0.01
LCT091014-1b*	40.25	0.71
LCT091514-3 (1)	105.03	46.81
LCT091514-3 (2)	114.63	68.59
LCTBV071714-5a	62.20	4.75
LCTV090314-4a	63.47	5.19
LCTV091014-1c	86.19	19.75
LCTV091014-1d	74.03	10.16

*The values for sample LCT091014-1b are based on estimated Pm, Sm, and AI values.

Telaga Bodas data for H-ASI and permeability shows very weak correlation (correlation coefficient of 0.19), however, this changes greatly depending on which outliers are removed. The correlation coefficient for the samples in the red box outlined in Figure 93,

where the three samples with relatively high permeability are removed, is 0.05 (no correlation). For the samples outline by the blue box, where the one sample with a high H-ASI value is removed, the correlation coefficient is 0.46, showing moderate positive correlation.

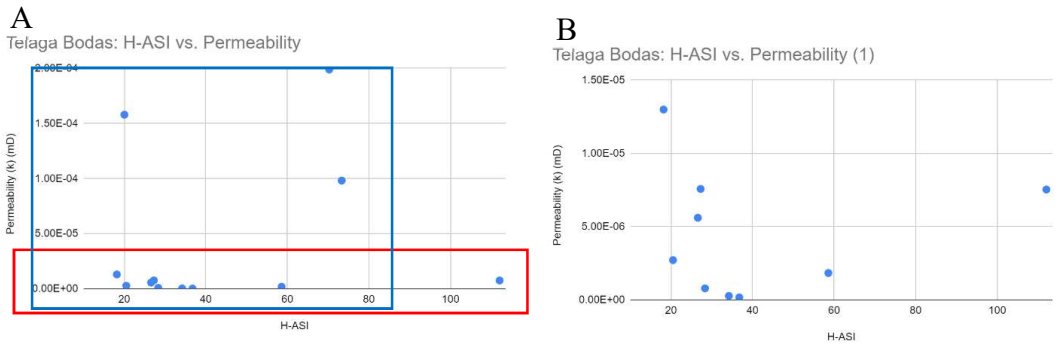

Figure 93. A Graph showing the relationship between the H-ASI values and permeability for the Telaga Bodas samples. The correlation coefficient is 0.19, showing weak positive correlation between the two parameters. The correlation coefficient for the samples in the red box is 0.05 (no correlation), and in the blue box is 0.46 (moderate positive correlation). B. Samples outlined in the red box (coefficient of 0.05).

The Lake City data for H-ASI and permeability has the same correlation coefficient as the Telaga Bodas data: 0.19 (Figure 94). There is minimal change in the correlation coefficient after removing the three samples with the highest permeability (coefficient of 0.11). The correlation coefficient for all samples combined is 0.08, showing no overall correlation between the H-ASI value and permeability.

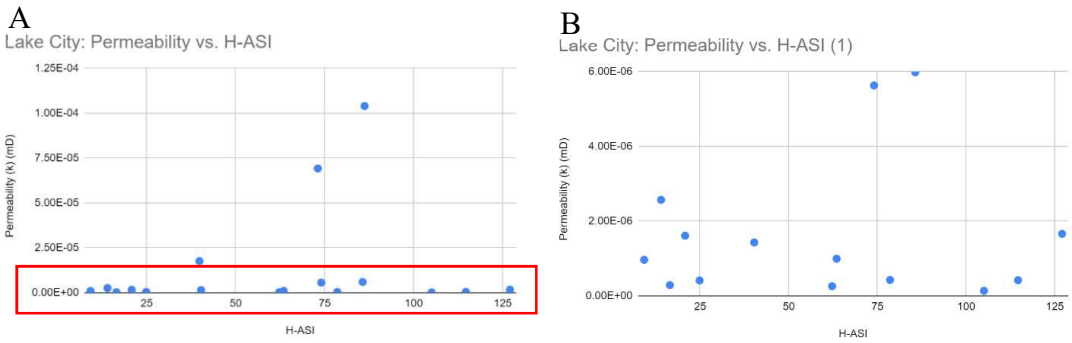

Figure 94. A. Graph showing the relationship between the H-ASI values and permeability for the Lake City samples. The correlation coefficient is 0.19, showing weak positive correlation between the two parameters. B. Samples outlined in the red box have a coefficient of 0.11.

Correlation between porosity and H-ASI is moderate for both Telaga Bodas and Lake City samples, however, the former displays moderate positive correlation (0.49) (Figure 95A) and the latter displays moderate negative correlation (-0.48) (Figure 95B), in direct contrast to each other. Combined data has weak negative correlation with a correlation coefficient of -0.24. Given that the two datasets have opposing trends, no conclusions can be drawn for any relationship between the H-ASI and porosity.

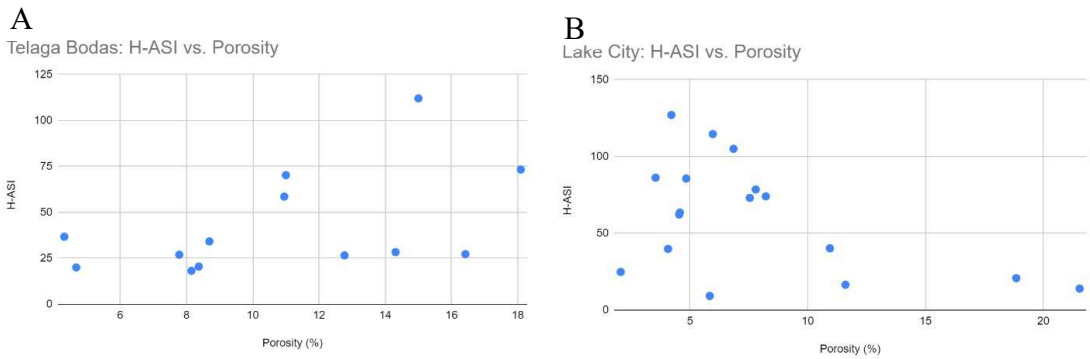

Figure 95. A. Graph showing the relationship between H-ASI and porosity for the Telaga Bodas samples. The correlation coefficient is 0.49, showing moderate positive correlation. B. Graph showing the relationship between H-ASI and porosity for the Lake City samples, which show moderate negative correlation with a coefficient of -0.48.

There is strong negative correlation between the H-ASI values and the percentage of soft minerals for the Telaga Bodas and Lake City data (Figure 96), with correlation coefficients of -0.85 and -0.94 respectively. The coefficient for the data combined is -0.91. The strong negative correlation shows a decrease in H-ASI with increasing soft mineral percentage, as expected, due to the basing of the H-ASI on Pm and Sm parameters, where high amounts of low hardness indexes sum up to lower values than the higher hardness indexes associated with stronger minerals.

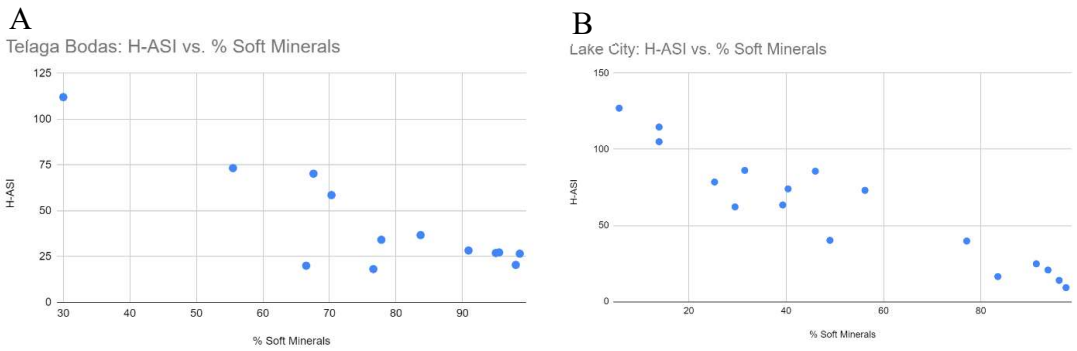

Figure 96. A. Graph showing the relationship between H-ASI and the percentage of soft minerals for the Telaga Bodas samples. The correlation coefficient is -0.85, showing strong negative correlation. B. Graph showing the relationship between H-ASI and the percentage of soft minerals for the Lake City sample. The correlation coefficient is -0.94, showing very strong negative correlation.

There is no correlation between the predicted UCS and permeability for the Telaga Bodas samples (Figure 97A). Removing the primary outlier leads to a correlation coefficient of 0.61, showing moderate-to-strong positive correlation between the two parameters. However, this outlier sample is the only one with a reasonable UCS estimate. The rest of the samples, as mentioned above, have unrealistically low UCS estimates.

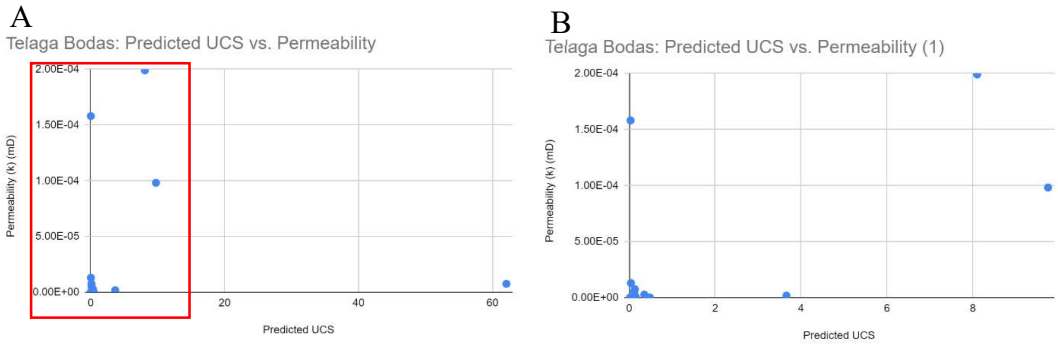

Figure 97. A Graph showing the relationship between the predicted UCS and permeability for the Telaga Bodas samples. There is no correlation between the two parameters with all samples considered. B. Samples outlined in the red box have a coefficient of 0.61, showing moderate-to-strong positive correlation when the primary outlier is removed.

Figure 98 shows the relationship between permeability and the predicted UCS for the Lake City samples. The correlation coefficient of -0.05 shows there is no correlation between the two parameters. Removing the three main outliers, which like with the Telaga Bodas samples, are the only realistic estimates for UCS, causes the correlation coefficient to increase to 0.56. With the Telaga Bodas and Lake City data combined, the correlation

coefficient is -0.09, showing no correlation overall between the predicted UCS and permeability.

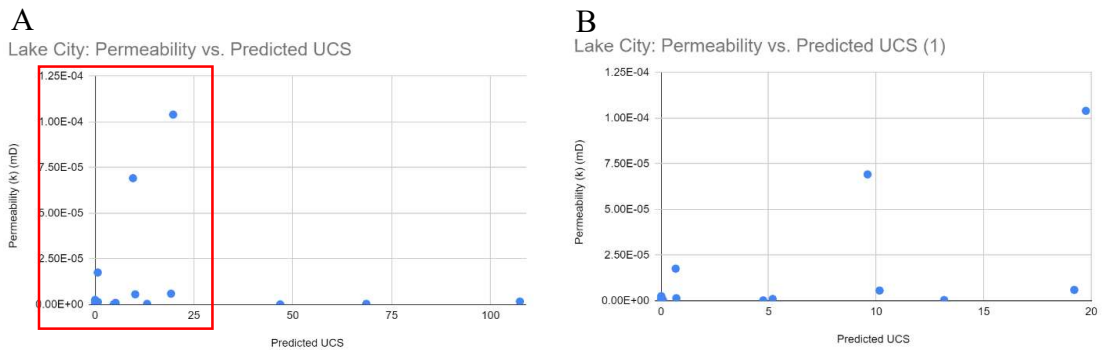

Figure 98. A. Graph showing the relationship between the predicted UCS and permeability for the Lake CIty samples. There is no correlation between the two parameters. B. Samples outlined in the red box have a coefficient of 0.56, showing a moderate positive correlation after removing the three main outliers from A.

Figure 99 shows the correlation between porosity and the predicted UCS. As with the relationship between porosity and H-ASI, the Telaga Bodas data (Figure 99A) displays positive correlation, with a coefficient of 0.37, and the Lake City data displays a negative correlation, with a coefficient of -0.29. With all data combined, the overall correlation is weak with a coefficient is -0.18. With porosity being an influential parameter in the ASI equation, it is not surprising that there is correlation between porosity and predicted UCS, with the expectation that increased porosity results in decreased strength, however, the Telaga Bodas data indicates the opposite, with increasing porosity resulting in an increase in strength.

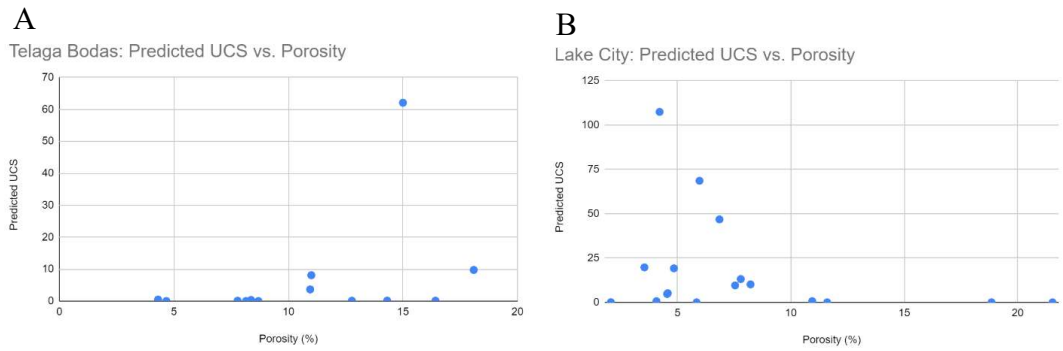

Figure 99. A. Graph showing the relationship between predicted UCS and porosity for the Telaga Bodas samples. The correlation coefficient is 0.37, showing moderate positive correlation. B. Graph showing the relationship between predicted UCS and porosity for the Lake City samples. The correlation coefficient is -0.29, showing moderate negative correlation.

As expected, the relationship between predicted UCS and the percentage of soft minerals displays a strong negative correlation, meaning that with increasing amounts of soft minerals, the strength decreases. The correlation coefficient for the Telaga Bodas samples and Lake City samples is -0.8 and -0.71 respectively (Figure 100). For all samples combined, the coefficient is -0.74.

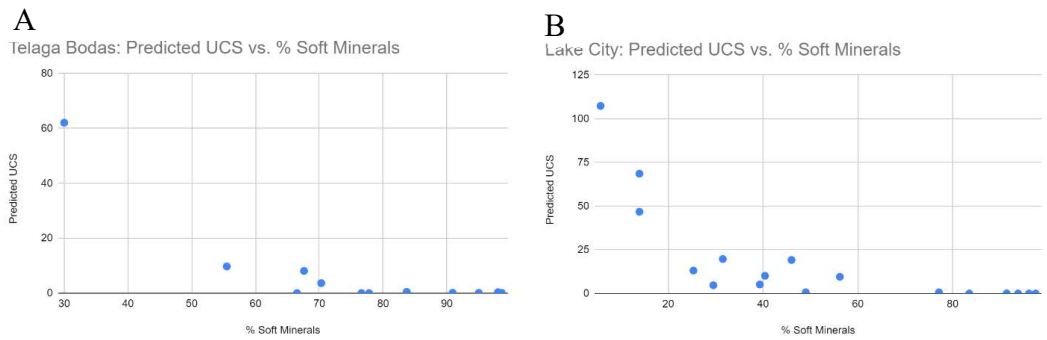

Figure 100. A Graph showing the relationship between predicted UCS and the percentage of soft minerals for the Telaga Bodas samples. The correlation coefficient is -0.8, showing strong negative correlation. B. Graph showing the relationship between predicted UCS and the percentage of soft minerals for the Lake City samples. The correlation coefficient is -0.71, also showing strong negative correlation.

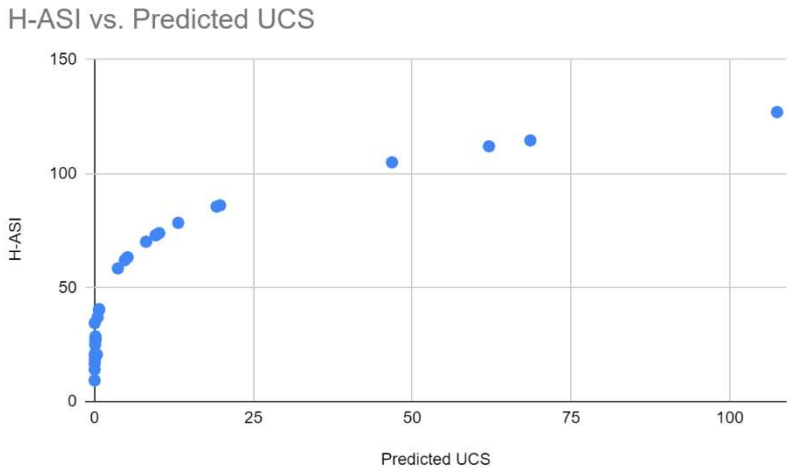

Figure 101. Graph showing the relationship between H-ASI and predicted UCS for all Telaga Bodas and Lake City samples combined. The correlation coefficient is 0.83, showing strong positive correlation.

As stated previously, Wyering et al., (2015) developed Equation 2 to estimate the strength of hydrothermally altered rocks based on the ASI equation (Equaton1), therefore, there should be a strong positive correlation between the H-ASI and Predicted UCS which is supported by the Telaga Bodas and Lake City data in Figure 101. The correlation coefficient for the combined data is 0.83. Separately, the Telaga Bodas data has a correlation coefficient of 0.85 and the Lake City samples have a coefficient of 0.82.

Overall, for the H-ASI and Predicted UCS values, H-ASI has a weak negative correlation with porosity (but a moderate positive correlation with the TB data and a moderate negative correlation with the LC data), a strong negative correlation with the percentages of soft minerals, and a strong positive correlation with the predicted UCS. The predicted UCS has weak correlation with porosity (but a weak-moderate positive correlation with the TB data and a weak-moderate negative correlation with the LC data), a strong negative correlation with the percentages of soft minerals, and a strong positive correlation with H-ASI.

2.3.6 UCS

Table 29 displays the UCS results for the Telaga Bodas samples, including the loading rate, maximum load and strength of the sample, and the time taken until failure occurred. Strength was recorded in psi and converted to MPa. The UCS data for the Lake City samples is in Table 30. The loading rate was adjusted depending on the expected strength of the sample. For example, the altered Lake City breccias (LCB) were more heavily fractured than other samples, so the loading rate was reduced to prevent failure upon early contact. All UCS results and post-failure sample photographs are in Appendix B8.

Table 29. UCS data for the Telaga Bodas samples.

Sample	Loading Rate (psi)	Load (lbf)	Strength (psi)	Time to failure (s)	UCS (MPa)
K33_0191_00	30	9404	13551.45	518.6	93.43
K33_0191_03	50	8056	12386.74	261.4	85.40
K33_0192_1276	50	9599	14759.07	192.9	101.76
K33_0192_1277.75	50	15170	23324.38	566.4	160.82
K33_0364_1752	50	10526	16184.34	316.8	111.59
K33_0364_1753	50	11352	17453.68	320.6	120.34
K33_0393_1833.2	50	28072	43161.41	988.4	297.59
K33_0393_1834	50	21289	32732.31	705.1	225.68
K33_0423_1916.3	50	9349	14374.62	199.9	99.11
K33_0423_1919	50	12624	19409.95	362.4	133.83
T2_0156_03	50	8227	12649.29	228.2	87.21
T2_0117_00	50	3635	5588.29	~53	38.53
T2_0117_03	30	6554	10077.24	218.8	69.48

Table 30. UCS data for the Lake City samples.

Sample	Loading Rate (psi)	Load (lbf)	Strength (psi)	Time to failure (s)	UCS (MPa)
LCB090314-1b	20	8837	13586.97	10.1	93.68
LCB090314-5	10	9502	14609.04	669.0	100.73
LCB091414-2	15	5684	8739.17	815.9	60.25
LCDLA082913-1	25	2421	3722.59	~142	25.67
LCDLA082913-2	25	5574	8570.39	448.5	59.09
LCG090714-2c	50	10264	15781.14	228.2	108.81
LCG090714-3a	50	7178	11036.48	266.5	76.09
LCG090714-3b	50	9001	13839.86	223.5	95.42
LCG091314-1b	50	9233	14195.90	304.9	97.88
LCT091014-1a	50	7391	11363.93	247.2	78.35
LCT091014-1b	50	8729	13421.66	467.5	92.54
LCT091514-3 (1)	50	17980	27645.16	812.5	190.61
LCT091514-3 (2)	50	17631	27108.51	652.6	186.91
LCTBV071714-5a	50	21250	32672.76	825.4	225.27
LCTV090314-4a	50	14797	22751.63	719.6	156.87
LCTV091014-1c	50	19275	29635.73	431.5	204.33
LCTV091014-1d	50	10543	16211.06	346.4	111.77

Results show that the UCS for the Telaga Bodas samples ranged from 38.53 MPa to 297.59 MPa. The Lake City samples ranged from 25.67 MPa to 225.27 MPa. These values are much higher than those predicted using the ASI equation. The comparison of predicted and actual UCS values are presented in Table 31 for the Telaga Bodas samples and Table 32 for the Lake City samples. All predicted UCS grossly underestimate the actual UCS, except for LCB090314-1b which overestimates UCS. Wyering et al., (2015) state that their UCS values obtained from the ASI equation for their data included an error of 7 MPa for the 50th percentile and 25 MPa for the 90th percentile. The Telaga Bodas and Lake City data vastly exceed these error margins, with 25 MPa being the smallest of the errors for the underestimated samples, and almost half of the samples having an error of over 100 MPa. The average difference between predicted and actual UCS for the Telaga Bodas data is 118.4 MPa, and for the Lake City data (except for the overestimated sample) is 104.5 MPa. Overall, the average difference for underestimated samples is 110.7 MPa.

Table 31. Predicted and actual UCS values for the Telaga Bodas samples.

Sample	Predicted UCS (MPa)	UCS (MPa)
K33_0191_00	0.13	93.43
K33_0191_03	0.12	85.40
K33_0192_1276	0.12	101.76
K33_0192_1277.75	0.15	160.82
K33_0364_1752	8.1	111.59
K33_0364_1753	9.75	120.34
K33_0393_1833.2	0.48	297.59
K33_0393_1834	0.03	225.68
K33_0423_1916.3	3.66	99.11
K33_0423_1919	62.08	133.83
T2_0156_03	0.35	87.21
T2_0117_00	0.04	38.53
T2_0117_03	0.02	69.48

Table 32. Predicted and actual UCS values for the Lake City samples.

Sample	Predicted UCS (MPa)	UCS (MPa)
LCB090314-1b	107.42	93.68
LCB090314-5	0.68	100.73
LCB091414-2	13.16	60.25
LCDLA082913-1	0.01	25.67
LCDLA082913-2	0.04	59.09
LCG090714-2c	0.00	108.81
LCG090714-3a	9.60	76.09
LCG090714-3b	0.09	95.42
LCG091314-1b	19.21	97.88
LCT091014-1a	0.01	78.35
LCT091014-1b	0.71	92.54
LCT091514-3 (1)	46.81	190.61
LCT091514-3 (2)	68.59	186.91
LCTBV071714-5a	4.75	225.27
LCTV090314-4a	5.19	156.87
LCTV091014-1c	19.75	204.33
LCTV091014-1d	10.16	111.77

The relationship between the actual UCS and permeability of the Telaga Bodas samples is shown in Figure 102. The correlation coefficient is weak at 0.18. By removing the three outlier samples with higher relative permeability, the coefficient becomes -0.52, showing moderate negative correlation, however, if the one outlier sample with the highest UCS is removed, the coefficient becomes 0.49, showing moderate positive correlation instead. A similar pattern can be seen with the Lake City data (Figure 103). The coefficient is 0.22 for all LC samples. After removing the two main outlier samples, the coefficient decreases to -0.17, however, removing the samples with higher relative permeability to get to the samples more closely grouped together gives a coefficient of -0.63. With both datasets combined, the correlation coefficient is 0.2, showing weak positive correlation overall.

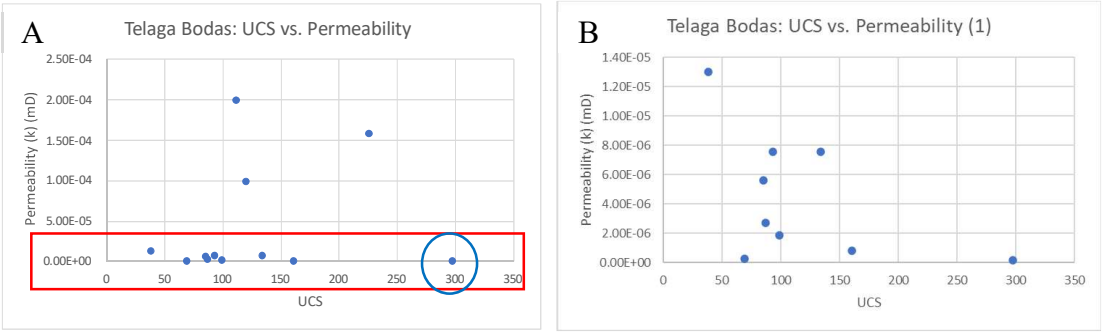

Figure 102. A. Graph showing the relationship between actual UCS and permeability for the Telaga Bodas samples. The correlation coefficient is 0.18, showing weak positive correlation. B. Subset of the samples outlined by the red box in A, after removing the 3 outlier samples. The correlation coefficient of the sample subset is -0.52 which now displays moderate negative correlation. The coefficient is 0.49 when only the sample in the blue circle in A is removed.

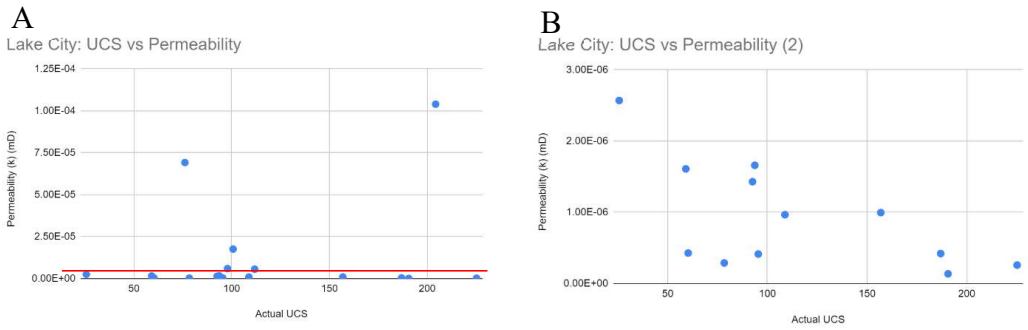

Figure 103. A. Graph showing the relationship between UCS and porosity for the Telaga Bodas samples. The correlation coefficient is -0.38, showing moderate negative correlation. B. Graph showing the relationship between UCS and porosity for the Lake City samples. The correlation coefficient is -0.58, also showing moderate negative correlation.

The relationship between actual UCS and predicted UCS is weak. The Telaga Bodas data has a coefficient of 0.03 and the Lake City data has a coefficient of 0.26 (Figure 104). By removing the outlier sample from the Lake City data, the coefficient increases to 0.54. There is minimal change in the coefficient after removing the outlier sample from the Telaga Bodas data. With all sample data combined, the overall correlation coefficient is 0.15. The coefficient increases to 0.29 if the LC Predicted UCS extreme value is removed, 0.24 if the TB Actual UCS extreme value is removed, and 0.41 if both are removed. At best, the correlation between the actual and predicted UCS is moderate, indicating that Equation 2 does not work for the Telaga Bodas and Lake City samples and is an ineffective tool for reliably estimating rock strength.

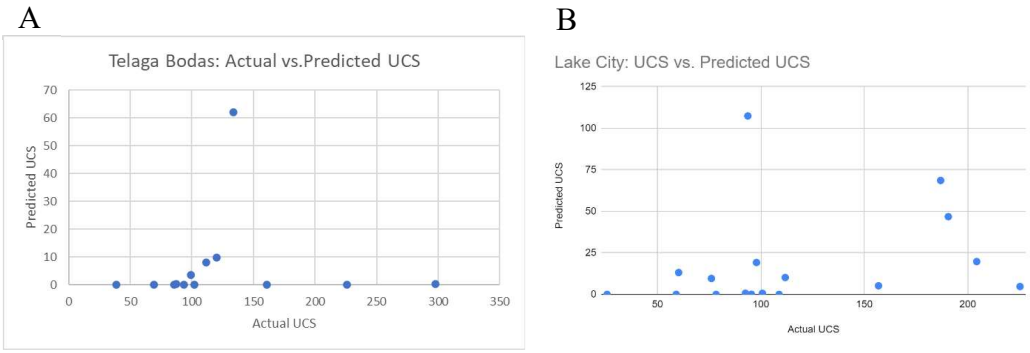

Figure 104. A. Graph showing the relationship between actual and predicted UCS for the Telaga Bodas samples. The correlation coefficient is 0.03, showing no correlation. B. Graph showing the relationship between actual and predicted UCS for the Lake City samples. The correlation coefficient is 0.26, showing weak correlation.

Figure 105 shows the relationship between UCS and the percentage of soft minerals. The Telaga Bodas samples have a correlation coefficient of -0.13 whereas the Lake City samples have a coefficient of -0.59, showing moderate negative correlation. When combined, the data has a coefficient of -0.33. With the removal of the most extreme TB sample, the coefficient for the TB data and overall data increases to -0.3 and -0.48 respectively.

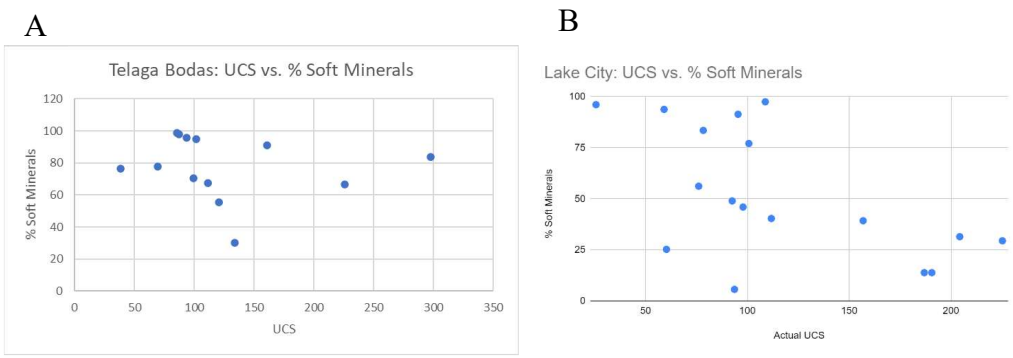

Figure 105. A. Graph showing the relationship between UCS and the percentage of soft minerals for the Telaga Bodas samples. The correlation coefficient is -0.13, showing weak negative correlation. B. Graph showing the relationship between UCS and the percentage of soft minerals for the Lake City samples. The correlation coefficient is -0.59, showing moderate negative correlation.

The correlation between the UCS and H-ASI for the Telaga Bodas samples is non-existent (coefficient of 0.03) The data appears to follow two separate trends as shown in Figure 106, yet it is unclear from the available data as to the cause of the two trends. There are no clear differences in parameter data to separate them. The Lake City data, however, has a coefficient of 0.49, showing moderate positive correlation. The coefficient for the combined data is weak at 0.26. This shows that for the combined data, the H-ASI cannot be used to accurately estimate UCS of the samples.

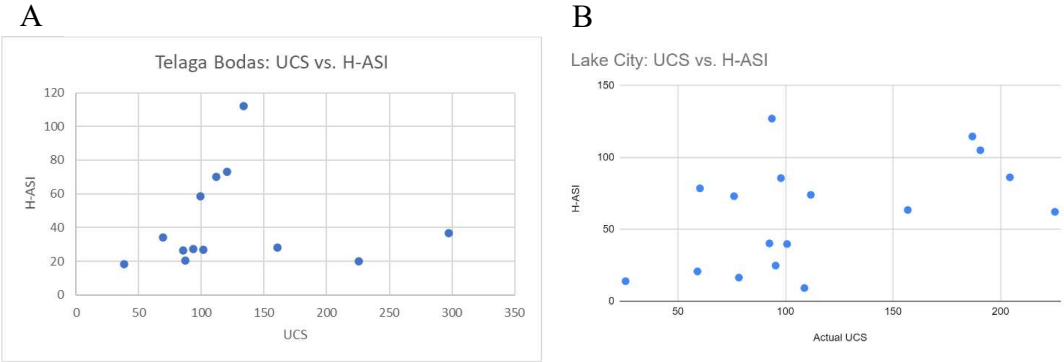

Figure 106. A. Graph showing the relationship between UCS and H-ASI for the Telaga Bodas samples. The correlation coefficient is -0.03, showing no correlation between the two parameters. B. Graph showing the relationship between UCS and H-ASI for the Lake City samples. The correlation coefficient is 0.49, showing moderate positive correlation.

2.3.7 Summary of Parameters

A summary of all parameter values for Telaga Bodas and Lake City samples are displayed in Tables 33 and 34. Sample names are abbreviated.

Table 33. Summary of parameters for the Telaga Bodas samples.

Sample	Pm	Sm	AI	Snf	Porosity	H-ASI	Predicted UCS	UCS	Permeability
0191_00	1.02	33.4	0.96	2	16.42	27.27	0.13	93.43	7.58e-06
0191_03	0	31.38	0.99	2	12.77	26.59	0.12	85.40	5.61e-06
1276	3.06	32.48	0.96	2	7.78	26.98	0.12	101.76	N.D.
1277.75	3.4	33.14	0.92	0	14.31	28.35	0.15	160.82	7.93e-07
1752	1.36	86.84	0.99	3	11.00	70.27	8.1	111.59	1.99e-04
1753	9.35	92.24	0.94	2	18.09	73.33	9.75	120.34	9.82e-05
1833.2	0	44.91	0.86	0	4.31	36.75	0.48	297.59	1.73e-07
1834	1.7	34.61	0.67	3	4.67	20.04	0.03	225.68	1.58e-04
1916.3	0	63.72	0.99	0	10.95	58.59	3.66	99.11	1.84e-06
1919	1.53	123.11	0.99	0	15.00	112.05	62.08	133.83	7.54e-06
0156_03	0	29.15	0.99	2	8.37	34.2	0.35	87.21	2.72e-06
0117_00	33.49	18.41	0.77	0	8.15	20.5	0.04	38.53	1.3e-05
0117_03	32.3	19.14	0.78	3	8.69	18.19	0.02	69.48	2.75e-07

Table 34. Summary of parameters for the Lake City samples.

Sample	Pm	Sm	AI	Snf	Porosity	ASI	Predicted UCS	UCS	Permeability
LCB-1b	159.8	0.57	0.06	3	4.21	127.04	107.42	93.68	1.66e-06
LCB-5	3.74	48.24	0.98	3	4.07	39.80	0.68	100.73	1.76e-05

LCB-2	125.97	3.25	0.25	3	7.79	78.54	13.16	60.25	4.28e-07
LCDLA-1	0	15.39	1	0	21.54	13.97	0.01	25.67	2.57e-06
LCDLA-2	0	22.71	1	0	18.85	20.77	0.04	59.09	1.61e-06
LCG-2c	4.08	10.71	0.98	2	5.84	9.20	0.00	108.81	9.66e-07
LCG-3a	0	84.47	1	2	7.54	73.07	9.60	76.09	6.78e-05
LCG-3b	0	28.9	1	3	2.06	24.84	0.09	95.42	4.14e-07
LCG-1b	0	102.04	1	3	4.84	85.65	19.21	97.88	5.98e-06
LCT-1a	18.87	17.57	0.89	0	11.60	16.46	0.01	78.35	2.89e-07
LCT-1b	78.2	13.99	0.54	0	10.94	40.25	0.71	92.54	1.43e-06
LCT-3 (1)	142.63	5.38	0.16	2	6.85	105.03	46.81	190.61	1.36e-07
LCT-3 (2)	142.63	5.38	0.16	0	5.97	114.63	68.59	186.91	4.21e-07
LCTBV-5a	59.33	76.87	0.65	2	4.54	62.20	4.75	225.27	2.59e-07
LCTV-4a	28.22	89.57	0.83	4	4.57	63.47	5.19	156.87	9.96e-07
LCTV-1c	23.12	108.89	0.87	2	3.54	86.19	19.75	204.33	1.04e-04
LCTV-1d	16.49	102.19	0.90	4	8.22	74.03	10.16	111.77	5.63e-06

Tables 35, 36, and 37 show a summary of the correlation coefficients for the Telaga Bodas samples, Lake City samples, and overall coefficients for the two datasets combined respectively. As expected, there is high correlation between the percentage of soft minerals and H-ASI due to the Sm parameter composing the H-ASI which is largely calculated from soft secondary minerals. This is consistently strong for each dataset and hence the overall data. There is also a consistent strong relationship between the percentage of soft minerals and the predicted UCS. As weaker minerals lead to a weaker rock, this correlation is expected. Following the equations and relationships laid out by Wyering et al., (2015), the correlation between the predicted UCS and H-ASI is also strong for both datasets and therefore for the overall data. However, the actual UCS doesn't hold the same level of correlation as would be expected. There are huge differences between the predicted and actual UCS measurements and no-weak correlation between them throughout all the data. The correlation between UCS and H-ASI and between UCS and the percentage of soft minerals are moderate for the Lake City data but none-existent

for the Telaga Bodas data, meaning the overall relationship between the parameters is weak to weak-moderate respectively. The implication of this is that the H-ASI and UCS equations do not work for the Telaga Bodas and Lake City samples tested and therefore were unable to provide realistic estimations of strength from the sample parameters.

The only correlation permeability has is moderate with the percentage of soft minerals, and only for the Telaga Bodas data, meaning permeability cannot be reliably used to estimate other parameters or for estimations of H-ASI or UCS. The relationship between porosity and other parameters was not as high as Wyering et al. (2015) had found. Where they had high correlation between porosity and UCS, the Telaga Bodas and Lake City data provided only moderate correlation. The relationship between porosity and predicted UCS, the percentage of soft minerals, and H-ASI was split between the datasets, with one dataset displaying a positive correlation and the other displaying a negative correlation, and all weak-moderate. Therefore, porosity is also a weak parameter in the H-ASI equation and unable to accurately or reliably be used in estimating other parameters, the H-ASI, or UCS.

Table 35. Correlation coefficients for each of the parameters for the Telaga Bodas samples. Yellow cells highlight weak coefficients between (-)0.3-0.45, orange moderate (-)0.46-0.69, green strong (-) 0.7-0.89, and blue very strong (-) 0.9+.

TB	Porosity	Permeability	Predicted UCS	% Soft Minerals	H-ASI
Porosity					
Permeability	-0.08				
Predicted UCS	0.37	-0.03			
% Soft Minerals	-0.24	-0.33	-0.80		
H-ASI	0.49	0.19	0.85	-0.85	
Actual UCS	-0.38	0.18	0.03	-0.13	0.03

Table 36. Correlation coefficients for each of the parameters for the Lake City samples. Yellow cells highlight weak coefficients between (-)0.3-0.45, orange moderate (-)0.46-0.69, green strong (-) 0.7-0.89, and blue very strong (-) 0.9+.

LC	Porosity	Permeability	Predicted UCS	% Soft Minerals	H-ASI
Porosity					
Permeability	-0.21				
Predicted UCS	-0.29	-0.05			
% Soft Minerals	0.47	-0.10	-0.70		

H-ASI	-0.48	0.19	0.82	-0.94	
Actual UCS	-0.58	0.22	0.26	-0.59	0.49

Table 37. Correlation coefficients for each of the parameters for all sample data combined. Yellow cells highlight weak coefficients between (-)0.3-0.45, orange moderate (-)0.46-0.69, green strong (-) 0.7-0.89, and blue very strong (-) 0.9+.

All data	**Porosity**	**Permeability**	**Predicted UCS**	**% Soft Minerals**	**H-ASI**
Porosity					
Permeability	-0.02				
Predicted UCS	-0.18	-0.09			
% Soft Minerals	0.36	-0.04	-0.74		
H-ASI	-0.24	0.08	0.83	-0.91	
Actual UCS	-0.44	0.20	0.15	-0.33	0.26

2.3.8 Fracture Index Revised

The only subjective variable in the H-ASI equation is the Fracture Index (Snf). A higher fracture index means a weaker rock sample, which means lower predicted UCS. Even with assuming a completely intact rock sample, with a Snf of 0, the predicted UCS still does not come close to the actual UCS values. Unfortunately, due to the discrepancies in the correlation between parameters, and since the original ASI did not include any samples with ASI values below 60, more data would be needed to revamp the H-ASI equation to work for the Telaga Bodas and Lake City samples, and to reassess the equations leading to more accurate UCS estimations which encompass a wider range of altered rock types.

In future work with the H-ASI parameters, more categories should be included for the Fracture Index parameter which account for categories which were not considered in the original ASI version. An example of these categories is shown in Table 38. The effects of multiple fractures would also have to be tested and compared to the relative impacts of the current index to create a more robust fracture index.

Table 38. Proposed Fracture Index categories for consideration in a new H-ASI.

Fracture Value (Snf)	**Fracture Type**	**Fracture Size**
0	No fractures	
1	Microfractures in thin section	
2	Short & thin - closed	<1mm wide; <10 mm long

3	Short & thin - open	<1mm wide; <10 mm long
4	Short & fat - closed	>1mm wide; <10 mm long
5	Short & fat - open	>1mm wide; <10 mm long
6	Long & thin - closed	<1mm wide; >10 mm long
7	Long & thin - open	<1mm wide; >10 mm long
8	Long & fat - closed	>1mm wide; >10 mm long
9	Long & fat - open	>1mm wide; >10 mm long
10	Multiple long & fat	>1mm wide; >10 mm long

2.4 Discussion

2.4.1 Core Imaging

The use of lab based hyperspectral imaging has increased in recent years and has been utilised in rapid, in-field, mineral identification. This type of imaging is both fast and non-destructive, and requires little preparation (Quigley & Yildirim, 2015; Martini et al., 2019) In addition, it doesn't require adjustment for atmospheric corrections etc, as with satellite and airborne imagers (Martini et al., 2019). Systems such as the Corescan HCI-3 and HyLogger have made field analysis much easier and faster with Corescan having the added advantage of a cloud-based database (Coreshed). However, the HCI-3 has its limitations. The Corescan HCI-3 provides imaging in the VNIR-SWIR spectrum (450-2500 nm range) but it is unable to differentiate some rock-forming minerals such as quartz and feldspar, so they are grouped into the aspectral category (Quigley & Yildirim, 2015; Martini et al., 2019). The HyLogger has Thermal Infrared (TIR) as an additional imaging range and is therefore capable of differentiating between these minerals (Quigley & Yildirim, 2015). This is a limitation which will be addressed with the Corescan-4 with the addition of Raman Systems and/or Mid-Infrared (MIR) imaging (Martini et al., 2019). Jackson et al., (2018) also suggested the inclusion of Long-wave Infrared (LWIR) to improve mineral speciation such as for the carbonate group. Though some mineral differentiation could be improved upon, the current HCI-3 can easily identify and distinguish clay minerals and species that are difficult and time-consuming to achieve without the use of hyperspectral data (Zhou et al., 2017; Martini et al., 2019).

Hyperspectral imaging was taken for the Telaga Bodas and Lake City rock surfaces, which is not necessarily indicative of the mineralogy of the smaller core samples taken from these. Infrared spectroscopy does not penetrate more than a few microns below the surface (Zhou et al., 2017), therefore, the mineral logs could be misrepresentative of the actual samples. There are clearly differences in mineralogy and alteration within similar samples and across short distances within the Lake City and Telaga Bodas samples, and the surface mineral proportions are assumed to represent the whole sample for the H-ASI and UCS calculations. While the differences across a couple of inches may be minimal and have little overall impact on the resulting Pm and Sm parameters, generalizing the findings to a

broader area could have significant impacts. A topic for potential future research would be to examine the mineralogical variation within the Telaga Bodas and Lake City samples. For example, a comparison between the modal mineral percentages used for the Telaga Bodas and Lake City samples and the mineral proportions for both the internal and external surfaces of the core samples post-UCS failure.

Uncertainties exist in the current data, such as aspectral mineralogy, unclassified pixels, which could be unmapped minerals, or minerals not in the spectral library, for example, and whether certain minerals (such as quartz) belong to the primary or secondary mineralogy categories. However, the use of hyperspectral data to improve upon the ASI allows for a level of accuracy and consistency to be achieved that was previously absent while also removing the problem of researcher subjectivity (Quigley & Yildirim, 2015; Zhou et al., 2017). Of the 19 samples which include aspectral minerals, only three samples provide a noticeable improvement in the predicted UCS when the mineral hardness index of 2.1 for quartz is used instead of the 1.7 for feldspar in the Pm calculations. These samples contain a ~75-85% aspectral minerals. For the remaining 16 samples, the impact of the aspectral minerals on the predicted UCS is negligible.

While scale may be an area for future research regarding the H-ASI, the inclusion of hyperspectral imaging and resulting data provides more accuracy in mineral identification and proportions resulting in increased confidence in the H-ASI mineral parameters than the original ASI. Using hyperspectral imaging and processing is a much more efficient method for determining mineralogy of large sections or areas of rock.

2.4.2 Samples

A sample size of 30 is not large enough to make big statements or to generalise findings, but instead to make observations based on the available data from the testing of these samples. During the initial stages of sample preparation, several samples were either unable to be cored due to size limitations of the original samples or proved to be too weak or too damaged to withstand the coring process, leading to sample failure or damage during or after coring. This potentially means there is some sample bias in the samples used for testing in this research, especially with the Telaga Bodas samples where the original samples were often much smaller than the Lake City samples, reducing the options for coring. For example, some clay-rich samples were unable to be cored due to swelling and getting stuck in the drill bit or disintegrating. Some of these samples had high amounts of montmorillonite, beidellite, and gypsum which are not well represented in other samples. The main limitation for the Lake City samples was the availability of both large enough samples to be cored paired with the availability of hyperspectral data on Coreshed for those samples. The main advantage of the samples used in this research is the variation in alteration type and intensity, providing a range of mineral data and variables. More samples would strengthen the results and findings from this research and possibly reduce the degree of conflicting correlation data between the Telaga Bodas and Lake City samples.

2.4.3 ASI

2.4.3.1 ASI Research

Though several articles published since 2015 have referenced Wyering et al., (2015), only two of them have referred to the Alteration Strength Index. Instead, most cite general statements, such as how hydrothermal alteration impacts rock strength. Aside from Wyering et al., (2017), who use their own mASI methodology in their research and reference the ASI, Mordensky et al., (2018) referred to the relationship between porosity and UCS and the importance of porosity in Wyering's ASI based on their own sample data. None of the current available studies appear to have used the ASI in determining rock strength for their samples and their research to validate the application of the ASI in other work. Acknowledging the power-law relationship between UCS and porosity and the impact porosity can have on rock strength is not the same as validating an entire equation based on data from other research. Therefore, my research is the only current, known research working to assess the validity and usage of the ASI. As shown by the results, the Telaga Bodas and Lake City sample data do not support the ASI equation, with contradicting correlation for some parameters also. More data is needed to establish whether this is a recurring issue with the ASI or if the Telaga Bodas and/or Lake City data is anomalous.

2.4.3.2 ASI Parameters

The parameters composing the ASI all play an important role in rock strength, however, the relationship between the UCS and the ASI parameters is moderate at best and inconsistent between the Telaga Bodas and Lake City datasets. The relationship between porosity and the actual UCS is the most consistent with a negative correlation of -0.38 to -0.58. Any correlation between the other parameters and H-ASI and predicted UCS hold little meaning if they cannot relate to the actual calculated UCS. Where some errors in mineralogy may occur, for example high amounts of unclassified minerals, the impacts on the resulting Pm and Sm parameters can be high, however, these differences make little difference to the H-ASI and predicted UCS values given scale of the discrepancies between these and the calculated UCS. Before addressing issues of a smaller scale, the relationship between predicted and actual UCS should first be addressed, especially with samples that have low H-ASI values (> 60) as these were not considered in the original ASI.

The Fracture Index is biased in that there would be no large open fractures in the core samples of my size otherwise the samples would have failed upon coring. Scaling the index in relation to the size of the cores tested is something for further consideration, for example, determining the surface area containing fractures and proportional fracture size as opposed to defined measured lengths and widths. In addition, the fracture index is a parameter which is subjective and requires expansion to include a wider range of fracture descriptions. Currently, the use of an expanded version of the fracture index, as proposed in Table 25, is not possible, as the higher Snf values would decrease the H-ASI and predicted UCS values, which in turn would only increase the difference between these and the actual UCS.

2.4.3.3 Porosity and Permeability

Permeability results for the Telaga Bodas and Lake City samples did not correlate with any of the other parameters and so cannot be included in the H-ASI to provide estimations of UCS. Neither can estimations of permeability be obtained from the H-ASI. More samples and further testing are needed to determine if a relationship may exist which can be incorporated into strength index estimations.

Generally, an increase in porosity should increase permeability, however, the connection between porosity and permeability is highly dependent on connectivity and permeability is influenced greatly by microstructures (Sperl & Trckova, 2008; Heap et al., 2019). Porosity and permeability are complex parameters in hydrothermal systems due to the fact they can increase or decrease strength depending on whether alteration dissolves or precipitates minerals, and is dependent on a multitude of factors including alteration intensity, rock type, temperature, and fluid composition (Heap et al., 2017). Heap et al., (2019) found that highly altered samples follow a different porosity-permeability trend to the similar trends of the unaltered and slightly altered samples. The highly altered samples displayed a wider range of permeabilities (over several orders of magnitude) over a narrow range of porosity, and at lower permeabilities than suggested by their corresponding porosity based on their data. Mielke et al., (2014) state that their findings show a general increase in the cluster size associated with each alteration intensity class with increasing alteration, implying increased heterogeneity of the rock textures. The Telaga Bodas and Lake City data, when plotted by alteration intensity (% soft minerals) do not show any definable trends for the low, medium, and high categories (soft mineral percentages ranges of 5-32%, 39-71%, and 76-84% respectively). The high permeability outlier samples belonged to the low and medium alteration categories and were removed from Figure 107 to see the spread of the low permeability samples more clearly. The really high intensity category (90-99% soft minerals) indicates a positive trend between porosity and permeability, with permeability increasing with increasing porosity, although this intensity group is composed of only eight data points, so more data is required to confirm this trend. The correlation is comparable to that of Heap et al., (2019), however, much shallower with the Telaga Bodas and Lake City samples covering a narrower range of permeability and larger range of porosity. Overall, the Telaga Bodas and Lake City results are inconclusive, and further testing of more samples is needed to see if the results follow trends identified by other research.

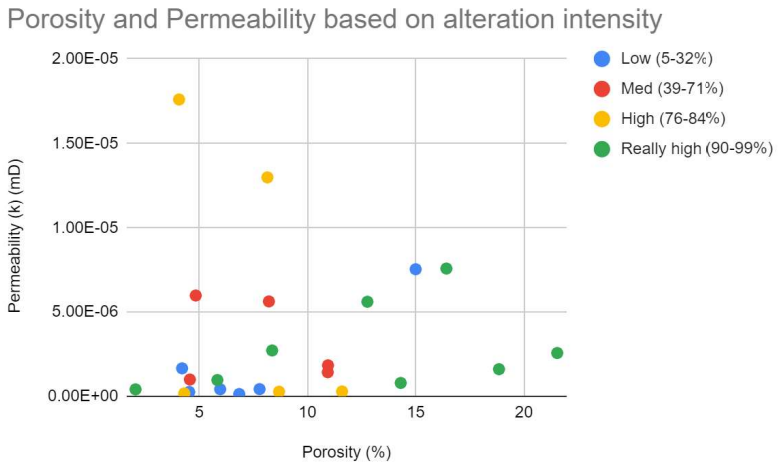

Figure 107. Graph of the porosity and permeability of the Telaga Bodas and Lake City samples based on alteration intensity (% soft minerals). Five outlier samples were removed for a closer look at the sample with low permeabilities. one of the removed samples was from the "low" category, and four were from the "med" category.

2.4.4 UCS

The range of UCS values obtained for the Telaga Bodas and Lake City samples is comparable with those of the samples analyzed by Wyering et al., (2015). Generally, strength decreases as porosity increases (Wyering et al., 2015; Siratovich et al., 2016) and this correlation was confirmed in the Telaga Bodas and Lake City sample results. Strength also decreases as alteration intensity increases (Wyering et al., 2015; Siratovich et al., 2016; Heap et al., 2017). Although the overall data shows weak correlations, the Lake City samples did have a negative correlation with the percentages of soft minerals, which relates directly to the alteration intensity. However, the UCS for the Telaga Bodas samples had no correlation at all with any parameter besides porosity, skewing the overall results to very weak or no correlation.

While Figure 104 shows no correlation between Predicted UCS and Actual UCS, it may indicate a need for calibration of the data, however, attempts to calibrate Equation 2 proved unfruitful. Any changes to the power law function led to wider dispersion of the data. Predicted UCS for low H-ASI values remained consistent while those with high H-ASI values showed large differences in predicted UCS, yet with no clear trend or relationship to the measured UCS values. The main problems appear to lie with samples having low H-ASI values, indicating a potential need for calibration of mineralogical parameters in Equation 1 to achieve more realistic UCS estimates for those samples.

2.5 Conclusion

The ASI has the potential for beneficial implications in the field of drilling and exploration, and the H-ASI reduces subjectivity and improves accuracy for the mineralogical components. The addition of hyperspectral imaging and analysis increases time efficiency

and accuracy allowing for faster mineralogical analysis while having the capability of being carried out in-field. However, the Telaga Bodas and Lake City results are inconclusive, especially with regards to the porosity and permeability, and more samples are needed to determine whether the data follows the trends identified in other research. The lack of correlation between predicted and observed measurements for the data obtained in this research identifies the need for further testing of the ASI equation to address the failure of the ASI to provide accurate estimations of rock strength for these samples.

3 Reference List

Bern, C.R., 2009. Soil chemistry in lithologically diverse datasets: the quartz dilution effect. Applied geochemistry, 24(8), pp.1429-1437.

Bove, D. J., Eberl, D. D., McCarty, D. K., and Meeker, G. P., 2002, Characterization and modeling of illite crystal particles and growth mechanisms in a zoned hydrothermal deposit, Lake City, Colorado: American Mineralogist, v. 87, p. 1546-1556.

Calvin, W. M., and Pace, E. L., 2016, Mapping alteration in geothermal drill core using a field portable spectroradiometer: Geothermics, V. 61, p. 12-23.

Chesworth, W. ed., 2007. Encyclopedia of soil science. Springer Science & Business Media.

Corescan, 2016, The Corescan System. Available from <http://www.corescan.com.au/services/the-corescan-system> [11 January 2016].

Crawford, K. M., 2013, Determination of bulk density of rock core using standard industry methods, Master's report, Michigan Technological University.

Ehrlich, R., 2007, The PVA Multivariate Unmixing System. Word Document, revised 9-30-07.

ENVI, 2015, Basic Hyperspectral Analysis Tutorial. Available from <https://www.l3harrisgeospatial.com/docs/hyperspectralanalysistutorial.html>

Foregs, 2005. Geochemical Atlas of Europe. Available from <http://weppi.gtk.fi/publ/foregsatlas/maps_table.php>

Garden, T. O., Gravley, D. M., Kennedy, B. M., Deering, C., and Chambefort, I., 2017, Controls on hydrothermal fluid flow in caldera-hosted settings: Evidence from Lake City caldera, USA: Geosphere, v. 13 (6).

Garden, T. O., Chambefort, I., Gravley, D. M., Deering, C. D., and Kennedy, B. M., 2020, Reconstruction of the fossil hydrothermal system at Lake City caldera, Colorado, U.S.A.: Constraints for caldera-hosted geothermal systems: Journal of Volcanology and Geothermal Research, v. 393.

Heap, M. J., Kennedy, B. M., Farquahrson, J. I., Ashworth, J., Mayer, K., Letham-Brake, M., Reuschle, T., Gilg, H, A., Scheu, B., Lavallee, Y., Siratovich, P., Cole, J., Jolly, A. D., Baud, P., and Dingwell, D. B., 2017, A multidisciplinary approach to quantify the permeability of the Whakaari/White Island volcanic hydrothermal system (Taupo Volcanic Zone, New Zealand): Journal of Volcanology and Geothermal Research, v. 322, p. 88-108.

Heap, M. J., Troll, V. R., Kushnir, A. R. L., Gilg, H. A., Collinson, A. S. D., Deegan, F. M., Darmawan, H., Seraphine, N., Neuberg, J., and Walter, T. R., 2019, Hydrothermal alteration of andesitic lava domes can lead to explosive volcanic behavior: Nature Communications, v. 10(1), p. 1-10.

Hellman, M.J., and M.S. Ramsey, 2004, Analysis of hot springs and associated deposits in Yellowstone National Park using ASTER and AVIRIS remote sensing: Journal of Volcanology and Geothermal Research, v. 135, p. 195-219.

Jackson, L., Parbhakar-Fox, A., Fox, N., Meffre, S., Cooke, D. R., Harris, A., and Savinova, E., 2018, Integrating hyperspectral analysis and mineral chemistry for geoenvironmental predication: 11th International Conference on Acid Rock Drainage International Mine Water Association WISA Mine Water Division, v. 2, p. 1075-1080.

Kennedy, B., Wilcock, J., and Stix, J., 2012, Caldera resurgence during magma replenishment and rejuvenation at Valles and Lake City calderas: Bulletin of Volcanology, v. 74, p. 1833-1847.

Kennedy, B., Stix, J., Hon, K., Deering, C., and Gelman, S., 2016, Magma storage, differentiation, and interaction at Lake City caldera, Colorado, USA: GSA Bulletin, v. 128 (5-6), p. 764-776.

Lipman, P. W., Steven, T. A., and Luedke, R. G., 1973, Revised volcanic history of the San Juan, Uncompahgre, Silverton, and Lake City calderas in the Western San Juan Mountains, Colorado, Journal of Research US Geological Survey, v. 1 (6), p. 627-642.

Martini, B. A., Harris, A. C., Carey, R., Goodey, N., Honey, F., and Tufilli, N., 2017, Automated hyperspectral core imaging – A revolutionary new tool for exploration, mining, and research. Proceedings of Exploration, v. 17, p. 911-922.

Martini, B. A., Bellian, J., Katz, D., Fonteneau, L. C., Carey, R., Guisinger, M., and Nordeng, S. H., 2019, Continuous Mineralogical Characterization of the Bakken-Three Forks Formatons: New Geological Insights from Hyperspectral Core Imaging: Unconventional Resources Technology Conference (No plaques with the art), 913.

Mielke, P., Bignall, G., and Sass, I., 2014, Predicting the effect of hydrothermal alteration on rock properties, Proceedings 36th New Zealand Geothermal Workshop, v. 24, p. 26.

Moore, J. N., Allis, R., Renner, J. L., Mildenhall, D., and McCulloch, J., 2002, Petrologic evidence for boiling to dryness in the Karaha-Telaga Bodas Geothermal System, Indonesia: PROCEEDINGS, Twenty-Seventh Workshop on Geothermal Reservoir Engineering, Stanford, California.

Moore, J. N., Christenson, B, W., Allis, R. G., Browne, P. R. L., Lutz, S. L., 2004, The mineralogical consequences and behaviour of descending acid-sulfate waters: An example from the Karaha-Telaga Bodas Geothermal System, Indonesia: The Canadian Mineralogist, v. 42, p. 1483-1499.

Moore, J. N., Allis, R. G., Nemčok, Poweel, T. S., Bruton, C. J., Wannamaker, P. E., Raharjo, I. B., and Norman, D. I., 2008, The evolution of volcano-hosted geothermal systems based on deep wells from Karaha-Telaga Bodas, Indonesia: American Journal of Science, v. 308, p. 1-48.

Moore, J. N., 2012, The evolution of a partially vapor-dominated geothermal system at Karaha-Telaga Bodas, Indonesia: Insights from mineral distributions and fluid inclusion measurements: PROCEEDINGS, New Zealand Geothermal Workshop, Auckland, New Zealand.

Mordensky, S. P., Villeneuve, M. C., Kennedy, B. M., Heap, M, J., Gravley, D. M., Farquharson, J. I., and Reuschle, T., 2018, Physical and mechanical property relationships of a shallow intrusion and volcanic host rock, Pinnacle Ridge, Mt. Ruapehu, New Zealand: Journal of Volcanology and Geothermal Research, v. 359, p. 1-20.

NASA: Jet Propulsion Laboratory, n.d., ASTER Spectral Library, Available from <http://speclib.jpl.nasa.gov/> [15 March 2016].

Nemčok, M., McCulloch, J., Nash, G., and Moore, J., 2001, Fault Kinematics in the Karaha-Telaga Bodas, Indonesia, Geothermal Field: An Interpretation Tool for Remote Sensing Data: GRC Transactions v. 25.

Nemčok, M., Moore, J. N., Allis, R., and McCulloch, J., 2004, Fracture development within a stratovolcano: the Karaha-Telaga Bodas geothermal field, Java volcanic arc: Cosgrove, J., W., and Engelder, T. (eds) 2004. The Initiation, Propagation, and Arrest of Joints and Other Fractures. Geological Society, London, Special Publications, v. 231, p. 223-242.

New England Research, 2016, BenchLan 7000 EX, Velocity and Permeability measurement system: User's manual. New England Research, Inc. Version 160801.

Queensland Government, 2016. Soil pH. Available from <https://www.qld.gov.au/environment/land/management/soil/soil-properties/ph-levels>

Quigley, M. A., and Yildirim, B. G., 2015, Mineral Identification and Domain Characterisation Using Two Automated Hyperspectral Core Logging Systems, Los Bronces Cu-Mo Porphyry Deposit: 13th SGA Biennal Meeting on Mineral Resources in a Sustainable World, p. 24-27.

Rengel, Z., 2011. Soil pH, soil health and climate change. In Soil health and climate change (pp. 69-85). Springer, Berlin, Heidelberg.

Rowell, D.L., 2014. Soil science: Methods & applications. Routledge.

Sabins, F, F., 1999, Remote sensing for mineral exploration: Ore Geology Reviews, v. 14, p. 157-183.

Sanford, R., 1992, Lead isotope compositions and paleohydrology of caldera-related epithermal veins, Lake City, Colorado: GSA Bulletin, v. 104 (10), p. 1236-1245.

Shacklette, H.T. and Boerngen, J.G., 1984. Element concentrations in soils and other surficial materials of the conterminous United States. USGS Professional Paper 1270.

Siratovich, P. A., Heap, M. J., Villeneuve, M. C., Cole, J. W., Kennedy, B. M., Davidson, J., and Reuschle, T., 2016, Mechanical behavior of the Rotokawa Andesites (New Zealand): Insight into permeability evolution and stress-induced behavior in an actively utilized geothermal reservoir: Geothermics, v. 64, p. 163-179.

Smith, D.B., Wang, X., Reeder, S. and Demetriades, A., 2012. The IUGS/IAGC task group on global geochemical baselines. Earth Science Frontiers (China University of Geosciences (Beijing); Peking University) 19(3), pp.1-6.

Smith, D.B., Smith, S.M. and Horton, J.D., 2013. History and evaluation of national-scale geochemical data sets for the United States. Geoscience Frontiers, 4(2), pp.167-183.

Smith, D.B., Cannon, W.F., Woodruff, L.G., Solano, F., Kilburn, J.E., and Fey, D.L., 2013. Geochemical and mineralogical data for soils of the conterminous United States. U.S. Geological Survey Data Series 801, 19 p., https://pubs.usgs.gov/ds/801/.

Soil Survey Staff. 1999. Soil taxonomy: A basic system of soil classification for making and interpreting soil surveys. 2nd edition. Natural Resources Conservation Service. U.S. Department of Agriculture Handbook 436.

Sperl, J., and Trckova, J., 2008, Permeability and porosity of rocks and their relationship based on laboratory testing: Acta Geodyn Geomater, v. 5 (149), p. 41-47.

Tadesse, A.W., Gereslassie, T., Xu, Q., Tang, X. and Wang, J., 2018. Concentrations, distribution, sources and ecological risk assessment of trace elements in soils from Wuhan, Central China. International journal of environmental research and public health, 15(12), p.2873.

USDA, Soil Science Division Staff, 2017, Soil Survey Manual. Agriculture Handbook No. 18. Government Printing Office, Washington, D.C.

Wilson, M.A., Burt, R., Indorante, S.J., Jenkins, A.B., Chiaretti, J.V., Ulmer, M.G. and Scheyer, J.M., 2008. Geochemistry in the modern soil survey program. Environmental monitoring and assessment, 139(1-3), pp.151-171.

Woodruff, L., Cannon, W.F., Smith, D.B. and Solano, F., 2015. The distribution of selected elements and minerals in soil of the conterminous United States. Journal of Geochemical Exploration, 154, pp.49-60.

Wu, W., Li, Y., Yan, M., Yang, L., Lei, J., & Liu, H. B. (2021). Surface soil metal elements variability affected by environmental and soil properties. PloS one, 16(7), e0254928. https://doi.org/10.1371/journal.pone.0254928

Wyering, L. D., Villeneuve, M. C., Wallis, I. C., Siratovich, P. A., Kennedy, B. M., and Gravley, D. M., 2015, The development and application of the alteration strength index equation: Engineering Geology, v. 199, p. 48-61.

Wyering, L. D., Villeneuve, M. C., Kennedy, B. M., Gravley, D. M., and Siratovich, P. A., 2017, Using drilling and geological parameters to estimate rock strength in hydrothermally altered rock - A comparison of mechanical specific energy, R/N-W/D chart and Alteration Strength Index, Geothermics, v. 69, p. 119-131.

Zhou, X., Jara, C., Bardoux, M., and Plasencia, C., 2017, Multi-scale integrated application of Spectral Geology and Remote Sensing for Mineral Exploration: Proc. 6th Decennial Int. Conf. Mineral Exploration, p. 21-25.

A Soils Appendix

A.1 Correlation Matrices

A.1.1 Top 5 Horizon: Geochemical

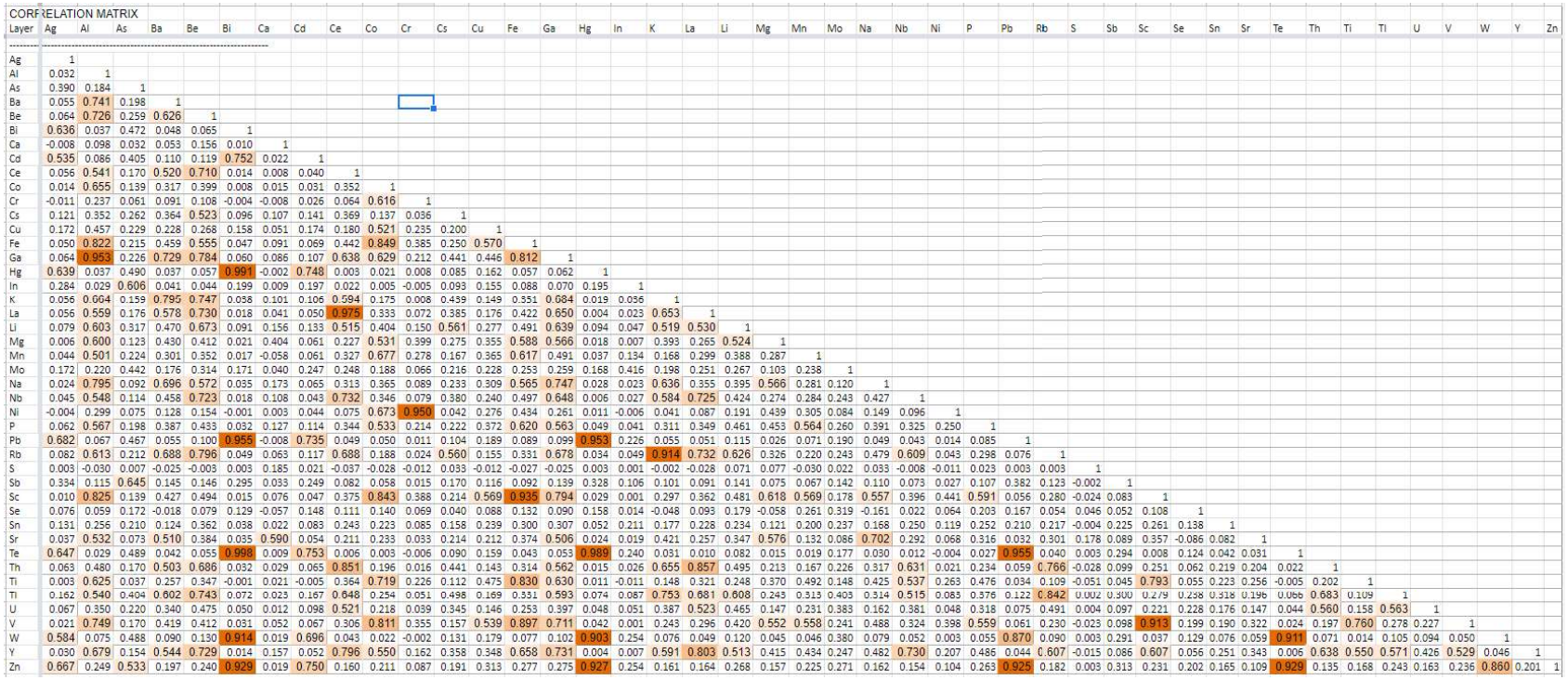

CORRELATION MATRIX

Layer	Ag	Al	As	Ba	Be	Bi	Ca	Cd	Ce	Co	Cr	Cs	Cu	Fe	Ga	Hg	In	K	La	Li	Mg	Mn	Mo	Na	Nb	Ni	P	Pb	Rb	S	Sb	Sc	Se	Sn	Sr	Te	Th	Ti	Tl	U	V	W	Y	Zn
Ag	1																																										
Al	0.032	1																																										
As	0.390	0.184	1																																									
Ba	0.055	0.741	0.198	1																																								
Be	0.064	0.726	0.259	0.626	1																																							
Bi	0.636	0.037	0.472	0.048	0.065	1																																					
Ca	-0.008	0.098	0.032	0.053	0.156	0.010	1																																				
Cd	0.535	0.086	0.405	0.110	0.119	0.752	0.022	1																																			
Ce	0.056	0.541	0.170	0.520	0.710	0.014	0.008	0.040	1																																		
Co	0.014	0.655	0.139	0.317	0.399	0.008	0.015	0.031	0.352	1																																	
Cr	-0.011	0.237	0.061	0.091	0.108	-0.004	-0.008	0.026	0.064	0.616	1																																
Cs	0.121	0.352	0.262	0.364	0.523	0.096	0.107	0.141	0.369	0.137	0.036	1																															
Cu	0.172	0.457	0.229	0.228	0.268	0.158	0.051	0.174	0.180	0.521	0.235	0.200	1																														
Fe	0.050	0.822	0.215	0.459	0.555	0.047	0.091	0.069	0.442	0.849	0.385	0.250	0.570	1																													
Ga	0.064	0.953	0.226	0.729	0.784	0.060	0.086	0.107	0.638	0.629	0.212	0.441	0.446	0.812	1																												
Hg	0.639	0.037	0.490	0.037	0.057	0.991	-0.002	0.748	0.003	0.021	0.008	0.085	0.162	0.057	0.062	1																											
In	0.284	0.029	0.606	0.041	0.044	0.199	0.009	0.197	0.022	0.005	-0.005	0.093	0.155	0.088	0.070	0.195	1																										
K	0.056	0.664	0.159	0.795	0.747	0.038	0.101	0.106	0.594	0.175	0.008	0.439	0.149	0.351	0.684	0.019	0.036	1																									
La	0.056	0.559	0.176	0.578	0.730	0.018	0.041	0.050	0.975	0.333	0.072	0.385	0.176	0.422	0.650	0.004	0.023	0.653	1																								
Li	0.079	0.603	0.317	0.470	0.673	0.091	0.156	0.133	0.515	0.404	0.150	0.561	0.277	0.491	0.639	0.094	0.047	0.519	0.530	1																					
Mg	0.006	0.600	0.123	0.430	0.412	0.021	0.404	0.061	0.227	0.531	0.399	0.275	0.355	0.588	0.566	0.018	0.007	0.393	0.265	0.524	1																				
Mn	0.044	0.501	0.224	0.301	0.352	0.017	-0.058	0.061	0.327	0.677	0.278	0.167	0.365	0.617	0.491	0.037	0.134	0.168	0.299	0.388	0.287	1																			
Mo	0.172	0.220	0.442	0.176	0.314	0.171	0.040	0.247	0.248	0.188	0.066	0.216	0.228	0.253	0.259	0.168	0.416	0.198	0.251	0.267	0.103	0.238	1																		
Na	0.024	0.795	0.092	0.696	0.572	0.035	0.173	0.065	0.313	0.365	0.089	0.233	0.309	0.565	0.747	0.028	0.023	0.636	0.355	0.395	0.566	0.281	0.120	1																	
Nb	0.045	0.548	0.114	0.458	0.723	0.018	0.108	0.043	0.732	0.346	0.079	0.380	0.240	0.497	0.648	0.006	0.027	0.584	0.725	0.424	0.274	0.284	0.243	0.427	1																
Ni	-0.004	0.299	0.075	0.128	0.154	-0.001	0.003	0.044	0.075	0.673	0.950	0.042	0.276	0.434	0.261	0.011	-0.006	0.041	0.087	0.191	0.439	0.305	0.084	0.149	0.096	1															
P	0.062	0.567	0.198	0.387	0.433	0.032	0.127	0.114	0.344	0.533	0.214	0.222	0.372	0.620	0.563	0.049	0.041	0.311	0.349	0.461	0.453	0.564	0.260	0.391	0.325	0.250	1														
Pb	0.682	0.067	0.467	0.055	0.100	0.955	-0.008	0.735	0.049	0.050	0.011	0.104	0.189	0.089	0.099	0.953	0.226	0.055	0.051	0.115	0.026	0.071	0.190	0.049	0.043	0.014	0.085	1													
Rb	0.082	0.613	0.212	0.688	0.796	0.049	0.063	0.117	0.688	0.188	0.024	0.560	0.155	0.331	0.678	0.034	0.049	0.914	0.732	0.626	0.326	0.220	0.243	0.479	0.609	0.043	0.298	0.076	1												
S	0.003	-0.030	0.007	-0.025	-0.003	0.003	0.185	0.021	-0.037	-0.028	-0.012	0.033	-0.012	-0.027	-0.025	0.003	0.001	-0.002	-0.028	0.071	0.077	-0.030	0.022	0.033	-0.008	-0.011	0.023	0.003	0.003	1											
Sb	0.334	0.115	0.645	0.145	0.146	0.295	0.033	0.249	0.082	0.058	0.015	0.170	0.116	0.092	0.139	0.328	0.106	0.101	0.091	0.141	0.075	0.067	0.142	0.110	0.073	0.027	0.107	0.382	0.123	-0.002	1										
Sc	0.010	0.825	0.139	0.427	0.494	0.015	0.076	0.047	0.375	0.843	0.388	0.214	0.569	0.935	0.794	0.029	0.001	0.297	0.362	0.481	0.618	0.569	0.178	0.557	0.396	0.441	0.591	0.056	0.280	-0.024	0.083	1									
Se	0.076	0.059	0.172	-0.018	0.079	0.129	-0.057	0.148	0.111	0.140	0.069	0.040	0.088	0.132	0.090	0.158	0.014	-0.048	0.093	0.179	-0.058	0.261	0.319	-0.161	0.022	0.064	0.203	0.167	0.054	0.046	0.052	0.108	1								
Sn	0.131	0.256	0.210	0.124	0.362	0.038	0.022	0.083	0.243	0.223	0.085	0.158	0.239	0.300	0.307	0.052	0.211	0.177	0.228	0.234	0.121	0.200	0.237	0.168	0.250	0.119	0.252	0.210	0.217	-0.004	0.225	0.261	0.138	1							
Sr	0.037	0.532	0.073	0.510	0.384	0.035	0.590	0.054	0.211	0.233	0.033	0.214	0.212	0.374	0.506	0.024	0.019	0.421	0.257	0.347	0.576	0.132	0.086	0.702	0.292	0.068	0.316	0.032	0.301	0.178	0.089	0.357	-0.086	0.082	1						
Te	0.647	0.029	0.489	0.042	0.055	0.998	0.009	0.753	0.006	0.003	-0.006	0.090	0.159	0.043	0.053	0.989	0.240	0.031	0.010	0.082	0.015	0.019	0.177	0.030	0.012	-0.004	0.027	0.955	0.040	0.003	0.294	0.008	0.124	0.042	0.031	1					
Th	0.063	0.480	0.170	0.503	0.686	0.032	0.029	0.065	0.851	0.196	0.016	0.441	0.143	0.314	0.562	0.015	0.026	0.655	0.857	0.495	0.213	0.167	0.226	0.317	0.631	0.021	0.234	0.059	0.766	-0.028	0.099	0.251	0.062	0.219	0.204	0.022	1				
Ti	0.003	0.625	0.037	0.257	0.347	-0.001	0.021	-0.005	0.364	0.719	0.226	0.112	0.475	0.830	0.630	0.011	-0.011	0.148	0.321	0.248	0.370	0.492	0.148	0.425	0.537	0.263	0.476	0.034	0.109	-0.051	0.045	0.793	0.055	0.223	0.256	-0.005	0.202	1			
Tl	0.162	0.540	0.404	0.602	0.743	0.072	0.023	0.167	0.648	0.254	0.051	0.498	0.169	0.331	0.593	0.074	0.087	0.753	0.681	0.608	0.243	0.313	0.403	0.314	0.515	0.083	0.376	0.122	0.842	0.002	0.300	0.279	0.238	0.318	0.196	0.066	0.683	0.109	1		
U	0.067	0.350	0.220	0.340	0.475	0.050	0.012	0.098	0.521	0.218	0.039	0.345	0.146	0.253	0.397	0.048	0.051	0.387	0.523	0.465	0.147	0.231	0.383	0.162	0.381	0.048	0.318	0.075	0.491	0.004	0.097	0.221	0.228	0.176	0.147	0.044	0.560	0.158	0.563	1	
V	0.021	0.749	0.170	0.419	0.412	0.031	0.052	0.067	0.306	0.811	0.355	0.157	0.539	0.897	0.711	0.042	0.001	0.243	0.296	0.420	0.552	0.558	0.241	0.488	0.324	0.398	0.559	0.061	0.230	-0.023	0.098	0.913	0.199	0.190	0.322	0.024	0.197	0.760	0.278	0.227	1
W	0.584	0.075	0.488	0.090	0.130	0.914	0.019	0.696	0.043	0.022	-0.002	0.131	0.179	0.077	0.102	0.903	0.254	0.076	0.049	0.120	0.045	0.046	0.380	0.079	0.052	0.003	0.055	0.870	0.090	0.003	0.291	0.037	0.129	0.076	0.059	0.911	0.071	0.014	0.105	0.094	0.050
Y	0.030	0.679	0.154	0.544	0.729	0.014	0.157	0.052	0.796	0.550	0.162	0.358	0.348	0.658	0.731	0.004	0.007	0.591	0.803	0.513	0.415	0.434	0.247	0.482	0.730	0.207	0.486	0.044	0.607	-0.015	0.086	0.607	0.056	0.251	0.343	0.006	0.638	0.550	0.571	0.426	0.529
Zn	0.667	0.249	0.533	0.197	0.240	0.929	0.019	0.750	0.160	0.211	0.087	0.191	0.313	0.277	0.275	0.927	0.254	0.161	0.164	0.268	0.157	0.225	0.271	0.162	0.154	0.104	0.263	0.925	0.182	0.003	0.313	0.231	0.202	0.165	0.109	0.929	0.135	0.168	0.243	0.163	0.236

Figure A-1. Correlation matrix for the Top 5 Horizon soil geochemical data, created via the Band Statistics tool in ArcGIS

A.1.2 A Horizon: Mineralogy

CORRELATION MATRIX

Layer	Quartz	K_fs	Plag	Total_fs	14A_Clays	10A_Clays	Kaolinite	Total_Clays	Gibbsite	Calcite	Dolomite	Aragonite	Total_Carbs	Analcime	Heulandite	Total_Zeolites	Gypsum	Talc	Hornblende	Serpentine	Hematite	Goethite	Pyroxene	Pyrite	Other	Amorphous
Quartz	1.000																									
K_fs	-0.317	1.000																								
Plag	-0.742	0.448	1.000																							
Total_fs	-0.700	0.703	0.951	1.000																						
14A_Clays	-0.296	-0.150	0.133	0.054	1.000																					
10A_Clays	-0.409	-0.064	0.063	0.028	0.239	1.000																				
Kaolinite	-0.148	-0.201	-0.043	-0.103	0.066	0.114	1.000																			
Total_Clays	-0.453	-0.180	0.071	-0.006	0.531	0.842	0.525	1.000																		
Gibbsite	-0.003	-0.085	-0.071	-0.086	0.033	-0.013	0.356	0.152	1.000																	
Calcite	-0.220	-0.075	-0.122	-0.123	-0.057	-0.026	-0.072	-0.068	-0.047	1.000																
Dolomite	-0.136	0.064	0.009	0.029	-0.027	0.027	-0.066	-0.018	-0.034	0.164	1.000															
Aragonite	-0.038	-0.083	-0.078	-0.091	-0.067	-0.103	-0.040	-0.113	-0.012	0.315	0.052	1.000														
Total_Carbs	-0.230	-0.063	-0.117	-0.115	-0.067	-0.033	-0.085	-0.082	-0.051	0.958	0.394	0.452	1.000													
Analcime	0.063	-0.027	-0.041	-0.042	-0.008	-0.070	-0.011	-0.057	-0.009	0.009	0.032	-0.011	0.014	1.000												
Heulandite	-0.136	0.156	0.121	0.151	-0.003	-0.016	-0.021	-0.022	-0.013	0.014	0.013	-0.012	0.013	0.011	1.000											
Total_Zeolites	-0.093	0.127	0.090	0.115	-0.006	-0.046	-0.024	-0.045	-0.015	0.016	0.025	-0.015	0.018	0.456	0.895	1.000										
Gypsum	-0.057	-0.021	-0.035	-0.035	-0.044	-0.044	-0.018	-0.053	-0.008	0.064	0.039	0.085	0.079	-0.008	-0.009	-0.011	1.000									
Talc	-0.092	-0.045	0.048	0.023	0.165	0.006	0.066	0.086	0.030	-0.027	-0.014	-0.007	-0.028	-0.011	0.010	0.004	-0.007	1.000								
Hornblende	-0.308	0.082	0.404	0.350	0.132	-0.045	0.060	0.037	0.045	-0.071	-0.020	-0.026	-0.071	-0.003	0.008	0.005	-0.025	0.353	1.000							
Serpentine	-0.131	-0.044	0.096	0.062	0.074	0.005	0.239	0.128	0.023	-0.026	-0.014	-0.007	-0.027	0.023	0.003	0.013	-0.001	0.285	0.131	1.000						
Hematite	-0.153	0.106	0.081	0.101	0.010	0.010	0.212	0.100	0.155	0.012	-0.025	-0.024	0.000	-0.013	0.076	0.062	-0.012	0.047	0.038	0.110	1.000					
Goethite	0.048	-0.079	-0.086	-0.095	0.000	-0.012	0.062	0.017	0.024	-0.011	-0.011	-0.013	-0.014	0.020	-0.006	0.004	-0.010	-0.008	-0.024	0.008	0.005	1.000				
Pyroxene	-0.341	-0.085	0.370	0.265	0.184	-0.052	0.116	0.073	0.007	0.002	-0.015	-0.015	-0.004	0.044	0.069	0.081	-0.014	0.014	0.065	0.074	0.106	-0.019	1.000			
Pyrite	-0.037	-0.019	0.003	-0.005	0.060	0.031	0.000	0.042	-0.007	0.007	0.021	-0.007	0.010	-0.006	-0.005	-0.007	-0.005	-0.004	0.005	-0.003	-0.012	-0.006	0.007	1.000		
Other	-0.094	-0.029	0.052	0.031	0.002	-0.025	0.058	0.007	0.066	0.026	0.071	0.089	0.054	0.007	0.026	0.026	0.112	0.018	0.060	0.035	0.042	0.008	0.068	0.008	1.000	
Amorphous	-0.779	-0.043	0.366	0.276	0.299	0.468	0.189	0.514	0.022	0.111	0.047	-0.011	0.105	-0.076	0.070	0.028	-0.025	0.078	0.141	0.104	0.103	0.003	0.237	0.059	0.059	1.000
Ag	-0.055	0.025	0.061	0.057	0.040	0.022	0.009	0.033	-0.009	-0.010	-0.007	-0.008	-0.011	-0.003	-0.004	-0.005	-0.006	0.012	0.019	-0.006	0.033	-0.009	0.009	-0.004	-0.008	0.035
Al	-0.861	0.343	0.770	0.731	0.359	0.520	0.298	0.617	0.076	-0.105	0.010	-0.141	-0.112	-0.064	0.110	0.070	-0.059	0.092	0.345	0.158	0.162	-0.055	0.293	0.022	0.047	0.605
As	-0.162	0.031	0.062	0.060	0.110	0.213	0.056	0.212	-0.027	0.022	0.036	-0.031	0.023	-0.024	0.009	-0.003	-0.019	0.022	0.007	0.022	0.157	0.072	-0.034	-0.001	-0.022	0.152
Ba	-0.662	0.578	0.638	0.708	0.108	0.399	-0.005	0.319	-0.068	-0.108	0.036	-0.128	-0.106	-0.059	0.146	0.103	-0.050	0.016	0.166	0.028	0.053	-0.051	0.069	-0.014	-0.012	0.413
Be	-0.670	0.465	0.481	0.544	0.174	0.515	0.105	0.470	-0.047	0.042	0.052	-0.114	0.030	-0.069	0.169	0.119	-0.028	0.016	0.130	0.027	0.164	0.019	0.064	-0.003	0.000	0.479
Bi	-0.081	0.054	0.054	0.061	0.039	0.066	0.016	0.067	-0.005	0.016	0.020	-0.006	0.018	-0.004	0.016	0.012	-0.008	-0.001	0.005	-0.005	0.029	-0.001	-0.009	-0.003	-0.005	0.055
C_total	-0.111	-0.193	-0.180	-0.210	0.068	-0.001	0.111	0.069	0.119	0.108	-0.007	0.120	0.112	-0.042	-0.046	-0.059	-0.025	0.014	0.016	-0.010	0.020	0.008	-0.030	0.084	0.052	0.420
C_inorganic	-0.231	-0.062	-0.115	-0.113	-0.067	-0.032	-0.086	-0.081	-0.051	0.953	0.412	0.449	1.000	0.014	0.013	0.018	0.079	-0.028	-0.070	-0.027	-0.001	-0.014	-0.004	0.010	0.055	0.106
C_organic	-0.064	-0.180	-0.156	-0.187	0.082	0.006	0.130	0.087	0.131	-0.084	-0.089	0.030	-0.089	-0.044	-0.048	-0.063	-0.042	0.020	0.031	-0.005	0.021	0.012	-0.029	0.083	0.042	0.402
Ca	-0.437	-0.001	0.113	0.089	-0.017	-0.005	-0.079	-0.043	-0.064	0.928	0.287	0.422	0.943	0.004	0.051	0.047	0.219	-0.003	0.050	0.005	0.031	-0.030	0.131	0.008	0.084	0.239
Cd	-0.099	0.066	0.045	0.059	0.010	0.090	-0.007	0.065	-0.021	0.003	0.009	-0.013	0.002	-0.013	-0.005	-0.010	-0.001	0.009	0.037	0.013	0.008	-0.012	-0.028	-0.004	-0.019	0.111
Ce	-0.423	0.367	0.249	0.325	0.068	0.505	0.156	0.450	0.054	-0.052	0.035	-0.135	-0.059	-0.038	0.138	0.105	-0.067	-0.020	0.020	-0.023	0.101	0.061	0.009	-0.024	0.005	0.320
Co	-0.562	-0.084	0.393	0.284	0.431	0.418	0.373	0.599	0.075	-0.123	-0.031	-0.101	-0.131	-0.041	0.049	0.025	-0.055	0.414	0.355	0.356	0.237	0.029	0.422	0.033	0.075	0.524
Cr	-0.230	-0.090	0.102	0.050	0.330	0.183	0.181	0.315	0.082	-0.077	-0.008	-0.034	-0.074	-0.018	0.022	0.012	-0.027	0.815	0.328	0.438	0.151	0.000	0.133	0.022	0.034	0.237
Cs	-0.364	0.219	0.162	0.204	0.131	0.353	0.052	0.317	-0.023	0.068	0.079	-0.020	0.074	0.008	0.153	0.139	-0.009	-0.008	0.013	-0.022	0.161	-0.011	0.016	-0.005	0.010	0.306
Cu	-0.131	-0.024	0.098	0.070	0.087	0.067	0.106	0.121	0.019	-0.013	-0.017	0.019	-0.012	-0.006	0.009	0.005	-0.004	0.050	0.084	0.072	0.076	-0.012	0.098	0.012	0.021	0.116
Fe	-0.725	0.045	0.576	0.474	0.460	0.465	0.392	0.650	0.115	-0.096	-0.023	-0.114	-0.107	-0.039	0.078	0.052	-0.057	0.201	0.390	0.239	0.323	0.118	0.463	0.038	0.086	0.583
Ga	-0.856	0.379	0.745	0.724	0.357	0.531	0.277	0.615	0.074	-0.094	0.007	-0.143	-0.103	-0.060	0.125	0.084	-0.059	0.076	0.318	0.125	0.188	-0.053	0.287	0.022	0.041	0.604
Hg	-0.089	-0.034	0.032	0.014	0.163	0.057	0.055	0.118	0.043	-0.040	-0.028	-0.003	-0.042	-0.024	-0.015	-0.024	-0.024	0.019	0.039	0.002	0.012	-0.002	0.012	0.036	0.006	0.129
In	-0.031	0.011	0.018	0.018	-0.012	0.000	0.061	0.022	-0.004	0.010	-0.008	-0.003	0.006	-0.004	-0.003	-0.005	-0.002	-0.003	0.007	-0.002	0.217	-0.004	-0.004	-0.002	-0.004	0.026
K	-0.607	0.795	0.540	0.705	0.013	0.397	-0.117	0.239	-0.102	-0.024	0.124	-0.130	-0.013	-0.057	0.160	0.117	-0.029	-0.028	0.099	-0.033	0.066	-0.089	-0.035	-0.013	-0.026	0.297
La	0.461	0.411	0.287	0.372	0.045	0.515	0.113	0.431	0.030	0.031	0.059	0.131	0.034	0.049	0.142	0.105	0.059	0.009	0.013	0.024	0.091	0.025	0.002	0.024	0.010	0.338
Li	-0.552	0.135	0.266	0.259	0.325	0.647	0.111	0.617	-0.026	0.059	0.164	-0.001	0.091	-0.021	0.078	0.060	0.005	0.020	0.051	0.011	0.065	-0.012	0.011	0.003	0.070	0.471
Mg	-0.691	0.130	0.508	0.449	0.348	0.301	0.050	0.352	-0.030	0.154	0.521	0.035	0.266	0.020	0.095	0.094	0.023	0.335	0.379	0.239	0.102	-0.054	0.338	0.025	0.197	0.482
Mn	-0.431	-0.044	0.262	0.193	0.284	0.399	0.257	0.488	0.034	-0.160	-0.031	-0.098	-0.163	-0.072	0.032	-0.003	-0.069	0.128	0.190	0.122	0.158	0.052	0.211	0.024	0.018	0.501
Mo	-0.225	0.083	0.096	0.105	0.049	0.237	0.106	0.231	-0.002	0.055	0.028	-0.029	0.049	-0.022	0.024	0.011	-0.008	0.014	0.038	0.011	0.163	0.006	0.009	-0.004	-0.002	0.209

Mo	-0.225	0.083	0.096	0.105	0.049	0.237	0.106	0.231	-0.002	0.055	0.028	-0.029	0.049	-0.022	0.024	0.011	-0.008	0.014	0.038	0.011	0.163	0.006	0.009	-0.004	-0.002	0.209
Na	-0.769	0.507	0.942	0.925	0.143	0.146	-0.091	0.114	-0.090	-0.075	0.046	-0.005	-0.054	-0.022	0.121	0.098	0.025	0.052	0.392	0.065	0.068	-0.096	0.257	0.004	0.102	0.383
Nb	-0.528	0.462	0.393	0.473	0.085	0.287	0.143	0.294	0.066	0.041	-0.008	-0.109	0.015	-0.035	0.211	0.172	-0.017	0.005	0.083	0.014	0.249	-0.010	0.179	-0.001	0.028	0.351
Ni	-0.247	-0.078	0.125	0.073	0.327	0.164	0.178	0.300	0.068	-0.053	-0.008	-0.035	-0.053	-0.017	0.014	0.005	-0.020	0.787	0.320	0.501	0.144	0.008	0.132	0.020	0.032	0.240
P	-0.587	0.065	0.389	0.332	0.268	0.449	0.119	0.460	0.029	-0.040	0.096	-0.025	-0.016	-0.043	0.054	0.029	-0.056	0.070	0.195	0.052	0.093	-0.006	0.250	0.045	0.054	0.585
Pb	-0.128	0.087	0.046	0.067	0.079	0.160	0.037	0.156	0.005	-0.041	-0.017	-0.041	-0.046	-0.035	0.003	-0.013	-0.034	0.026	0.032	-0.017	0.041	-0.008	0.001	0.014	-0.005	0.143
Rb	-0.541	0.680	0.377	0.536	0.075	0.510	-0.042	0.372	-0.067	-0.017	0.093	-0.122	-0.013	-0.072	0.145	0.097	-0.033	-0.033	0.031	-0.042	0.079	-0.066	-0.086	-0.010	-0.029	0.315
S	-0.078	-0.024	-0.040	-0.040	-0.034	-0.025	-0.026	-0.040	-0.009	0.084	0.052	0.089	0.100	-0.010	-0.008	-0.012	0.985	-0.008	-0.028	-0.008	-0.012	-0.011	-0.014	0.008	0.093	0.009
Sb	-0.094	0.066	0.077	0.084	0.021	0.050	-0.007	0.040	-0.012	0.017	0.011	-0.012	0.015	-0.011	0.022	0.015	-0.006	0.006	0.013	0.001	0.015	0.002	0.000	-0.003	-0.003	0.069
Sc	-0.711	-0.015	0.565	0.445	0.497	0.482	0.411	0.683	0.115	-0.112	-0.014	-0.106	-0.118	-0.027	0.056	0.038	-0.054	0.191	0.426	0.249	0.216	-0.018	0.462	0.045	0.079	0.582
Se	-0.035	-0.125	-0.177	-0.184	0.200	0.284	0.188	0.349	0.092	-0.033	-0.054	-0.032	-0.047	-0.045	-0.047	-0.062	-0.013	0.007	-0.042	-0.018	0.008	0.093	-0.065	0.082	0.007	0.163
Sn	-0.111	0.039	0.082	0.079	0.106	0.087	0.020	0.106	0.002	0.001	-0.027	-0.010	-0.007	-0.018	0.009	0.000	-0.016	0.028	0.079	-0.002	0.066	-0.013	0.014	0.001	-0.001	0.084
Sr	-0.638	0.283	0.579	0.559	0.011	0.031	-0.061	0.000	-0.069	0.347	0.144	0.446	0.410	-0.001	0.140	0.124	0.203	0.014	0.205	0.032	0.062	-0.054	0.229	-0.007	0.140	0.342
Te	-0.044	0.033	0.040	0.043	0.011	0.019	0.023	0.027	-0.008	0.009	0.013	-0.007	0.010	0.000	-0.001	-0.001	0.002	-0.002	0.013	-0.002	0.048	0.048	-0.010	-0.004	-0.007	0.017
Th	-0.390	0.480	0.247	0.363	0.004	0.444	0.080	0.353	0.045	-0.012	0.049	-0.105	-0.016	-0.030	0.141	0.112	-0.054	-0.040	0.000	-0.040	0.094	0.021	-0.083	-0.015	0.005	0.228
Tl	-0.545	-0.013	0.488	0.384	0.305	0.255	0.399	0.452	0.169	-0.115	-0.099	-0.123	-0.144	-0.003	0.079	0.069	-0.059	0.105	0.319	0.164	0.283	-0.010	0.524	0.038	0.100	0.444
Tl	-0.275	0.345	0.081	0.184	0.077	0.430	0.007	0.336	-0.039	-0.021	0.014	-0.051	-0.024	-0.036	0.083	0.058	-0.032	-0.012	-0.044	-0.029	0.035	-0.036	-0.095	0.008	-0.040	0.225
U	-0.269	0.195	0.108	0.154	0.049	0.374	0.099	0.326	0.025	-0.018	0.034	-0.020	-0.011	-0.037	0.059	0.036	-0.038	-0.028	-0.016	-0.013	0.023	0.011	-0.062	-0.010	-0.008	0.248
V	-0.654	-0.037	0.512	0.395	0.494	0.477	0.343	0.649	0.083	-0.114	-0.024	-0.110	-0.123	-0.035	0.039	0.019	-0.059	0.151	0.338	0.217	0.209	0.029	0.476	0.038	0.066	0.553
W	-0.169	0.106	0.145	0.152	0.031	0.098	0.018	0.088	-0.009	0.013	0.022	-0.017	0.014	-0.012	0.023	0.015	-0.010	0.001	0.063	0.000	0.081	-0.009	-0.006	-0.001	-0.007	0.115
Y	-0.650	0.325	0.449	0.470	0.163	0.464	0.153	0.451	-0.018	0.042	0.035	-0.098	0.028	-0.049	0.120	0.085	-0.042	0.058	0.183	0.073	0.163	0.017	0.216	-0.004	0.022	0.527
Zn	-0.539	0.093	0.356	0.316	0.326	0.468	0.196	0.525	0.011	-0.071	0.009	-0.085	-0.074	-0.063	0.030	-0.001	-0.043	0.105	0.210	0.118	0.148	0.002	0.160	0.023	0.012	0.501

Figure A-2. Correlation matrix for the A Horizon soil mineralogy data, created via the Band Statistics tool in ArcGIS

A.1.3 A Horizon: Geochemical

Layer	Ag	Al	As	Ba	Be	Bi	C_total	C_inorg	C_org	Ca	Cd	Ce	Co	Cr	Cs	Cu	Fe	Ga	Hg	In	K	La	Li	Mg	Mn	Mo	Na	Nb
Ag	1.000																											
Al	0.057	1.000																										
As	0.188	0.176	1.000																									
Ba	0.046	0.734	0.179	1.000																								
Be	0.054	0.723	0.218	0.626	1.000																							
Bi	0.646	0.082	0.327	0.082	0.099	1.000																						
C_total	-0.002	-0.136	-0.012	-0.231	-0.106	-0.009	1.000																					
C_inorganic	-0.011	-0.110	0.023	-0.104	0.031	0.018	0.110	1.000																				
C_organic	0.000	-0.113	-0.017	-0.209	-0.112	-0.013	0.979	-0.090	1.000																			
Ca	0.005	0.083	0.034	0.041	0.143	0.028	0.077	0.941	-0.113	1.000																		
Cd	0.215	0.099	0.170	0.133	0.116	0.271	0.012	0.003	0.011	0.018	1.000																	
Ce	0.019	0.535	0.168	0.522	0.709	0.062	-0.135	-0.057	-0.123	-0.003	0.054	1.000																
Co	0.025	0.655	0.131	0.314	0.392	0.023	0.000	-0.130	0.027	0.006	0.035	0.339	1.000															
Cr	-0.007	0.273	0.068	0.101	0.123	0.003	0.032	-0.074	0.048	-0.029	0.047	0.070	0.653	1.000														
Cs	0.111	0.360	0.233	0.338	0.494	0.187	-0.070	0.076	-0.086	0.121	0.124	0.350	0.151	0.044	1.000													
Cu	0.028	0.145	0.056	0.057	0.079	0.026	-0.016	-0.012	-0.014	0.025	0.058	0.041	0.168	0.100	0.052	1.000												
Fe	0.059	0.827	0.192	0.439	0.531	0.061	-0.026	-0.106	-0.004	0.070	0.058	0.426	0.844	0.425	0.253	0.185	1.000											
Ga	0.067	0.969	0.192	0.719	0.783	0.094	-0.097	-0.102	-0.076	0.084	0.102	0.602	0.625	0.246	0.414	0.135	0.819	1.000										
Hg	0.469	0.071	0.378	0.030	0.044	0.693	0.221	-0.042	0.229	-0.031	0.207	0.004	0.079	0.060	0.095	0.028	0.099	0.087	1.000									
In	0.020	0.018	0.511	0.028	0.029	0.088	0.011	0.005	0.010	0.015	0.086	0.006	0.002	-0.003	0.061	0.047	0.074	0.045	0.045	1.000								
K	0.043	0.654	0.157	0.803	0.746	0.090	-0.225	-0.010	-0.223	0.088	0.134	0.591	0.159	0.012	0.406	0.017	0.318	0.682	-0.002	0.018	1.000							
La	0.020	0.554	0.167	0.580	0.731	0.065	-0.138	-0.033	-0.131	0.028	0.066	0.970	0.314	0.075	0.359	0.040	0.400	0.617	-0.003	0.007	0.653	1.000						
Li	0.090	0.603	0.287	0.457	0.667	0.172	-0.054	0.094	-0.072	0.152	0.128	0.530	0.389	0.172	0.553	0.084	0.480	0.625	0.145	0.021	0.523	0.537	1.000					
Mg	0.029	0.600	0.115	0.422	0.409	0.054	-0.081	0.275	-0.135	0.376	0.074	0.233	0.558	0.459	0.285	0.118	0.591	0.573	0.030	0.005	0.388	0.265	0.530	1.000				
Mn	0.048	0.481	0.211	0.287	0.339	0.042	0.201	-0.161	0.235	-0.076	0.070	0.357	0.671	0.298	0.157	0.097	0.594	0.477	0.130	0.127	0.157	0.323	0.375	0.271	1.000			
Mo	0.090	0.239	0.434	0.189	0.303	0.158	0.040	0.050	0.030	0.078	0.255	0.255	0.184	0.070	0.211	0.077	0.262	0.264	0.120	0.504	0.211	0.258	0.285	0.129	0.240	1.000		
Na	0.058	0.786	0.086	0.703	0.565	0.062	-0.200	-0.053	-0.190	0.163	0.070	0.309	0.352	0.108	0.226	0.093	0.541	0.761	0.024	0.014	0.643	0.353	0.392	0.548	0.243	0.128	1.000	
Nb	0.028	0.549	0.102	0.455	0.721	0.059	-0.091	0.015	-0.094	0.119	0.044	0.699	0.327	0.087	0.376	0.088	0.478	0.634	0.001	0.021	0.569	0.695	0.418	0.276	0.276	0.241	0.438	1.000
Ni	-0.005	0.279	0.067	0.107	0.137	0.005	0.014	-0.053	0.025	-0.003	0.049	0.058	0.658	0.936	0.046	0.101	0.420	0.249	0.056	-0.003	0.025	0.067	0.173	0.501	0.278	0.075	0.131	0.085
P	0.064	0.570	0.178	0.411	0.420	0.064	0.197	-0.013	0.201	0.103	0.131	0.358	0.505	0.215	0.234	0.107	0.609	0.577	0.137	0.027	0.320	0.366	0.450	0.448	0.549	0.284	0.398	0.338
Pb	0.579	0.131	0.258	0.084	0.184	0.665	0.196	-0.046	0.203	-0.038	0.266	0.168	0.107	0.040	0.150	0.065	0.141	0.166	0.576	0.080	0.140	0.164	0.195	0.027	0.180	0.200	0.057	0.117
Rb	0.049	0.613	0.196	0.675	0.801	0.108	-0.155	-0.011	-0.153	0.054	0.139	0.672	0.180	0.035	0.547	0.023	0.316	0.668	0.026	0.026	0.903	0.713	0.628	0.324	0.210	0.247	0.489	0.596
S	-0.004	-0.055	-0.011	-0.046	-0.020	-0.005	0.021	0.100	0.000	0.242	0.003	-0.061	-0.051	-0.025	-0.003	-0.005	-0.052	-0.054	-0.011	-0.001	-0.023	-0.052	0.027	0.041	-0.056	0.010	0.017	-0.016
Sb	0.166	0.087	0.722	0.127	0.101	0.208	-0.017	0.015	-0.020	0.029	0.100	0.073	0.030	0.011	0.147	0.026	0.054	0.093	0.382	0.053	0.107	0.079	0.125	0.052	0.046	0.120	0.083	0.059
Sc	0.051	0.837	0.133	0.421	0.489	0.044	-0.038	-0.116	-0.014	0.058	0.052	0.371	0.841	0.433	0.231	0.188	0.938	0.807	0.095	-0.004	0.286	0.354	0.479	0.616	0.554	0.196	0.534	0.396
Se	0.039	0.053	0.126	-0.047	0.060	0.086	0.371	-0.047	0.380	-0.078	0.097	0.090	0.125	0.081	0.021	0.006	0.140	0.074	0.207	-0.011	-0.058	0.075	0.157	-0.072	0.245	0.321	-0.171	0.017
Sn	0.065	0.121	0.091	0.048	0.171	0.030	0.074	-0.007	0.075	0.015	0.045	0.090	0.087	0.040	0.050	0.057	0.139	0.145	0.073	0.093	0.079	0.082	0.100	0.058	0.080	0.098	0.096	0.099
Sr	0.040	0.451	0.067	0.451	0.348	0.056	-0.033	0.409	-0.115	0.580	0.052	0.185	0.182	0.018	0.194	0.059	0.299	0.434	0.009	0.011	0.376	0.227	0.320	0.501	0.095	0.109	0.623	0.260
Te	0.622	0.040	0.390	0.050	0.039	0.928	-0.013	0.010	-0.015	0.018	0.273	0.018	0.007	-0.005	0.143	0.031	0.047	0.050	0.641	0.249	0.043	0.020	0.111	0.029	0.046	0.203	0.036	0.011
Th	0.026	0.494	0.159	0.516	0.699	0.082	-0.189	-0.015	-0.186	0.030	0.077	0.852	0.180	0.015	0.419	0.032	0.299	0.550	0.000	0.008	0.648	0.853	0.504	0.215	0.180	0.225	0.335	0.609
Ti	0.040	0.638	0.035	0.257	0.336	0.020	0.010	-0.145	0.041	0.017	-0.007	0.338	0.706	0.259	0.143	0.161	0.833	0.639	0.070	-0.008	0.129	0.297	0.250	0.380	0.484	0.150	0.414	0.525
Tl	0.075	0.349	0.332	0.377	0.540	0.129	-0.080	-0.023	-0.075	-0.005	0.190	0.526	0.138	0.036	0.449	0.014	0.183	0.400	0.115	0.054	0.522	0.545	0.438	0.129	0.168	0.362	0.162	0.407
U	0.032	0.336	0.184	0.327	0.456	0.073	-0.051	-0.010	-0.048	0.016	0.109	0.491	0.189	0.042	0.300	0.039	0.230	0.362	0.063	0.028	0.365	0.490	0.425	0.138	0.225	0.385	0.165	0.341
V	0.046	0.763	0.159	0.415	0.407	0.048	-0.057	-0.122	-0.032	0.042	0.081	0.315	0.805	0.397	0.185	0.172	0.901	0.730	0.093	-0.004	0.236	0.299	0.417	0.551	0.529	0.264	0.467	0.330
W	0.361	0.171	0.351	0.183	0.218	0.590	-0.035	0.014	-0.038	0.048	0.202	0.125	0.062	0.013	0.226	0.048	0.135	0.190	0.392	0.291	0.179	0.134	0.206	0.112	0.104	0.359	0.171	0.135
Y	0.020	0.676	0.136	0.546	0.725	0.053	-0.130	0.029	-0.137	0.160	0.064	0.767	0.535	0.177	0.360	0.109	0.638	0.720	-0.001	0.001	0.579	0.786	0.500	0.423	0.436	0.249	0.479	0.727
Zn	0.383	0.595	0.348	0.406	0.497	0.446	0.081	-0.072	0.096	0.032	0.305	0.365	0.517	0.264	0.301	0.201	0.609	0.600	0.387	0.158	0.352	0.369	0.519	0.389	0.512	0.374	0.376	0.351

Layer	Ni	P	Pb	Rb	S	Sb	Sc	Se	Sn	Sr	Te	Th	Ti	Tl	U	V	W	Y	Zn
Ni	1.000																		
P	0.206	1.000																	
Pb	0.034	0.212	1.000																
Rb	0.034	0.307	0.189	1.000															
S	-0.020	-0.028	-0.017	-0.025	1.000														
Sb	0.016	0.084	0.199	0.107	-0.004	1.000													
Sc	0.424	0.581	0.114	0.287	-0.052	0.043	1.000												
Se	0.068	0.186	0.226	0.031	0.018	0.025	0.119	1.000											
Sn	0.044	0.131	0.279	0.099	-0.010	0.058	0.125	0.052	1.000										
Sr	0.039	0.296	0.009	0.260	0.225	0.065	0.283	-0.112	0.034	1.000									
Te	-0.002	0.039	0.652	0.051	0.004	0.195	0.013	0.063	0.035	0.042	1.000								
Th	0.005	0.239	0.160	0.756	-0.053	0.089	0.255	0.041	0.079	0.189	0.036	1.000							
Ti	0.250	0.485	0.076	0.107	-0.061	0.018	0.790	0.069	0.096	0.206	-0.002	0.183	1.000						
Tl	0.037	0.246	0.234	0.639	-0.022	0.282	0.176	0.212	0.083	0.103	0.088	0.593	0.041	1.000					
U	0.029	0.298	0.146	0.457	-0.026	0.080	0.221	0.218	0.059	0.133	0.040	0.531	0.135	0.462	1.000				
V	0.378	0.541	0.099	0.237	-0.051	0.064	0.909	0.212	0.081	0.259	0.021	0.216	0.762	0.197	0.236	1.000			
W	0.019	0.110	0.381	0.194	-0.006	0.173	0.098	0.060	0.071	0.108	0.561	0.168	0.060	0.164	0.154	0.094	1.000		
Y	0.189	0.484	0.121	0.593	-0.036	0.061	0.605	0.026	0.088	0.306	0.007	0.626	0.538	0.419	0.387	0.525	0.129	1.000	
Zn	0.265	0.581	0.546	0.383	-0.026	0.163	0.580	0.220	0.176	0.207	0.425	0.287	0.428	0.339	0.304	0.547	0.354	0.468	1.000

Figure A-3. Correlation matrix for the A Horizon soil geochemical data, created via the Band Statistics tool in ArcGIS

A.1.4 C Horizon: Mineralogy

Layer	Quartz	K_fs	Plag	Total_fs	14A_Clays	10A_Clays	Kaolinite	Total_Clays	Gibbsite	Calcite	Dolomite	Aragonite	Total_Carbs	Analcime	Heulandite	Total_Zeolites	Gypsum	Talc	Hornblende	Serpentine	Hematite	Goethite	Pyroxene	Pyrite	Other	Amorphous
Quartz	1.000																									
K_fs	-0.278	1.000																								
Plag	-0.653	0.480	1.000																							
Total_fs	-0.612	0.718	0.955	1.000																						
14A_Clays	-0.341	-0.109	0.134	0.069	1.000																					
10A_Clays	-0.102	-0.267	-0.198	-0.247	0.156	1.000																				
Kaolinite	0.019	-0.268	-0.203	-0.251	-0.091	0.117	1.000																			
Total_Clays	-0.164	-0.369	-0.201	-0.284	0.378	0.704	0.701	1.000																		
Gibbsite	0.070	-0.099	-0.143	-0.147	-0.078	0.002	0.468	0.285	1.000																	
Calcite	-0.301	-0.060	-0.151	-0.140	-0.101	-0.083	-0.177	-0.201	-0.105	1.000																
Dolomite	-0.128	0.045	-0.027	-0.006	0.035	-0.123	-0.160	-0.164	-0.080	0.097	1.000															
Aragonite	-0.051	-0.052	-0.058	-0.063	-0.080	-0.063	-0.039	-0.090	-0.016	0.183	0.006	1.000														
Total_Carbs	-0.311	-0.039	-0.146	-0.129	-0.082	-0.129	-0.219	-0.248	-0.123	0.903	0.489	0.303	1.000													
Analcime	-0.041	0.023	0.014	0.019	0.025	-0.009	0.018	0.016	0.023	0.022	-0.004	-0.006	0.015	1.000												
Heulandite	-0.151	0.122	0.119	0.135	0.025	-0.053	-0.038	-0.047	-0.021	0.016	-0.032	-0.011	-0.001	-0.008	1.000											
Total_Zeolites	-0.157	0.123	0.117	0.135	0.032	-0.053	-0.031	-0.039	-0.013	0.022	-0.031	-0.013	0.004	0.314	0.947	1.000										
Gypsum	-0.096	-0.015	-0.058	-0.051	-0.044	-0.064	-0.057	-0.090	-0.032	0.107	0.018	-0.009	0.096	-0.006	0.010	0.007	1.000									
Talc	-0.099	-0.038	0.078	0.049	0.121	-0.009	0.050	0.070	0.003	-0.043	-0.032	-0.005	-0.050	-0.005	0.008	0.006	-0.011	1.000								
Hornblende	-0.242	0.138	0.397	0.362	0.041	-0.087	0.023	-0.020	0.016	-0.117	-0.042	-0.025	-0.119	0.014	-0.005	0.000	-0.042	0.272	1.000							
Serpentine	-0.058	-0.029	0.017	0.004	0.044	-0.004	0.073	0.061	0.027	-0.022	-0.014	-0.003	-0.024	0.001	-0.005	-0.005	-0.007	0.406	0.126	1.000						
Hematite	-0.096	0.062	0.015	0.033	0.008	0.006	0.319	0.218	0.279	-0.058	-0.088	-0.022	-0.087	-0.006	0.063	0.058	-0.023	0.054	0.023	0.048	1.000					
Goethite	0.085	-0.142	-0.182	-0.192	-0.061	0.135	0.298	0.254	0.109	-0.072	-0.075	-0.017	-0.093	0.011	-0.017	-0.013	-0.022	-0.010	-0.043	-0.004	0.038	1.000				
Pyroxene	-0.355	-0.050	0.403	0.303	0.145	-0.099	0.069	0.040	0.025	-0.045	-0.058	-0.007	-0.062	0.063	0.077	0.093	-0.029	0.028	0.079	0.019	0.122	-0.039	1.000			
Pyrite	-0.035	0.017	0.038	0.036	0.014	0.016	0.008	0.019	0.054	-0.012	-0.022	-0.005	-0.019	-0.004	0.005	0.003	-0.008	-0.004	-0.001	-0.001	0.016	-0.001	-0.009	1.000		
Other	-0.080	-0.009	-0.005	-0.007	-0.043	0.000	0.150	0.085	0.194	0.010	-0.025	0.011	0.000	0.074	0.090	0.109	0.008	0.059	0.046	0.162	0.064	0.057	-0.002	0.092	1.000	
Amorphous	-0.783	-0.001	0.369	0.293	0.430	0.171	-0.130	0.161	-0.181	0.212	0.023	0.012	0.188	0.008	0.123	0.119	0.022	0.066	0.038	0.033	-0.004	-0.077	0.237	0.021	0.004	1.000
Ag	0.007	-0.002	-0.025	-0.020	-0.003	0.090	0.060	0.090	0.035	-0.042	-0.033	-0.007	-0.049	-0.006	-0.003	-0.004	-0.014	0.002	-0.010	0.012	0.020	0.074	-0.008	-0.001	0.062	-0.020
Al	-0.682	0.175	0.548	0.493	0.364	0.370	0.432	0.625	0.215	-0.255	-0.140	-0.137	-0.290	0.030	0.073	0.079	-0.103	0.112	0.290	0.065	0.229	0.097	0.275	0.057	0.123	0.494
As	-0.176	-0.083	-0.018	-0.043	0.200	0.343	0.005	0.269	-0.060	0.022	0.045	-0.013	0.035	0.006	-0.009	-0.007	-0.018	0.044	-0.045	0.006	0.098	0.174	-0.064	-0.012	-0.007	0.220
Ba	-0.577	0.438	0.493	0.539	0.236	0.140	-0.162	0.055	-0.124	-0.022	-0.033	-0.085	-0.044	0.048	0.148	0.156	-0.032	0.009	0.108	0.004	0.012	-0.080	0.055	0.030	0.052	0.512
Be	-0.510	0.272	0.271	0.306	0.218	0.443	0.130	0.415	-0.012	-0.037	-0.112	-0.090	-0.089	0.014	0.124	0.122	-0.066	-0.019	0.047	0.002	0.105	0.113	0.053	0.018	0.083	0.439
Bi	-0.206	0.019	-0.010	-0.001	0.157	0.364	0.146	0.360	0.066	-0.047	-0.084	-0.025	-0.077	-0.012	0.044	0.038	-0.045	-0.002	-0.040	-0.003	0.180	0.112	-0.052	0.006	0.023	0.247
C_total	-0.336	-0.052	-0.033	-0.044	0.011	0.001	-0.195	-0.126	-0.117	0.620	0.267	0.303	0.672	0.012	0.015	0.018	0.053	-0.018	-0.026	-0.006	-0.060	-0.096	-0.004	-0.013	0.000	0.302
C_inorganic	-0.310	-0.037	-0.144	-0.127	-0.079	-0.131	-0.221	-0.250	-0.123	0.891	0.516	0.298	0.999	0.015	-0.002	0.003	0.094	-0.050	-0.118	-0.024	-0.089	-0.094	-0.063	-0.019	-0.001	0.186
C_organic	-0.189	-0.036	0.079	0.050	0.083	0.113	-0.076	0.042	-0.054	0.084	-0.066	0.156	0.067	0.003	0.021	0.021	-0.007	0.018	0.066	0.012	-0.005	-0.050	0.049	-0.001	0.004	0.253
Ca	-0.464	0.013	0.017	0.018	-0.051	-0.154	-0.244	-0.268	-0.147	0.931	0.299	0.284	0.943	0.023	0.042	0.047	0.241	-0.025	-0.033	-0.018	-0.071	-0.113	0.041	-0.010	0.015	0.309
Cd	-0.069	0.040	0.029	0.036	0.029	0.033	-0.038	0.004	-0.029	-0.005	-0.006	-0.010	-0.008	-0.006	0.001	-0.001	0.029	0.007	0.017	0.021	-0.015	-0.015	-0.026	-0.001	-0.001	0.103
Ce	-0.302	0.196	0.105	0.149	0.167	0.447	0.221	0.460	0.166	-0.123	-0.145	-0.101	-0.177	0.026	0.076	0.080	-0.093	-0.040	0.022	-0.017	0.142	0.235	0.000	0.028	0.131	0.240
Co	-0.485	-0.131	0.338	0.224	0.461	0.287	0.206	0.462	0.027	-0.173	-0.053	-0.081	-0.178	0.022	0.049	0.053	-0.072	0.367	0.296	0.241	0.247	0.075	0.446	0.024	0.081	0.440
Cr	-0.175	-0.107	0.074	0.022	0.279	0.138	0.136	0.267	0.053	-0.116	-0.048	-0.026	-0.120	0.006	0.005	0.007	-0.039	0.661	0.248	0.464	0.200	0.022	0.153	0.016	0.075	0.165
Cs	-0.298	0.102	0.027	0.056	0.190	0.413	0.015	0.313	-0.051	-0.025	-0.049	-0.033	-0.046	-0.001	0.105	0.099	-0.017	-0.018	-0.056	-0.022	0.084	0.050	-0.027	0.010	0.040	0.369
Cu	-0.384	-0.028	0.284	0.216	0.281	0.162	0.191	0.318	0.067	-0.094	-0.054	-0.049	-0.108	0.016	0.052	0.055	-0.038	0.170	0.224	0.075	0.227	0.042	0.257	0.035	0.074	0.311
Fe	-0.537	-0.079	0.397	0.288	0.415	0.371	0.437	0.647	0.185	-0.248	-0.135	-0.110	-0.279	0.026	0.044	0.050	-0.097	0.210	0.328	0.128	0.338	0.248	0.446	0.032	0.110	0.393
Ga	-0.618	0.166	0.456	0.418	0.353	0.441	0.440	0.668	0.230	-0.259	-0.154	-0.143	-0.301	0.023	0.084	0.087	-0.102	0.063	0.217	0.042	0.236	0.132	0.255	0.038	0.128	0.451
Hg	-0.111	-0.094	0.071	0.024	0.207	0.205	0.186	0.313	0.128	-0.139	-0.037	0.007	-0.131	-0.009	-0.034	-0.035	-0.061	0.046	0.077	0.020	0.077	0.099	0.054	0.023	0.067	0.071
In	-0.294	-0.013	0.155	0.118	0.205	0.267	0.245	0.387	0.105	-0.092	-0.105	-0.068	-0.130	0.002	0.036	0.035	-0.055	0.053	0.127	0.024	0.260	0.108	0.130	0.013	0.050	0.246
K	-0.529	0.726	0.457	0.607	0.122	0.257	-0.259	0.017	-0.161	-0.047	0.070	-0.108	-0.027	0.024	0.109	0.111	-0.025	-0.038	0.089	-0.032	0.031	-0.126	-0.063	0.034	0.004	0.361
La	-0.359	0.269	0.158	0.216	0.178	0.436	0.126	0.395	0.094	-0.090	-0.113	-0.096	-0.136	0.033	0.091	0.097	-0.081	-0.042	-0.003	-0.021	0.118	0.115	-0.011	0.023	0.120	0.300
Li	-0.374	-0.026	0.025	0.011	0.311	0.605	0.064	0.497	-0.036	0.003	0.009	0.034	0.011	0.020	0.035	0.039	0.000	0.004	-0.057	-0.011	0.037	0.098	-0.040	0.024	0.029	0.409
Mg	-0.590	0.102	0.351	0.313	0.337	0.014	-0.169	0.013	-0.117	0.115	0.690	0.005	0.378	0.041	0.049	0.060	0.028	0.317	0.265	0.238	0.008	-0.132	0.233	0.015	0.088	0.448
Mn	-0.442	-0.017	0.353	0.275	0.394	0.219	-0.009	0.257	-0.071	-0.120	0.042	-0.069	-0.094	-0.002	0.058	0.054	-0.075	0.128	0.188	0.069	0.112	0.032	0.282	0.007	-0.002	0.430
Mo	-0.109	-0.045	-0.033	-0.041	0.056	0.240	0.096	0.220	0.039	-0.005	0.087	-0.017	0.029	0.005	0.013	0.014	0.008	-0.005	-0.008	0.010	0.069	0.132	-0.025	-0.010	0.053	0.090

Na	-0.694	0.542	0.947	0.934	0.153	-0.134	-0.272	-0.204	-0.176	-0.100	-0.005	0.010	-0.084	0.049	0.123	0.133	-0.031	0.070	0.371	0.008	-0.010	-0.199	0.269	0.058	0.004	0.430
Nb	-0.457	0.293	0.284	0.324	0.155	0.222	0.249	0.346	0.141	-0.042	-0.177	-0.086	-0.120	0.005	0.157	0.151	-0.038	-0.007	0.084	0.000	0.216	0.092	0.196	0.018	0.084	0.327
Ni	-0.205	-0.096	0.091	0.040	0.290	0.105	0.126	0.245	0.047	-0.093	-0.015	-0.031	-0.089	0.000	0.004	0.003	-0.032	0.635	0.238	0.576	0.196	0.019	0.150	0.023	0.098	0.192
P	-0.467	0.081	0.359	0.312	0.224	0.198	-0.056	0.154	-0.049	-0.005	0.021	-0.003	0.004	0.035	0.067	0.075	-0.029	0.061	0.159	0.019	0.060	0.119	0.253	0.007	0.121	0.414
Pb	-0.105	0.115	-0.003	0.036	0.085	0.335	0.109	0.294	0.060	-0.121	-0.110	-0.048	-0.153	-0.010	0.027	0.023	-0.065	-0.030	0.006	-0.013	0.091	0.121	-0.079	0.002	0.055	0.101
Rb	-0.435	0.521	0.226	0.355	0.172	0.493	-0.124	0.259	-0.109	-0.053	-0.027	-0.106	-0.071	0.008	0.090	0.088	-0.040	-0.048	-0.013	-0.033	0.051	-0.013	-0.118	0.025	0.006	0.359
S	-0.120	-0.014	-0.058	-0.050	-0.038	-0.056	-0.068	-0.090	-0.038	0.135	0.026	0.007	0.125	-0.003	0.016	0.015	0.990	-0.015	-0.050	-0.008	-0.028	-0.026	-0.028	-0.009	0.016	0.049
Sb	-0.291	0.060	0.123	0.118	0.169	0.236	-0.069	0.148	-0.071	0.035	0.005	-0.025	0.028	-0.008	0.019	0.015	-0.007	0.036	-0.016	0.015	0.045	0.048	-0.042	0.000	0.002	0.341
Sc	-0.524	-0.148	0.368	0.242	0.423	0.369	0.489	0.684	0.223	-0.250	-0.118	-0.096	-0.271	0.028	0.027	0.034	-0.097	0.186	0.357	0.107	0.248	0.158	0.440	0.040	0.117	0.392
Se	0.027	-0.245	-0.256	-0.286	0.150	0.319	0.316	0.445	0.171	-0.038	-0.096	-0.005	-0.072	-0.001	-0.037	-0.035	0.090	0.008	-0.056	0.020	0.078	0.230	-0.044	-0.018	0.103	0.007
Sn	-0.328	0.058	0.122	0.116	0.209	0.472	0.290	0.535	0.165	-0.122	-0.190	-0.068	-0.190	0.001	0.077	0.074	-0.076	-0.014	0.051	0.002	0.194	0.132	0.064	0.003	0.056	0.281
Sr	-0.537	0.251	0.419	0.417	-0.019	-0.162	-0.202	-0.234	-0.132	0.371	0.045	0.389	0.386	0.041	0.108	0.116	0.392	0.008	0.120	-0.010	-0.019	-0.126	0.173	0.010	0.061	0.316
Te	-0.010	0.012	0.012	0.014	0.005	0.003	0.035	0.027	0.054	-0.022	-0.024	-0.005	-0.029	-0.005	0.026	0.023	-0.007	0.048	0.034	0.002	0.110	0.066	-0.008	0.010	0.021	-0.007
Th	-0.255	0.268	0.042	0.124	0.093	0.434	0.251	0.448	0.207	-0.106	-0.159	-0.092	-0.167	0.006	0.085	0.083	-0.084	-0.060	-0.040	-0.022	0.146	0.148	-0.110	0.030	0.109	0.197
Ti	-0.451	-0.060	0.431	0.321	0.290	0.192	0.421	0.491	0.232	-0.234	-0.219	-0.107	-0.301	0.031	0.067	0.074	-0.094	0.113	0.293	0.053	0.288	0.069	0.548	0.031	0.101	0.298
Tl	-0.345	0.249	0.048	0.122	0.256	0.582	-0.037	0.397	-0.069	-0.061	0.052	-0.118	-0.047	-0.011	0.043	0.037	-0.061	-0.053	-0.083	-0.026	0.000	0.050	-0.146	0.000	0.020	0.356
U	-0.232	0.063	-0.011	0.013	0.109	0.421	0.186	0.403	0.098	-0.030	-0.032	0.026	-0.034	-0.002	0.038	0.036	-0.005	-0.038	-0.038	-0.003	0.051	0.154	-0.089	0.002	0.114	0.208
V	-0.494	-0.184	0.331	0.200	0.466	0.362	0.344	0.599	0.137	-0.216	-0.075	-0.096	-0.226	0.022	0.018	0.024	-0.056	0.168	0.266	0.089	0.201	0.169	0.446	0.021	0.089	0.420
W	-0.226	0.124	0.201	0.202	0.051	0.067	-0.015	0.046	-0.020	0.015	-0.058	-0.018	-0.014	0.022	0.025	0.030	-0.022	0.017	0.119	-0.004	0.058	0.017	0.010	0.008	0.002	0.188
Y	-0.521	0.180	0.287	0.289	0.281	0.317	0.038	0.305	-0.043	0.008	-0.065	-0.072	-0.030	-0.004	0.097	0.090	-0.057	0.028	0.115	0.010	0.108	0.098	0.188	0.020	0.054	0.497
Zn	-0.596	0.014	0.388	0.312	0.430	0.461	0.114	0.489	-0.007	-0.125	-0.075	-0.096	-0.149	0.008	0.053	0.052	-0.054	0.134	0.228	0.082	0.140	0.037	0.256	0.030	0.063	0.556

Figure A-4. Correlation matrix for the C Horizon soil mineralogy data, created via the Band Statistics tool in ArcGIS

A.1.5 C Horizon: Geochemical

Layer	Ag	Al	As	Ba	Be	Bi	C_total	C_inorgar	C_organic	Ca	Cd	Ce	Co	Cr	Cs	Cu	Fe	Ga	Hg	In	K	La	Li	Mg	Mn	Mo	Na
Ag	1.000																										
Al	0.064	1.000																									
As	0.091	0.208	1.000																								
Ba	0.021	0.503	0.166	1.000																							
Be	0.173	0.626	0.271	0.438	1.000																						
Bi	0.216	0.349	0.421	0.189	0.497	1.000																					
C_total	-0.027	-0.157	0.054	-0.024	-0.009	-0.003	1.000																				
C_inorganic	-0.050	-0.290	0.036	-0.044	-0.092	-0.079	0.670	1.000																			
C_organic	0.006	0.035	0.044	0.005	0.066	0.062	0.783	0.063	1.000																		
Ca	-0.052	-0.181	0.028	0.062	-0.024	-0.063	0.663	0.937	0.103	1.000																	
Cd	0.018	0.053	0.085	0.088	0.045	0.073	0.032	-0.008	0.050	0.007	1.000																
Ce	0.056	0.538	0.215	0.351	0.662	0.366	-0.136	-0.179	-0.031	-0.145	0.024	1.000															
Co	0.030	0.612	0.202	0.218	0.335	0.149	-0.059	-0.176	0.071	-0.101	0.030	0.312	1.000														
Cr	0.012	0.267	0.109	0.051	0.085	0.052	-0.026	-0.120	0.066	-0.098	0.031	0.084	0.667	1.000													
Cs	0.061	0.336	0.324	0.265	0.494	0.434	-0.002	-0.046	0.037	-0.023	0.070	0.344	0.165	0.040	1.000												
Cu	0.215	0.478	0.161	0.175	0.219	0.253	-0.037	-0.108	0.042	-0.035	0.056	0.164	0.517	0.242	0.172	1.000											
Fe	0.055	0.817	0.267	0.250	0.445	0.277	-0.119	-0.278	0.077	-0.187	0.018	0.441	0.806	0.426	0.219	0.554	1.000										
Ga	0.069	0.947	0.228	0.453	0.702	0.399	-0.151	-0.301	0.052	-0.210	0.041	0.637	0.571	0.226	0.411	0.420	0.790	1.000									
Hg	0.061	0.270	0.268	0.001	0.147	0.167	0.111	-0.130	0.260	-0.129	0.082	0.119	0.239	0.150	0.136	0.212	0.330	0.286	1.000								
In	0.091	0.444	0.559	0.154	0.369	0.416	-0.030	-0.132	0.070	-0.084	0.040	0.345	0.326	0.137	0.259	0.388	0.499	0.495	0.261	1.000							
K	0.022	0.474	0.181	0.666	0.592	0.240	-0.025	-0.024	-0.011	0.032	0.087	0.459	0.119	-0.012	0.401	0.129	0.171	0.472	-0.005	0.163	1.000						
La	0.057	0.529	0.218	0.445	0.669	0.355	-0.124	-0.137	-0.051	-0.094	0.041	0.919	0.282	0.090	0.372	0.149	0.384	0.620	0.083	0.309	0.562	1.000					
Li	0.033	0.474	0.467	0.281	0.563	0.420	0.052	0.011	0.062	0.025	0.071	0.461	0.318	0.129	0.571	0.226	0.374	0.516	0.245	0.293	0.420	0.491	1.000				
Mg	-0.032	0.292	0.152	0.283	0.139	0.029	0.273	0.395	0.040	0.350	0.047	0.019	0.446	0.378	0.109	0.272	0.306	0.222	0.083	0.091	0.289	0.077	0.272	1.000			
Mn	0.007	0.450	0.254	0.291	0.311	0.178	0.061	-0.091	0.161	-0.035	0.080	0.282	0.615	0.249	0.180	0.348	0.558	0.433	0.263	0.321	0.207	0.260	0.310	0.332	1.000		
Mo	0.306	0.167	0.496	0.056	0.189	0.242	0.048	0.032	0.039	0.011	0.146	0.170	0.137	0.051	0.223	0.201	0.213	0.201	0.187	0.393	0.124	0.173	0.233	0.093	0.132	1.000	
Na	-0.030	0.552	0.029	0.581	0.336	0.044	0.005	-0.083	0.077	0.073	0.053	0.156	0.282	0.068	0.089	0.256	0.333	0.460	0.049	0.144	0.582	0.224	0.126	0.384	0.326	-0.015	1.000
Nb	0.084	0.575	0.106	0.320	0.689	0.345	-0.081	-0.124	-0.006	-0.034	0.011	0.646	0.303	0.088	0.338	0.225	0.484	0.671	0.120	0.382	0.415	0.608	0.346	0.061	0.253	0.147	0.305
Ni	0.014	0.267	0.109	0.067	0.090	0.041	-0.020	-0.087	0.047	-0.067	0.050	0.072	0.681	0.937	0.036	0.256	0.413	0.215	0.153	0.129	0.001	0.080	0.131	0.439	0.261	0.061	0.087
P	0.051	0.402	0.190	0.331	0.319	0.167	0.146	0.005	0.198	0.088	0.092	0.263	0.372	0.135	0.228	0.276	0.444	0.389	0.191	0.223	0.301	0.294	0.280	0.317	0.463	0.151	0.366
Pb	0.149	0.285	0.211	0.168	0.369	0.336	-0.018	-0.154	0.106	-0.149	0.084	0.421	0.144	0.051	0.261	0.172	0.232	0.347	0.250	0.215	0.285	0.394	0.306	-0.048	0.199	0.229	0.038
Rb	0.049	0.504	0.269	0.543	0.728	0.422	-0.034	-0.071	0.015	-0.035	0.083	0.596	0.159	0.018	0.580	0.126	0.231	0.571	0.057	0.254	0.866	0.669	0.609	0.167	0.226	0.184	0.354
S	-0.005	-0.102	0.001	-0.014	-0.055	-0.031	0.086	0.123	0.012	0.272	0.028	-0.088	-0.073	-0.042	0.001	-0.034	-0.100	-0.099	-0.051	-0.053	-0.013	-0.073	0.024	0.047	-0.075	0.023	-0.024
Sb	0.172	0.239	0.673	0.309	0.282	0.391	0.037	0.027	0.027	0.060	0.159	0.190	0.156	0.086	0.488	0.207	0.177	0.248	0.291	0.269	0.274	0.227	0.398	0.173	0.208	0.411	0.173
Sc	0.040	0.822	0.176	0.219	0.415	0.217	-0.119	-0.271	0.070	-0.187	0.015	0.382	0.774	0.388	0.198	0.544	0.927	0.784	0.313	0.429	0.124	0.328	0.348	0.318	0.500	0.155	0.307
Se	0.145	0.173	0.259	-0.049	0.119	0.250	0.068	-0.074	0.153	-0.081	0.126	0.155	0.112	0.104	0.152	0.123	0.242	0.221	0.286	0.154	-0.124	0.103	0.229	-0.075	0.066	0.356	-0.246
Sn	0.066	0.570	0.380	0.198	0.651	0.486	-0.015	-0.193	0.141	-0.144	0.049	0.591	0.289	0.097	0.434	0.266	0.514	0.686	0.321	0.670	0.334	0.555	0.503	0.006	0.312	0.311	0.146
Sr	-0.030	0.137	0.039	0.322	0.099	-0.006	0.315	0.381	0.104	0.540	0.028	-0.002	0.046	-0.040	0.046	0.086	0.029	0.079	-0.047	-0.006	0.242	0.063	0.143	0.291	0.076	-0.007	0.470
Te	0.209	0.041	0.024	-0.025	0.032	0.196	-0.027	-0.030	-0.012	-0.020	0.010	0.034	0.058	0.004	0.034	0.643	0.075	0.045	0.014	0.212	0.003	0.015	0.006	0.001	0.023	0.069	0.001
Th	0.082	0.518	0.208	0.330	0.643	0.477	-0.172	-0.169	-0.088	-0.143	0.038	0.786	0.132	0.022	0.438	0.115	0.306	0.614	0.102	0.296	0.509	0.804	0.487	-0.039	0.121	0.179	0.125
Ti	0.020	0.702	0.046	0.173	0.314	0.149	-0.163	-0.303	0.037	-0.186	-0.009	0.343	0.661	0.255	0.108	0.494	0.852	0.682	0.250	0.396	0.053	0.295	0.190	0.159	0.438	0.090	0.331
Tl	0.136	0.462	0.401	0.429	0.656	0.455	-0.013	-0.045	0.020	-0.058	0.141	0.584	0.222	0.053	0.552	0.148	0.276	0.533	0.154	0.276	0.669	0.633	0.610	0.159	0.282	0.447	0.154
U	0.189	0.391	0.333	0.246	0.487	0.419	-0.011	-0.035	0.016	-0.021	0.086	0.484	0.151	0.034	0.410	0.178	0.264	0.450	0.183	0.238	0.339	0.495	0.508	0.068	0.152	0.485	0.062
V	0.145	0.713	0.265	0.249	0.317	0.236	-0.108	-0.224	0.045	-0.143	0.067	0.296	0.739	0.360	0.197	0.552	0.865	0.671	0.312	0.377	0.092	0.263	0.343	0.330	0.515	0.320	0.270
W	0.008	0.214	0.288	0.213	0.253	0.322	0.014	-0.015	0.032	0.039	0.041	0.157	0.090	0.016	0.189	0.132	0.157	0.218	0.070	0.368	0.203	0.169	0.182	0.077	0.142	0.209	0.232
Y	0.035	0.531	0.190	0.380	0.635	0.267	-0.020	-0.032	0.002	0.048	0.035	0.692	0.472	0.167	0.337	0.290	0.528	0.576	0.088	0.347	0.455	0.736	0.414	0.224	0.409	0.180	0.313
Zn	0.080	0.708	0.382	0.422	0.544	0.366	0.045	-0.149	0.186	-0.058	0.167	0.461	0.627	0.301	0.385	0.504	0.728	0.692	0.349	0.507	0.402	0.457	0.545	0.351	0.591	0.293	0.404

Layer	Nb	Ni	P	Pb	Rb	S	Sb	Sc	Se	Sn	Sr	Te	Th	Ti	Tl	U	V	W	Y	Zn
Nb	1.000																			
Ni	0.079	1.000																		
P	0.265	0.139	1.000																	
Pb	0.284	0.021	0.153	1.000																
Rb	0.508	0.014	0.259	0.399	1.000															
S	-0.034	-0.034	-0.015	-0.056	-0.026	1.000														
Sb	0.167	0.097	0.186	0.262	0.304	0.012	1.000													
Sc	0.419	0.374	0.392	0.189	0.187	-0.101	0.131	1.000												
Se	0.115	0.074	0.051	0.211	0.039	0.107	0.216	0.209	1.000											
Sn	0.614	0.072	0.258	0.451	0.528	-0.071	0.277	0.460	0.246	1.000										
Sr	0.100	-0.023	0.215	-0.061	0.106	0.428	0.112	0.011	-0.122	-0.036	1.000									
Te	0.041	0.012	0.017	0.091	0.021	-0.005	0.029	0.035	0.025	0.079	-0.007	1.000								
Th	0.585	0.004	0.156	0.443	0.704	-0.077	0.226	0.259	0.179	0.598	-0.022	0.072	1.000							
Ti	0.522	0.237	0.373	0.128	0.070	-0.102	0.055	0.822	0.135	0.429	0.043	0.075	0.213	1.000						
Tl	0.406	0.050	0.244	0.468	0.834	-0.045	0.385	0.236	0.241	0.523	-0.014	0.012	0.658	0.068	1.000					
U	0.344	0.027	0.230	0.372	0.500	0.018	0.315	0.232	0.368	0.453	0.077	0.039	0.598	0.138	0.626	1.000				
V	0.327	0.341	0.390	0.198	0.154	-0.051	0.249	0.866	0.378	0.371	0.037	0.044	0.195	0.757	0.298	0.303	1.000			
W	0.197	0.017	0.137	0.093	0.228	-0.014	0.236	0.121	0.025	0.312	0.115	0.033	0.205	0.103	0.167	0.325	0.102	1.000		
Y	0.592	0.184	0.410	0.255	0.519	-0.050	0.209	0.479	0.030	0.501	0.106	0.021	0.489	0.447	0.503	0.350	0.417	0.193	1.000	
Zn	0.471	0.305	0.508	0.417	0.462	-0.044	0.365	0.682	0.218	0.567	0.111	0.081	0.347	0.575	0.513	0.367	0.669	0.238	0.563	1

Figure A-5. Correlation matrix for the C Horizon soil geochemical data, created via the Band Statistics tool in ArcGIS

B Hyperspectral Alteration Strength Index Appendix

B.1 Modal Percentages

B.1.1 Telaga Bodas Samples

Table B-1. Modal percentages from hyperspectral data for the Telaga Bodas K-33_0191_00 core sample.

Depth from	Depth to	MINERAL ABUNDANCES											
K-33_0191_00		unclassified	alunogen	aspectral	carbonate	chlorite	epidote	iron oxide	gypsum	kaolinite	magnetite	prehnite	white mica
1274.9	1275	1.81	0.00	5.36	0.84	35.94	0.16	0.00	14.68	0.03	0.88	0.03	40.27
1275	1275.1	0.00	0.00	0.00	0.02	42.80	0.54	0.00	13.20	0.00	0.00	0.06	43.38
1275.1	1275.2	0.00	0.00	0.00	0.00	41.65	1.39	0.00	14.07	0.00	0.00	0.03	42.86
1275.2	1275.3	0.24	0.00	0.07	0.04	44.56	0.26	0.11	9.89	0.00	0.00	0.04	44.79
1275.3	1275.4	0.00	0.00	0.00	0.05	42.50	1.44	0.00	12.12	0.00	0.00	0.05	43.85
1275.4	1275.5	0.00	0.00	0.00	0.10	40.01	1.62	0.00	16.29	0.00	0.00	0.06	41.92
1275.5	1275.6	9.91	0.18	0.16	0.21	33.47	1.44	0.00	14.96	0.02	0.65	0.01	38.99
1275.6	1275.7	2.55	0.81	0.02	0.04	36.32	1.44	0.00	22.17	0.01	0.16	0.06	36.41
1275.7	1275.8	10.12	1.31	0.67	0.06	29.44	0.20	0.00	26.30	0.08	2.19	0.06	29.56
1275.8	1275.9	2.11	0.01	0.45	0.11	40.49	0.36	0.00	16.77	0.00	0.02	0.04	39.63
1275.9	1276	1.15	0.00	0.12	0.25	38.04	1.54	0.00	19.93	0.00	0.00	0.08	38.88
1276	1276.1	0.00	0.00	0.00	0.11	35.09	0.37	0.22	28.40	0.00	0.00	0.12	35.70
	Average:	2.32	0.19	0.57	0.15	38.36	0.90	0.03	17.40	0.01	0.33	0.05	39.69

Table B-2. Modal percentages from hyperspectral data for the Telaga Bodas K-33_0191_03 core sample.

Depth from	**Depth to**	**MINERAL ABUNDANCES**							
K-33_0191_03		unclassified	aspectral	carbonate	chlorite	epidote	gypsum	prehnite	white mica
1272.9	1273	0.12	0.01	1.52	54.07	0.77	0.64	0.11	42.76
1273	1273.1	0.00	0.08	2.19	46.25	1.60	0.04	0.10	49.73
1273.1	1273.2	0.00	0.11	0.09	48.76	0.77	0.10	0.07	50.09
1273.2	1273.3	0.08	0.39	0.07	48.81	0.92	2.11	0.04	47.58
1273.3	1273.4	0.00	0.10	0.02	44.16	0.37	10.80	0.09	44.45
1273.4	1273.5	0.04	0.00	0.08	48.02	0.78	1.78	0.11	49.19
1273.5	1273.6	0.00	0.00	0.01	48.02	0.42	3.41	0.29	47.85
1273.6	1273.7	0.00	0.00	0.21	47.43	1.70	1.58	0.17	48.92
1273.7	1273.8	0.00	0.00	0.02	49.05	0.53	0.99	0.07	49.33
1273.8	1273.9	0.00	0.02	0.06	49.50	0.28	0.03	0.05	50.06
1273.9	1274	0.00	0.01	0.03	49.27	0.25	0.61	0.08	49.76
1274	1274.1	0.72	0.02	0.09	47.79	0.73	2.40	0.05	48.20
	Average:	0.08	0.06	0.37	48.43	0.76	2.04	0.10	48.16

Table B-3. Modal percentages from hyperspectral data for the Telaga Bodas K-33_0192_1276 core sample.

Depth from	**Depth to**	**MINERAL ABUNDANCES**									
K-33_0192_1276		unclassified	aspectral	beidellite	carbonate	chlorite	epidote	iron oxide	gypsum	kaolinite	magnetite
1275.9	1276	1.15	0.12	0.00	0.25	38.04	1.54	0.00	19.93	0.00	0.00
1276	1276.1	0.00	0.00	0.00	0.11	35.09	0.37	0.22	28.40	0.00	0.00
1276.1	1276.2	1.15	0.82	7.00	0.01	54.25	0.02	0.02	0.02	0.00	0.28
1276.2	1276.3	0.18	0.02	2.39	0.02	56.57	0.03	0.03	0.00	0.00	0.03
1276.3	1276.4	1.04	0.55	14.84	0.00	44.79	0.00	0.30	0.00	0.00	0.77

1276.4	1276.5	5.99	6.67	8.45	0.00	24.11	0.00	0.04	0.00	0.01	0.37
1276.5	1276.6	0.15	0.10	7.46	1.42	57.43	1.40	0.00	30.28	0.00	0.01
1276.6	1276.7	0.08	0.12	24.67	0.59	55.77	0.81	0.00	17.45	0.00	0.18
1276.7	1276.8	3.99	7.28	38.53	0.12	41.69	0.43	0.00	2.52	0.26	0.31
1276.8	1276.9	0.34	1.40	43.24	0.54	51.31	0.85	0.00	2.01	0.00	0.02
1276.9	1277	0.94	2.98	47.33	0.83	43.46	1.18	0.00	0.19	0.00	2.46
	Average:	1.36	1.82	17.63	0.35	45.68	0.60	0.05	9.16	0.02	0.40

montmorillonite	prehnite	white mica	zeolite
0.01	0.08	38.88	0.00
0.00	0.12	35.70	0.00
0.25	0.04	36.14	0.00
0.27	0.05	40.40	0.01
2.17	0.06	35.49	0.00
0.13	0.01	54.22	0.00
0.06	0.24	1.43	0.01
0.03	0.15	0.11	0.04
0.07	0.11	4.70	0.00
0.02	0.21	0.05	0.00
0.05	0.23	0.35	0.00
0.28	0.12	22.50	0.01

Table B-4. Modal percentages from hyperspectral data for the Telaga Bodas K-33_0192_1277.75 core sample.

Depth from	Depth to	MINERAL ABUNDANCES										
K-33_0192_1277.75		unclassified	aspectral	beidellite	carbonate	chlorite	epidote	kaolinite	magnetite	montmorillonite	prehnite	white mica
1277.7	1277.8	5.93	2.02	1.19	0.04	56.34	0.12	0.02	0.87	0.03	0.08	33.36

Table B-5. Modal percentages from hyperspectral data for the Telaga Bodas K-33_0364_1752 core sample.

Depth from	Depth to	MINERAL ABUNDANCES								
K-33_0364_1752		unclassified	aspectral	carbonate	chlorite	epidote	gypsum	magnetite	prehnite	white mica
1751.9	1752	0.10	0.00	0.00	57.25	42.47	0.06	0.04	0.01	0.06
1752	1752.1	0.18	0.55	0.00	61.20	37.59	0.07	0.00	0.40	0.00
1752.1	1752.2	0.47	4.80	0.15	58.61	34.25	0.01	0.01	1.71	0.01
1752.2	1752.3	0.04	0.00	0.00	68.82	28.68	0.00	0.00	2.45	0.00
1752.3	1752.4	0.43	1.26	0.05	71.92	18.39	0.00	0.07	7.88	0.00
1752.4	1752.5	0.23	1.80	0.01	70.24	12.03	0.01	0.02	15.68	0.00
1752.5	1752.6	0.11	0.25	0.00	89.25	6.51	0.00	0.03	3.85	0.00
1752.6	1752.7	0.16	0.00	0.00	94.86	3.49	0.00	0.25	1.24	0.00
1752.7	1752.8	0.08	0.73	0.36	72.46	10.30	0.00	0.06	16.02	0.00
1752.8	1752.9	0.16	0.42	0.01	58.93	24.17	0.00	0.00	16.31	0.00
1752.9	1753	0.59	0.00	0.00	54.70	26.22	0.00	0.00	18.49	0.00
1753	1753.1	0.61	0.03	0.01	52.42	35.75	0.03	0.00	11.13	0.00
	Average:	0.26	0.82	0.05	67.55	23.32	0.01	0.04	7.93	0.01

Table B-6. Modal percentages from hyperspectral data for the Telaga Bodas K-33_0364_1753 core sample.

Depth from	Depth to	MINERAL ABUNDANCES								
K-33_0364_1753		unclassified	aspectral	chlorite	epidote	gypsum	magnetite	montmorillonite	prehnite	wairakite
1752.9	1753	0.59	0.00	54.70	26.22	0.00	0.00	0.00	18.49	0.00
1753	1753.1	0.61	0.03	52.42	35.75	0.03	0.00	0.00	11.13	0.00
1753.1	1753.2	0.75	0.17	63.65	31.29	0.01	0.00	0.00	4.14	0.00
1753.2	1753.3	0.94	6.26	63.97	28.78	0.00	0.00	0.00	0.06	0.00
1753.3	1753.4	0.88	5.53	38.35	49.93	0.00	0.00	0.00	3.28	2.03
1753.4	1753.5	0.63	18.64	51.96	21.33	0.01	0.06	0.81	3.41	3.13
1753.5	1753.6	0.82	7.79	63.23	27.97	0.00	0.00	0.00	0.19	0.00
	Average:	0.74	5.49	55.47	31.61	0.01	0.01	0.12	5.81	0.74

Table B-7. Modal percentages from hyperspectral data for the Telaga Bodas K-33_0393_1833.2 core sample.

Depth from	Depth to	MINERAL ABUNDANCES						
K-33_0393_1833.2		unclassified	aspectral	carbonate	chlorite	epidote	magnetite	prehnite
1833.1	1833.2	18.59	0.08	0.02	78.72	0.02	2.48	0.09
1833.2	1833.3	9.94	0.11	0.01	88.77	0.12	1.01	0.04
	Average:	14.26	0.09	0.02	83.74	0.07	1.75	0.06

Table B-8. Modal percentages from hyperspectral data for the Telaga Bodas K-33_0393_1834 core sample.

Depth from	Depth to	MINERAL ABUNDANCES						
K-33_0393_1834		unclassified	aspectral	carbonate	chlorite	epidote	magnetite	prehnite
1833.9	1834	15.54	0.00	0.09	84.30	0.00	0.07	0.01
1834	1834.1	16.33	0.23	0.00	83.04	0.01	0.36	0.03
1834.1	1834.2	22.07	4.11	0.00	70.59	0.00	3.23	0.00
1834.2	1834.3	35.90	0.35	0.00	63.35	0.00	0.36	0.04

1834.3	1834.4	41.43	0.52	0.00	57.35	0.00	0.67	0.03
1834.4	1834.5	55.44	1.17	0.05	41.18	0.00	2.09	0.06
1834.5	1834.6	46.28	1.26	0.04	52.24	0.01	0.11	0.05
1834.6	1834.7	49.79	2.61	0.04	47.55	0.00	0.01	0.01
1834.7	1834.8	26.31	0.13	0.25	73.25	0.03	0.01	0.03
1834.8	1834.9	6.91	0.00	0.00	92.39	0.02	0.64	0.03
	Average:	31.60	1.04	0.05	66.53	0.01	0.75	0.03

Table B-9. Modal percentages from hyperspectral data for the Telaga Bodas K-33_0423_1916.3 core sample.

Depth from	**Depth to**	**MINERAL ABUNDANCES**										
K-33_0423_1916.3		unclassified	beidellite	carbonate	chlorite	epidote	iron oxide	gypsum	montmorillonite	prehnite	white mica	wairakite
1916.3	1916.4	0.03	0.02	0.02	20.56	28.47	0.18	0.43	0.99	0.15	48.66	0.49

Table B-10. Modal percentages from hyperspectral data for the Telaga Bodas K-33_0423_1919 core sample.

Depth from	**Depth to**	**MINERAL ABUNDANCES**								
K-33_0423_1919		unclassified	aspectral	chlorite	epidote	gypsum	montmorillonite	prehnite	white mica	wairakite
1918.9	1919	0.06	0.68	1.96	90.03	0.08	0.00	0.04	7.15	0.00
1919	1919.1	0.14	2.63	10.22	50.43	0.10	0.13	0.20	35.58	0.55
1919.1	1919.2	0.00	0.07	11.58	43.88	0.16	0.14	0.01	44.04	0.12
1919.2	1919.3	0.00	0.00	9.44	90.56	0.00	0.00	0.00	0.00	0.00
	Average:	0.05	0.85	8.30	68.72	0.09	0.07	0.06	21.69	0.17

Table B-11. Modal percentages from hyperspectral data for the Telaga Bodas T-2_0156_03 core sample.

Depth from	Depth to	MINERAL ABUNDANCES									
T-2_0156_03		unclassified	aspectral	beidellite	chlorite	epidote	iron oxide	gypsum	kaolinite	montmorillonite	white mica
802.6	802.7	0.47	0.10	1.15	55.98	0.31	0.09	0.05	0.08	2.21	39.56
802.7	802.8	0.33	0.00	2.97	68.32	0.03	0.01	0.34	0.00	14.08	13.92
802.8	802.9	0.17	0.00	7.57	77.68	0.13	0.03	0.00	0.00	3.61	10.80
802.9	803	5.52	0.16	4.10	69.86	0.01	0.98	0.00	0.17	0.92	18.27
803	803.1	1.53	0.00	3.13	71.71	0.06	1.02	0.17	0.10	3.77	18.50
803.1	803.2	1.03	0.00	2.96	76.51	0.04	0.75	0.00	0.02	11.45	7.21
803.2	803.3	0.10	0.00	5.53	86.09	0.07	0.61	0.00	0.00	4.24	3.36
803.3	803.4	0.21	0.00	6.31	81.11	0.06	0.93	0.03	0.01	3.16	8.19
	Average:	1.17	0.03	4.22	73.41	0.09	0.55	0.07	0.05	5.43	14.98

Table B-12. Modal percentages from hyperspectral data for the Telaga Bodas T-2_0117_00 core sample.

Depth from	Depth to	MINERAL ABUNDANCES									
T-2_0117_00		unclassified	aspectral	beidellite	carbonate	chlorite	iron oxide	gypsum	kaolinite	magnetite	montmorillonite
695.1	695.2	5.19	40.79	35.30	0.00	14.97	0.00	1.64	0.08	0.05	0.76
695.2	695.3	1.97	16.26	73.09	0.09	7.32	0.17	0.06	0.00	0.27	0.00
695.3	695.4	1.37	22.91	46.12	0.00	25.60	0.09	0.03	0.03	0.00	0.59
695.4	695.5	0.54	20.12	46.19	0.01	30.90	0.00	0.10	0.01	0.15	0.00
695.5	695.6	0.25	20.50	53.12	0.00	24.79	0.00	0.01	0.00	0.05	0.00
695.6	695.7	2.12	17.98	49.99	0.00	28.06	0.03	0.04	0.08	0.05	0.05
695.7	695.8	5.01	19.00	60.81	0.00	12.01	0.02	0.70	0.20	0.07	0.76
695.8	695.9	1.87	9.48	51.96	0.00	35.06	0.02	0.07	0.00	0.00	0.16

695.9	696	1.17	9.92	43.57	0.00	42.22	0.61	0.36	0.00	0.06	0.28
	Average:	2.17	19.66	51.13	0.01	24.55	0.11	0.33	0.04	0.08	0.29

white mica	wairakite
1.09	0.12
0.02	0.75
2.46	0.81
0.73	1.24
0.01	1.27
0.56	1.03
1.15	0.25
0.70	0.68
1.60	0.21
0.93	0.71

Table B-13. Modal percentages from hyperspectral data for the Telaga Bodas T-2_0117_03 core sample.

Depth from	**Depth to**	**MINERAL ABUNDANCES**									
T-2_0117_03		unclassified	aspectral	beidellite	carbonate	chlorite	iron oxide	gypsum	kaolinite	magnetite	montmorillonite
693.2	693.3	5.79	19.51	57.11	0.00	7.35	0.15	8.93	0.25	0.06	0.52
693.3	693.4	1.47	35.99	31.56	0.00	22.08	0.00	7.72	0.14	0.01	0.37
693.4	693.5	4.23	37.45	31.65	0.17	19.82	0.00	4.68	0.06	0.05	1.50
693.5	693.6	1.33	22.44	48.85	0.00	25.45	0.00	1.50	0.02	0.08	0.23
693.6	693.7	5.13	21.06	48.56	0.00	22.28	0.00	2.37	0.00	0.01	0.50
693.7	693.8	0.84	7.69	54.13	3.23	33.08	0.04	0.02	0.00	0.00	0.61
693.8	693.9	1.16	3.57	58.31	0.00	36.27	0.00	0.08	0.03	0.01	0.28

693.9	694	1.21	4.44	66.53	2.48	24.20	0.00	0.60	0.00	0.16	0.05
	Average:	2.64	19.02	49.59	0.74	23.82	0.02	3.24	0.06	0.05	0.51

white mica	wairakite
0.12	0.19
0.64	0.01
0.35	0.02
0.04	0.06
0.00	0.10
0.13	0.22
0.07	0.22
0.01	0.30
0.17	0.14

B.1.2 Lake City Samples

Table B-14. Modal percentages from hyperspectral data for the Lake City LCB090314-5 core sample.

Sample ID		Aspectral	Carbonate	Chlorite	Magnetite	Montmorillonite	White Mica	Silica/ Quartz	Tourmaline	Iron Oxide
LCB090314-5	Average %:	2.18	0.07	8.26	0.54	0.13	68.78	5.87	0.03	14.13

Table B-15. Modal percentages from hyperspectral data for the Lake City LCB090314-1b core sample.

Sample ID		Amethyst	Aspectral	Magnetite	White Mica
LCB090314-1b	Average %:	0.24	94.05	0.01	5.70

Table B-16. Modal percentages from hyperspectral data for the Lake City LCB091414-2 core sample.

Sample ID		Amethyst	Aspectral	Carbonate	Chlorite	Epidote	Fluorite	Magnetite	White Mica	Silica/Quartz
LCB091414-2	Average %:	0.12	74.11	0.57	0.55	0.24	0.05	0.01	24.14	0.21

Table B-17. Modal percentages from hyperspectral data for the Lake City LCDLA082913-1 core sample.

Sample ID		Jarosite	Montmorillonite	Iron Oxide
LCDLA082913_1	Average %:	0.46	96.11	3.43

Table B-18. Modal percentages from hyperspectral data for the Lake City LCDLA082913-2 core sample.

Sample ID		Jarosite	Montmorillonite	White Mica	Iron Oxide
LCDLA082913_2	Average %:	3.70	90.14	0.04	6.12

Table B-19. Modal percentages from hyperspectral data for the Lake City LCG090714-2c core sample.

Sample ID		Aspectral	Chlorite	Montmorillonite	White Mica	Silica/Quartz
LCG090714-2c	Average %:	2.38	2.39	6.04	89.07	0.11

Table B-20. Modal percentages from hyperspectral data for the Lake City LCG090714-3a core sample.

Sample ID		Aspectral	Montmorillonite	White Mica	Silica/Quartz	Iron Oxide
LCGO90714-3a	Average %:	0.03	3.61	52.64	11.44	32.28

Table B-21. Modal percentages from hyperspectral data for the Lake City LCG090714-3b core sample.

Sample ID		Aspectral	Chlorite	Kaolinite	Magnetite	Montmorillonite	White Mica	Silica/Quartz	Iron Oxide
LCG090714-3b	Average %:	0.03	12.89	0.10	0.09	3.54	74.99	0.81	7.55

Table B-22. Modal percentages from hyperspectral data for the Lake City LCG091314-1b core sample.

Sample ID		Aspectral	Epidote	Montmorillonite	White Mica	Silica/Quartz	Iron Oxide
LCG091314-1b	Average %:	0.01	0.02	0.68	45.30	14.10	39.88

Table B-23. Modal percentages from hyperspectral data for the Lake City LCT091014-1a core sample.

Sample ID		Aspectral	Carbonate	Chlorite	Montmorillonite	White Mica	Silica/Quartz	Iron Oxide
LCT091014-1a	Average %:	11.13	0.27	1.11	0.10	82.36	0.73	4.31

Table B-24. Estimated modal percentages from hyperspectral data for the Lake City LCT091014-1b core sample.

Sample ID		Aspectral	Montmorillonite	White Mica	Silica/Quartz	Iron Oxide	
LCT091014-1b*	Average %:	46.00	0.10	49.00	1.90	3.00	*Estimated

Table B-25. Modal percentages from hyperspectral data for the Lake City LCT091514-3 core sample.

Sample ID		Aspectral	Dickite	Kaolinite	Magnetite	Montmorillonite	White Mica	Silica/Quartz	Smoky Quartz?	Iron Oxide
LCT091514-3	Average %:	83.90	0.03	0.15	0.01	3.82	10.07	1.88	0.10	0.03

Table B-26. Modal percentages from hyperspectral data for the Lake City LCTBV071716-5a core sample.

Sample ID		Aspectral	Carbonate	Fluorite	Jarosite	Montmorillonite	White Mica	Silica/Quartz	Iron Oxide
LCTBV071716-5a	Average %:	34.87	0.01	0.03	1.20	6.21	22.12	31.06	4.50

Table B-27. Modal percentages from hyperspectral data for the Lake City LCTV090314-4a core sample.

Sample ID		Aspectral	Dickite	Epidote	Jarosite	Montmorillonite	White Mica	Silica/Quartz	Iron Oxide
LCTV090314-4a	Average %:	16.64	20.83	0.16	0.18	0.05	18.51	28.82	14.82

Table B-28. Modal percentages from hyperspectral data for the Lake City LCTV091014-1c core sample.

Sample ID		Aspectral	Montmorillonite	White Mica	Silica/Quartz	Iron Oxide
LCTV091014-1c	Average %:	13.58	5.24	26.27	30.55	24.36

Table B-29. Modal percentages from hyperspectral data for the Lake City LCTV091014-1d core sample.

Sample ID		Aspectral	Jarosite	Montmorillonite	White Mica	Silica/Quartz	Iron Oxide
LCTV091014-1d	Average %:	9.66	0.01	9.53	30.92	33.26	16.62

B.2 Estimated Modal Percentages for LCT091014-1b

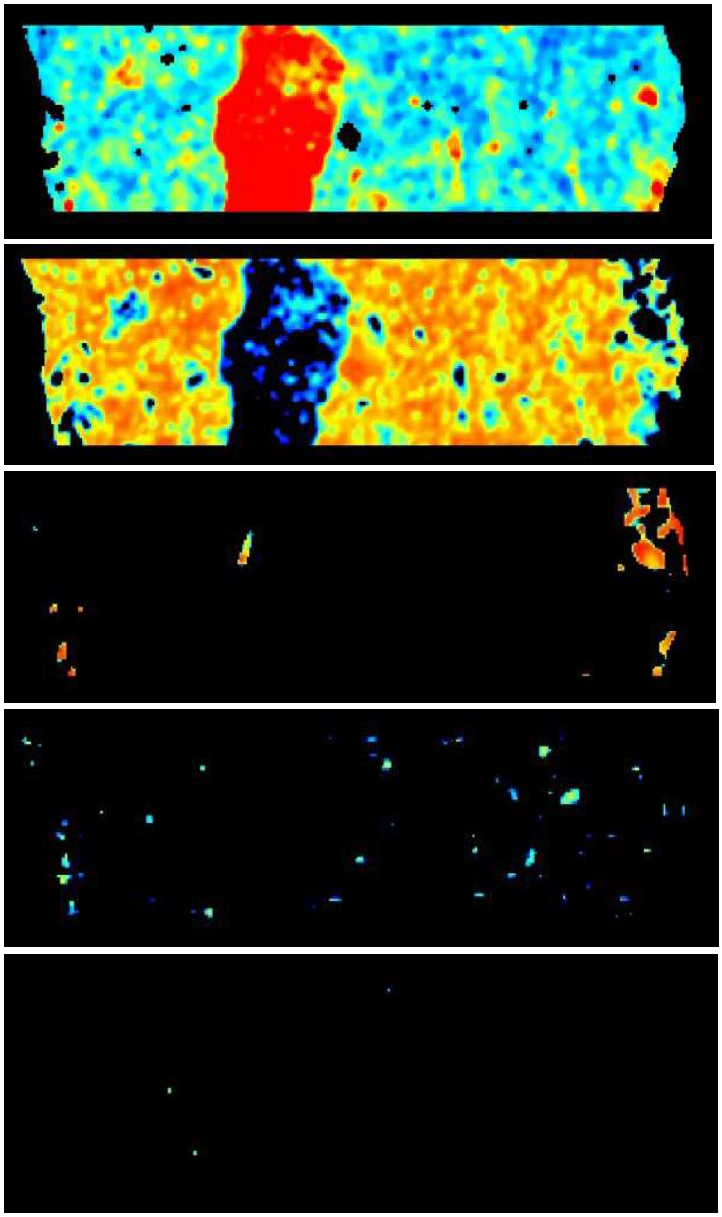

White Mica: 49%

Aspectral: 46%

Fe-Ox: 3%

Silica/Quartz: 1.9%

Montmorillonite: 0.1%

Figure B-1. Individual mineral maps for LCT091014-1b from Coreshed and the estimated assigned percentages.

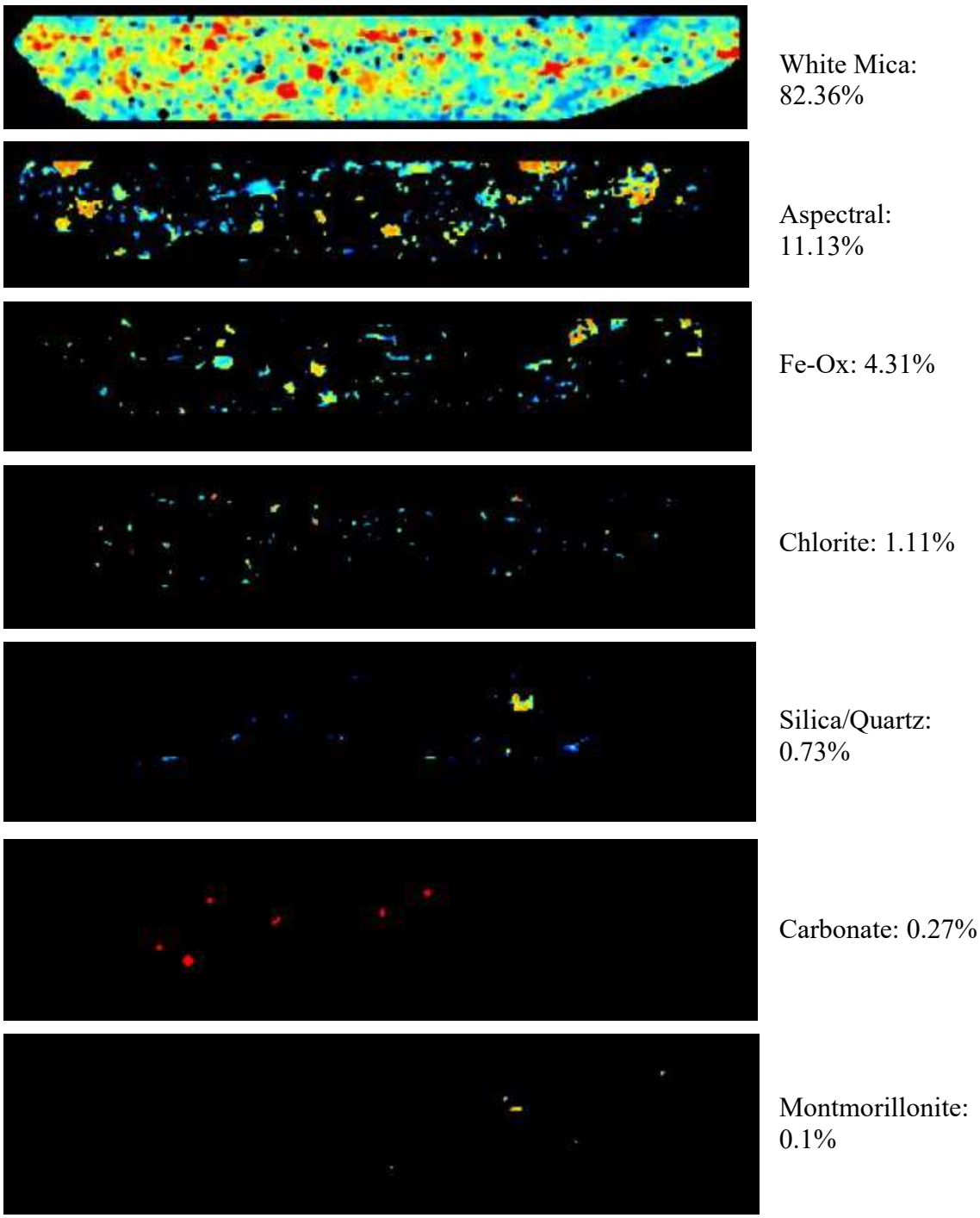

Figure B-2. For comparison, the individual mineral maps for LCT091014-1a from Coreshed and their modal percentages as provided by Corescan

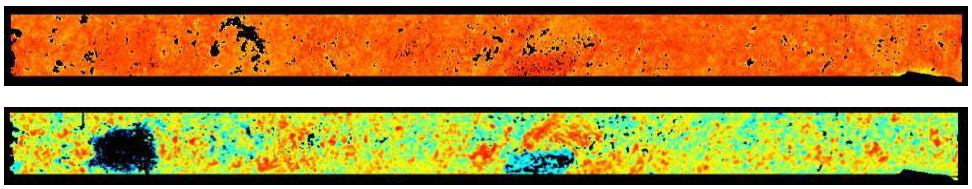

Chlorite: 47.93%

White Mica: 48.25%

Figure B-3. For comparison, the chlorite and white mica mineral maps for K33_0191_03 from Coreshed and the calculated modal percentages as provided by Corescan.

B.3 ASI and H-ASI Mineral Parameters Based on Modal Percentages

B.3.1 Telaga Bodas Samples

Table B-30. ASI and H-ASI mineral parameters based on modal percentages for Telaga Bodas samples. Red rows relate to primary mineralogy and purple rows relate to secondary mineralogy. Grey rows are unclassified. Cat = Category, H I = Hardness Index.

Core Sample	Mineral	P / S	Corescan Abundance %	Cat	Rank	Rep. %	Hardness	H I	Pm	Sm	AI	Pm (H-ASI)	Sm (H-ASI)
0117_00	Beidellite	S	51.1	A	1	50	1-2	0.1	42.5	18.9	77.3	33.49	18.41
	Chlorite	S	24.6	C	5	25	2-2.5	0.5					
	Aspectral	P?	19.7	C	-	25	6-6.5	1.7		Aspectral: Assume feldspar			
	Unclassified	?	2.2	?	?	?	?	?					
	White mica	S	0.9	R	11	1	1-2	0.1		White mica: Assume illite			
	Wairakite	S	0.7	R	11	1	5.5-6	1.3					
0117_03	Beidellite	S	49.6	A	1	50	1-2	0.1	42.5	20	77.8	32.3	19.14
	Chlorite	S	23.8	C	5	25	2-2.5	0.5					
	Aspectral	P?	19	C	-	25	6-6.5	1.7					
	Gypsum	S	3.2	R	7	3	2	0.5					
	Unclassified	?	2.6	?	?	?	?	?					
	Carbonate	S	0.7	R	11	1	3	0.9		Carbonate: Assume calcite			
	Montmorillonite	S	0.5	R	11	1	1-2	0.1					
0156_03	Chlorite	S	73.4	A	1	50	2-2.5	0.5	0	29.15	98.6	0	40.18
	White mica	S	15	M	4	15	1-2	0.1					

	Montmorillonite	S	5.4	M	8	5	1-2	0.1					
	Beidellite	S	4.2	R	4	4.5	1-2	0.1					
	Unclassified	?	1.2	?	?	?	?	?					
	Iron Oxide	S	0.6	R	11	1	5.5-6.5	1.7		Fe-Ox: Assume hematite, same hardness as magnetite			
0191_00	White mica	S	39.7	C	2	40	1-2	0.1	8.5	34.45	96.4	1.02	33.4
	Chlorite	S	38.4	C	2	40	2-2.5	0.5					
	Gypsum	S	17.4	M	3	17.5	2	0.5					
	Unclassified	?	2.3	?	?	?	?	?					
	Epidote	S	0.9	R	11	1	6-7	1.7					
	Aspectral	P?	0.6	R	-	5	6-6.5	1.7					
0191_03	White mica	S	48.2	A	1	50	1-2	0.1	0	32.7	99.4	0	31.38
	Chlorite	S	48.4	A	1	50	2-2.5	0.5					
	Gypsum	S	2	R	8	2	2	0.5					
	Epidote	S	0.8	R	11	1	6-7	1.7					
0192_01	Chlorite	S	56.3	A	1	50	2-2.5	0.5	8.5	30.3	91.8	3.4	33.14
1277.75	White mica	S	33.4	C	4	35	1-2	0.1					
	Beidellite	S	1.2	R	7	1	1-2	0.1					
	Unclassified	?	5.9	?	?	?	?	?					
	Aspectral	P?	2	R	-	5	6-6.5	1.7					
	Magnetite	S	0.9	R	11	1	5.5-6.5	1.7					

1276	Chlorite	S	45.7	C	1	45	2-2.5	0.5	8.5	33.45	95.6	3.06	32.48
	White mica	S	22.5	C	5	25	1-2	0.1					
	Beidellite	S	17.6	M	3	17.5	1-2	0.1					
	Gypsum	S	9.2	M	6	10	2	0.5					
	Aspectral	P?	1.8	R	-	5	6-6.5	1.7					
	Unclassified	?	1.4	?	?	?	?	?					
	Epidote	S	0.6	R	11	1	6-7	1.7					
1752	Chlorite	S	67.6	A	1	50	2-2.5	0.5	8.5	80.25	98.8	1.36	86.84
	Epidote	S	23.3	C	5	25	6-7	1.7					
	Prehnite	S	7.9	M	7	7.5	6-6.5	1.7					
	Aspectral	P?	0.8	R	-	5	6-6.5	1.7					
1753	Chlorite	S	55.5	A	1	50	2-2.5	0.5	8.5	85.8	93.6	9.35	92.24
	Epidote	S	31.6	C	4	30	6-7	1.7					
	Prehnite	S	5.8	M	8	5	6-6.5	1.7					
	Aspectral	P?	5.5	R	-	5	6-6.5	1.7					
	Wairakite	S	0.7	R	11	1	5.5-6	1.3					
	Unclassified	?	0.7	?	?	?	?	?					
1834	Chlorite	S	66.5	A	1	50	2-2.5	0.5	8.5	26.7	67.3	1.7	34.61
	Unclassified	?	31.6	?	?	?	?	?					
	Aspectral	P?	1	R	-	5	6-6.5	1.7					
	Magnetite	S	0.8	R	11	1	5.5-6.5	1.7					

1833.2	Chlorite	S	83.7	A	1	50	2-2.5	0.5	0	28.4	85.5	0	44.91
	Unclassified	?	14.3	?	?	?	?	?					
	Magnetite	S	1.8	R	9	2	5.5-6.5	1.7					
1919	Epidote	S	68.7	A	1	50	6-7	1.7	8.5	90.75	98.7	1.53	123.11
	White mica	S	21.7	M	2	20	1-2	0.1					
	Chlorite	S	8.3	M	7	7.5	2-2.5	0.5					
	Aspectral	P?	0.9	R	-	5	6-6.5	1.7					
1916.3	White mica	S	48.7	A	1	50	1-2	0.1	0	66.1	98.8	0	63.72
	Epidote	S	28.5	C	4	30	6-7	1.7					
	Chlorite	S	20.6	M	2	20	2-2.5	0.5					
	Montmorillonite	S	1	R	11	1	1-2	0.1					

B.3.2 Lake City Samples

Table B-31. ASI and H-ASI mineral parameters based on modal percentages for Lake City samples. Red rows relate to primary mineralogy and purple rows relate to secondary mineralogy. Grey rows are unclassified. Yellow rows show the parameter values if silica/quartz is included as primary mineralogy (Pm columns) and secondary mineralogy (Sm and AI columns). Cat = Category, H I = Hardness Index.

Core Sample	Mineral	P / S	Corescan Abundance %	Cat	Rank	Rep. %	Hardness	H I	Pm	Sm	AI	Pm (H-ASI)	Sm (H-ASI)
B-5	White mica	S	68.8	A	1	50	1-2	0.1	8.5	35.95	91.7	3.74	35.85

	Iron Oxide	S	14.1	M	4	15	5.5-6.5	1.7					
	Chlorite	S	8.3	M	7	7.5	2-2.5	0.5					
	Silica/Quartz	P/S?	5.9	R/M	-/8	5	7	2.1	19	46.45	97.6	16.13	48.24
	Aspectral	P?	2.2	R	-	5	6-6.5	1.7					
	Magnetite	S	0.5	R	11	1	5.5-6.5	1.7					
B-2	Aspectral	P?	74.1	A	-	50	6-6.5	1.7	85	3.9	25.3	125.97	3.25
	White mica	S	24.1	C	5	25	1-2	0.1					
	Carbonate	S	0.6	R	11	1	3	0.9					
	Chlorite	S	0.6	R	11	1	2-2.5	0.5					
B-1b	Aspectral	P?	94	A	-	50	6-6.5	1.7	85	0.5	5.7	159.8	0.57
	White mica	S	5.7	M	8	5	1-2	0.1					
G-3a	White mica	S	52.6	A	1	50	1-2	0.1	0	56.35	88.5	0	60.53
	Iron Oxide	S	32.3	C	4	30	5.5-6.5	1.7					
	Silica/Quartz	P/S?	11.4	M	-/5	10 / 12.5	7	2.1	21	82.6	99.9	23.94	84.47
	Montmorillonite	S	3.6	R	6	3.5	1-2	0.1					
G-1b	White mica	S	45.3	C	1	45	1-2	0.1	0	72.6	85.9	0	72.43
	Iron Oxide	S	39.9	C	2	40	5.5-6.5	1.7					
	Silica/Quartz	P/S?	14.1	M	-/4	10 / 15	7	2.1	21	104.1	100	29.61	102.04
	Montmorillonite	S	0.7	R	11	1	1-2	0.1					

G-3b	White mica	S	75	A	1	50	1-2	0.1	0	24.35	99	0	27.22
	Chlorite	S	12.9	M	5	12.5	2-2.5	0.5					
	Iron Oxide	S	7.6	M	7	7.5	5.5-6.5	1.7					
	Montmorillonite	S	3.5	R	6	3.5	1-2	0.1					
	Silica/Quartz	P/S?	0.8	R	-/11	5 / 1	7	2.1	10.5	26.45	99.8	1.68	28.9
G-2c	White mica	S	89.1	A	1	50	1-2	0.1	8.5	6.75	97.5	4.08	10.71
	Montmorillonite	S	6	M	8	5	1-2	0.1					
	Chlorite	S	2.4	R	8	2.5	2-2.5	0.5					
	Aspectral	P?	2.4	R	-	5	6-6.5	1.7					
T-1a	White mica	S	82.4	A	1	50	1-2	0.1	17	13.15	87.8	18.87	16.1
	Aspectral	P?	11.1	M	-	10	6-6.5	1.7					
	Iron Oxide	S	4.3	M	4	4.5	5.5-6.5	1.7					
	Chlorite	S	1.1	R	11	1	2-2.5	0.5					
	Silica/Quartz	P/S?	0.7	R	-/11	5 / 1	7	2.1	27.5	15.25	88.5	20.34	17.57
T-1b	White mica	S	49	A	1	50	1-2	0.1	85	10.1	52	78.2	10
Estimate	Aspectral	P?	46	A	-	50	6-6.5	1.7					
	Iron Oxide	S	3	R	7	3	5.5-6.5	1.7					
	Silica/Quartz	P/S?	1.9	R	-/9	5 / 2	7	2.1	95.5	14.3	53.9	82.19	13.99
TV-1c	Silica/Quartz	P/S?	30.6	C	-/4	25 / 30	7	2.1	69.5	108.5	86.5	87.38	108.89
	White mica	S	26.3	C	5	25	1-2	0.1	17	45.5	55.9	23.12	44.63

	Iron Oxide	S	24.4	C	5	25	5.5-6.5	1.7					
	Aspectral	P?	13.6	M	-	10	6-6.5	1.7					
	Montmorillonite	S	5.2	M	8	5	1-2	0.1					
TV-1d	Silica/Quartz	P/S?	33.3	C	-/3	25 / 35	7	2.1	69.5	107.25	90.3	86.42	102.19
	White mica	S	30.9	C	4	30	1-2	0.1	17	33.75	57	16.49	32.26
	Iron Oxide	S	16.6	M	3	17.5	5.5-6.5	1.7					
	Aspectral	P?	9.7	M	-	10	6-6.5	1.7					
	Montmorillonite	S	9.5	M	6	10	1-2	0.1					
T-3	Aspectral	P?	83.9	A	-	50	6-6.5	1.7	85	1.4	13.9	142.63	1.39
	White mica	S	10.1	M	6	10	1-2	0.1					
	Montmorillonite	S	3.8	R	5	4	1-2	0.1					
	Silica/Quartz	P/S?	1.9	R	-9	5 / 2	7	2.1	95.5	5.6	15.8	146.62	5.38
TBV-5a	Aspectral	P?	34.9	C	-	25	6-6.5	1.7	42.5	11.05	34	59.33	11.56
	Silica/Quartz	P/S?	31.1	C	-/4	25 / 30	7	2.1	95	74.05	65.1	124.64	76.87
	White mica	S	22.1	M	2	20	1-2	0.1					
	Montmorillonite	S	6.2	M	8	5	1-2	0.1					
	Iron Oxide	S	4.5	R	4	4.5	5.5-6.5	1.7					
	Jarosite	S	1.2	R	11	1	2.5-3.5	0.9					

TV-4a	Silica/Quartz	P/S?	28.8	C	-/4	25 / 30	7	2.1	69.5	92.25	82.9	88.7	89.57
	Dickite	S	20.8	M	2	20	1.5-2	0.1	17	29.25	54.1	28.22	29.09
	White mica	S	18.5	M	3	17.5	1-2	0.1					
	Aspectral	P?	16.6	M	-	10	6-6.5	1.7					
	Iron Oxide	S	14.8	M	4	15	5.5-6.5	1.7					
DLA-2	Montmorillonite	S	90.1	A	1	50	1-2	0.1	0	16.65	99.9	0	22.71
	Iron Oxide	S	6.1	M	8	5	5.5-6.5	1.7					
	Jarosite	S	3.7	R	6	3.5	2.5-3.5	0.9					
DLA-1	Montmorillonite	S	96.1	A	1	50	1-2	0.1	0	10.95	99.5	0	15.39
	Iron Oxide	S	3.4	R	6	3.5	5.5-6.5	1.7					

B.4 ASI and H-ASI Parameter Values Summary

Table B-32. ASI and H-ASI parameter values and estimated UCS for all samples using Pm, Sm, and AI values from Appendix B.3 where silica/quartz is assigned to secondary mineralogy.

Sample	Porosity (%)	Pm (ASI)	Sm (ASI)	AI	Pm (H-ASI)	Sm (H-ASI)	Snf	ASI	H-ASI	Predicted UCS

T2_0117_00	8.15	42.5	18.9	0.77	33.49	18.41	0	22.78	20.50	0.04
T2_0117_03	8.69	42.5	20	0.78	32.3	19.14	3	20.61	18.19	0.02
T2_0156_03	8.37	0	29.15	0.99	0	40.18	2	24.81	34.20	0.35
K33_0191_00	16.42	8.5	34.45	0.96	1.02	33.4	2	28.35	27.27	0.13
K33_0191_03	12.77	0	32.7	0.99	0	31.38	2	27.70	26.59	0.12
K33_0192_1276	7.78	8.5	33.45	0.96	3.06	32.48	2	27.99	26.98	0.12
K33_0192_1277.75	14.31	8.5	30.3	0.92	3.4	33.14	0	26.32	28.35	0.15
K33_0364_1752	11	8.5	80.25	0.99	1.36	86.84	3	65.01	70.27	8.10
K33_0364_1753	18.09	8.5	85.8	0.94	9.35	92.24	2	68.20	73.33	9.75
K33_0393_1833.2	4.31	0	28.4	0.86	0	44.91	0	23.24	36.75	0.48
K33_0393_1834	4.67	8.5	26.7	0.67	1.7	34.61	3	17.43	20.04	0.03
K33_0423_1916.3	10.95	0	66.1	0.99	0	63.72	0	60.78	58.59	3.66
K33_0423_1919	15	8.5	90.75	0.99	1.53	123.11	0	82.68	112.05	62.08
LCB090314-5(2/2)	4.07	8.5	46.45	0.98	3.74	48.24	3	28.41	39.80	0.68
LCB090314-1b	4.21	85	0.5	0.06	159.8	0.57	3	67.58	127.04	107.42
LCB091414-2	7.79	85	3.9	0.25	125.97	3.25	3	53.35	78.54	13.16
LCDLA082913-1	21.54	0	10.95	1.00	0	15.39	0	9.94	13.97	0.01
LCDLA082913-2	18.85	0	16.65	1.00	0	22.71	0	15.23	20.77	0.04
LCG090714-2c	5.84	8.5	6.75	0.98	4.08	10.71	2	5.93	9.20	0.00
LCG090714-3a	7.54	0	82.6	1.00	0	84.47	2	43.18	73.07	9.60
LCG090714-3b	2.06	0	26.45	1.00	0	28.9	3	20.76	24.84	0.09
LCG091314-1b	4.84	0	104.1	1.00	0	102.04	3	52.34	85.65	19.21
LCT091014-1a	11.6	17	15.25	0.89	18.87	17.57	0	12.65	16.46	0.01

LCT091014-1b	10.94	85	14.3	0.54	78.2	13.99	0	42.86	40.25	0.71
LCT091514-3(1)	6.85	85	5.6	0.16	142.63	5.38	2	63.72	105.03	46.81
LCT091514-3(2)	5.97	85	5.6	0.16	142.63	5.38	0	69.55	114.63	68.59
LCTBV071714-5a	4.54	42.5	74.05	0.65	59.33	76.87	2	27.96	62.20	4.75
LCTV090314-4a	4.57	17	92.25	0.83	28.22	89.57	4	18.96	63.47	5.19
LCTV091014-1c	3.54	17	108.5	0.87	23.12	108.89	2	29.17	86.19	19.75
LCTV091014-1d	8.22	17	107.25	0.90	16.49	102.19	4	20.93	74.03	10.16

B.5 Core Photographs and Fractures

B.5.1 Telaga Bodas Samples

1. K33_0191_00

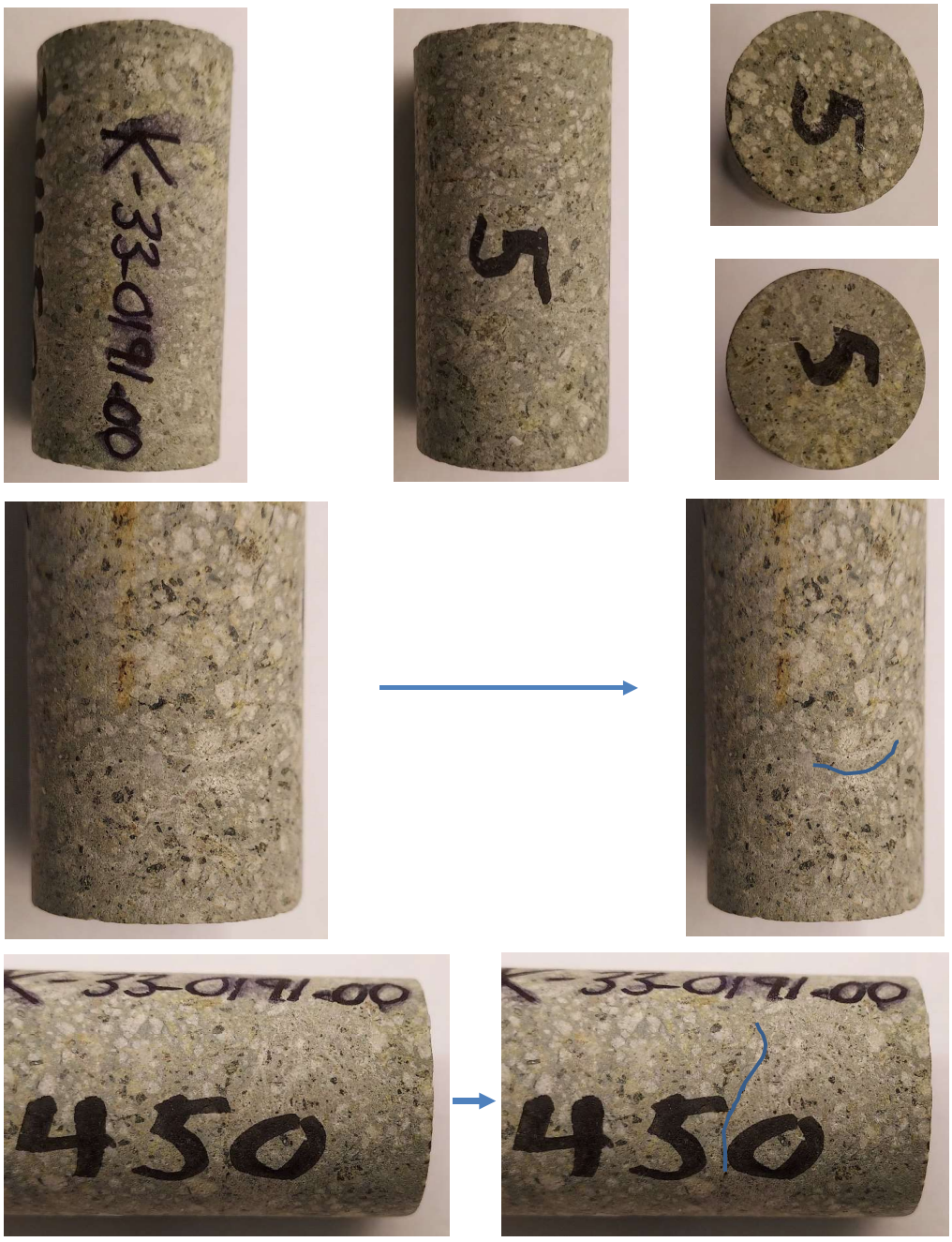

Figure B-4. Core photographs and annotated fractures for K33_0191_00

2. K33_0191_03

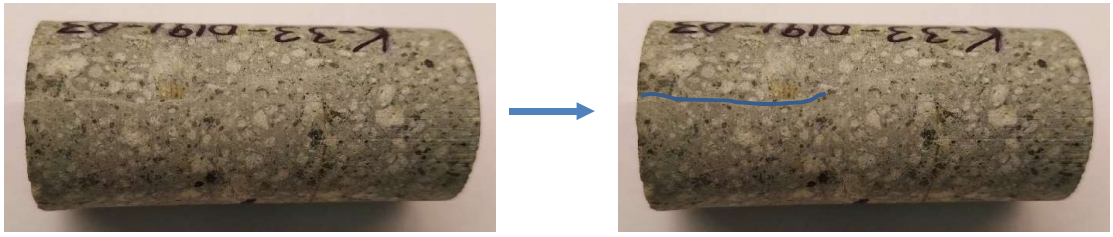

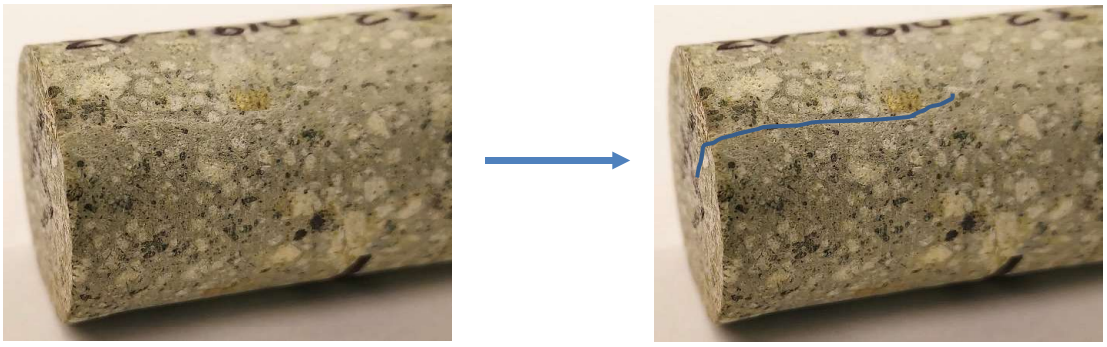

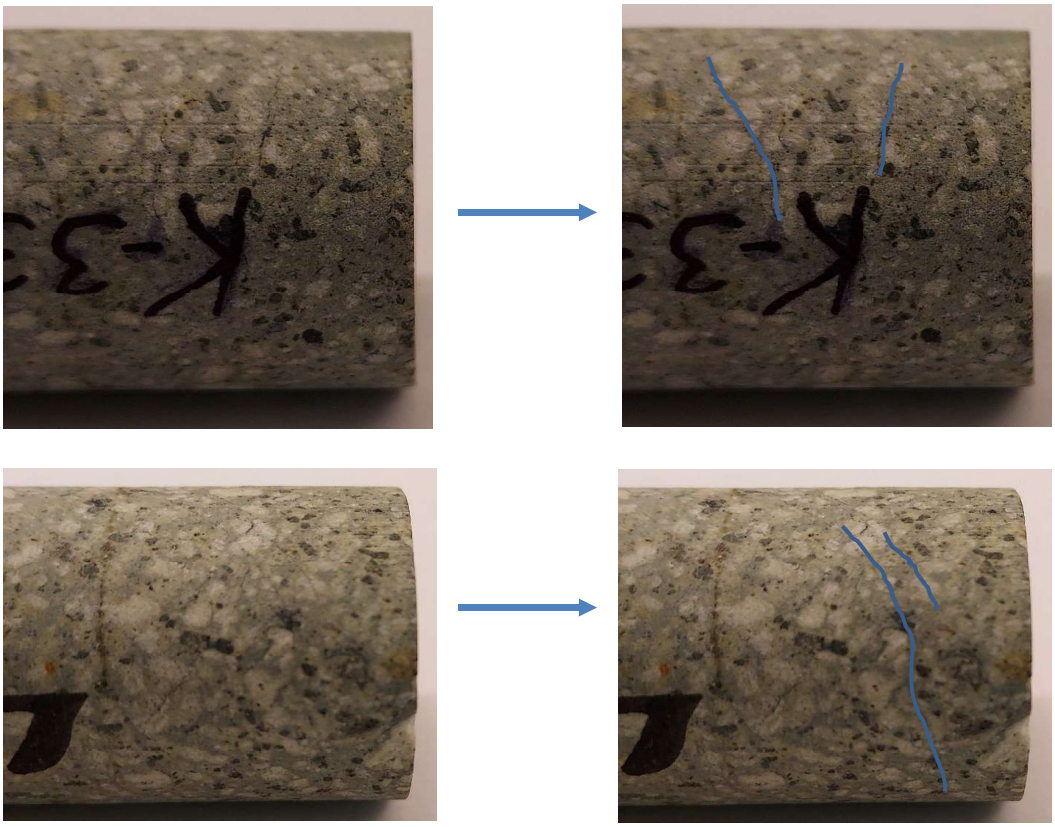

Figure B-5. Core photographs and annotated fractures for K33_0191_03

3. K33_0192_1276

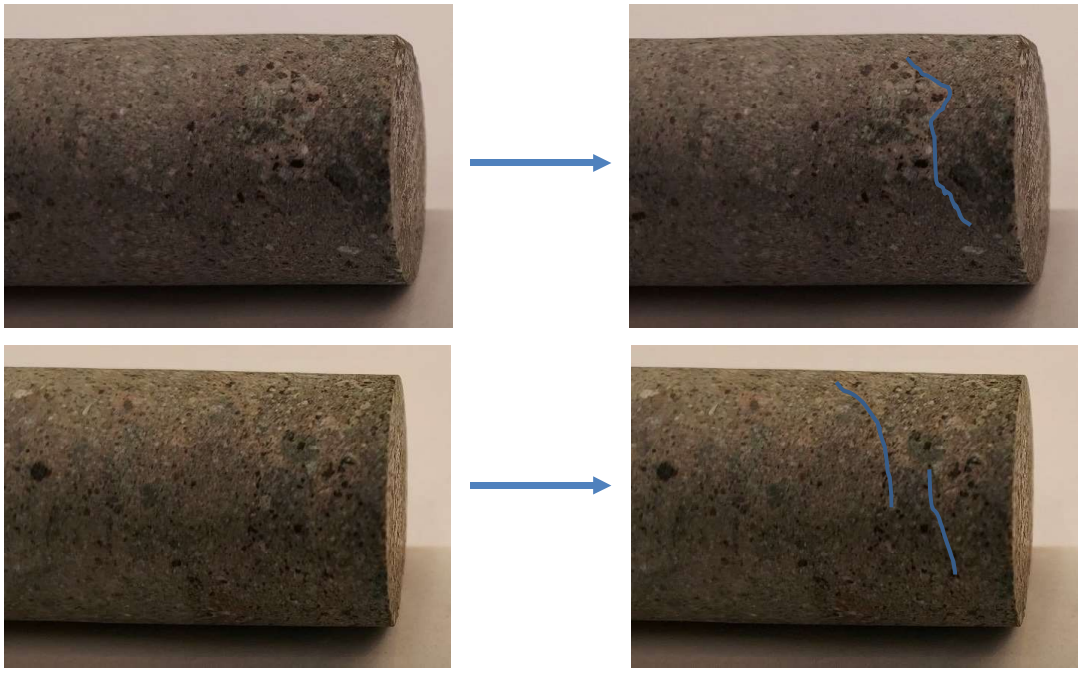

Figure B-6. Core photographs and annotated fractures for K33_0192_1276

4. K33_0192_1277.75

Figure B-7. Core photographs and annotated fractures for K33_0192_1277.75

5. K33_0364_1752

Figure B-8. Core photographs and annotated fractures for K33_0364_1752

6. K33_0364_1753

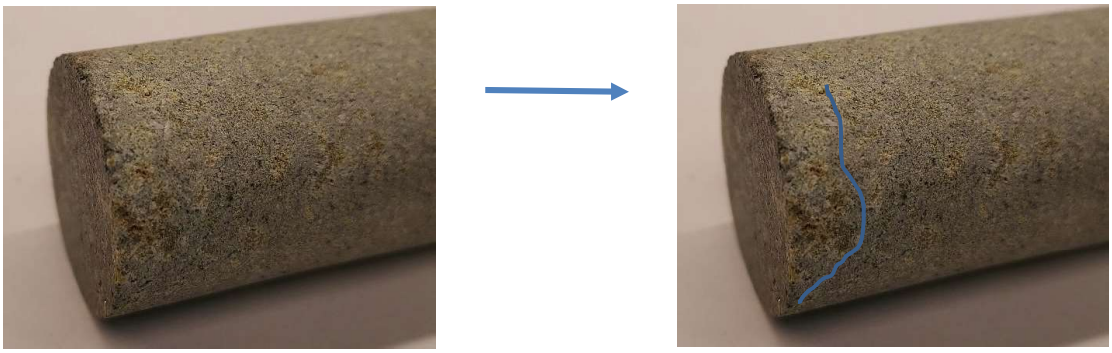

Figure B-9. Core photographs and annotated fractures for K33_0364_1753

7. K33_0393_1833.2

Figure B-10. Core photographs and annotated fractures for K33_0393_1833.2

8. K33_0393_1834

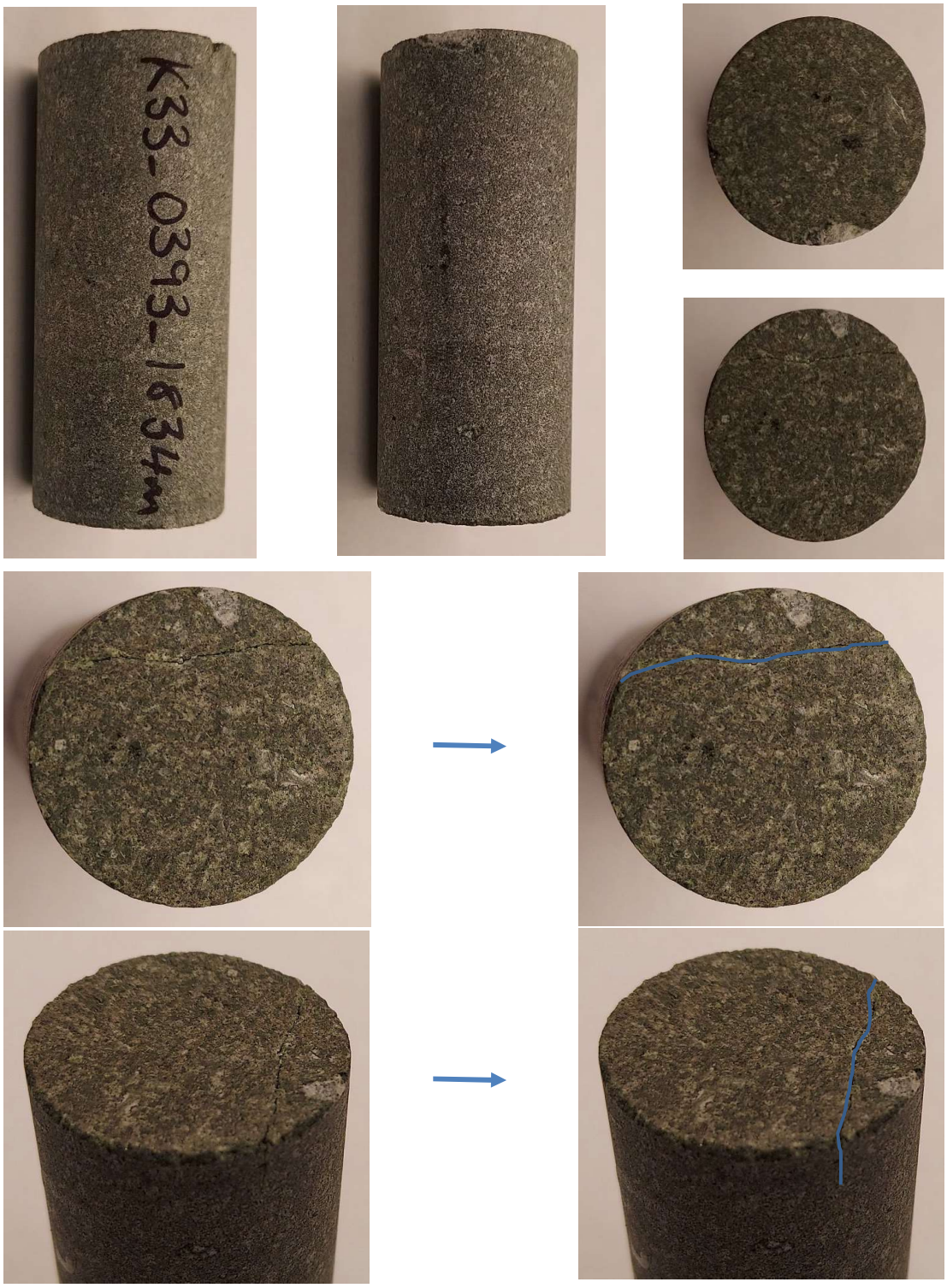

Figure B-11. Core photographs and annotated fractures for K33_0393_1834

9. K33_0423_1916.3

Figure B-12. Core photographs and annotated fractures for K33_0423_1916.3

10. K33_0423_1919

Figure B-13. Core photographs and annotated fractures for K33_0423_1919

11. T2_0156_03

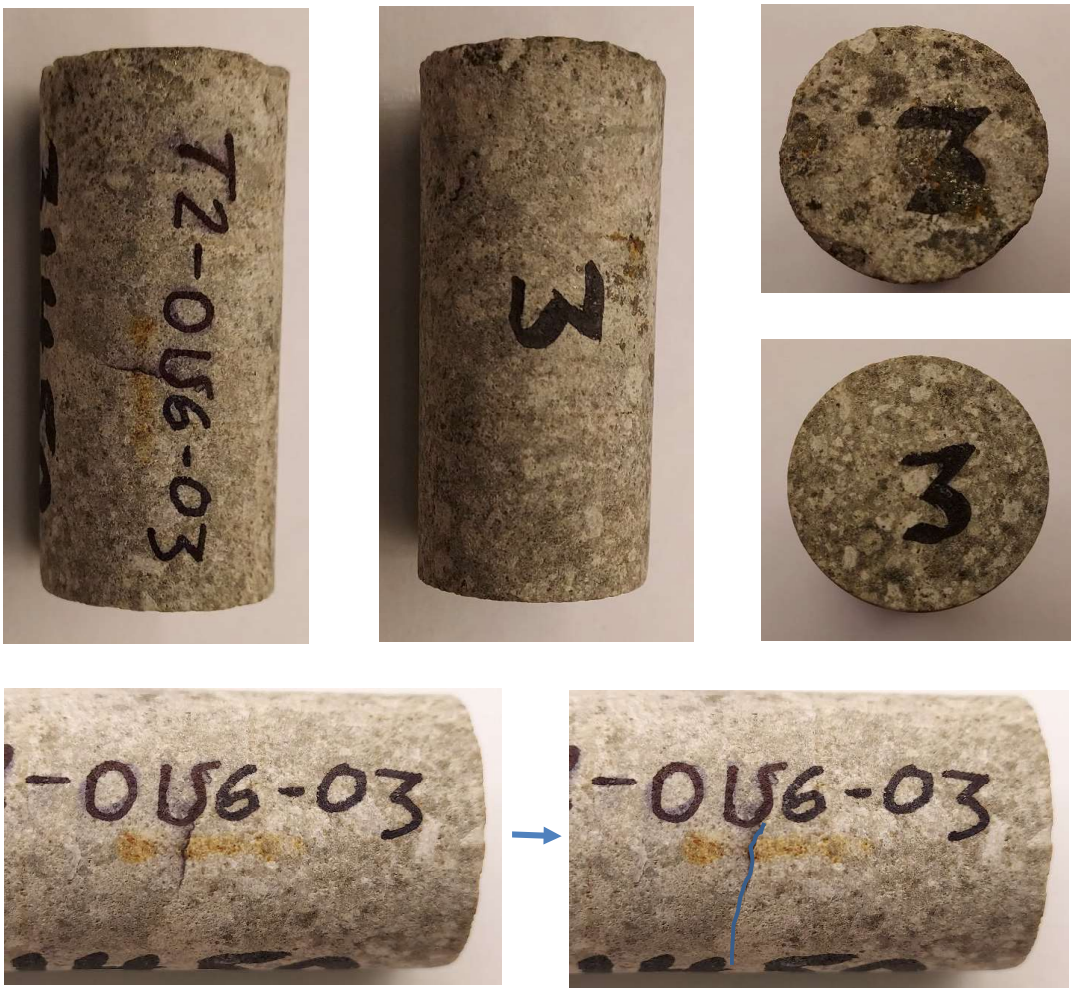

Figure B-14. Core photographs and annotated fractures for T2_0156_03

12. T2_0117_00

Figure B-15. Core photographs and annotated fractures for T2_0117_00

13. T2_0117_03

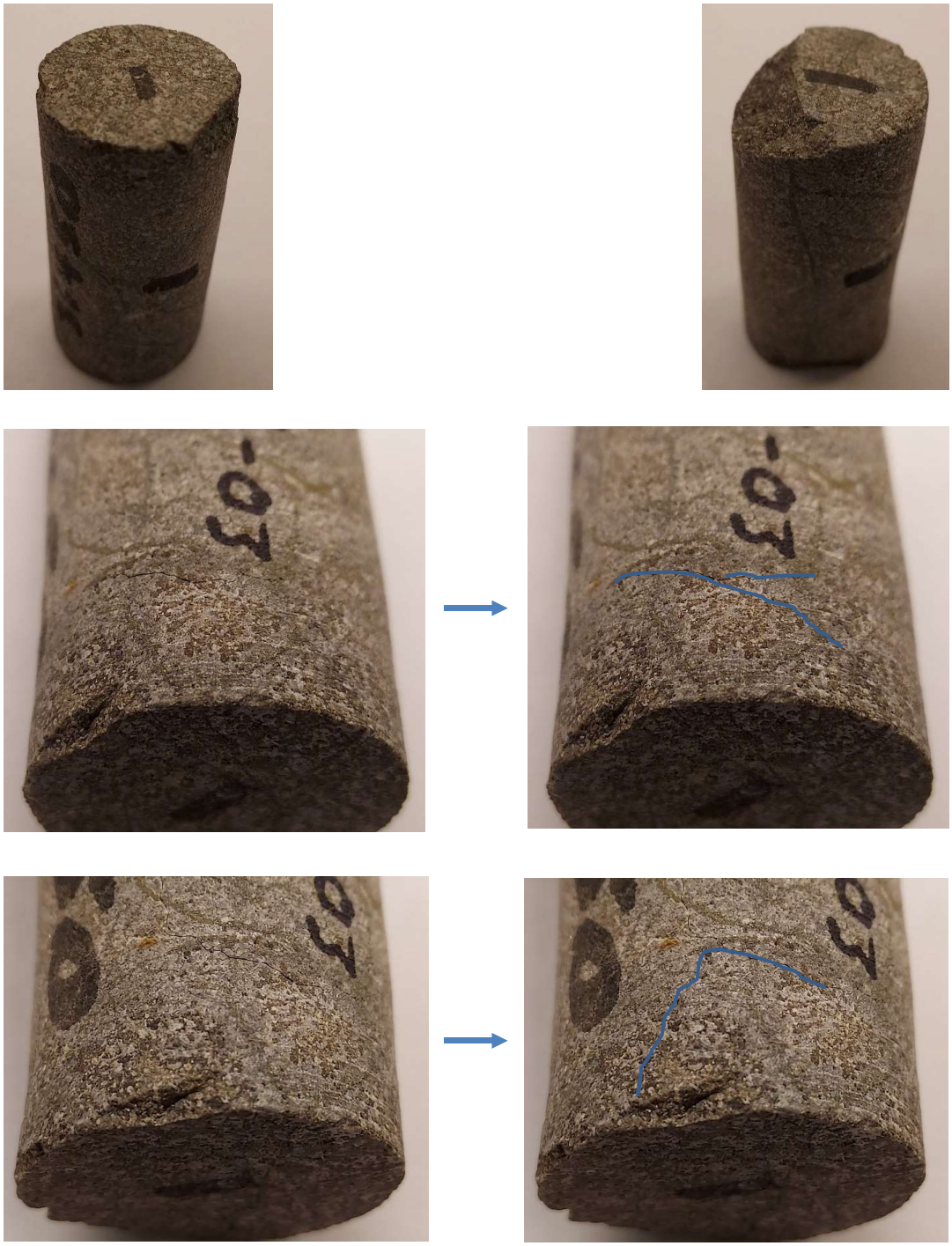

Figure B-16. Core photographs and annotated fractures for T2_0117_03

B.5.2 Lake City Samples

1. LCB090314_1b

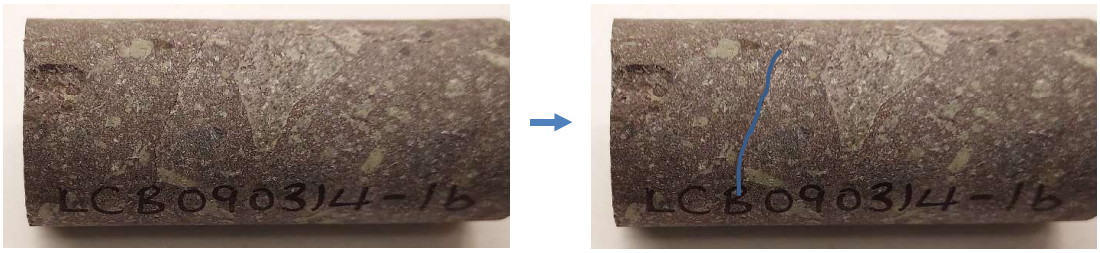

Figure B-17. Core photographs and annotated fractures for LCB090314-1b

2. LCB090314-5

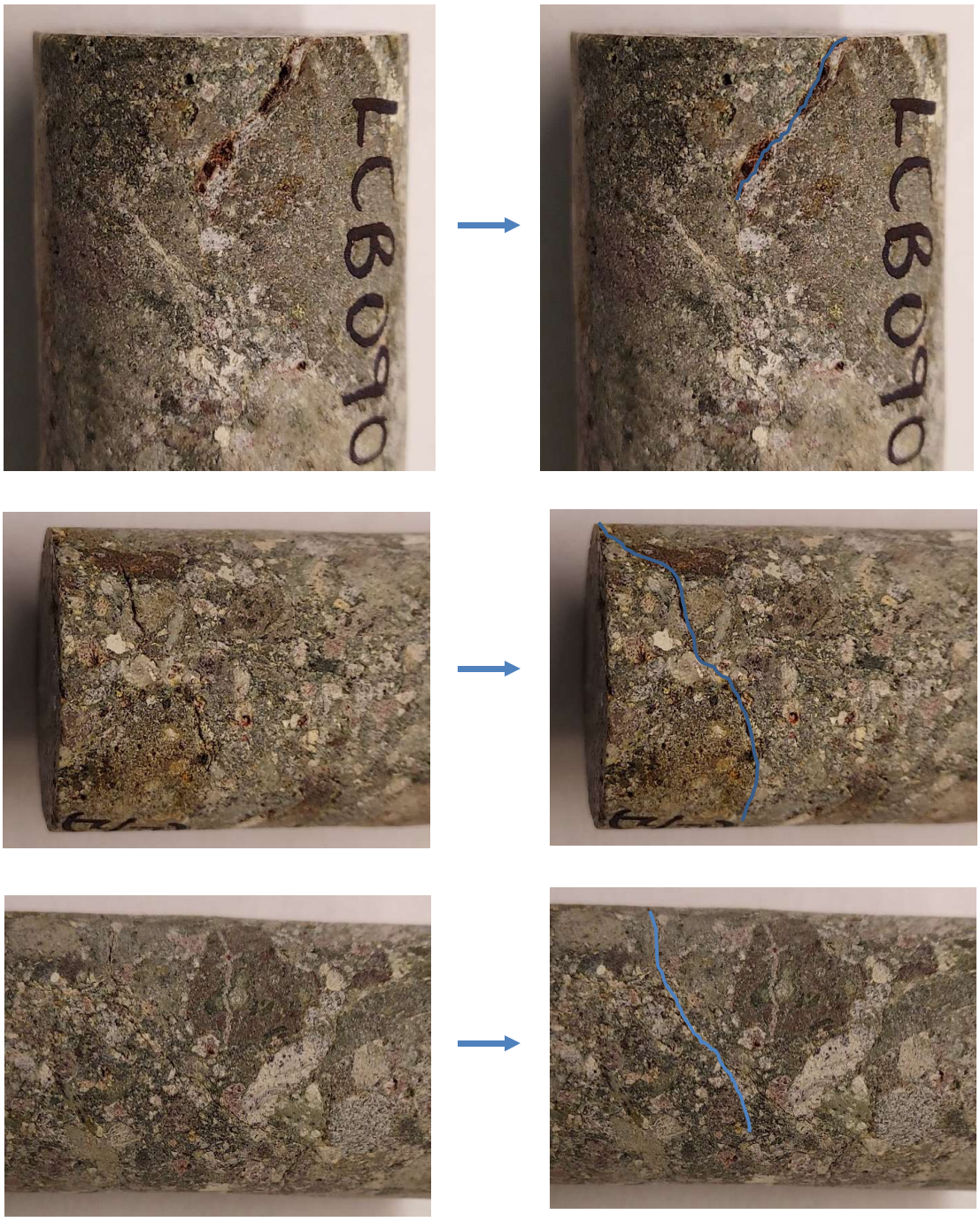

Figure B-18. Core photographs and annotated fractures for LCB090314-5

3. LCB091414-2

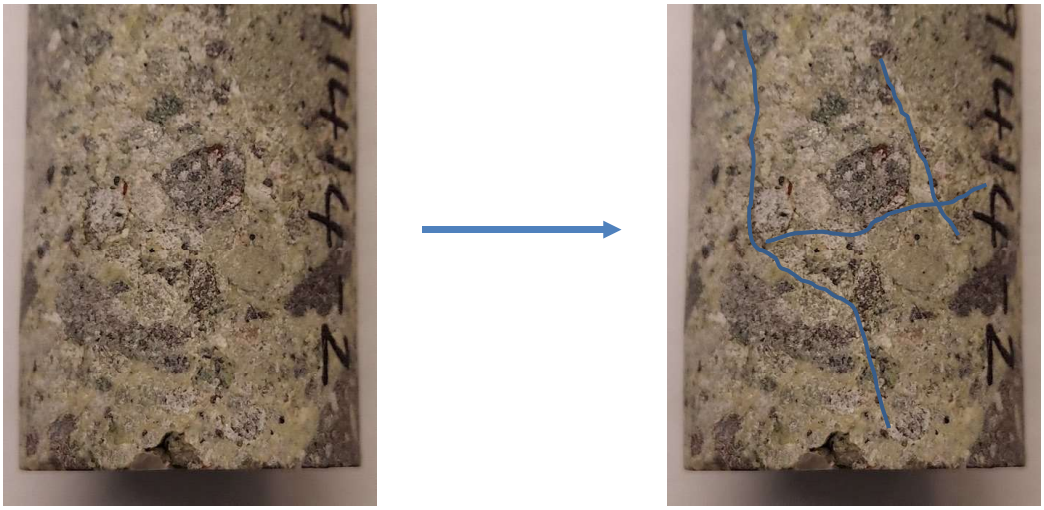

Figure B-19. Core photographs and annotated fractures for LCB091414-2

4. LCDLA082913-1

Figure B-20. Core photographs and annotated fractures for LCDLA082913-1

5. LCDLA082913-2

Figure B-21. Core photographs and annotated fractures for LCDLA082913-2

6. LCG090714-2c

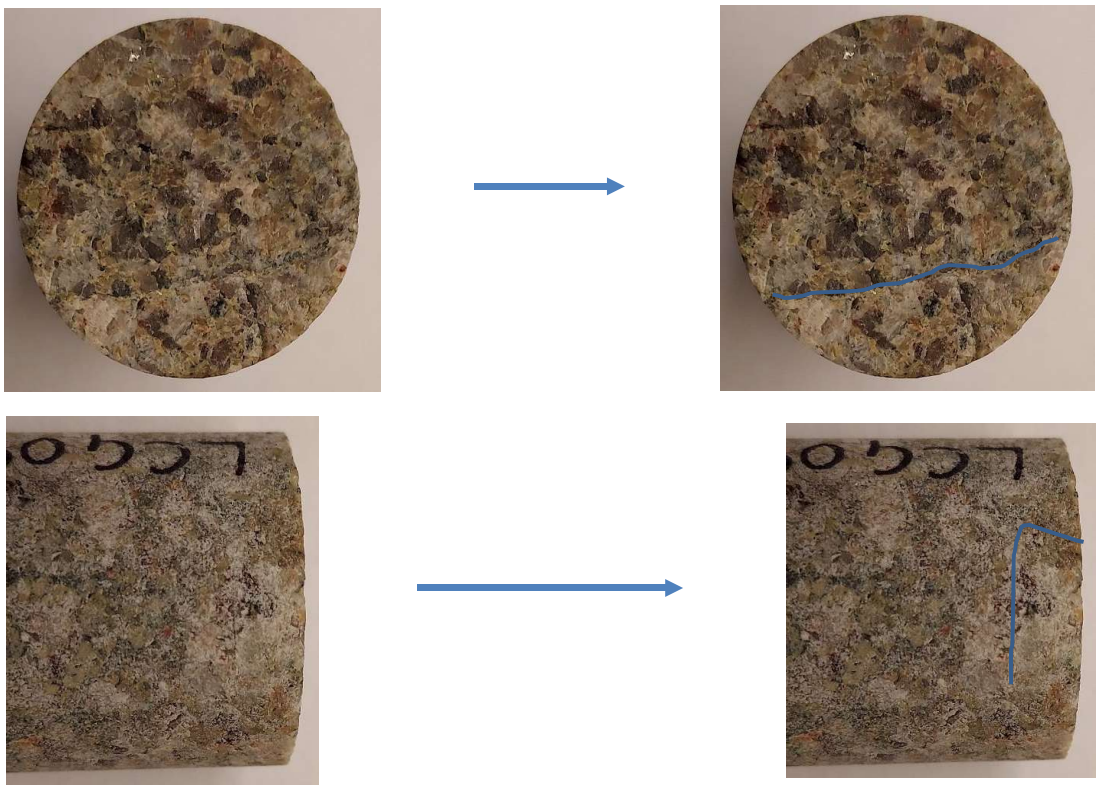

Figure B-22. Core photographs and annotated fractures for LCG090714-2c

7. LCG090714-3a

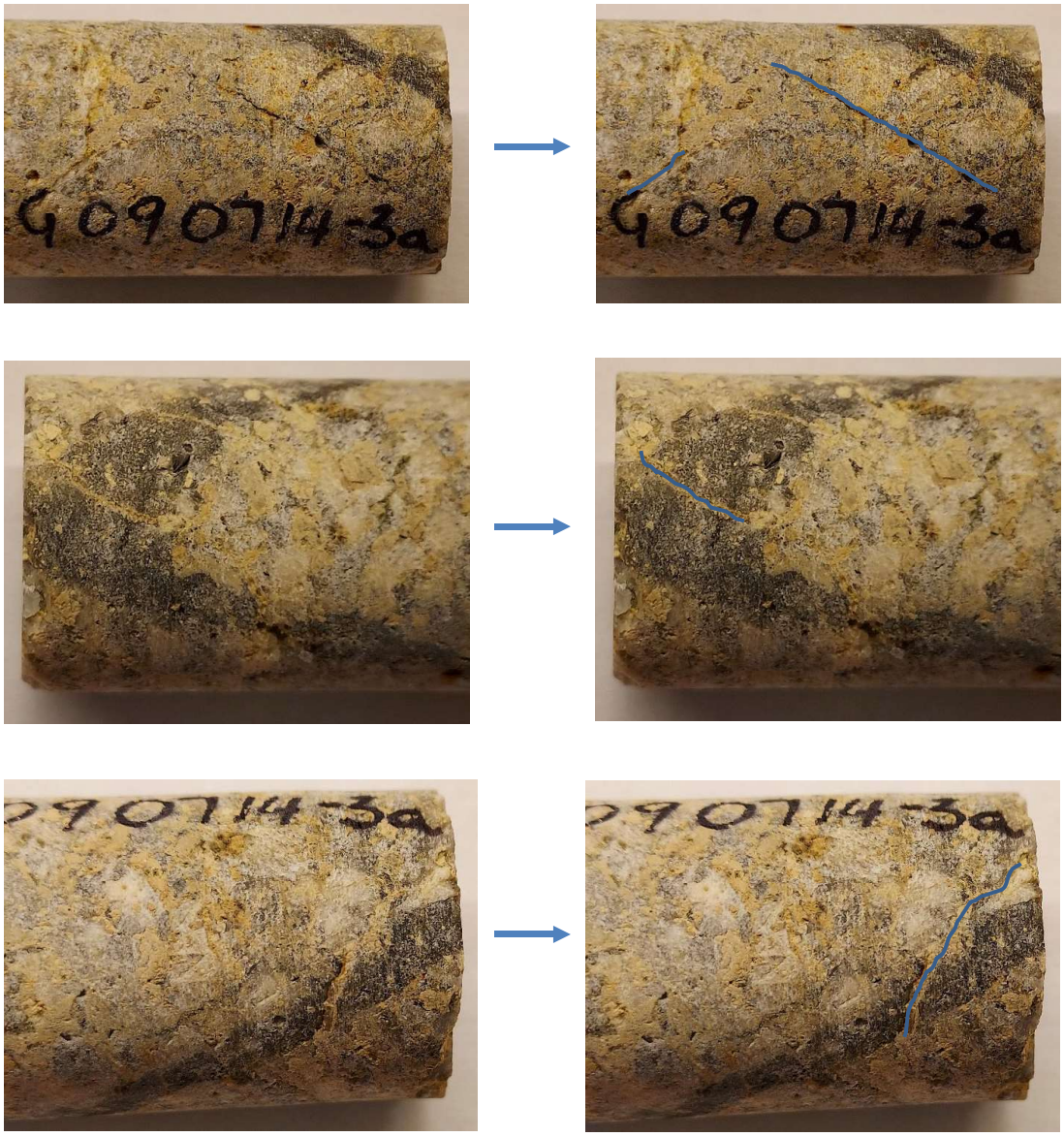

Figure B-23. Core photographs and annotated fractures for LCG090714-3a

8. LCG090714-3b

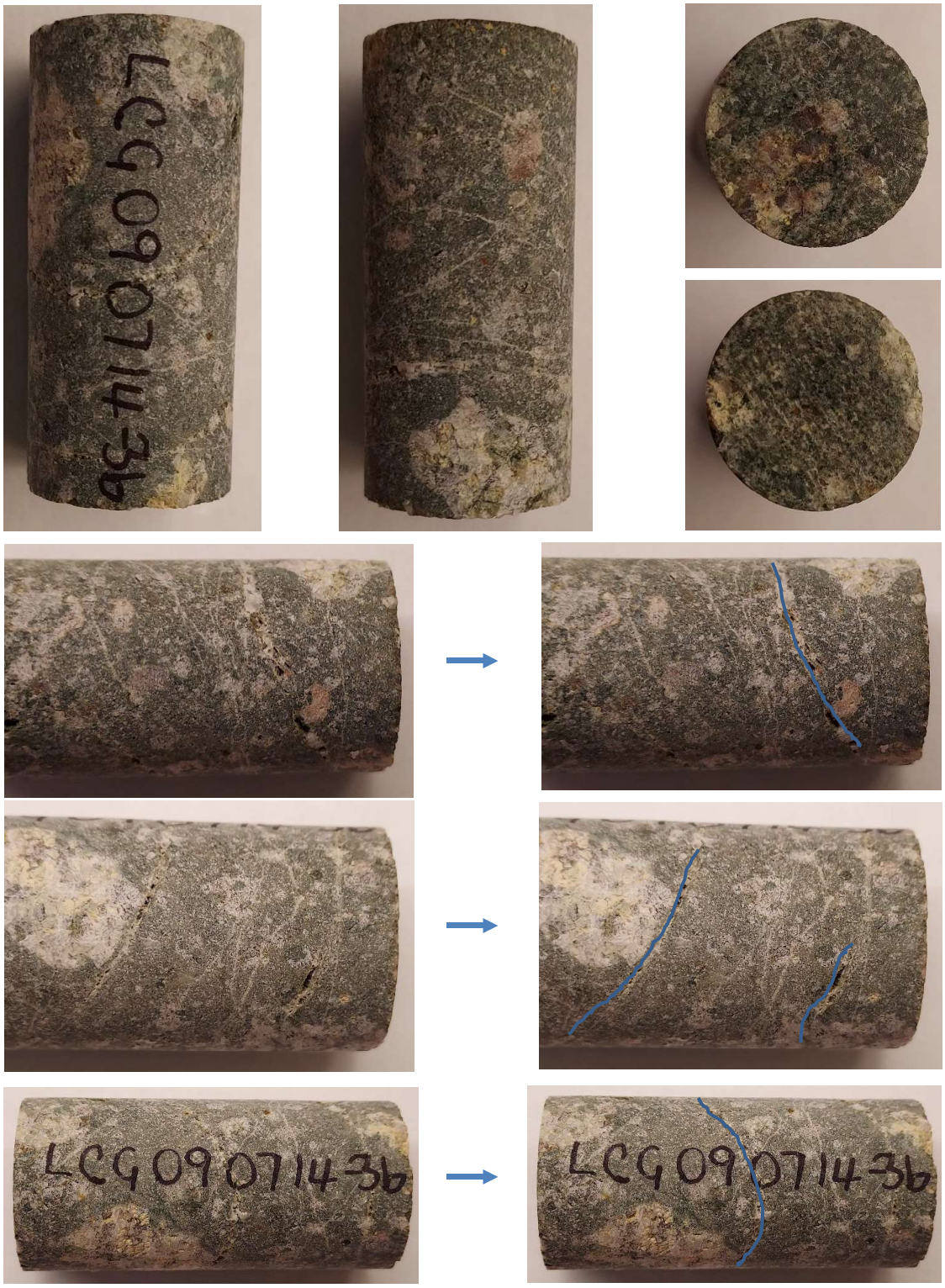

Figure B-24. Core photographs and annotated fractures for LCG090714-3b

9. LCG091314-1b

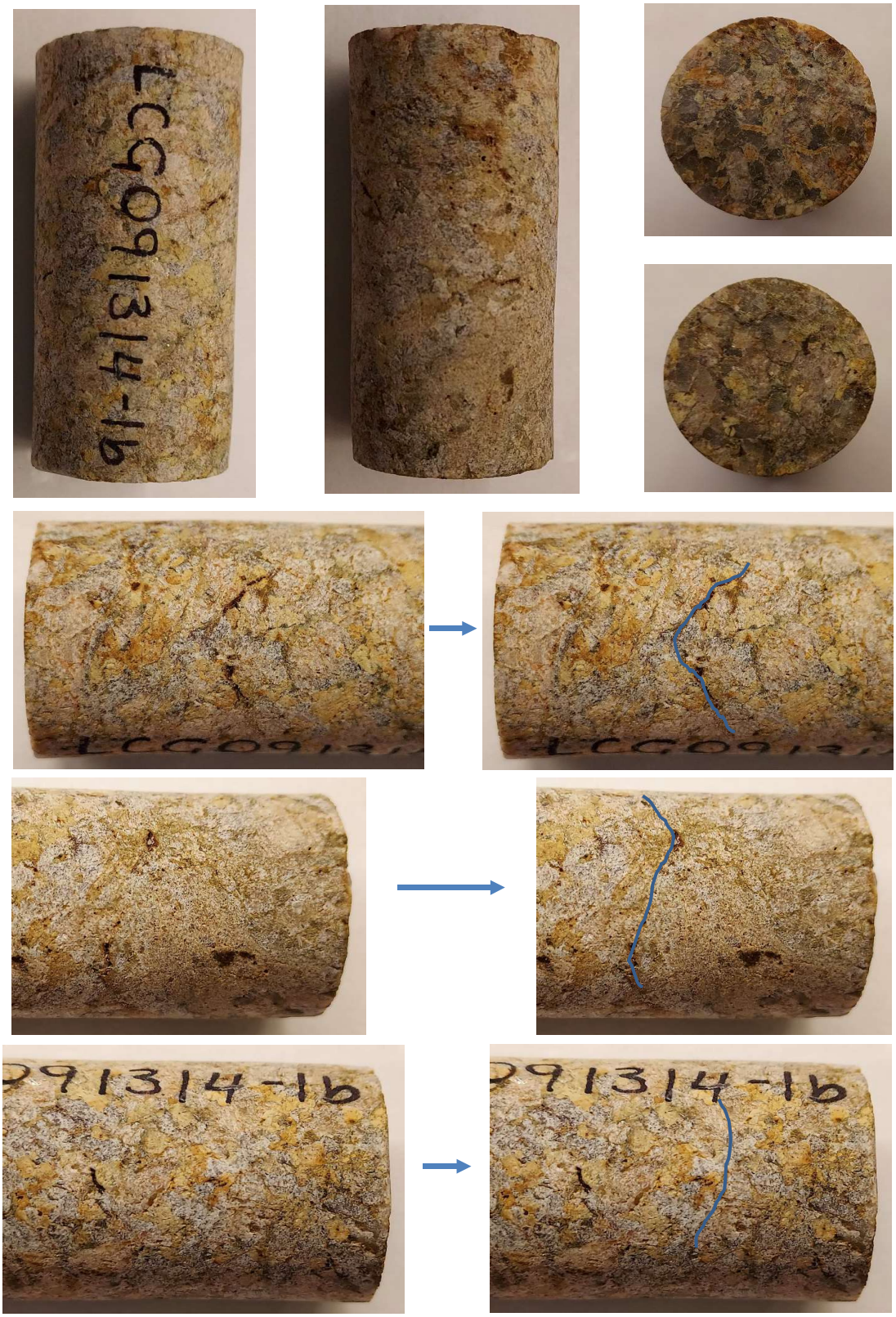

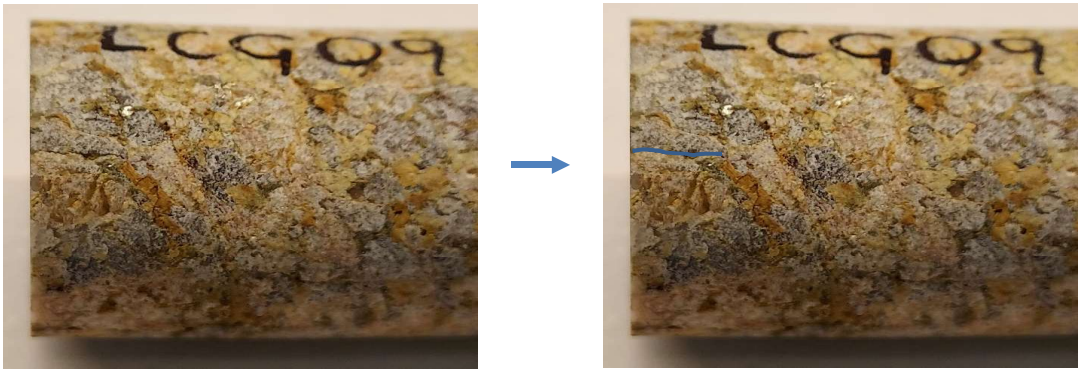

Figure B-25. Core photographs and annotated fractures for LCG090714-1b

10. LCT091014-1a

Figure B-26. Core photographs and annotated fractures for LCT091014-1a

11. LCT091014-1b

Figure B-27. Core photographs and annotated fractures for LCT091014-1b

12. LCT091514-3(1)

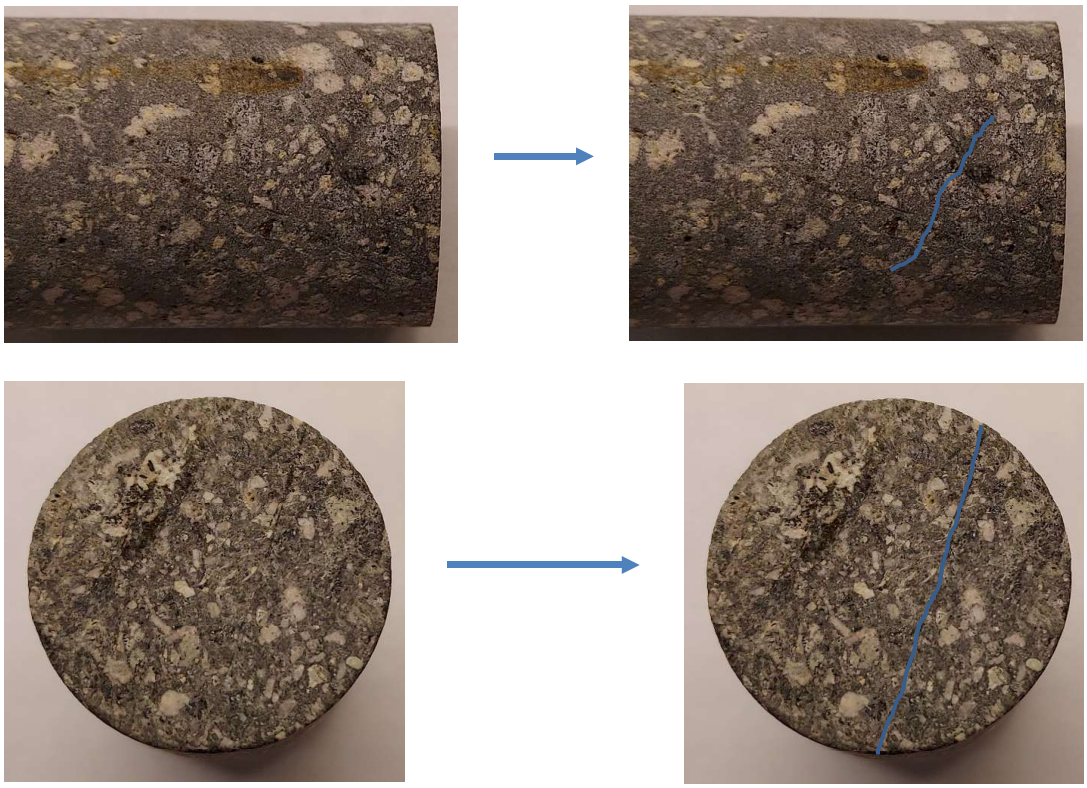

Figure B-28. Core photographs and annotated fractures for LCT091514-3(1)

13. LCT091514-3(2)

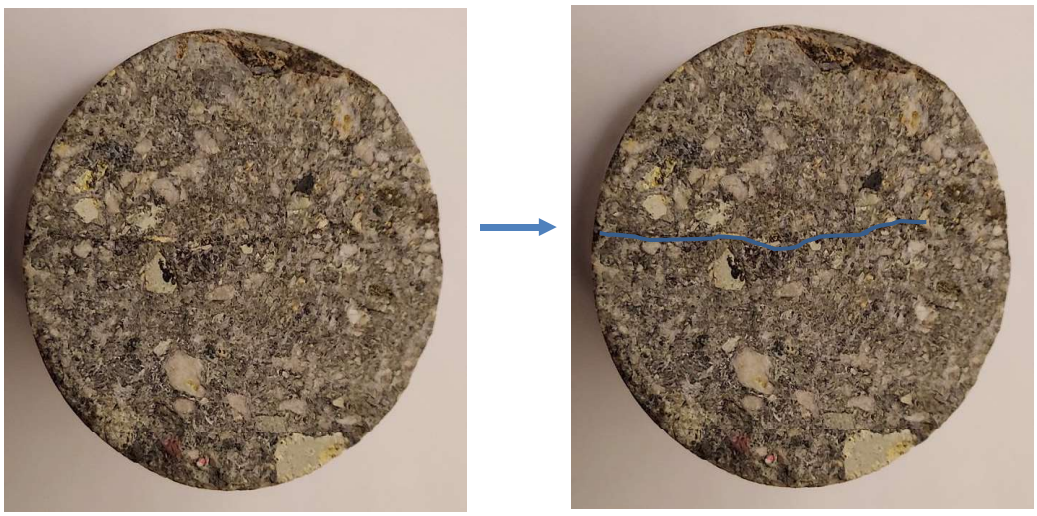

Figure B-29. Core photographs and annotated fractures for LCT091514-3(2)

14. LCTBV071714-5a

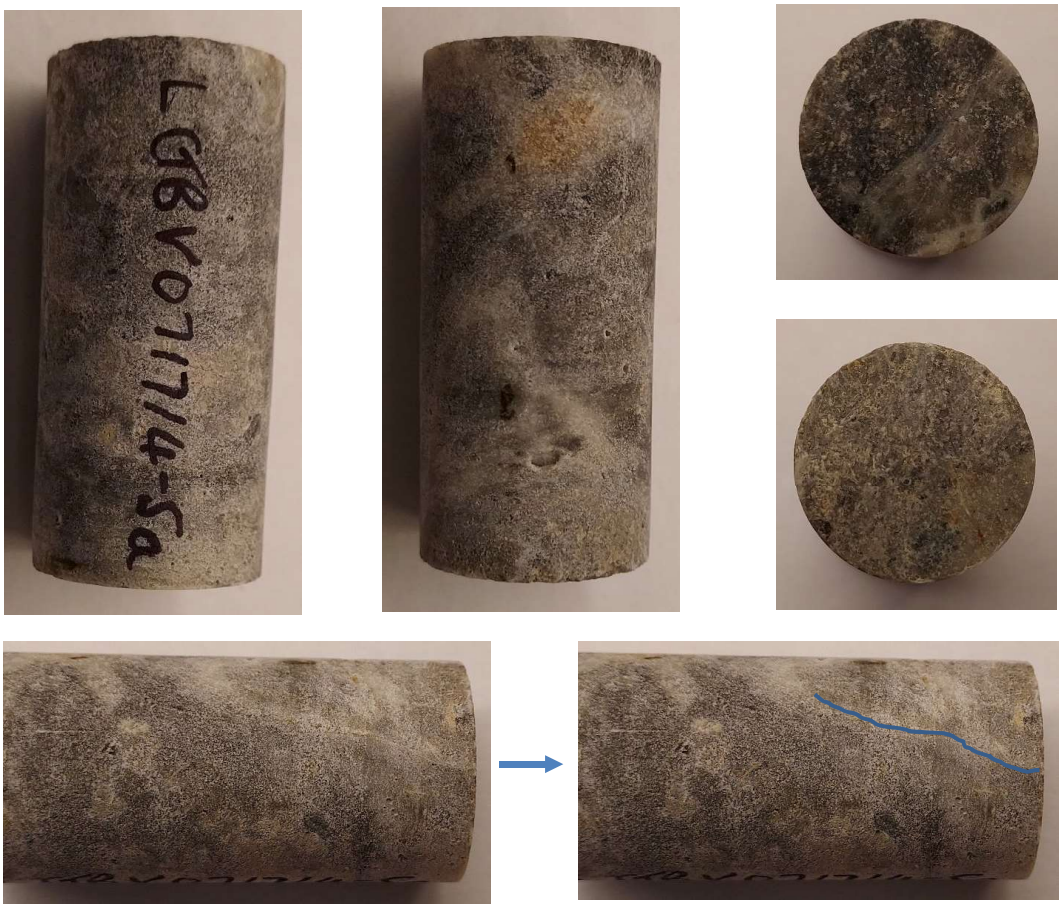

Figure B-30. Core photographs and annotated fractures for LCTBV071714-5a

15. LCTV090314-4a

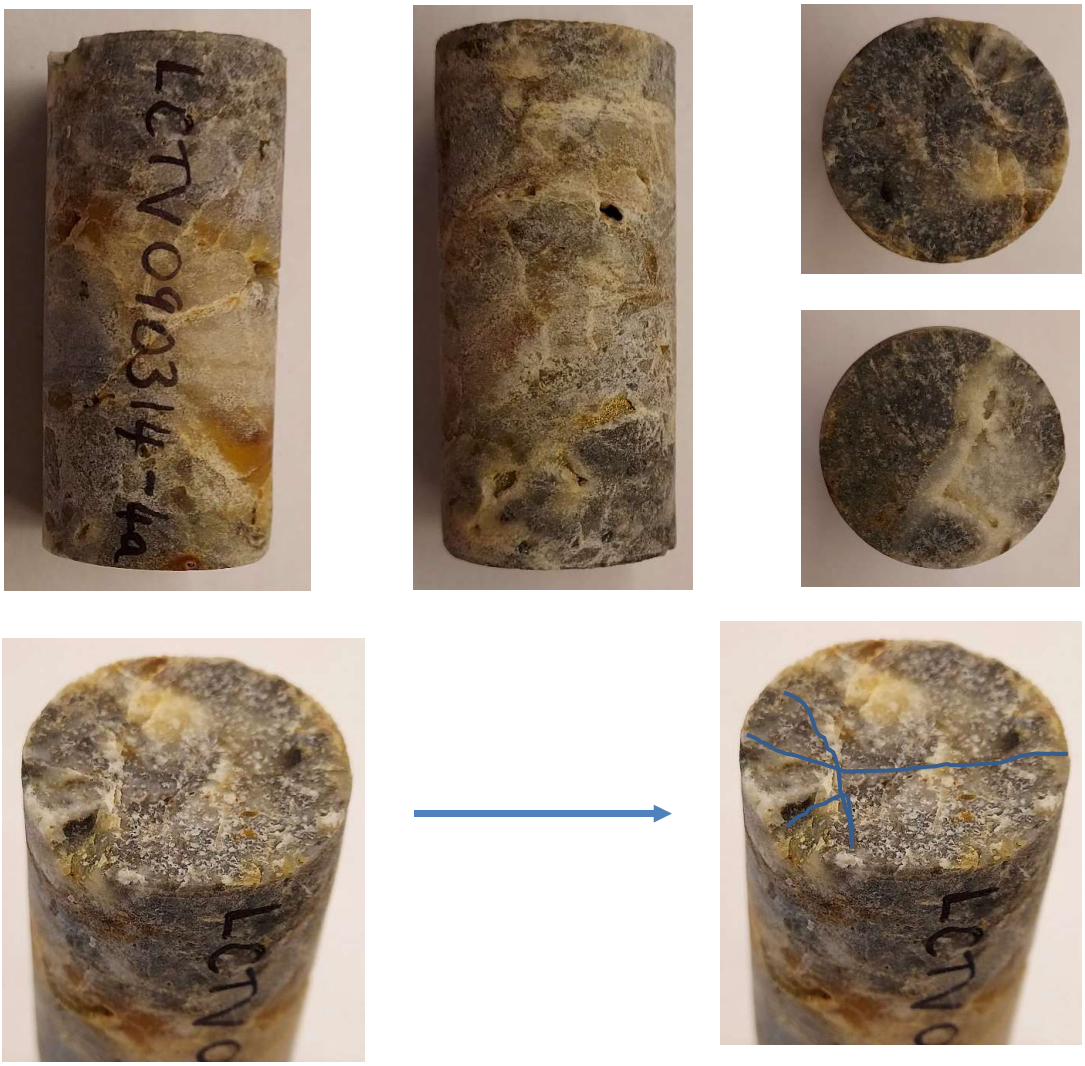

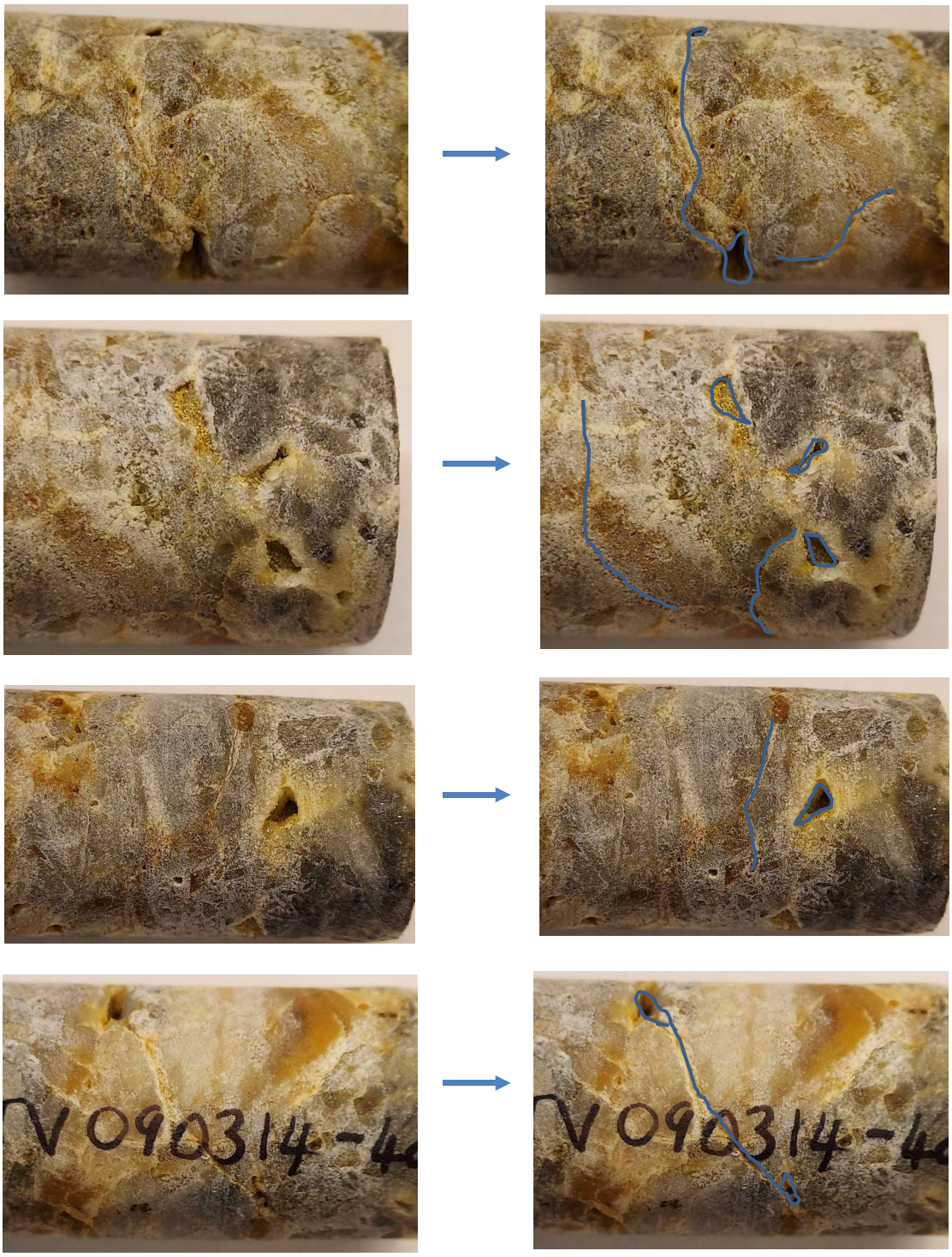

Figure B-31. Core photographs and annotated fractures for LCTV090314-4a

16. LCTV091014-1c

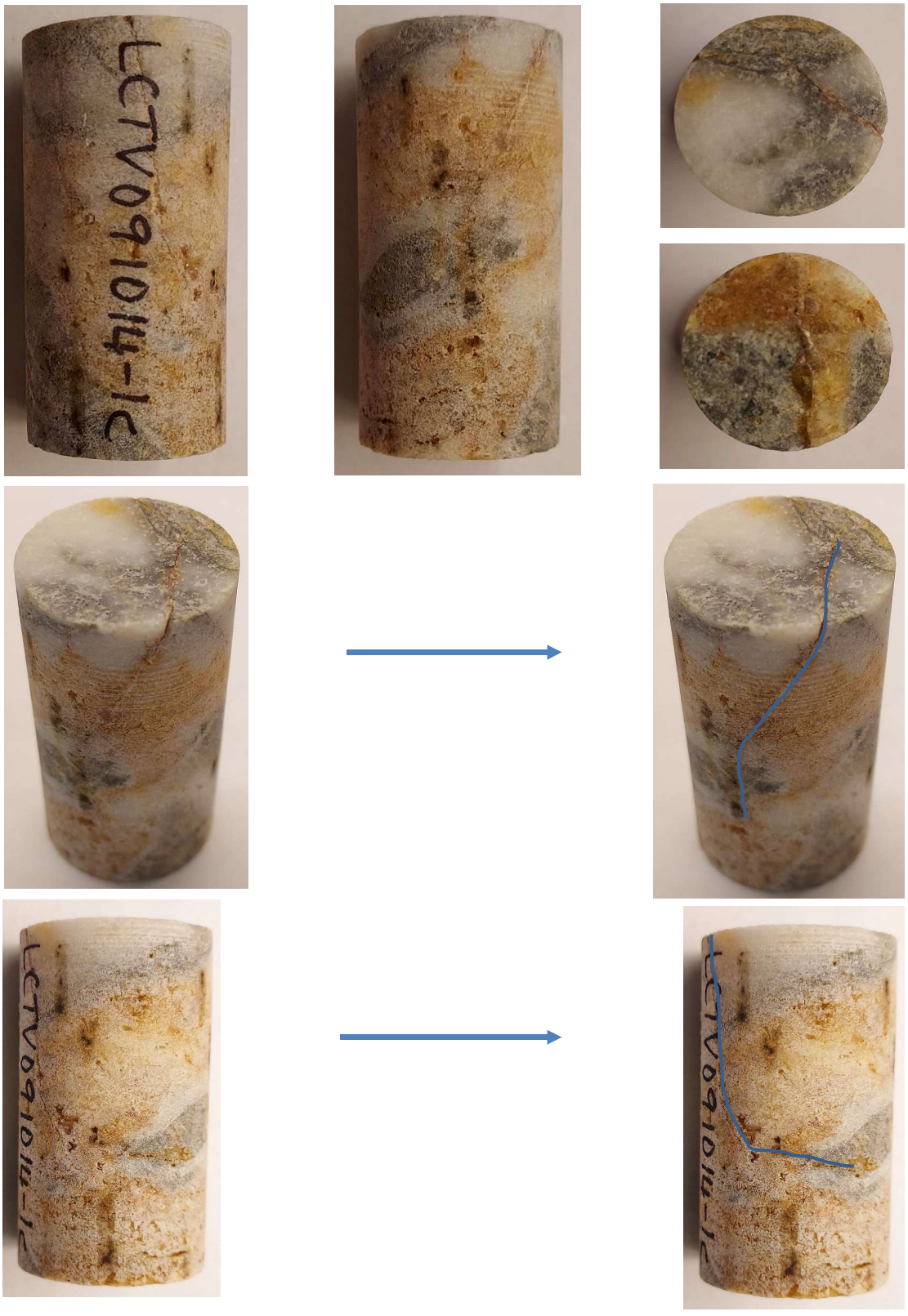

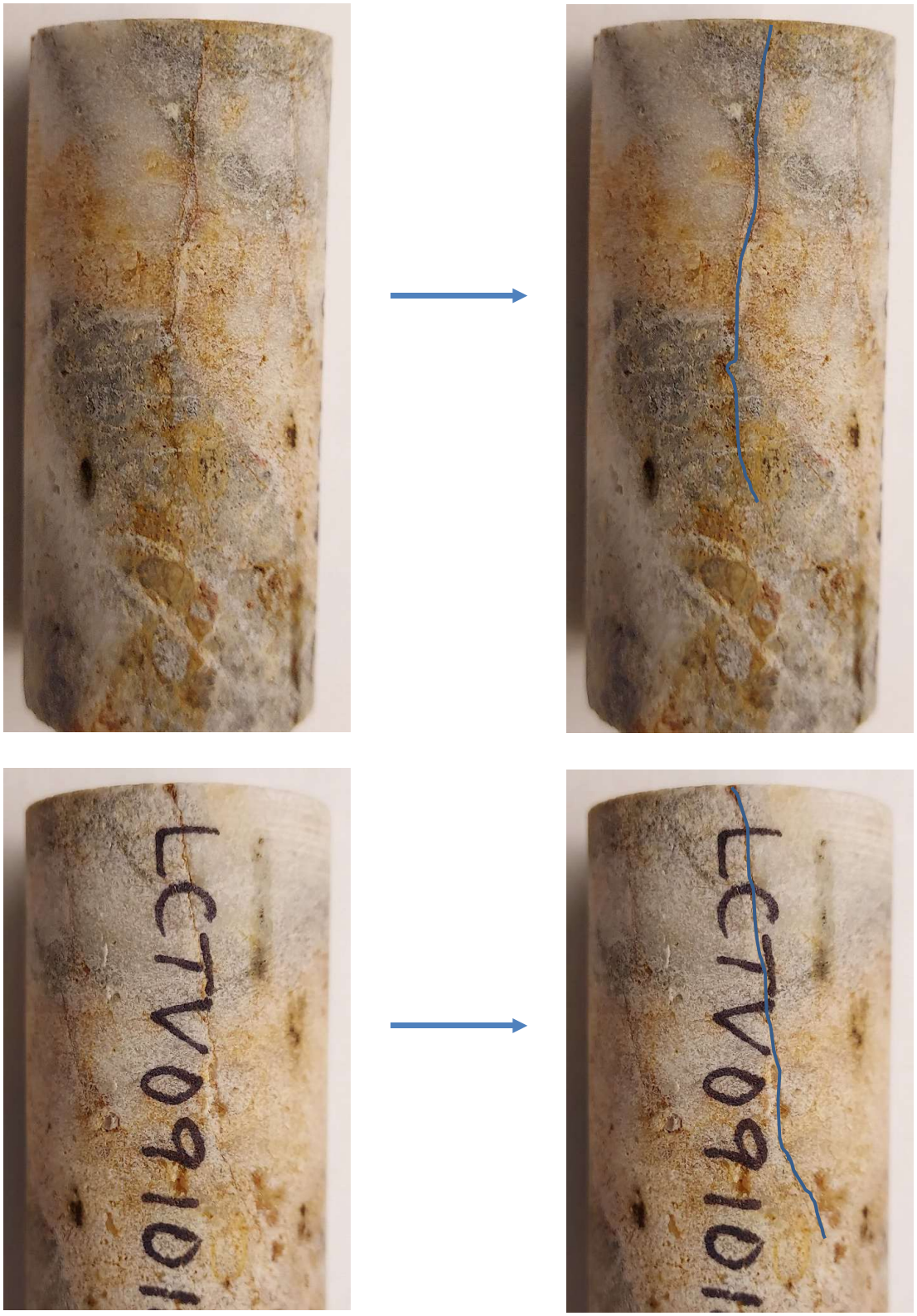

Figure B-32. Core photographs and annotated fractures for LCTV091014-1c

17. LCTV091014-1d

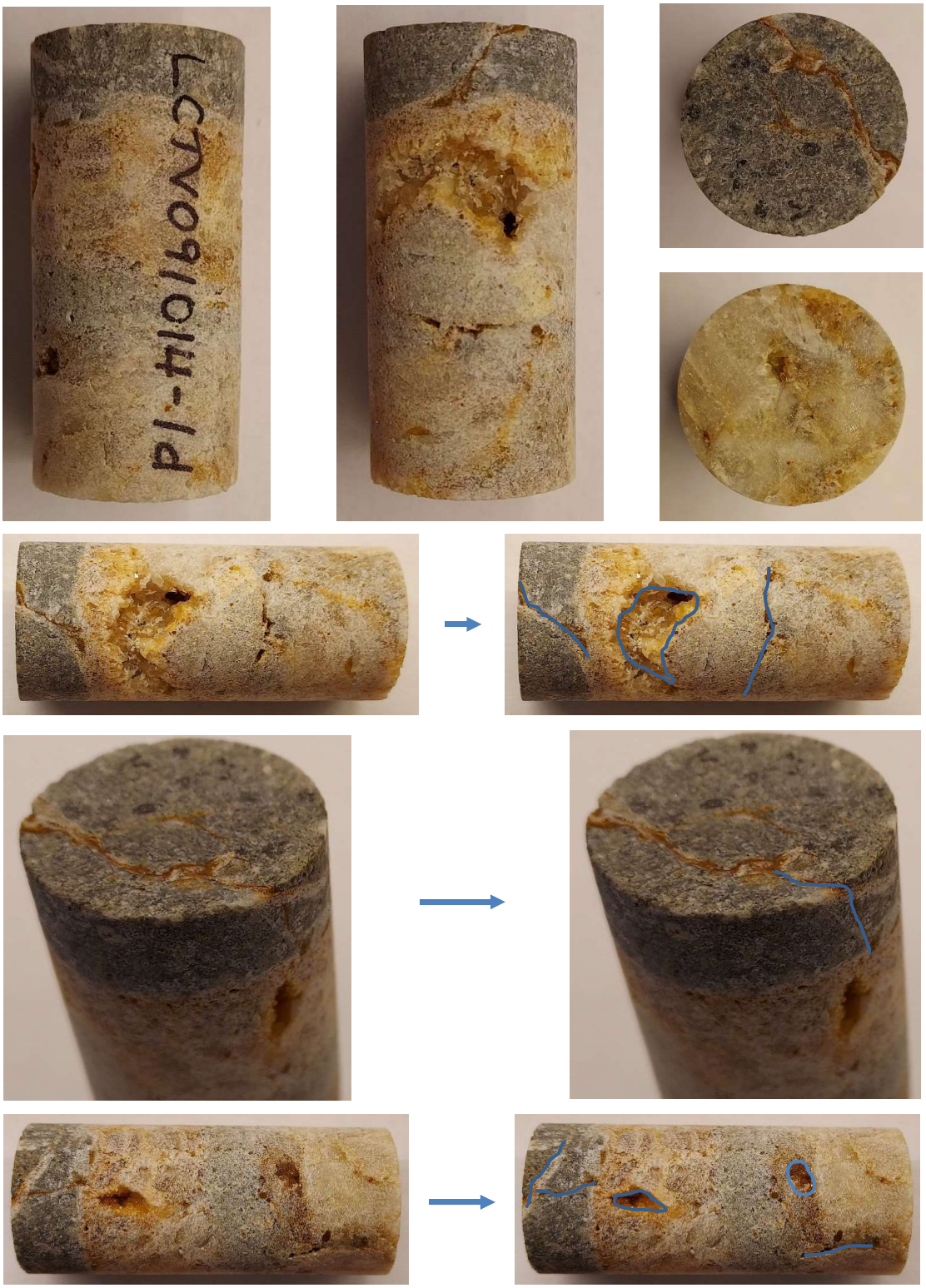

Figure B-33. Core photographs and annotated fractures for LCTV091014-1d

B.6 Permeability

B.6.1 Telaga Bodas Samples

1. K33_0191_00

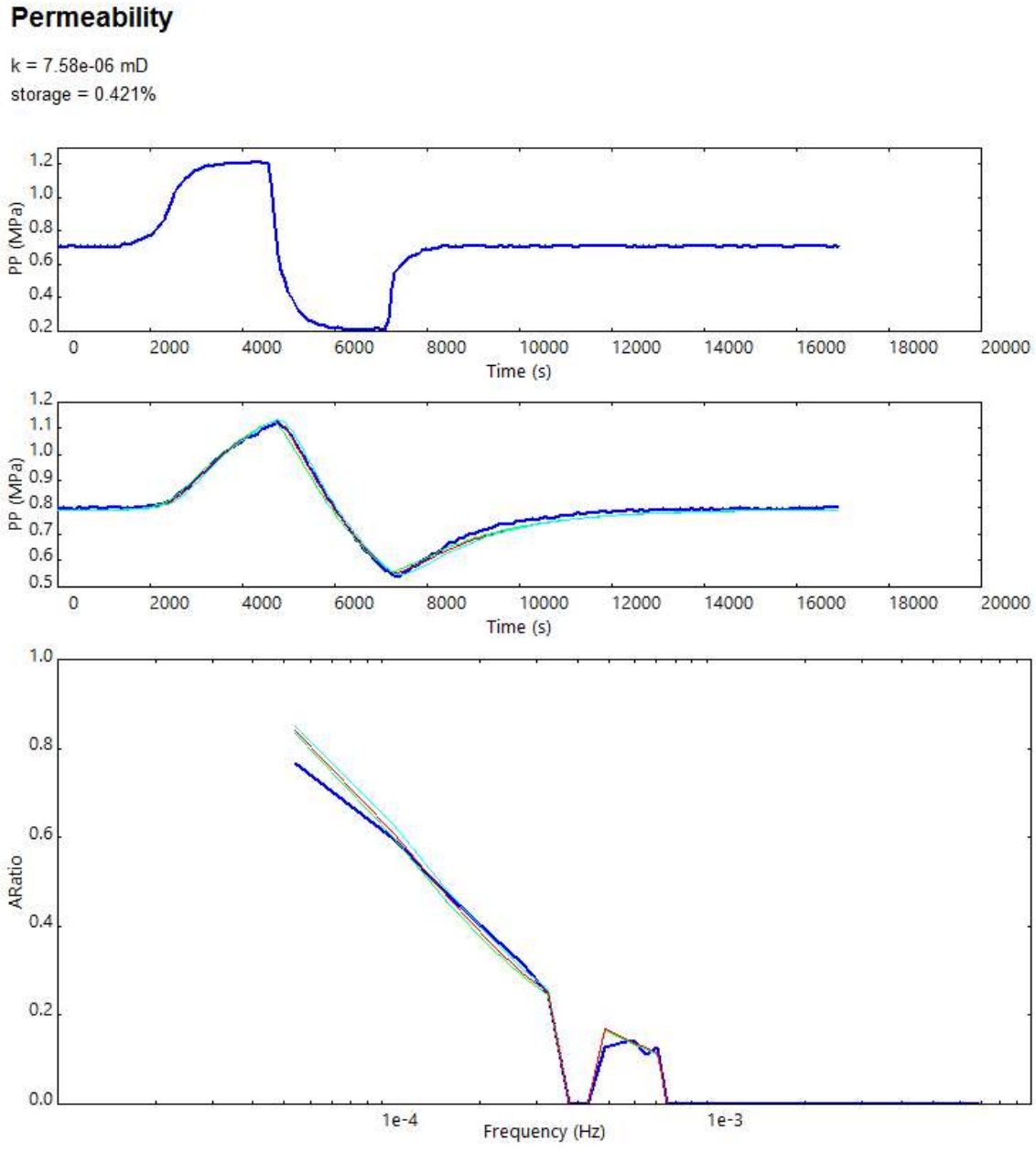

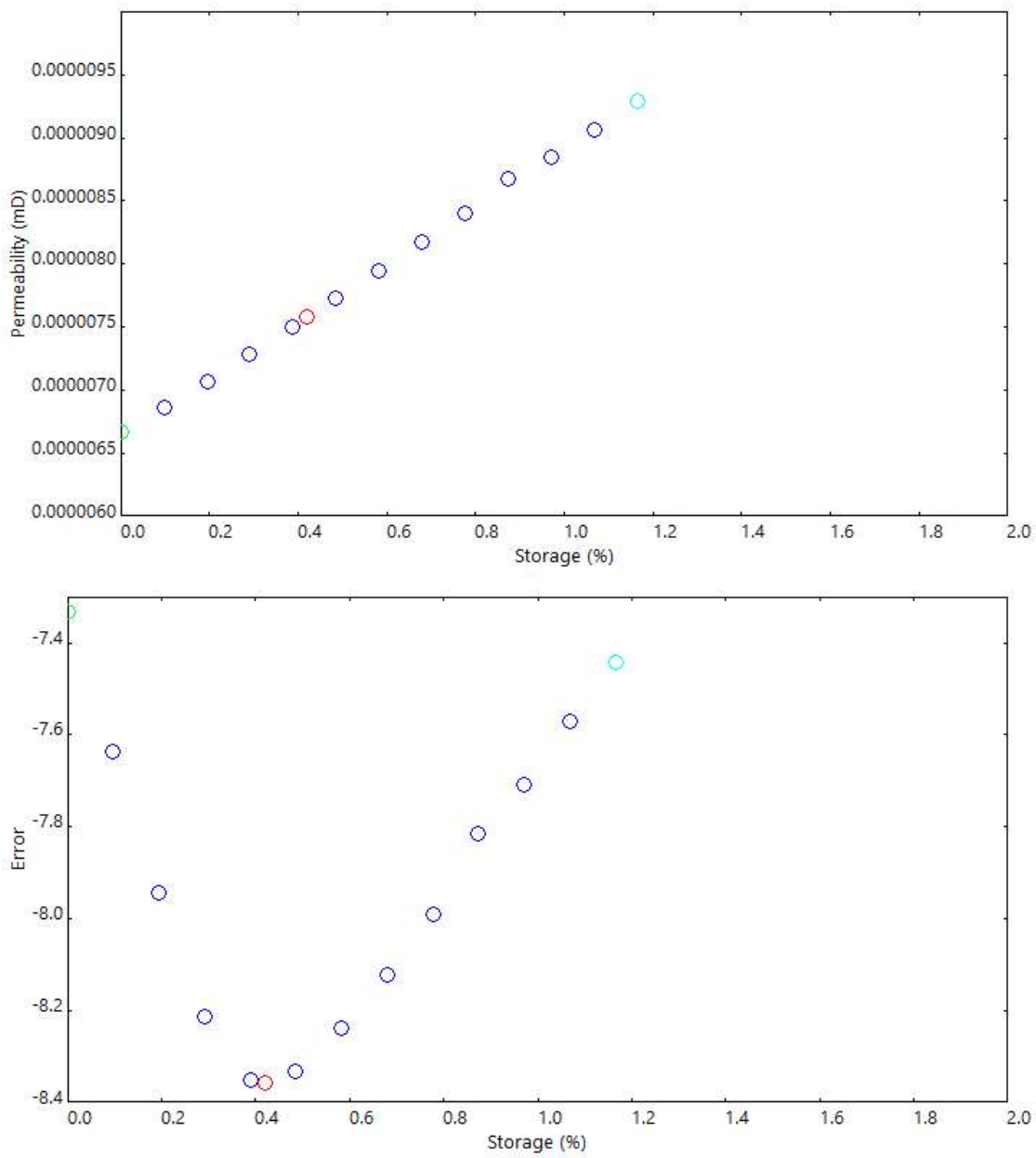

Figure B-34. Permeability results for sample K33_0191_00

2. K33_0191_03

Permeability

k = 5.61e-06 mD
storage = 0.210%

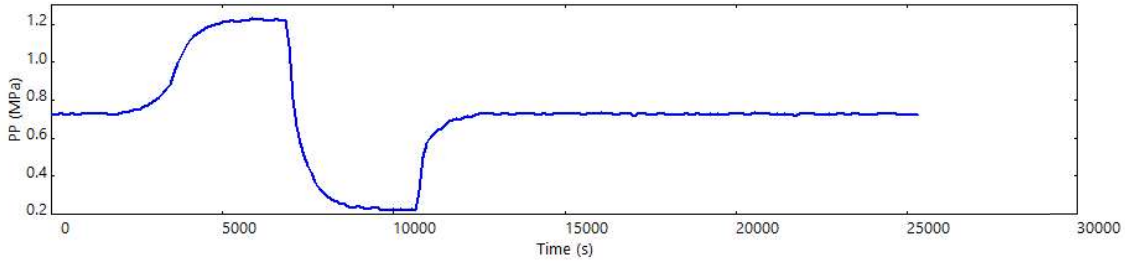

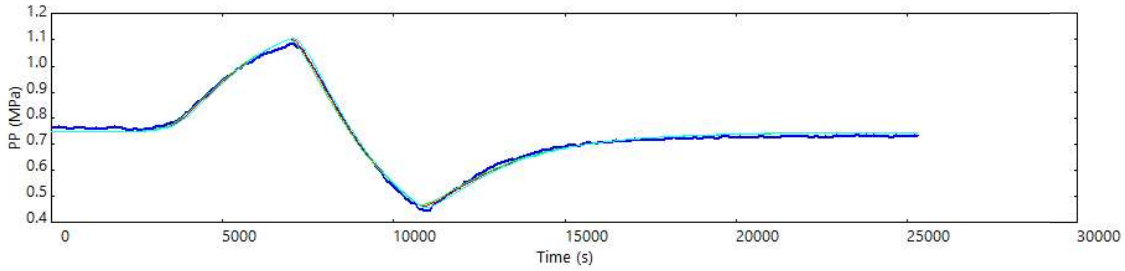

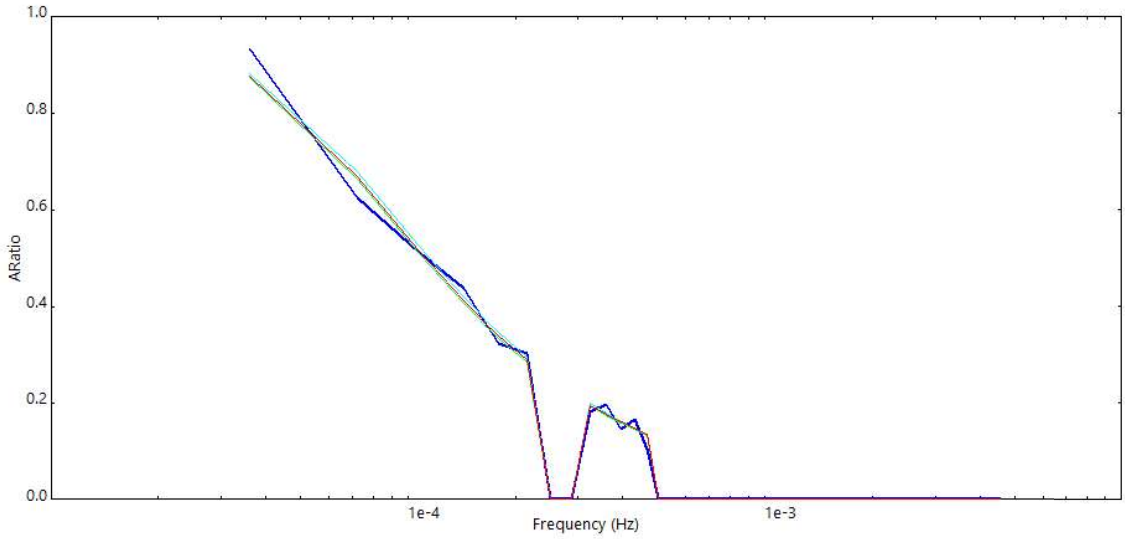

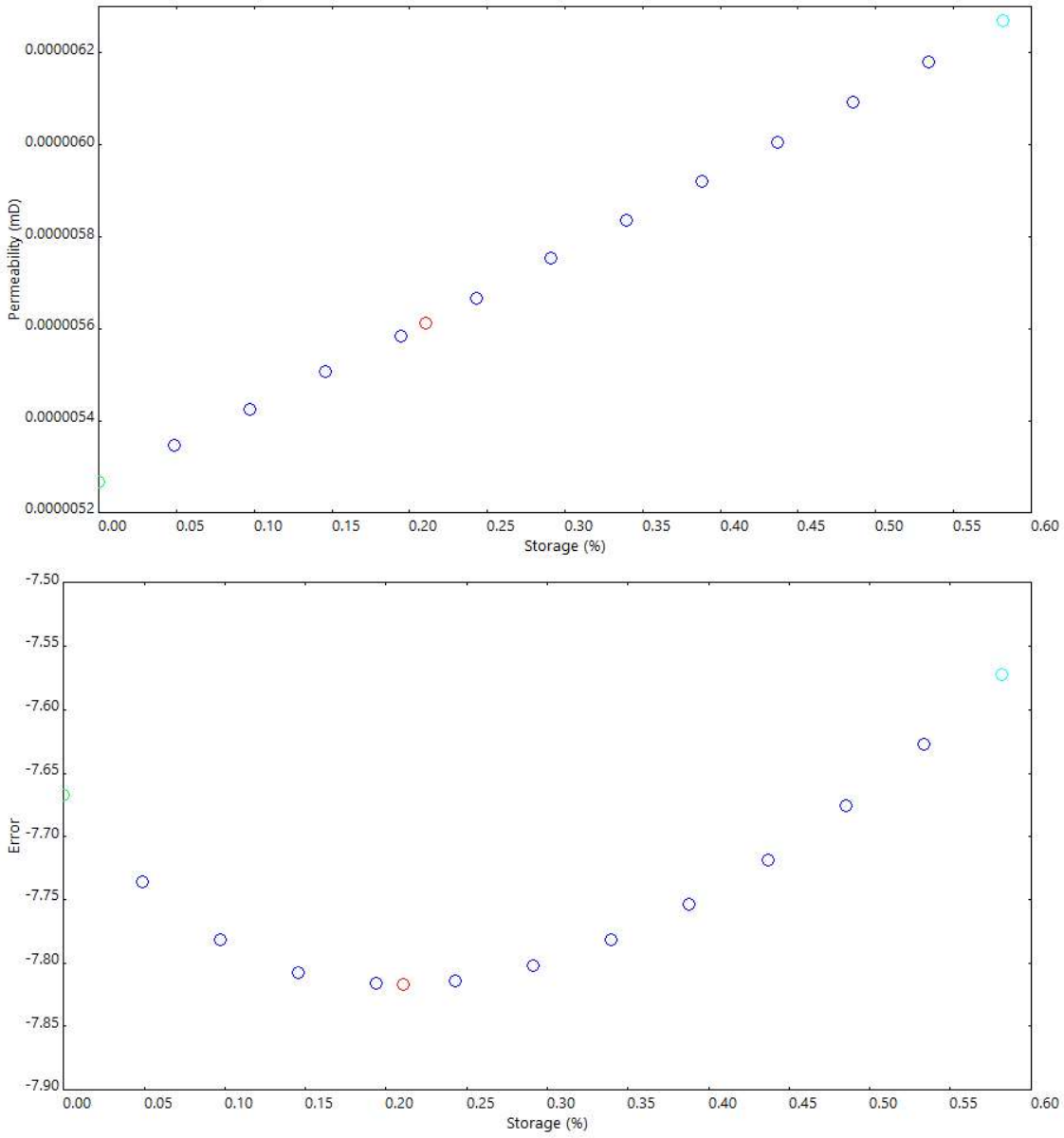

Figure B-35. Permeability results for sample K33_0191_03

3. K33_0192_1277.75

Permeability

k = 7.93e-07 mD
storage = 0.087%

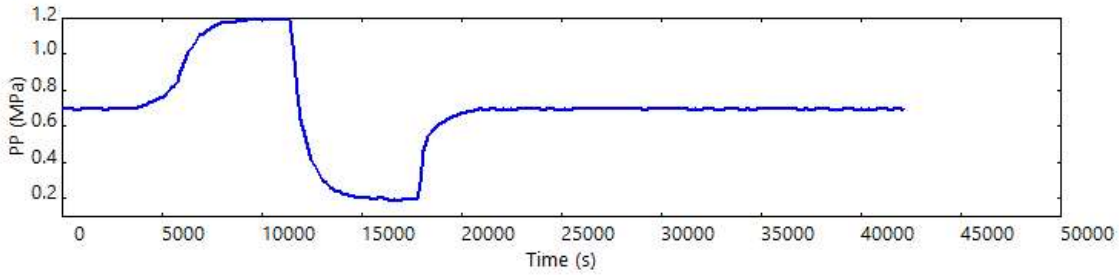

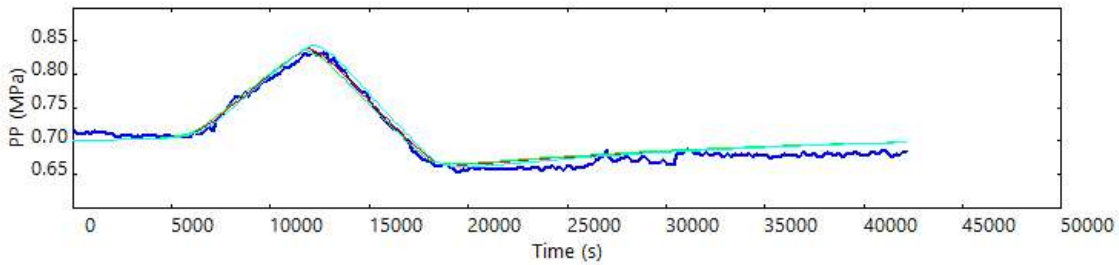

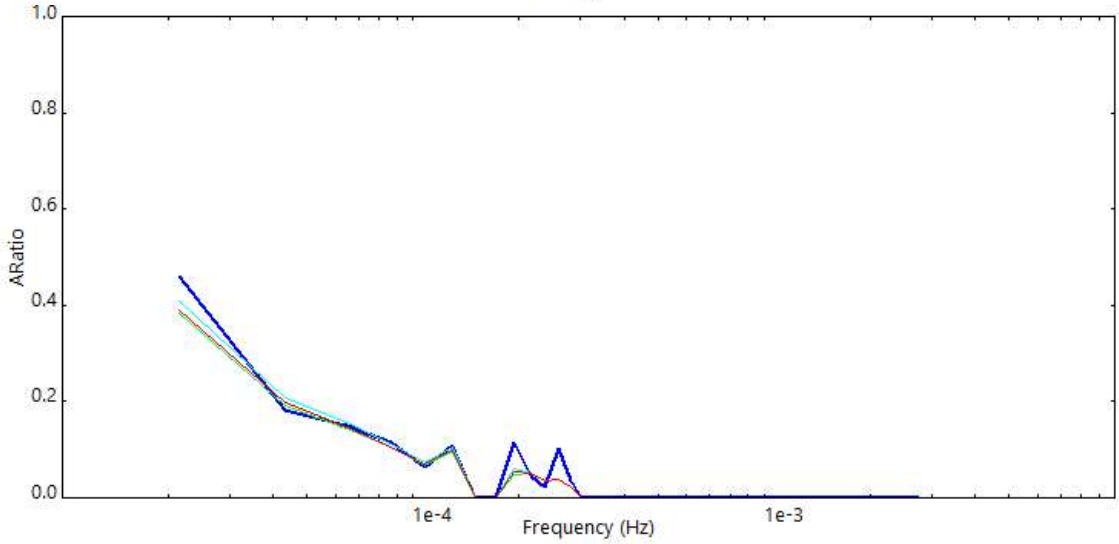

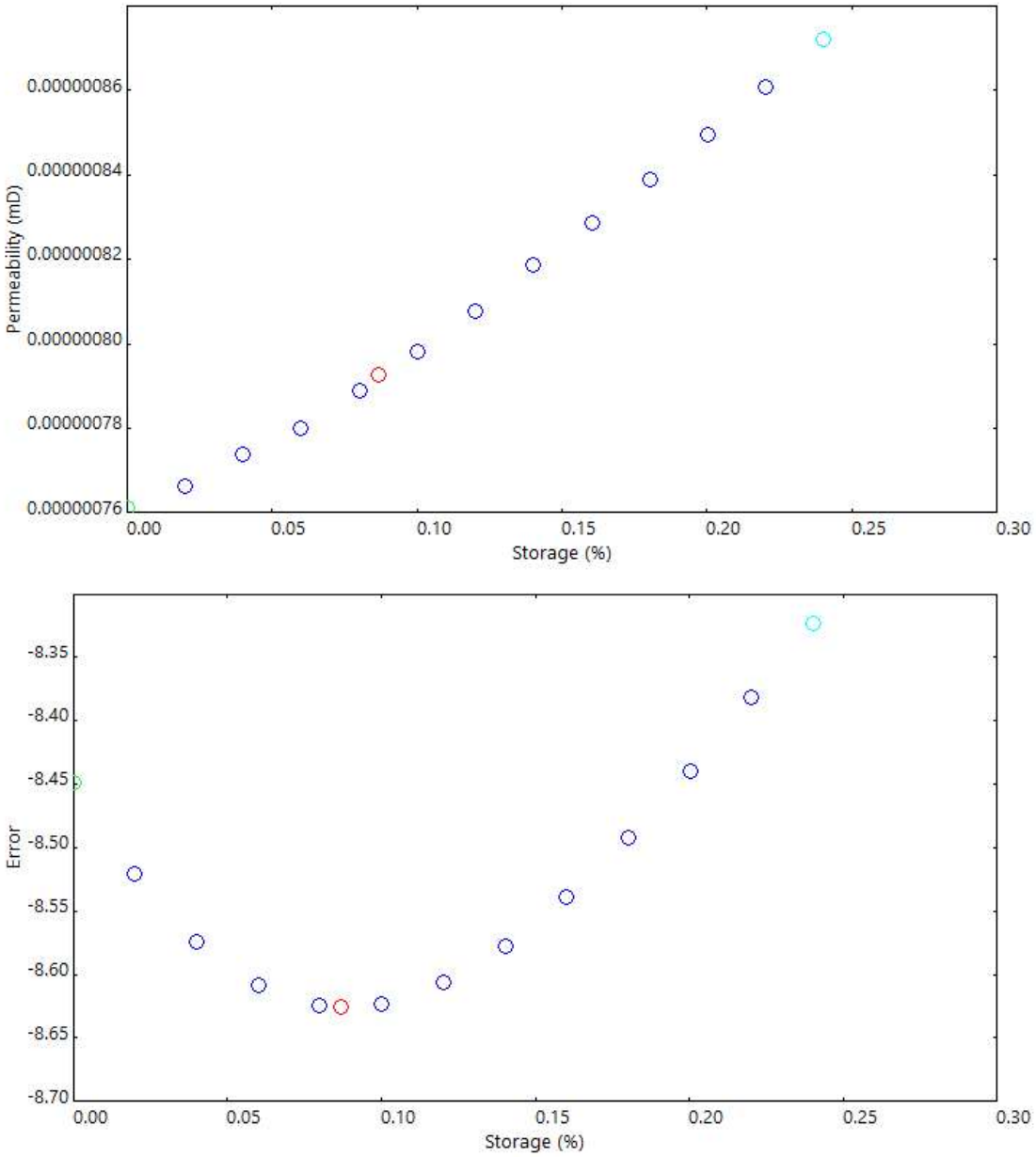

Figure B-36. Permeability results for sample K33_0192_1277.75

4. K33_0364_1752

Permeability

k = 0.000199 mD
storage = 0.731%

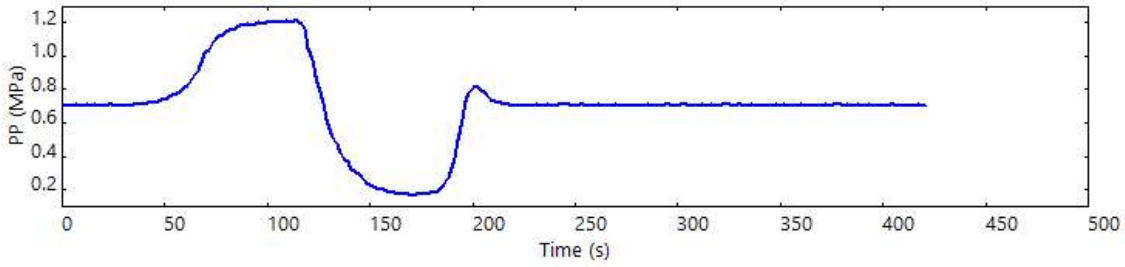

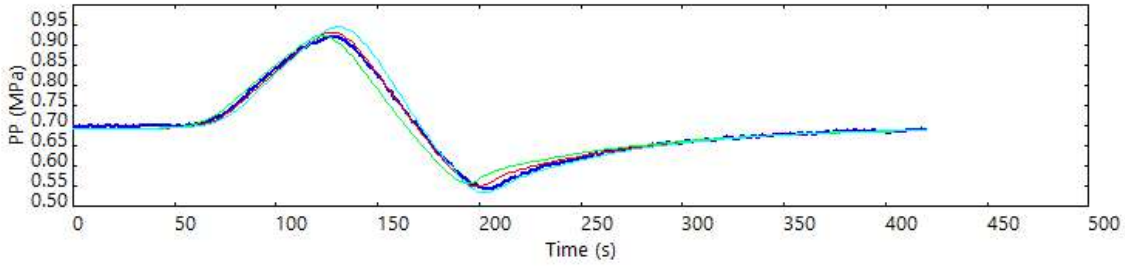

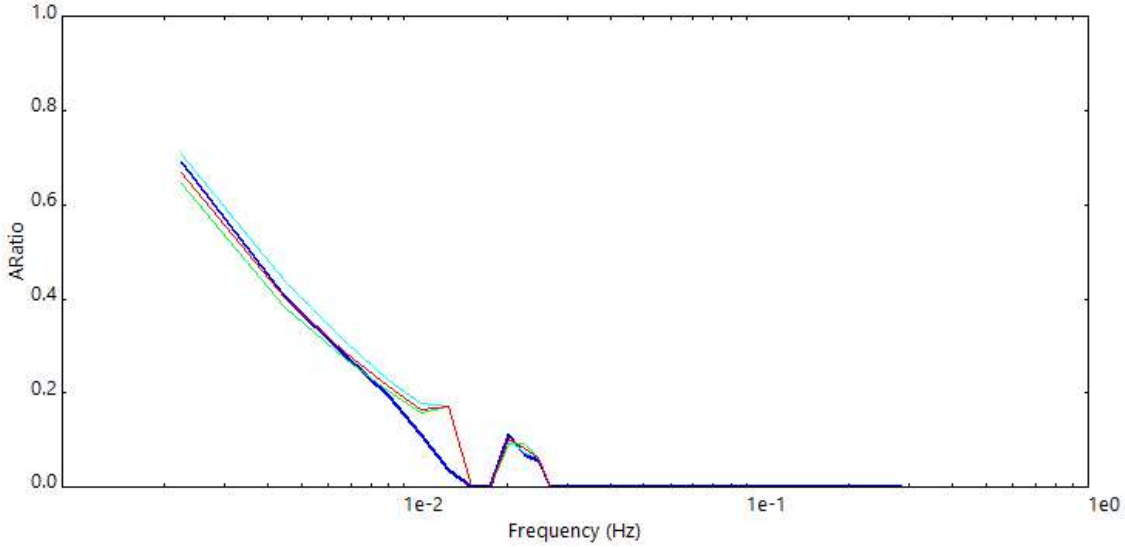

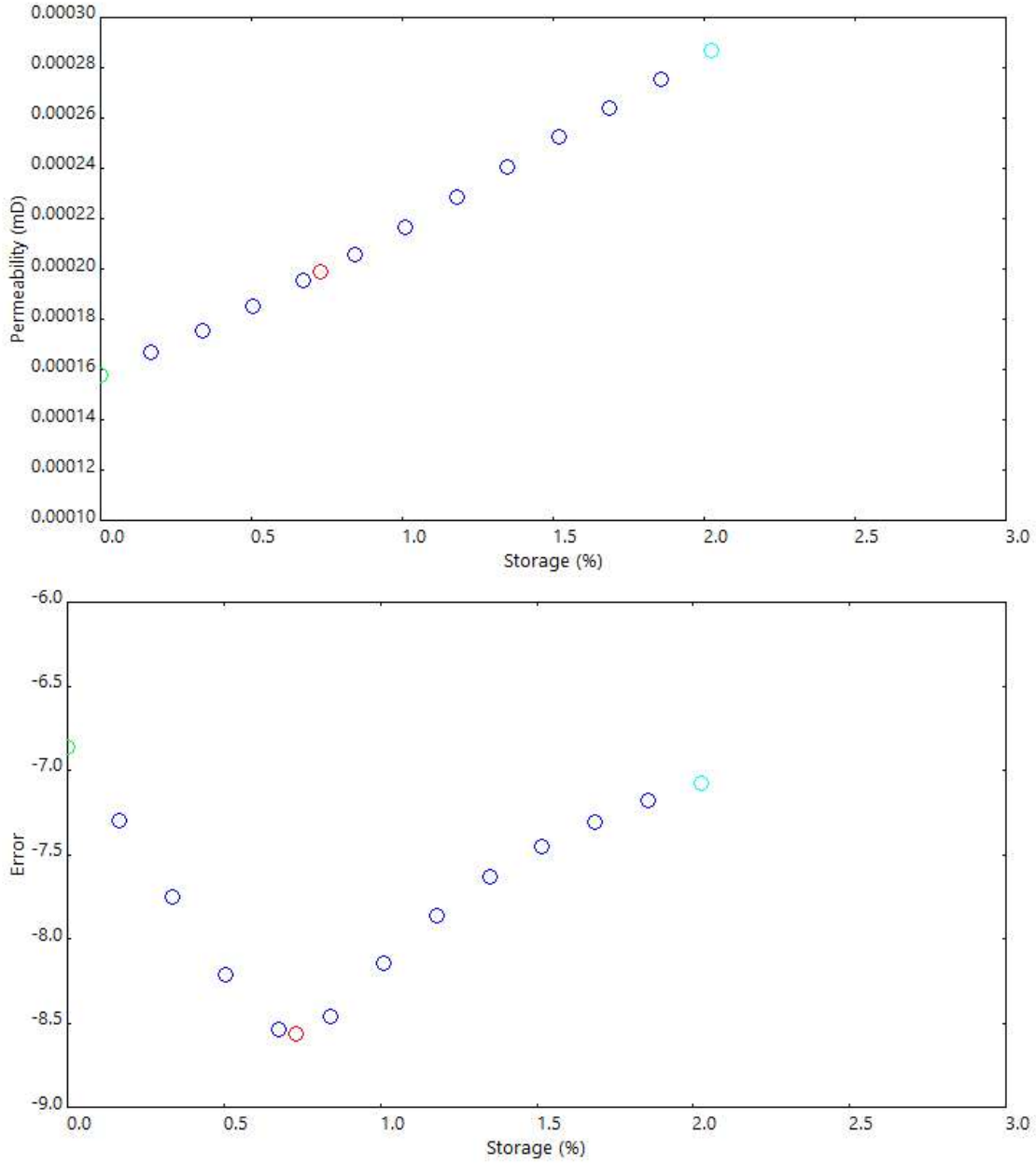

Figure B-37. Permeability results for sample K33_0364_1752

5. K33_0364_1753

Permeability

k = 9.82e-05 mD
storage = 0.248%

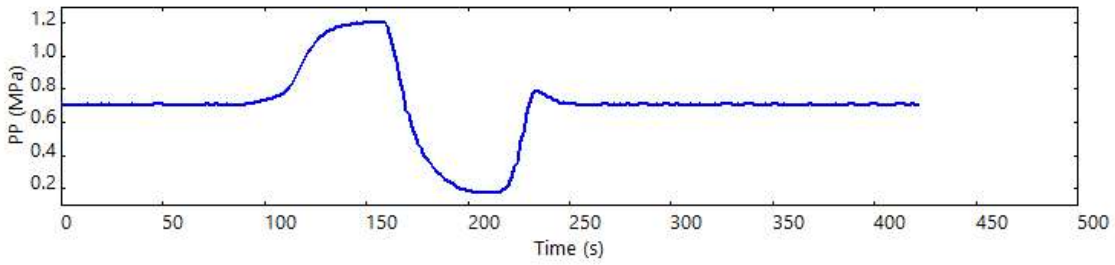

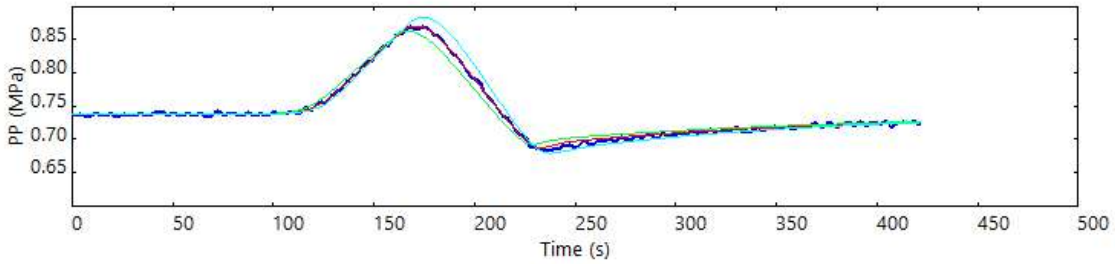

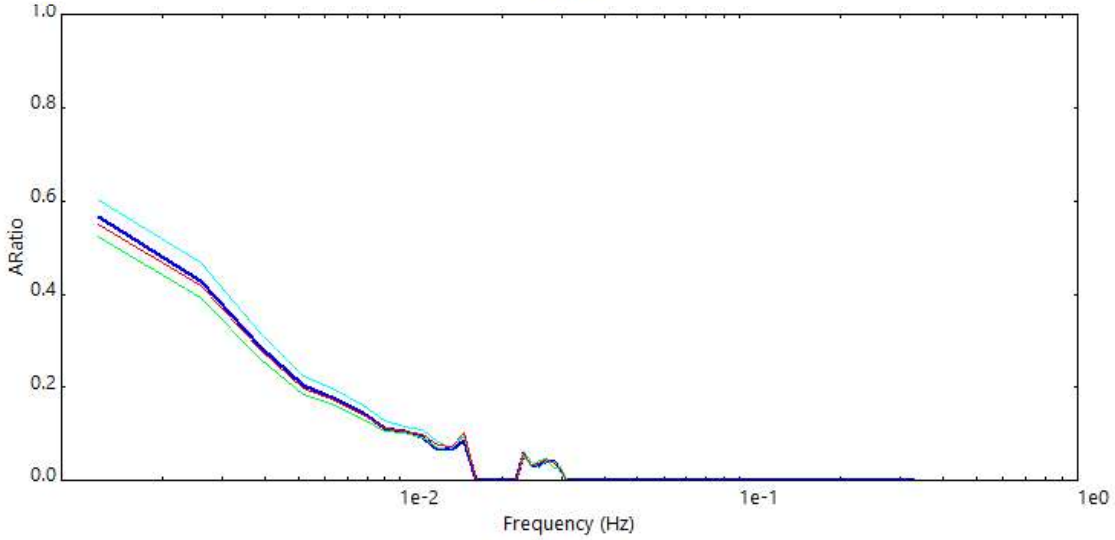

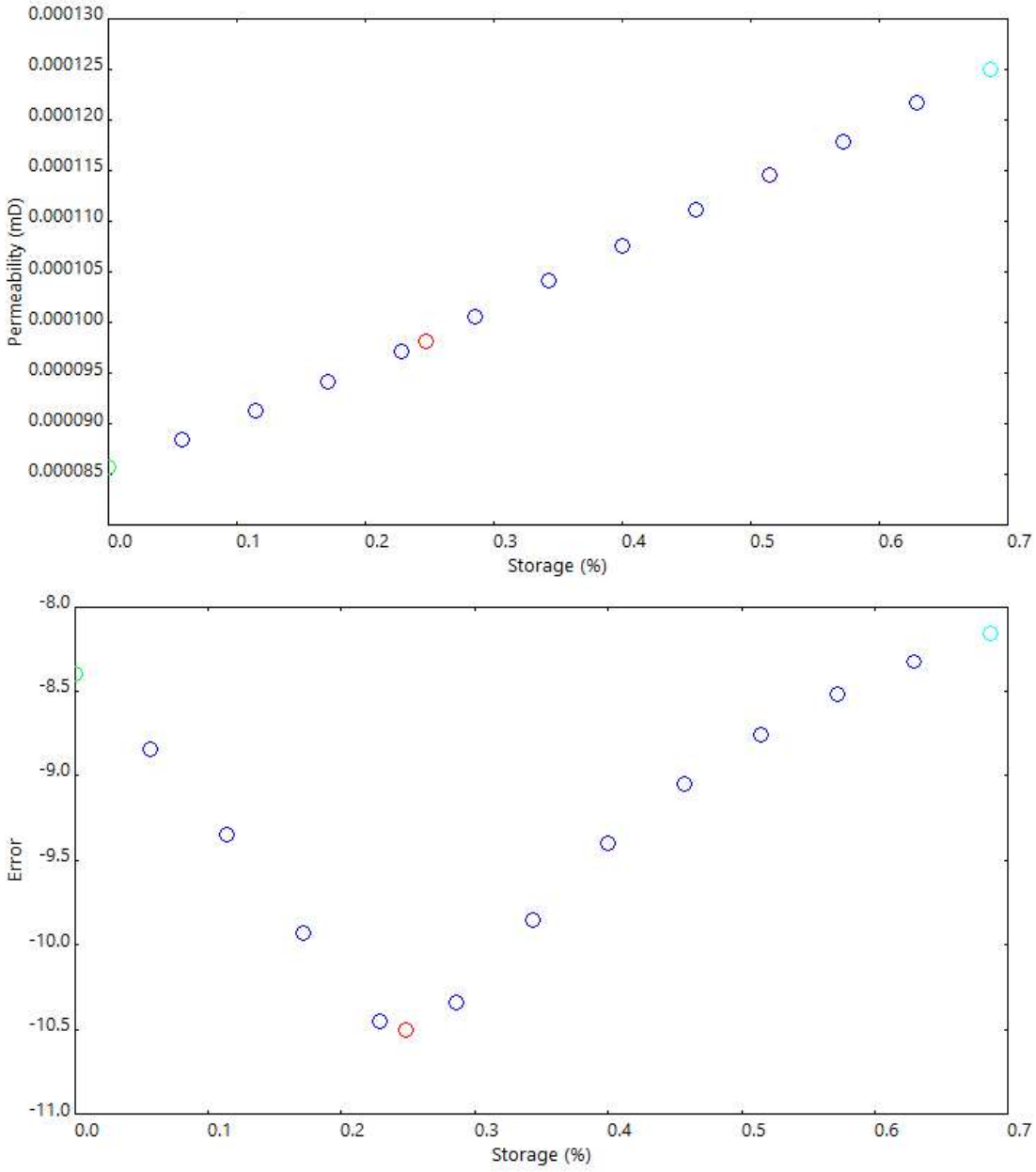

Figure B-38. Permeability results for sample K33_0364_1753

6. K33_0393_1834

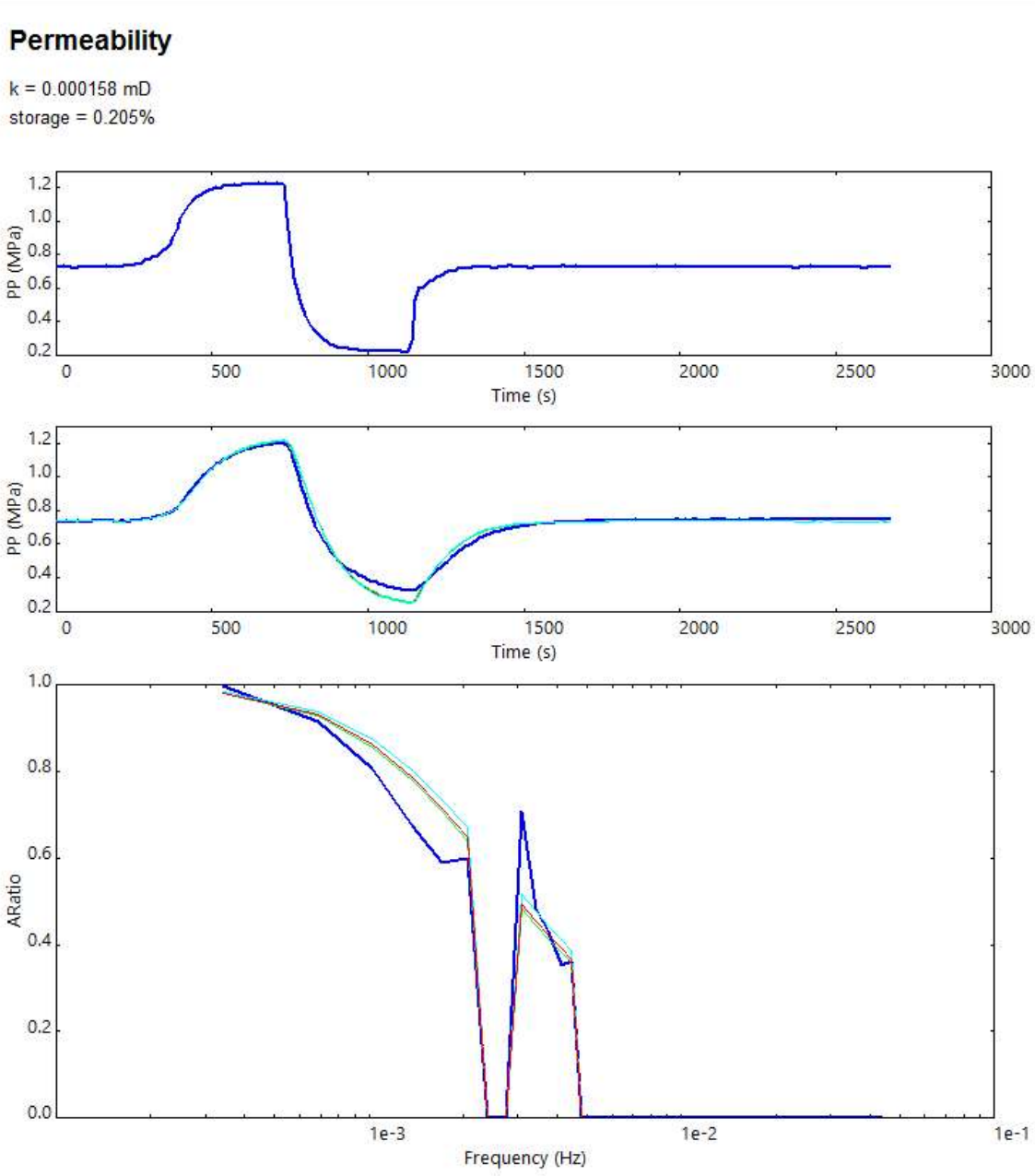

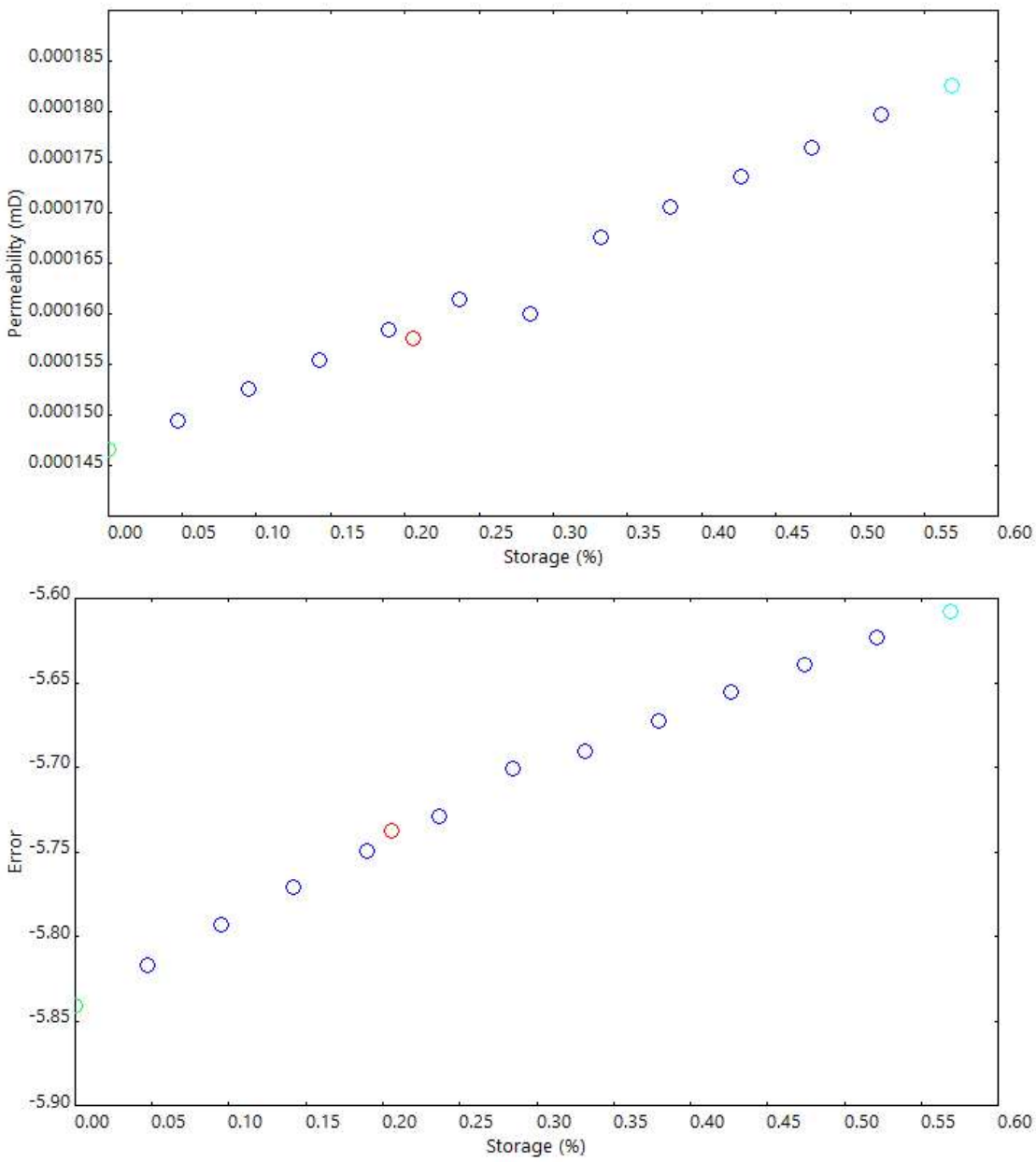

Figure B-39. Permeability results for sample K33_0393_1834

7. K33_0423_1916.3

Permeability

k = 1.84e-06 mD
storage = 0.090%

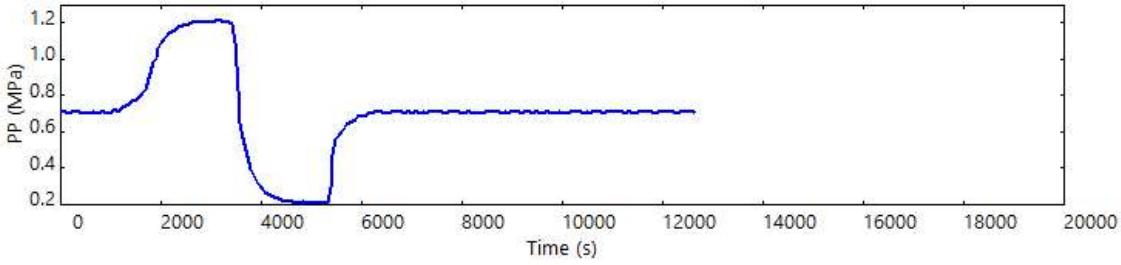

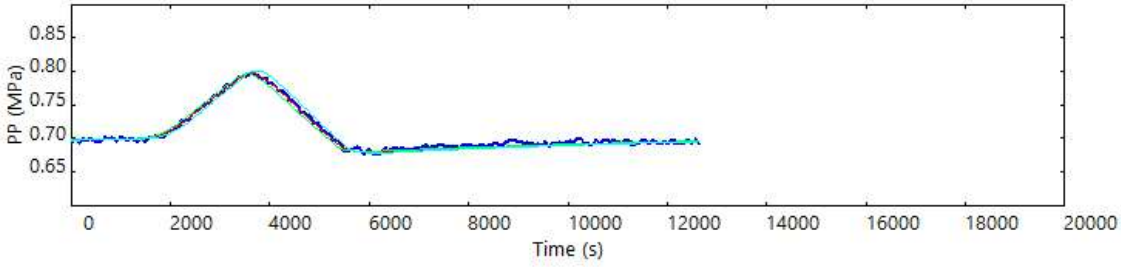

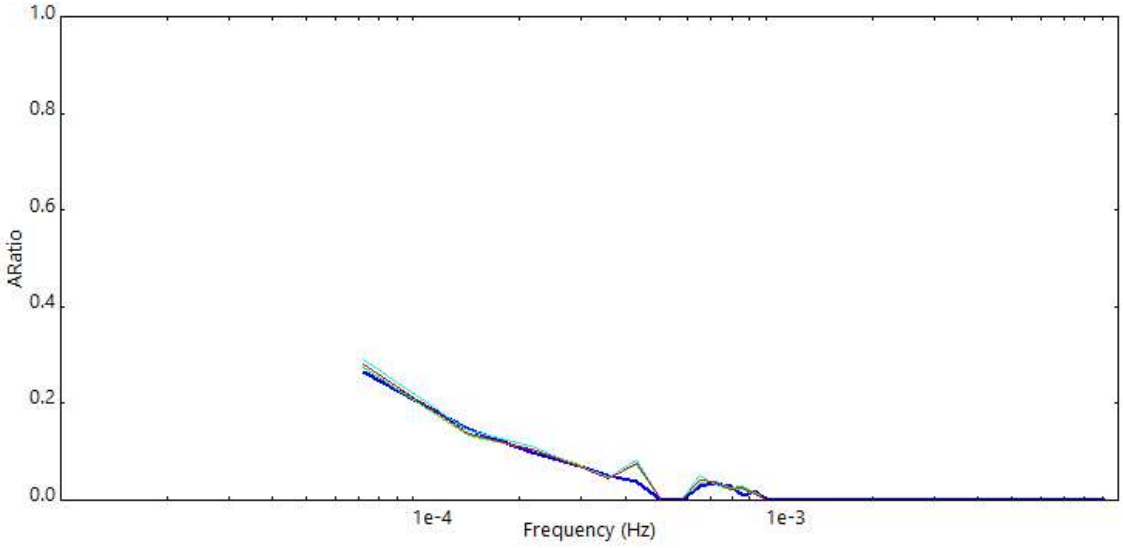

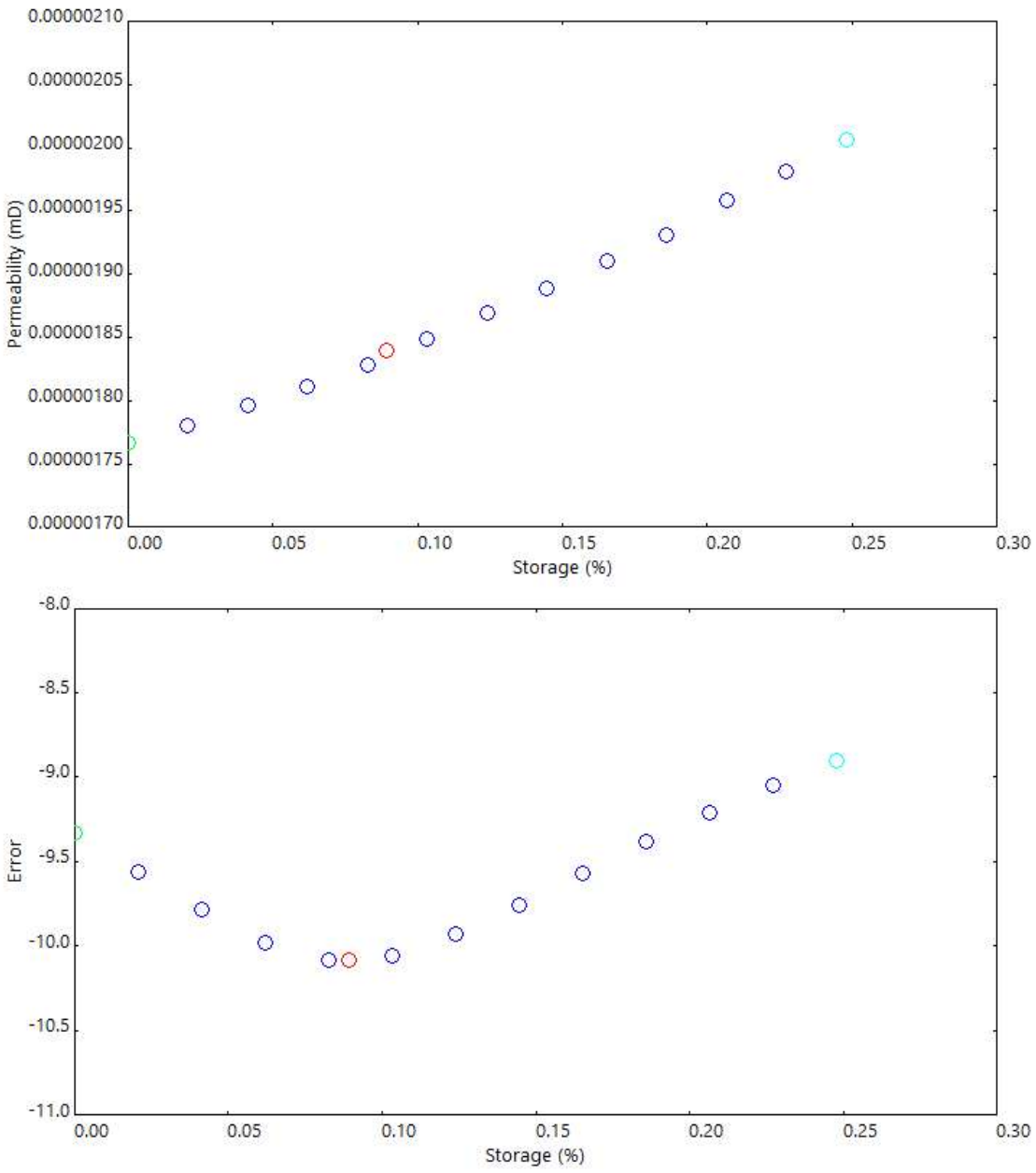

Figure B-40. Permeability results for sample K33_0423_1916.3

8. K33_0423_1919

Permeability

k = 7.54e-06 mD
storage = 0.790%

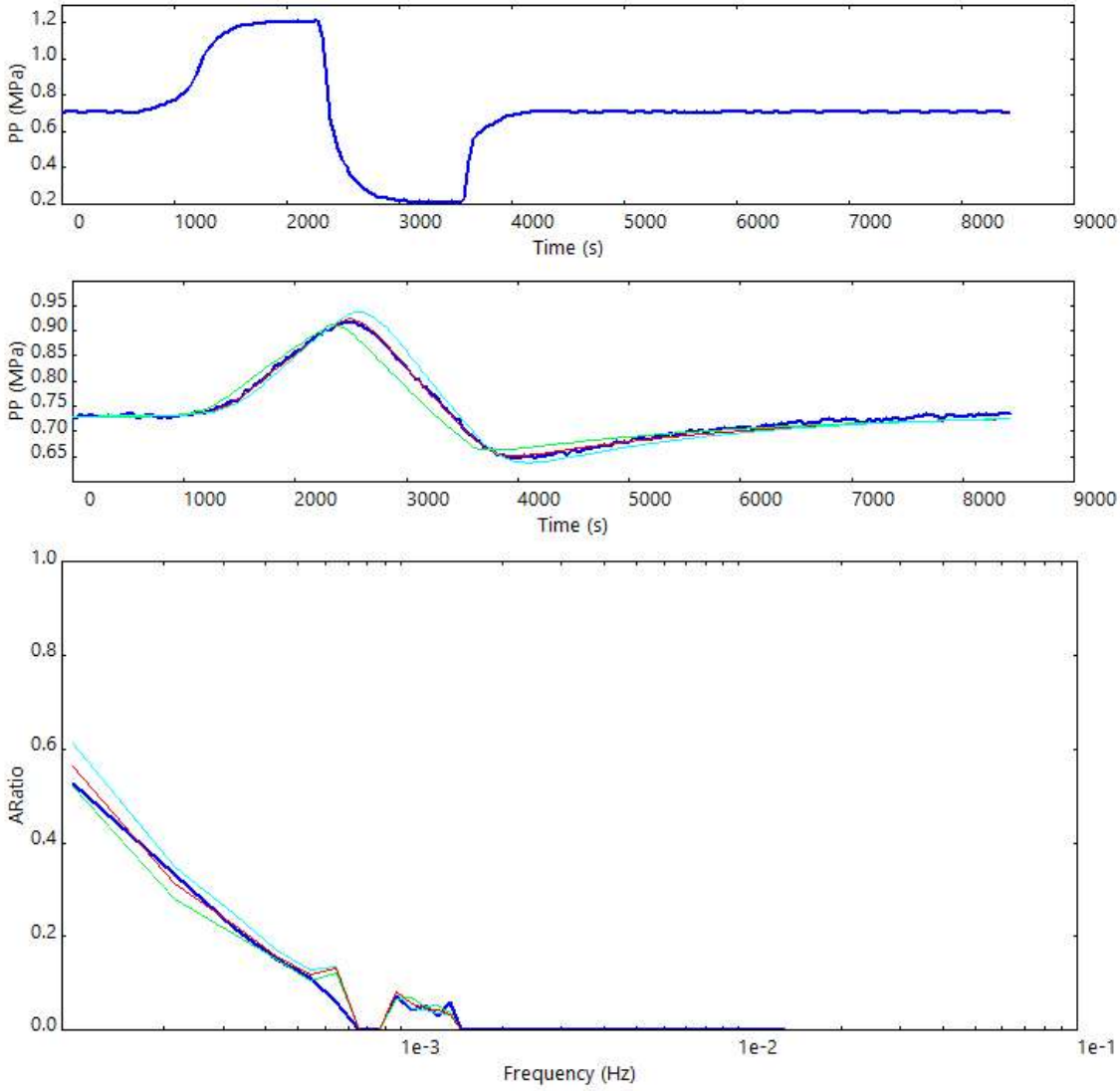

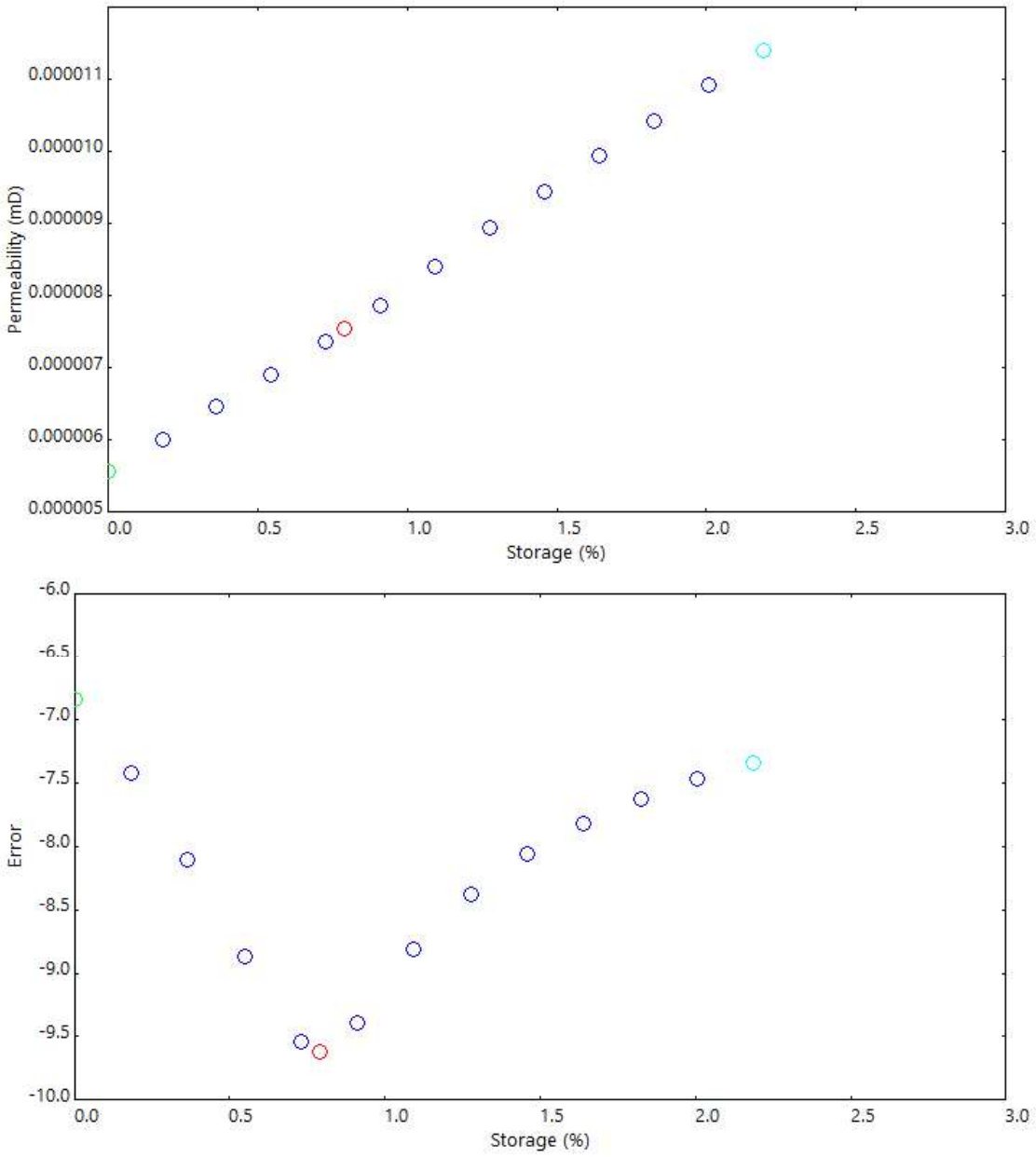

Figure B-41. Permeability results for sample K33_0423_1919

9. T2_0156_03

Permeability

k = 2.72e-06 mD
storage = 0.127%

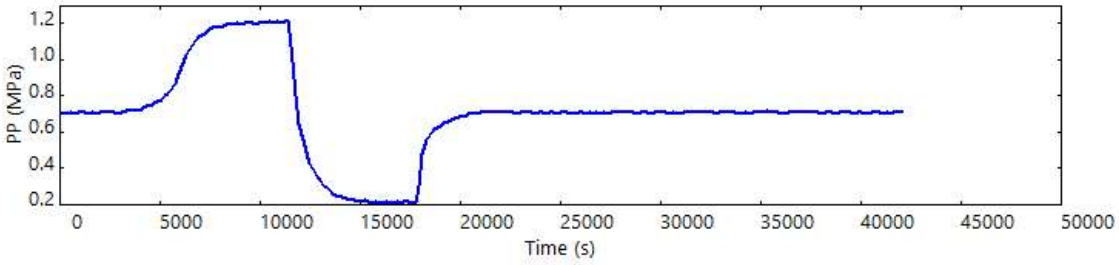

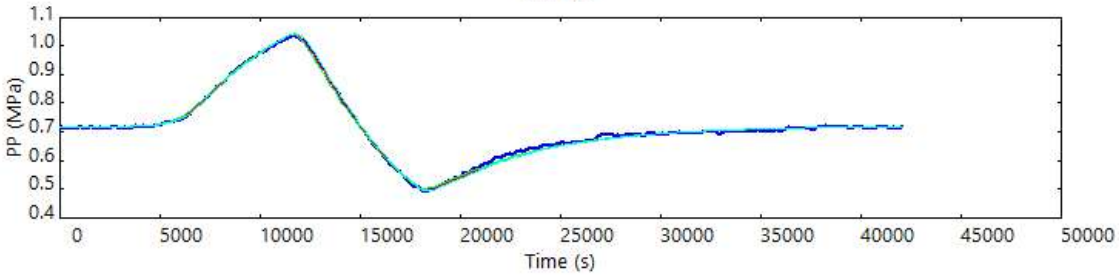

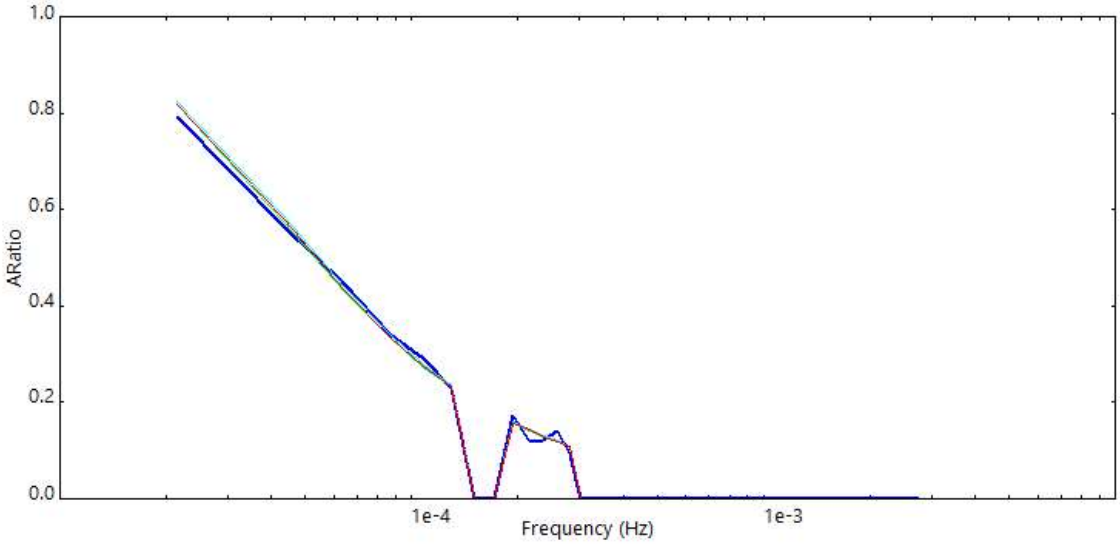

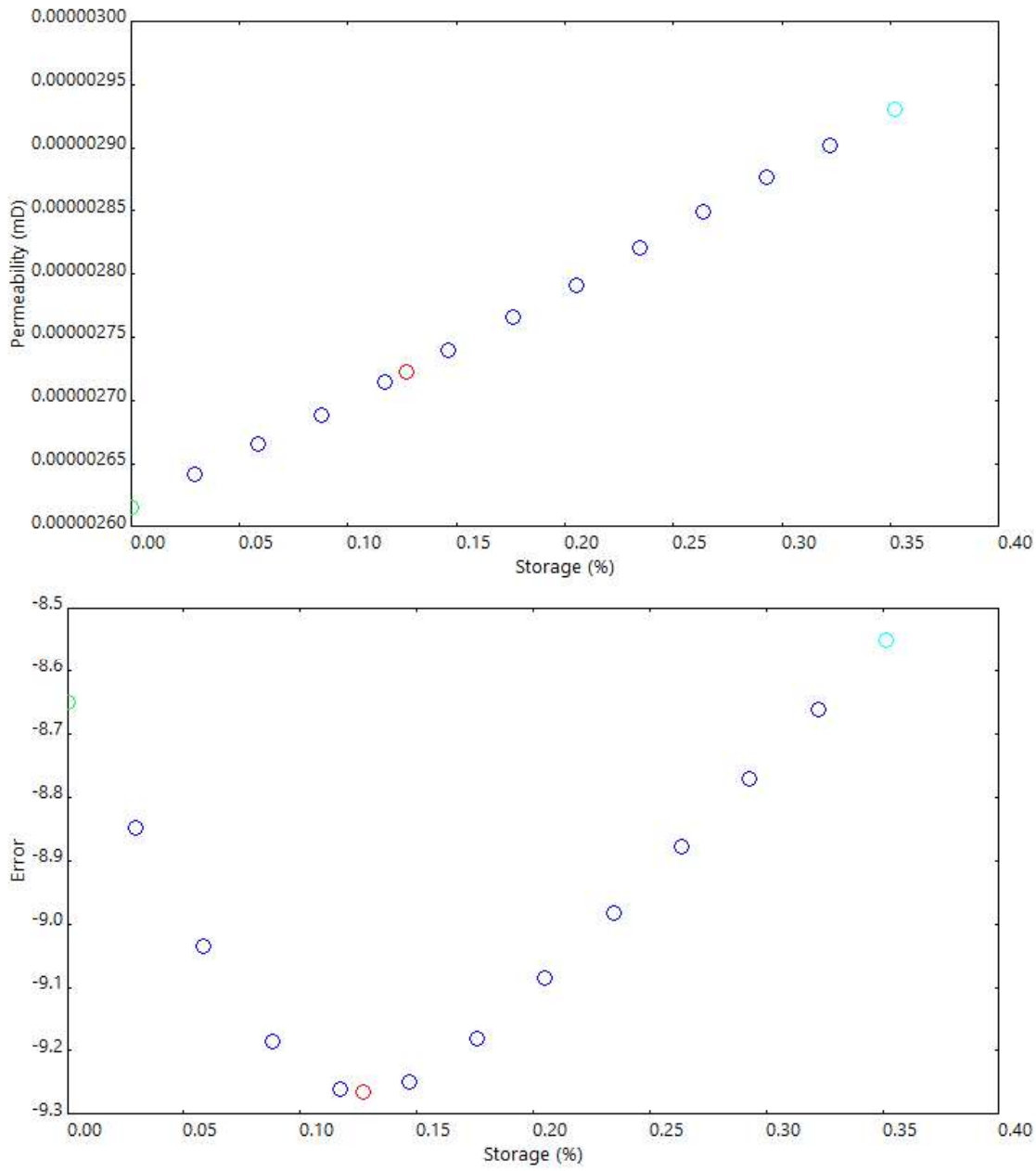

Figure B-42. Permeability results for sample T2_0156_03

10. T2_0117_00

Permeability

k = 1.3e-05 mD
storage = 0.168%

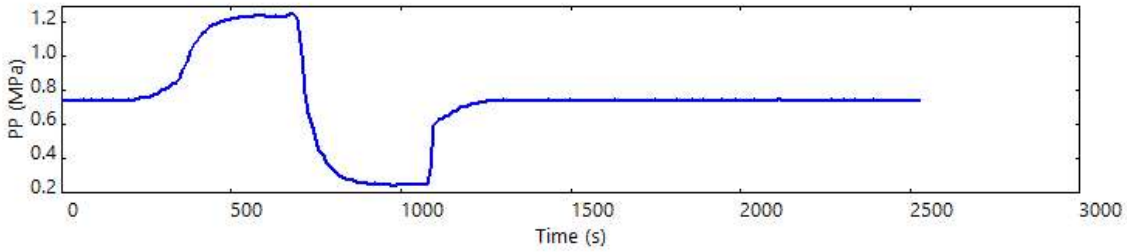

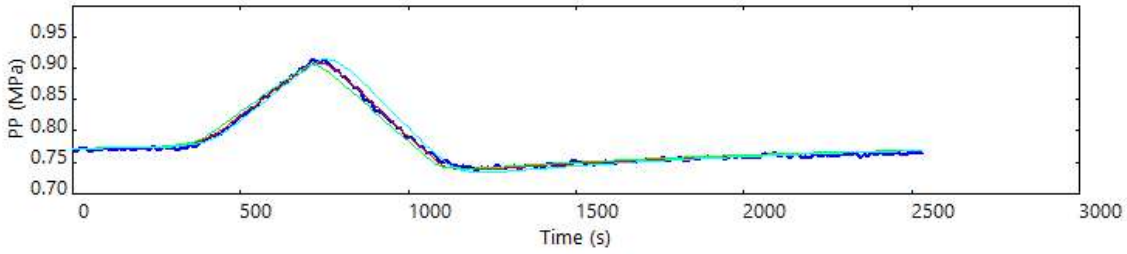

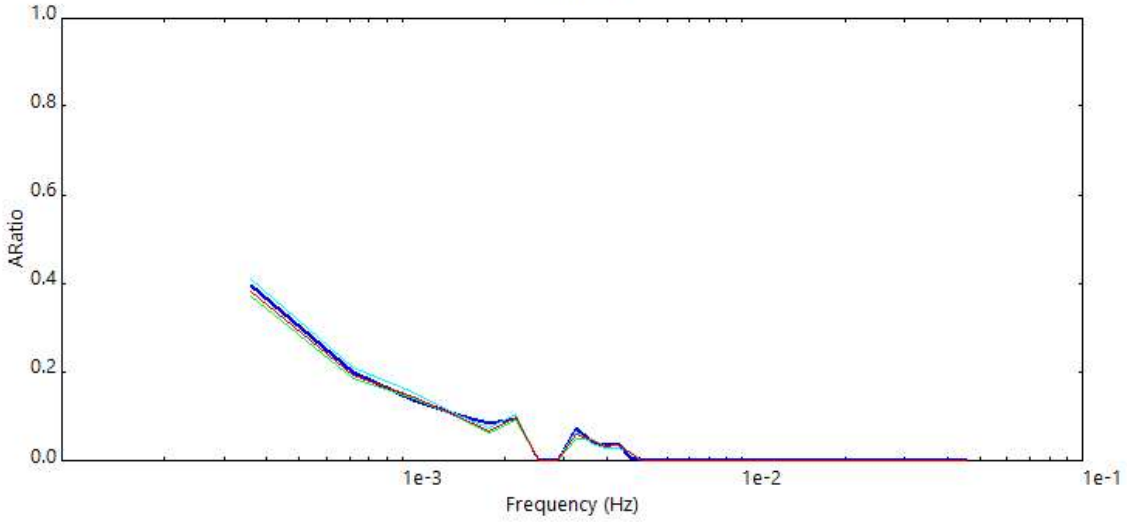

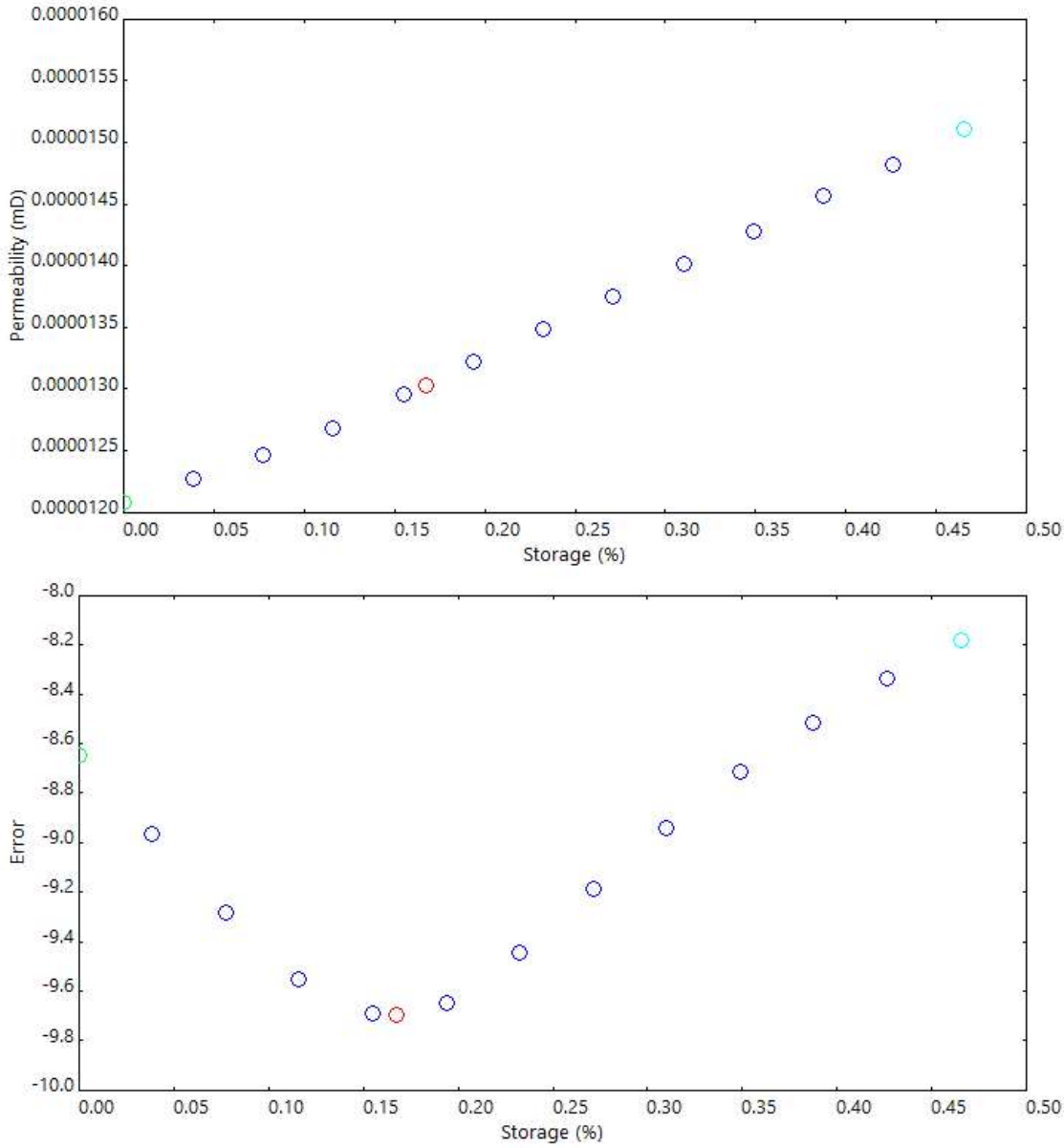

Figure B-43. Permeability results for sample T2_0117_00

11. T2_0117_03

Permeability

k = 2.75e-07 mD

storage = 0.119%

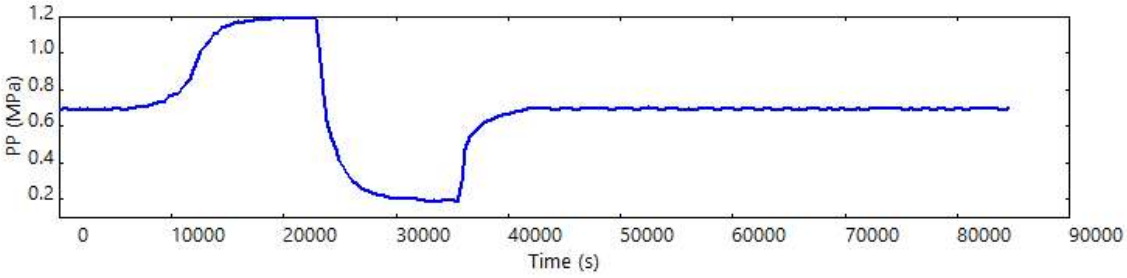

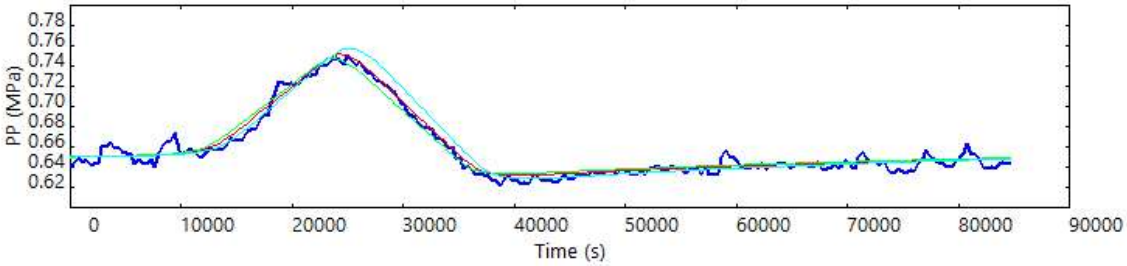

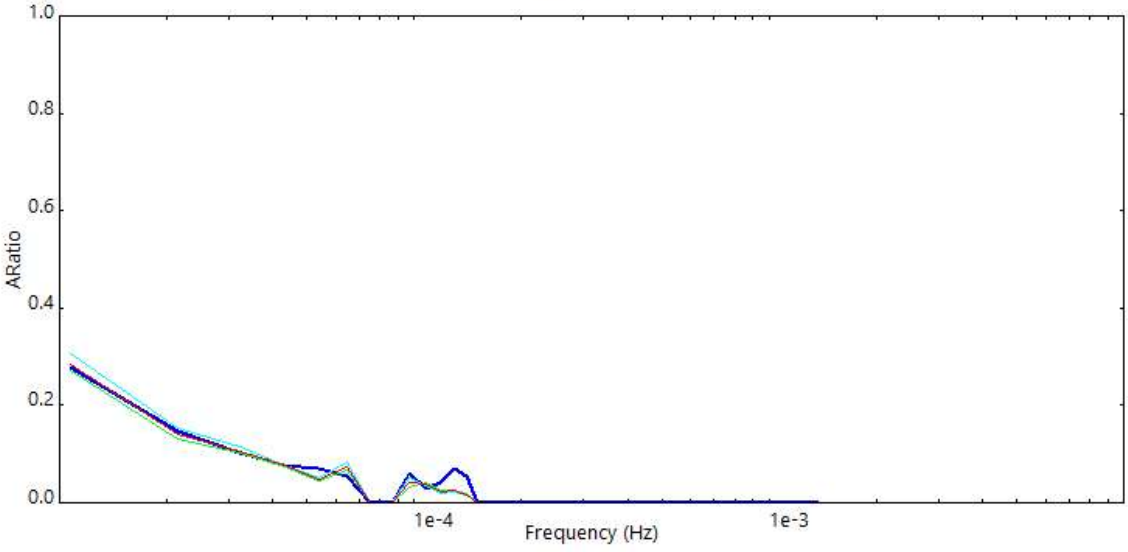

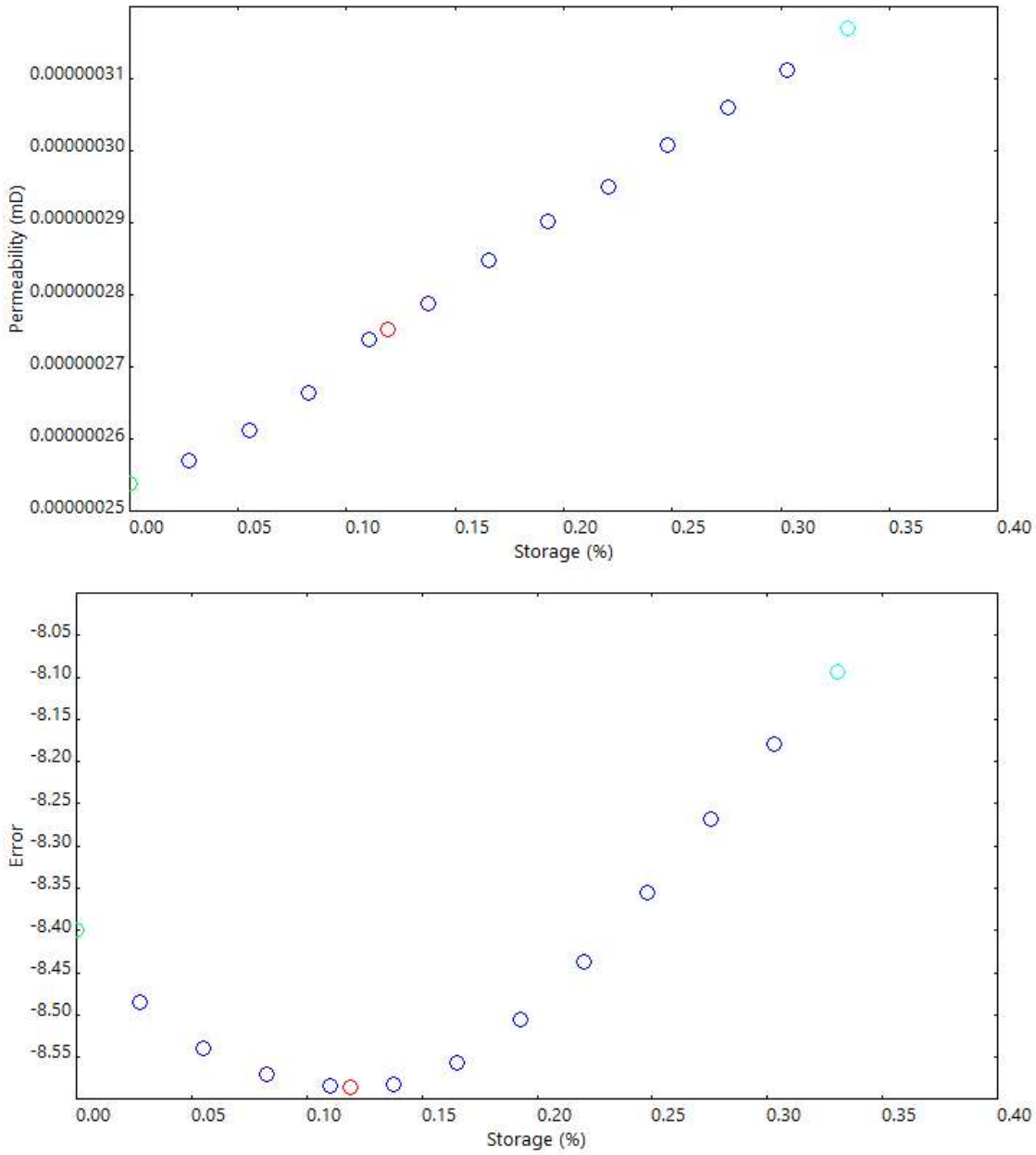

Figure B-44. Permeability results for sample T2_0117_03

B.6.2 Lake City Samples

1. LCB090314-1b

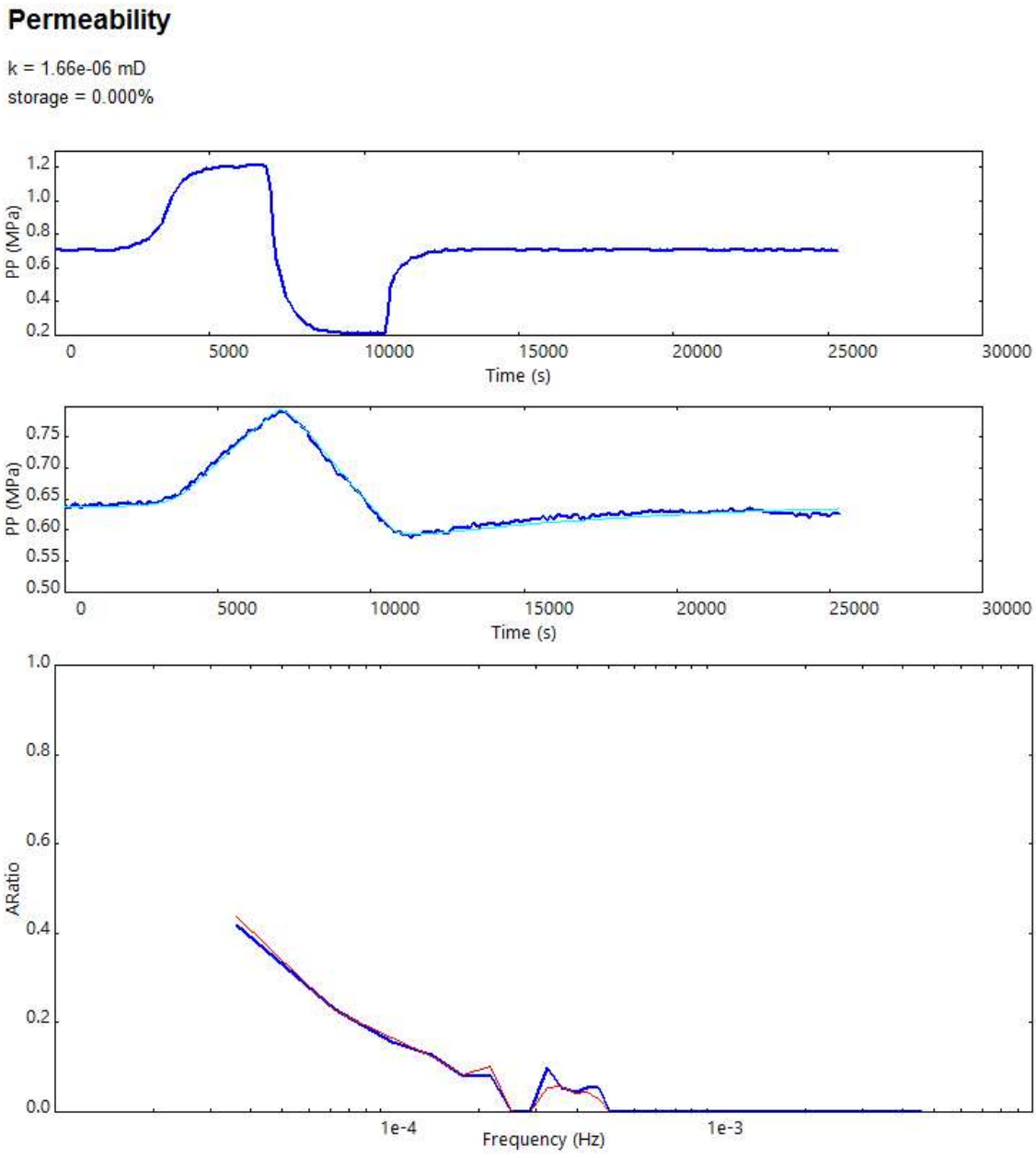

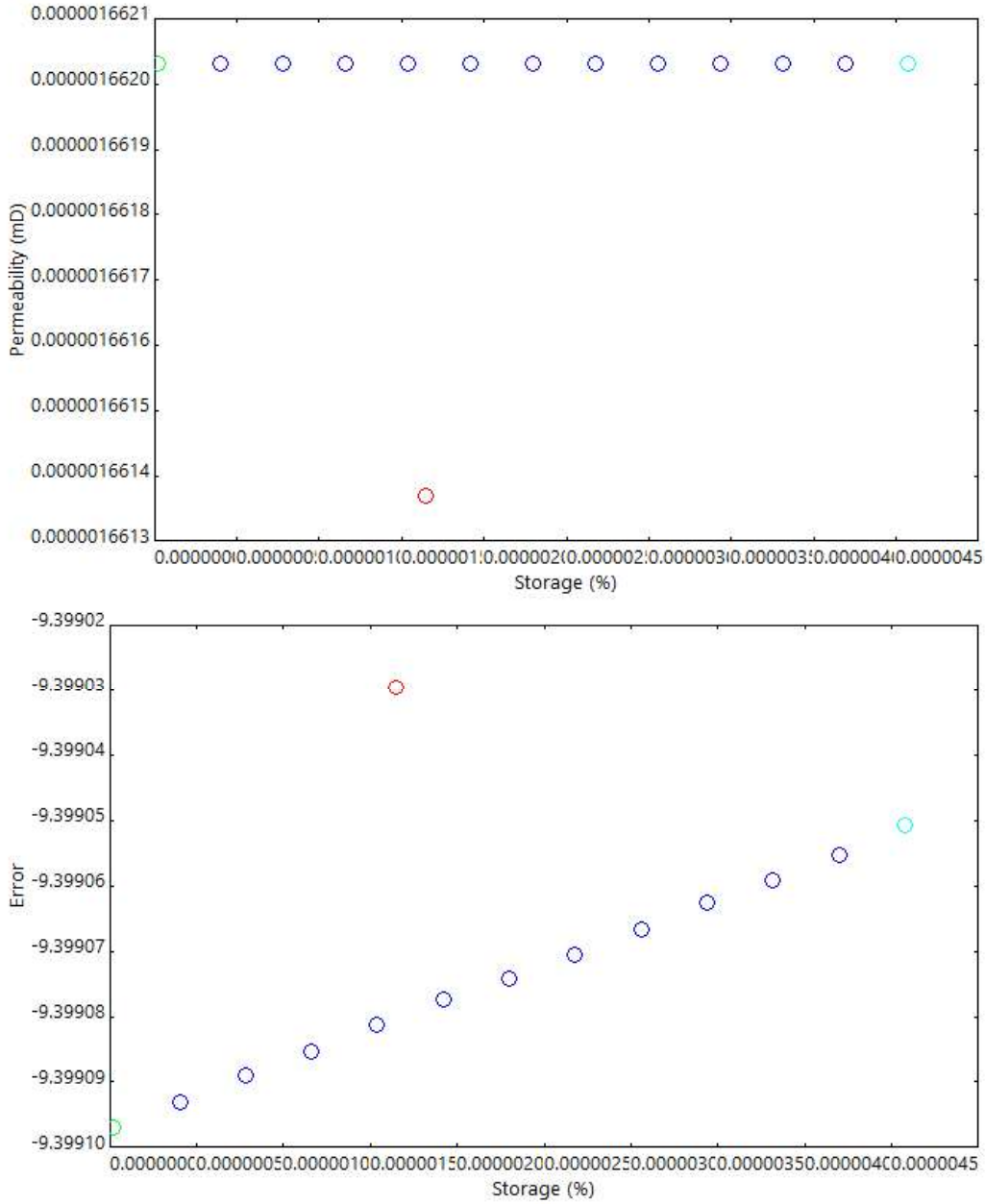

Figure B-45. Permeability results for sample LCB090314-1b

2. LCB090314-5

Permeability

k = 1.76e-05 mD
storage = 0.211%

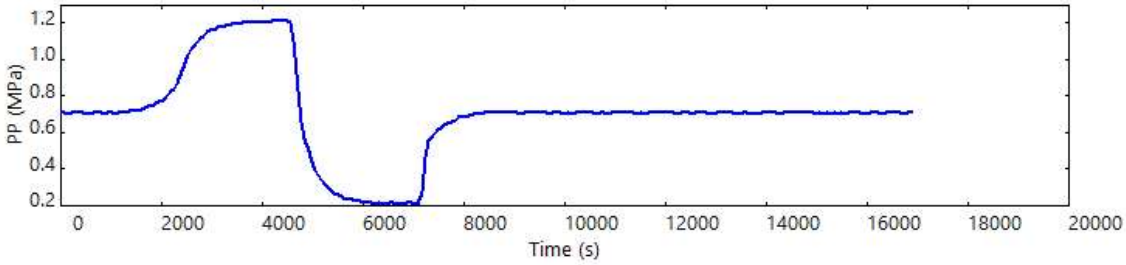

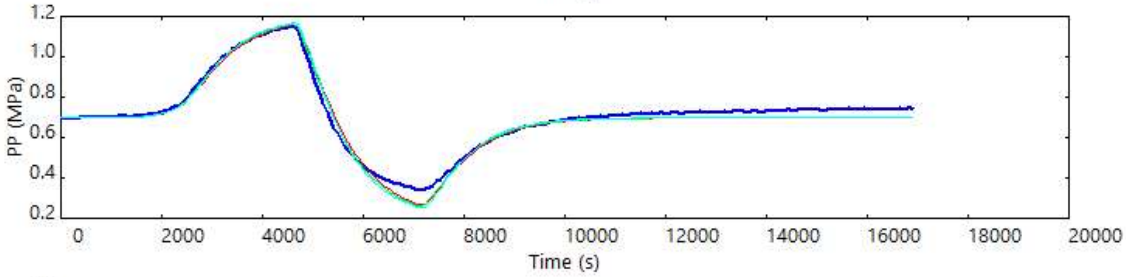

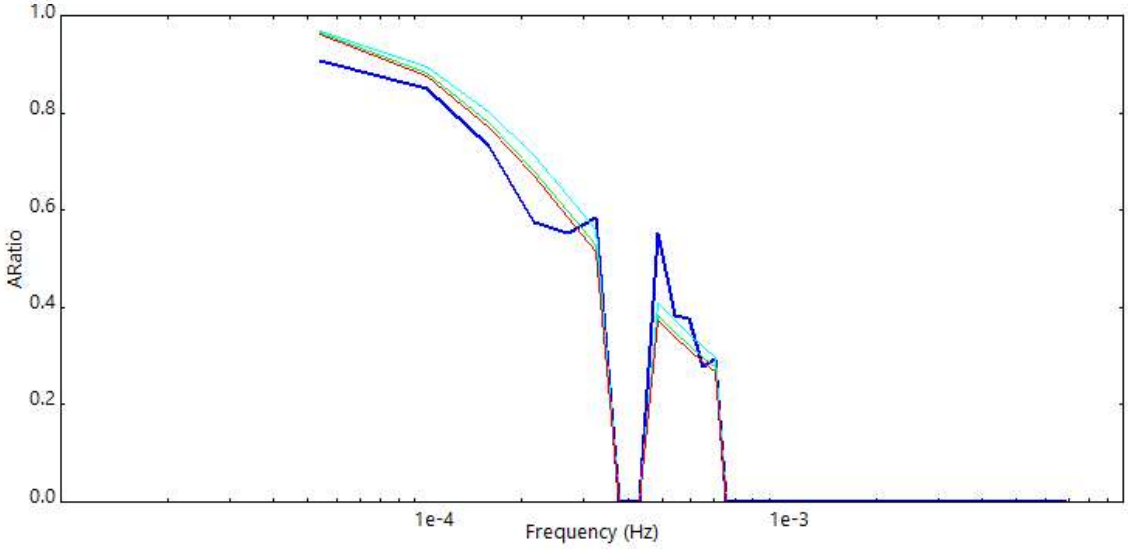

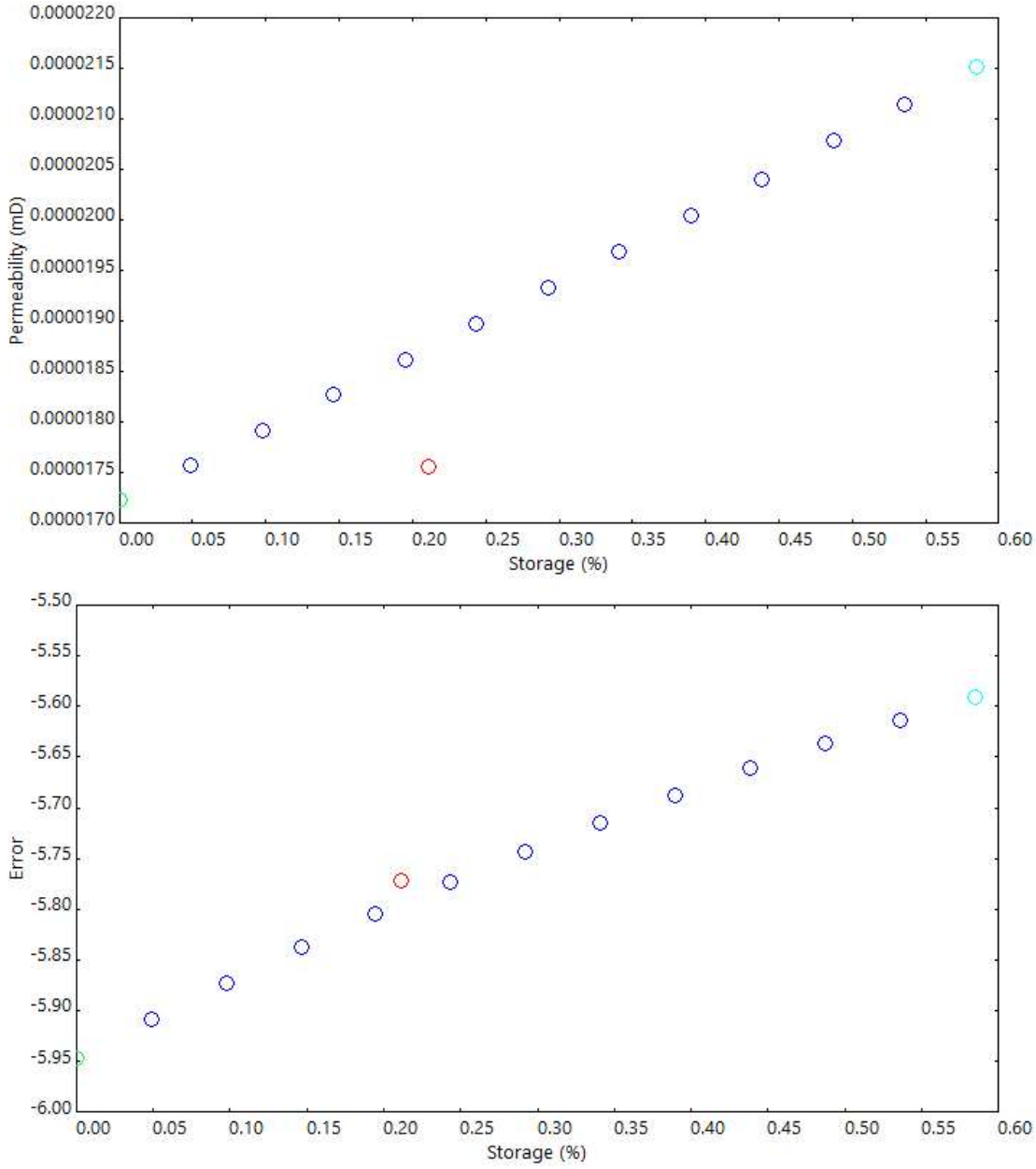

Figure B-46. Permeability results for sample LCB090314-5

3. LCB091414-2

Permeability

k = 4.28e-07 mD
storage = 0.046%

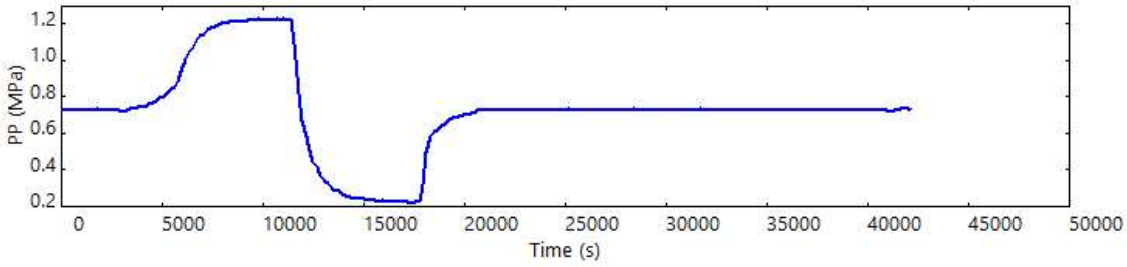

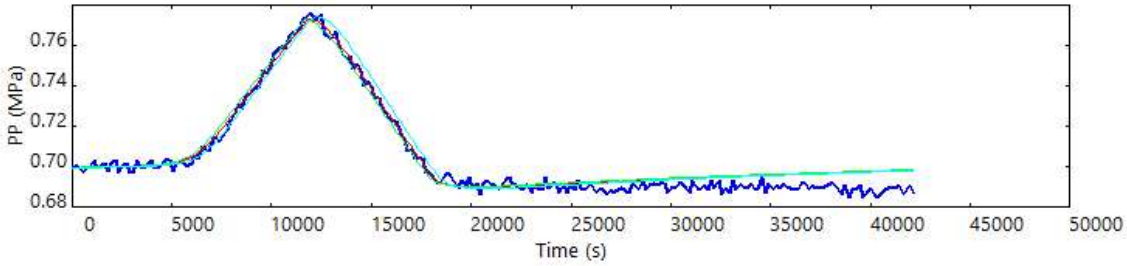

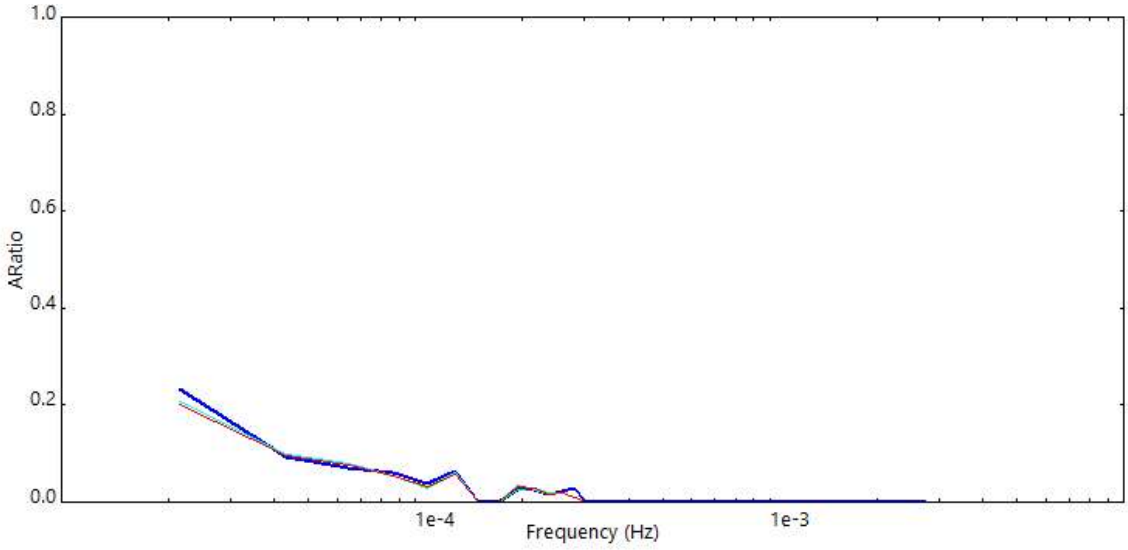

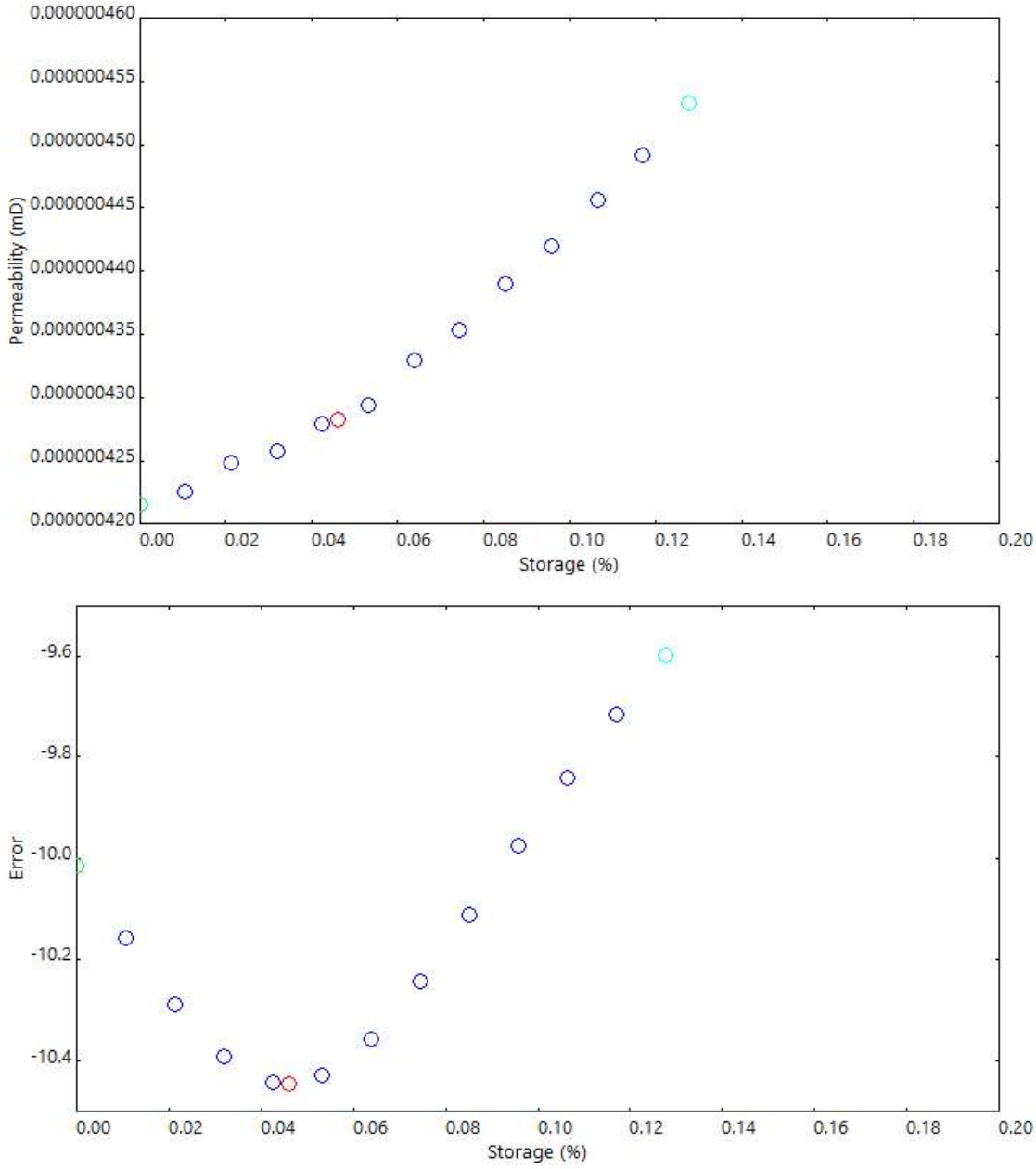

Figure B-47. Permeability results for sample LCB09031414-2

4. LCDLA082913-1

Permeability

k = 2.57e-06 mD
storage = 0.490%

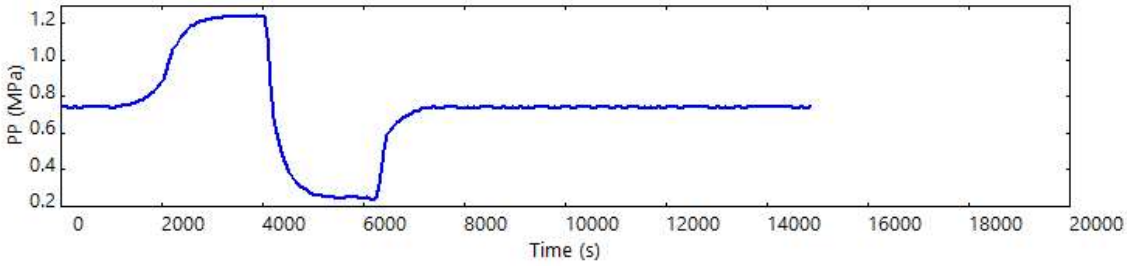

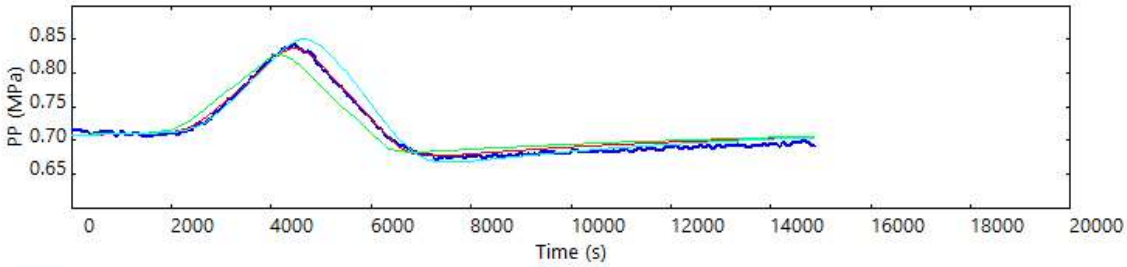

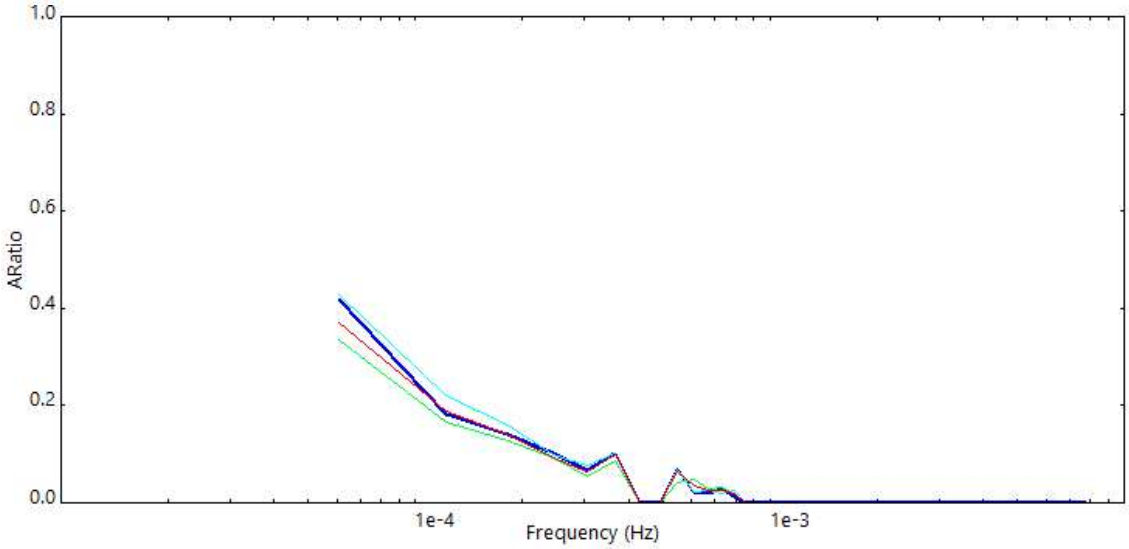

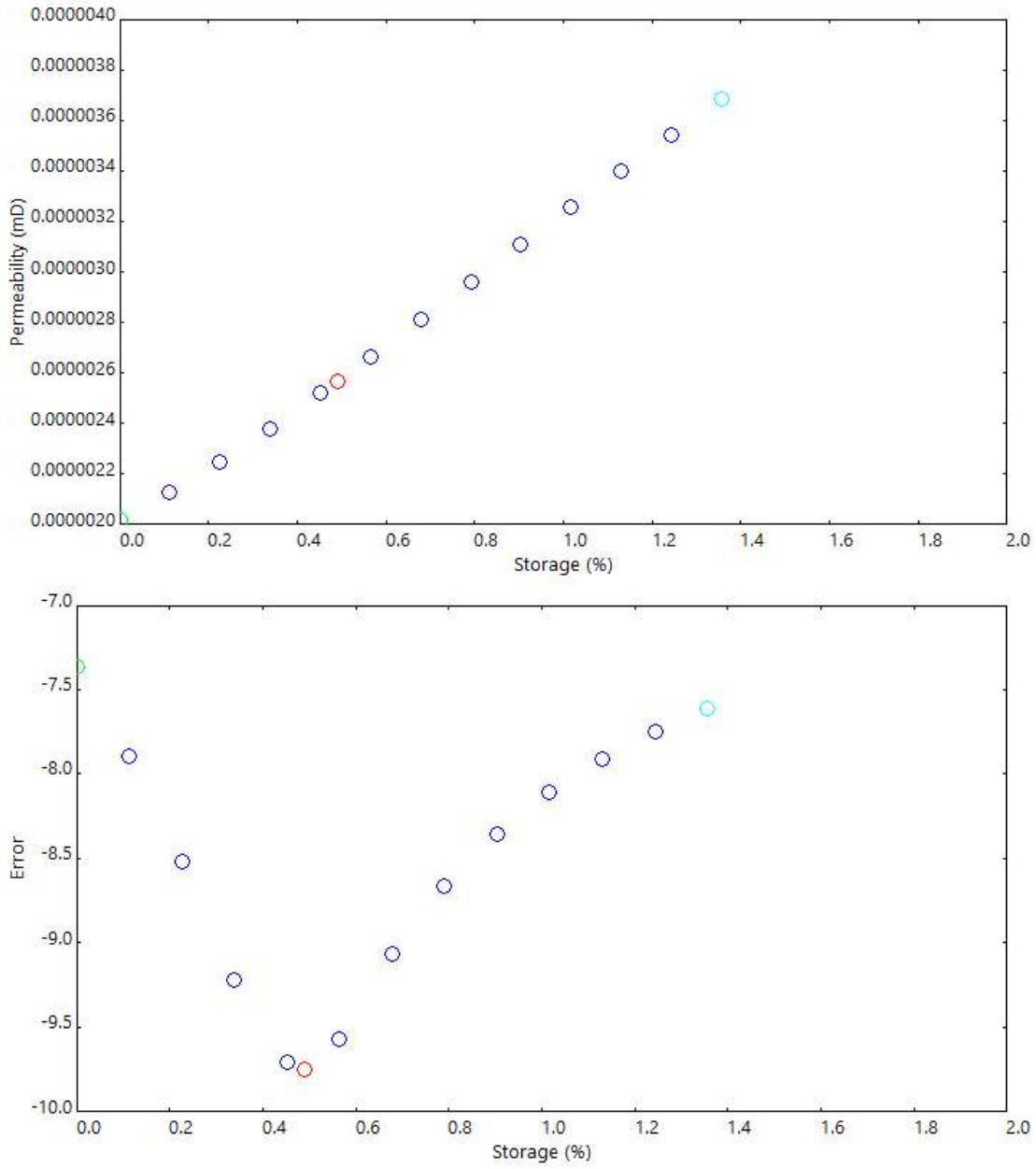

Figure B-48. Permeability results for sample LCDLA082913-1

5. LCDLA082913-2

Permeability

k = 1.61e-06 mD
storage = 1.204%

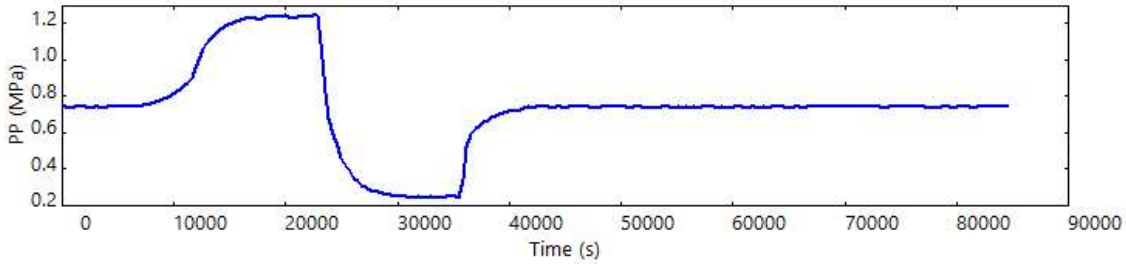

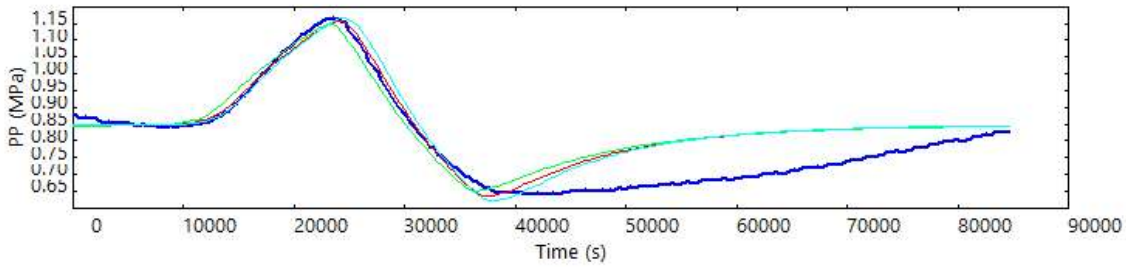

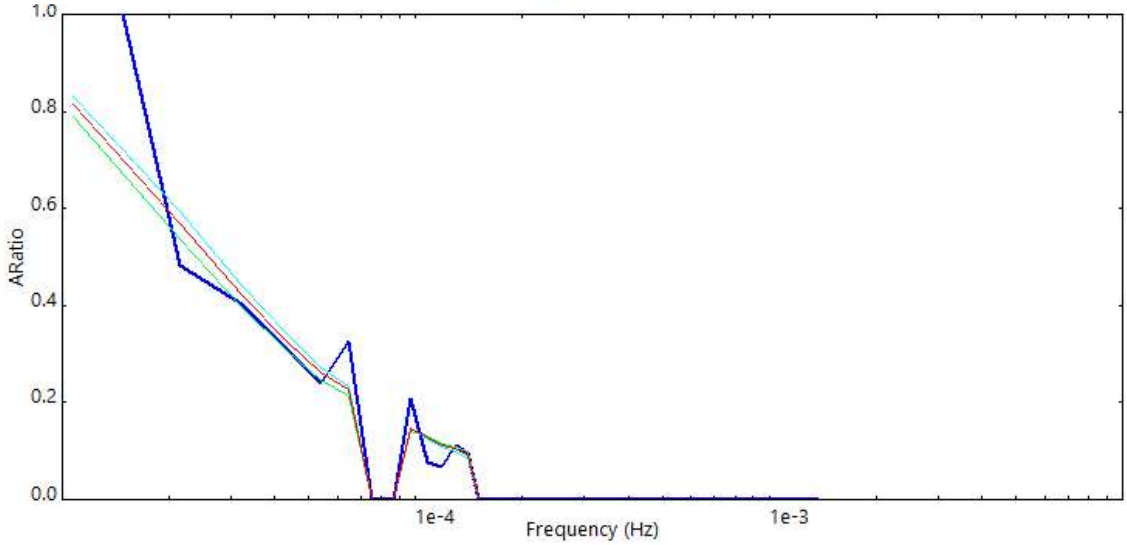

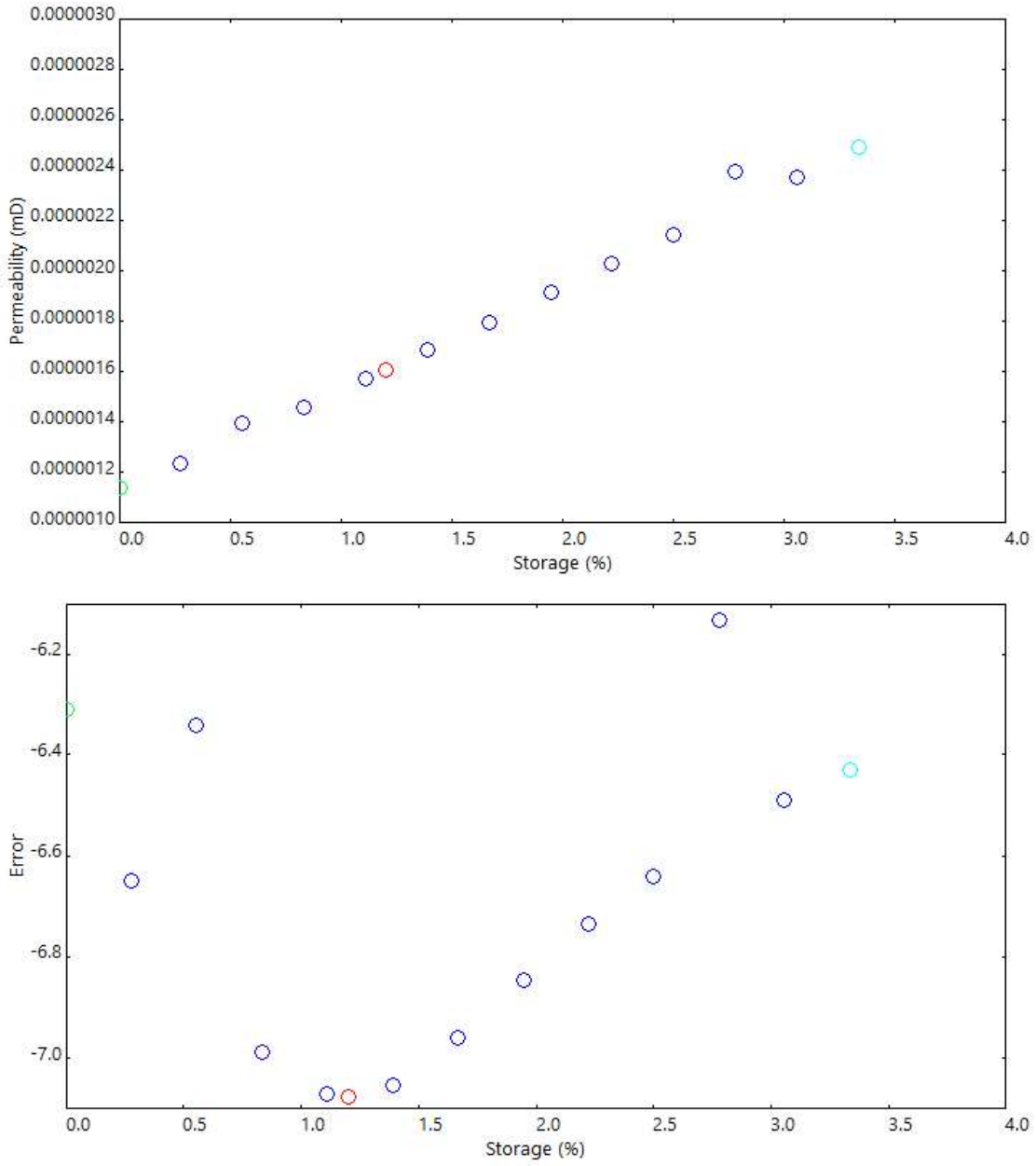

Figure B-49. Permeability results for sample LCDLA082913-2

6. LCG090714-2c

Permeability

k = 9.66e-07 mD
storage = 0.363%

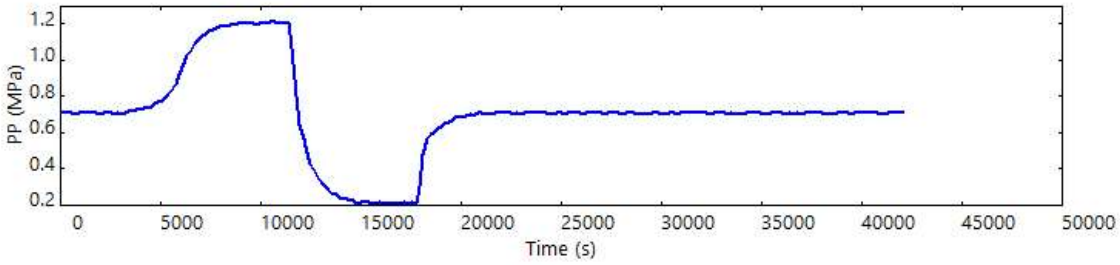

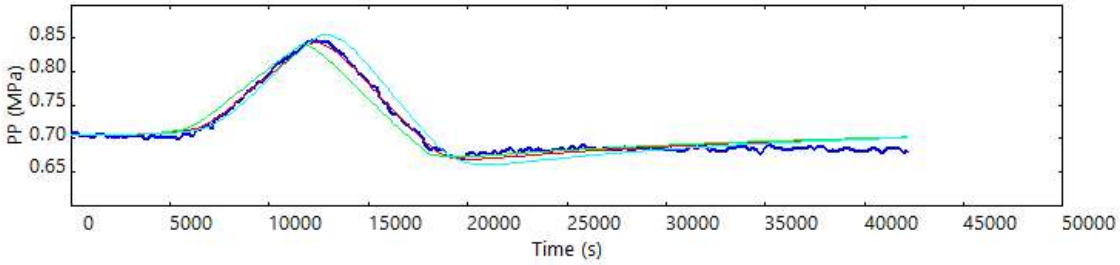

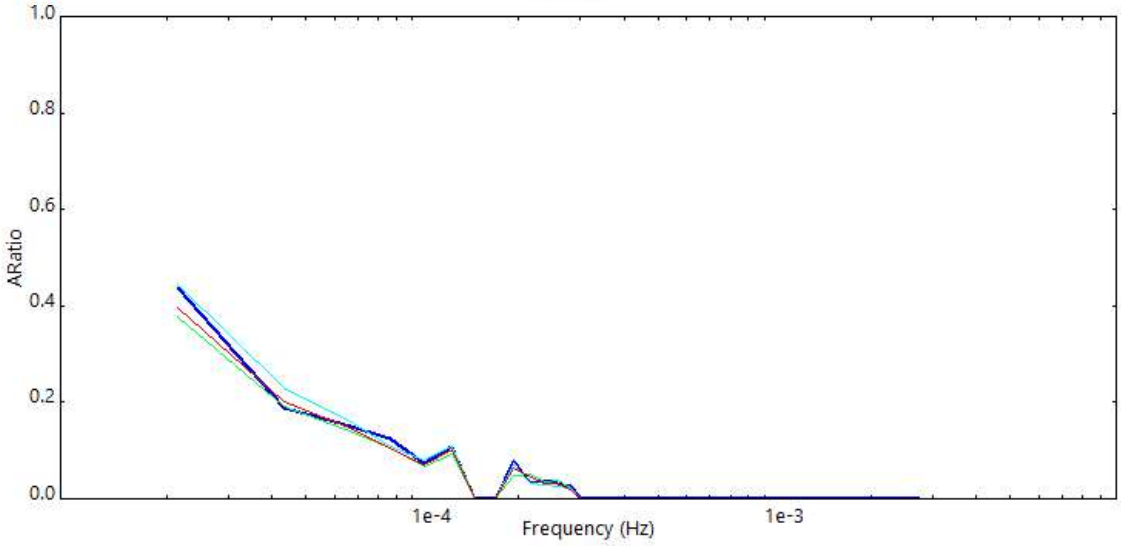

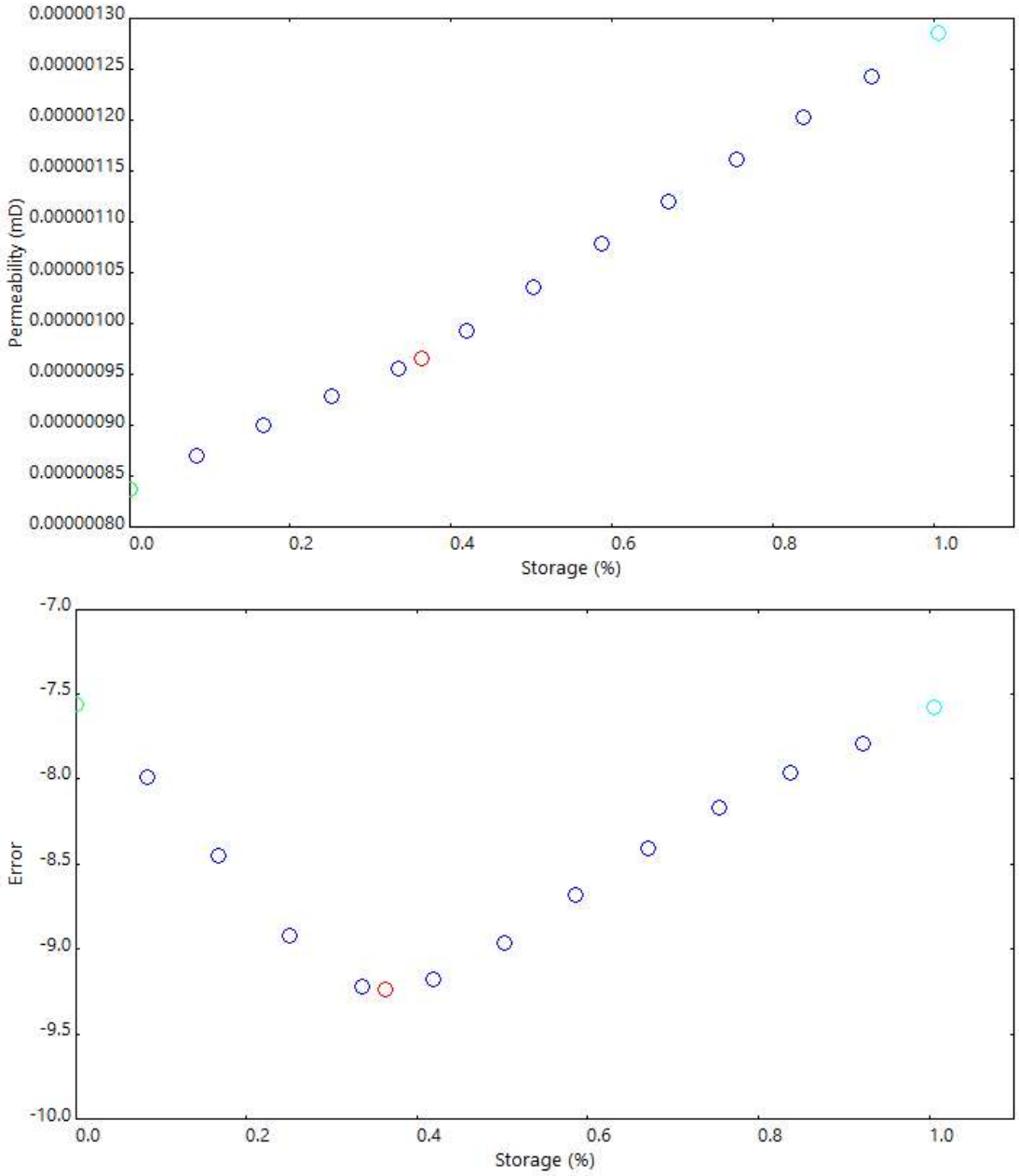

Figure B-50. Permeability results for sample LCG090714-2c

7. LCG090714-3a

Permeability

k = 6.78e-05 mD
storage = 0.187%

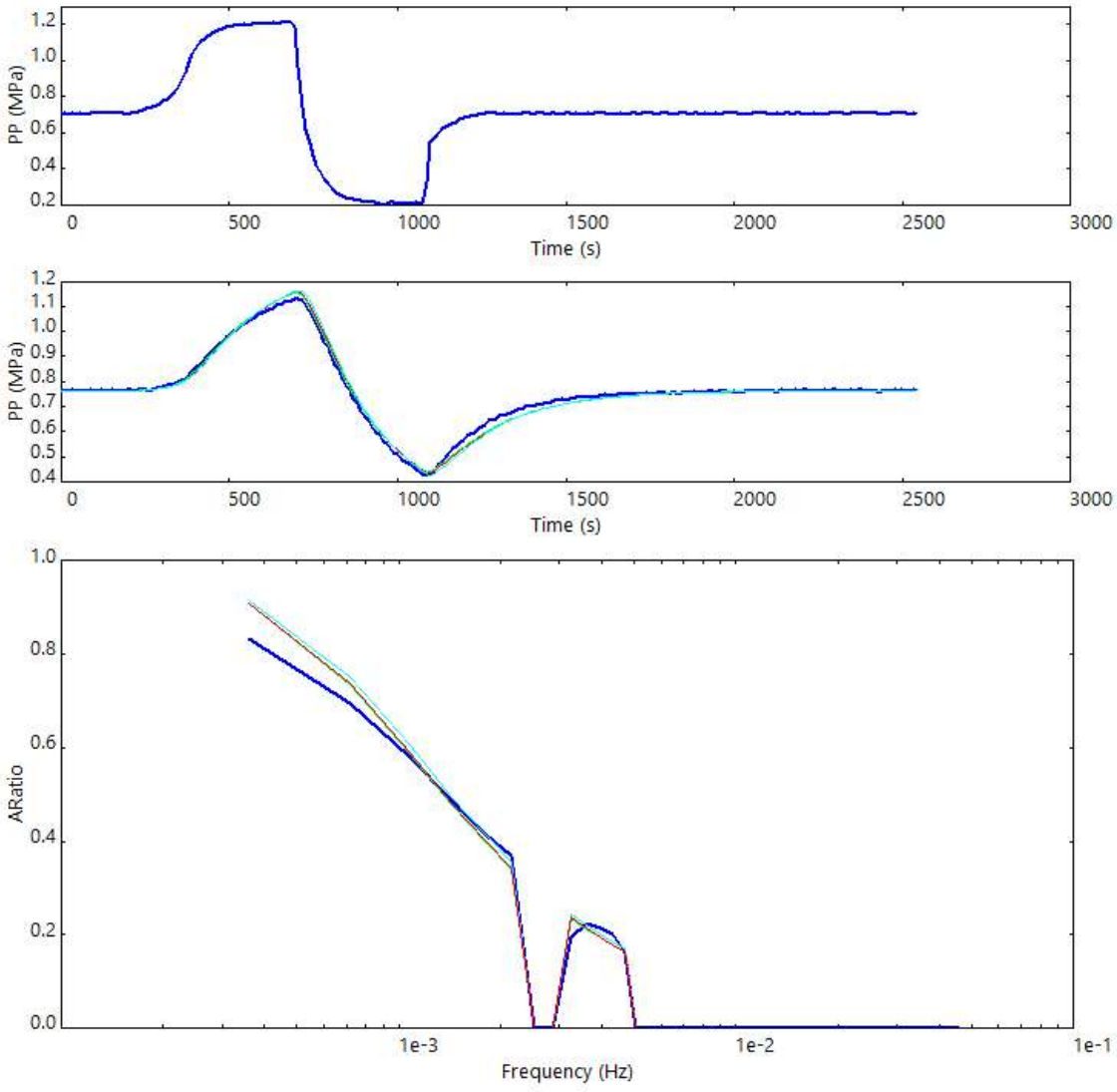

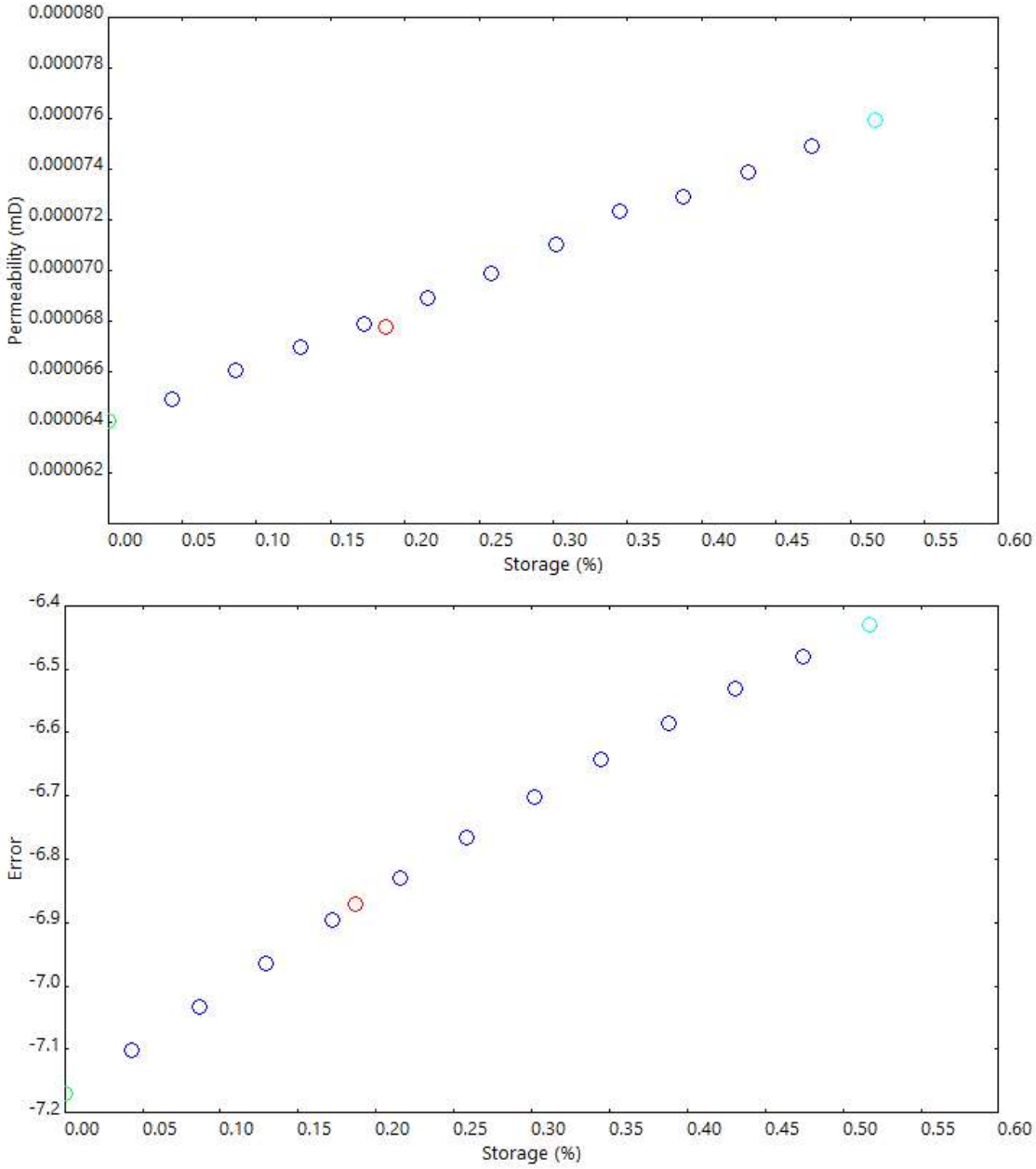

Figure B-51. Permeability results for sample LCG090714-3a

8. LCG090714-3b

Permeability

k = 4.14e-07 mD
storage = 0.510%

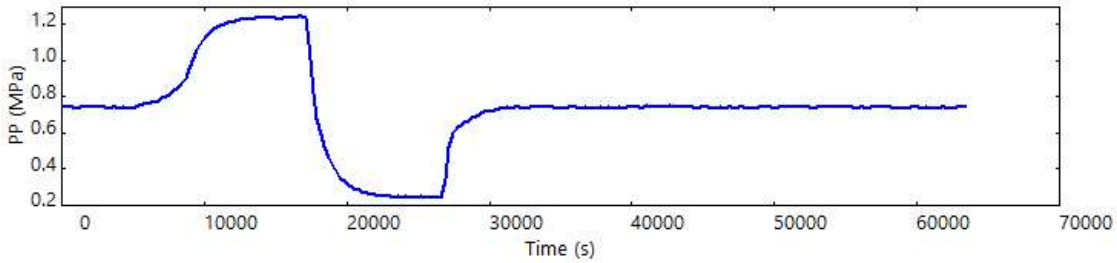

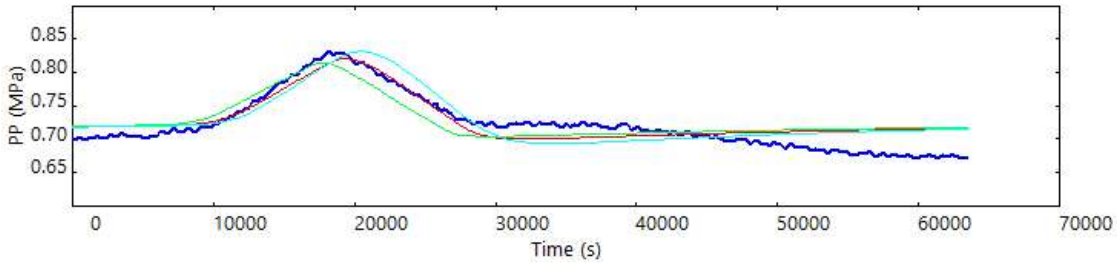

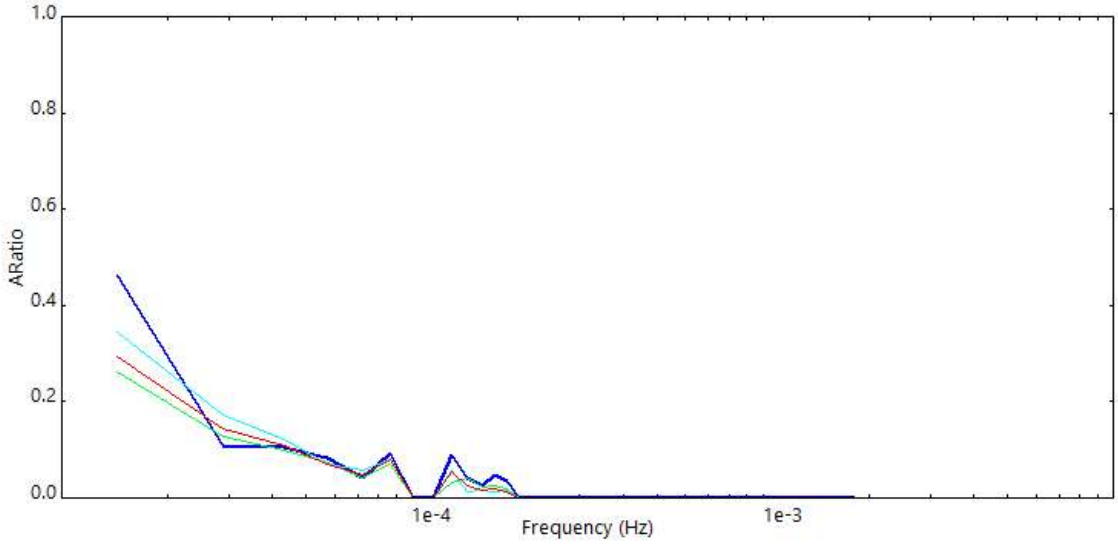

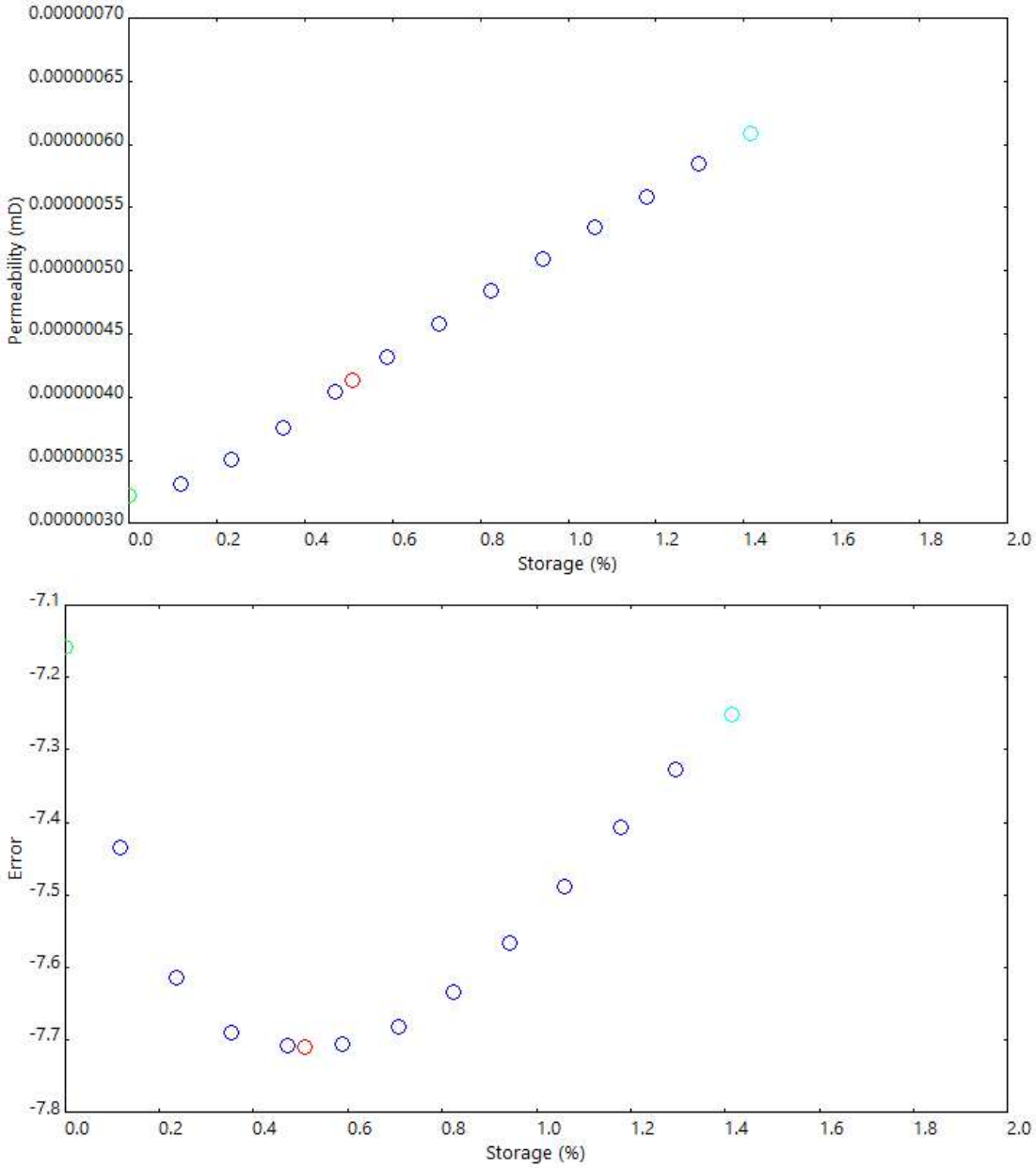

Figure B-52. Permeability results for sample LCG090714-3b

9. LCG091314-1b

Permeability

k = 5.98e-06 mD
storage = 0.287%

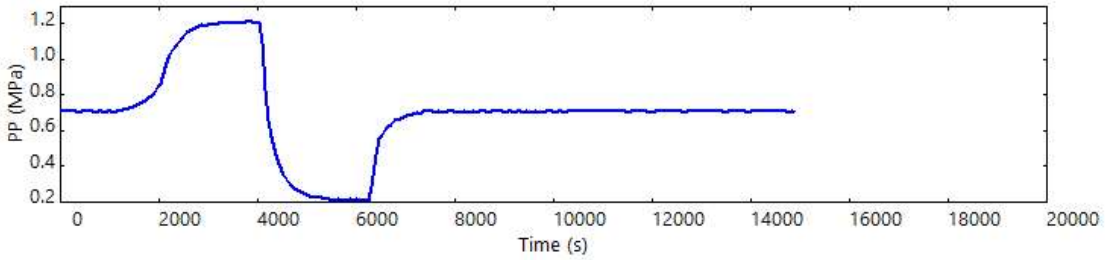

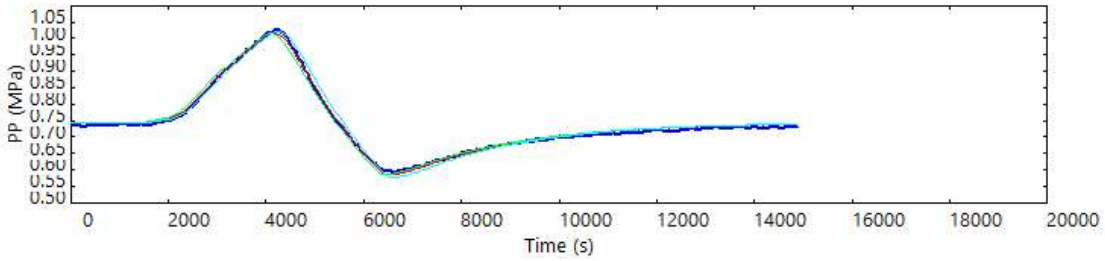

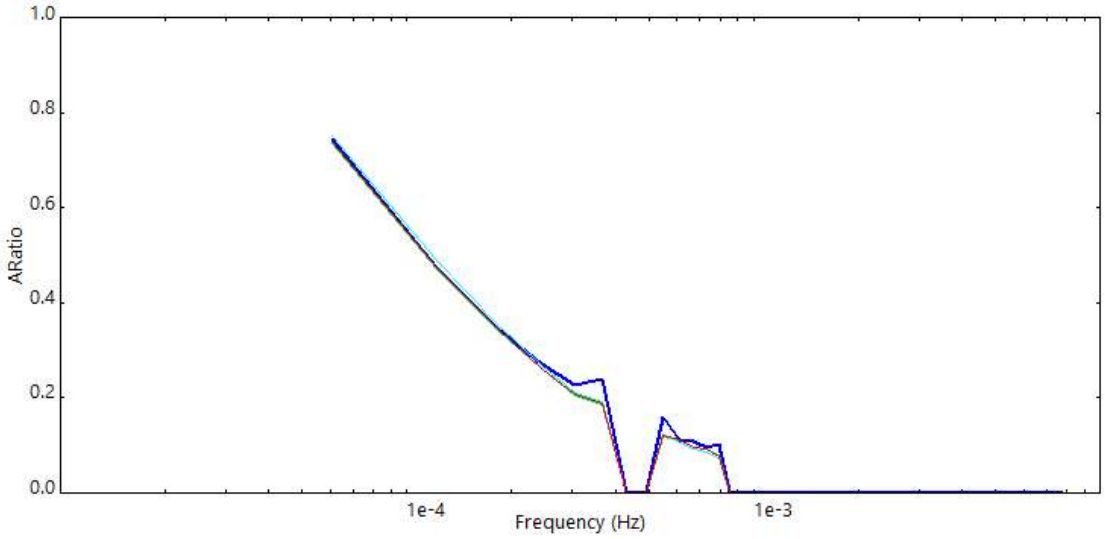

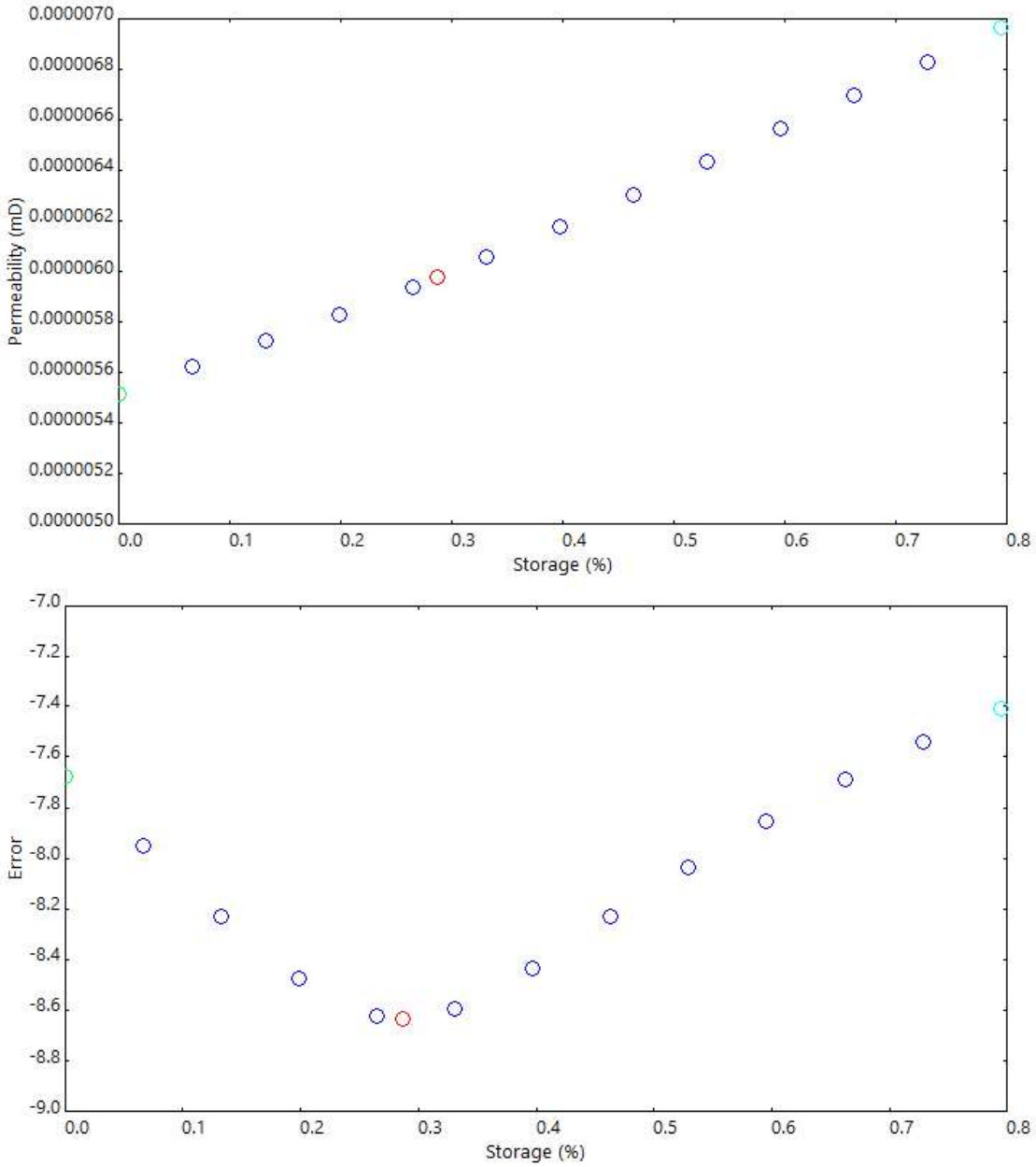

Figure B-53. Permeability results for sample LCG091314-1b

10. LCT091014-1a

Permeability

k = 2.89e-07 mD
storage = 0.182%

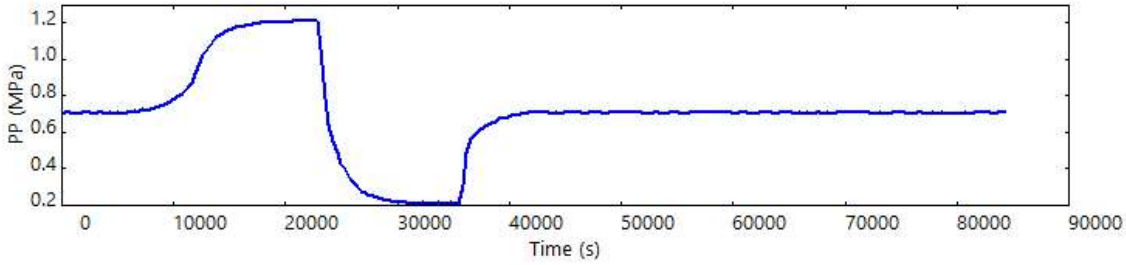

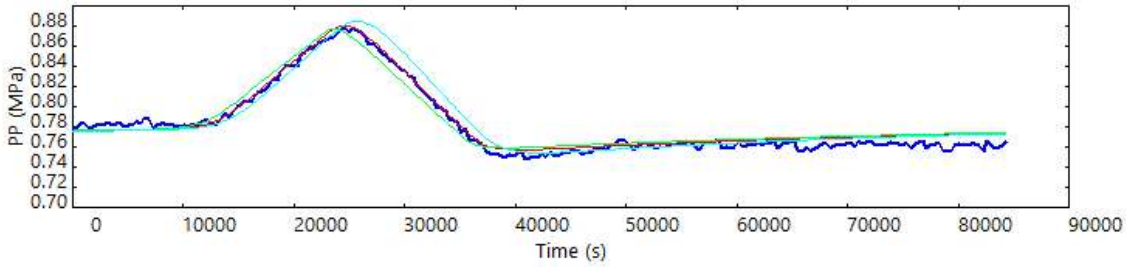

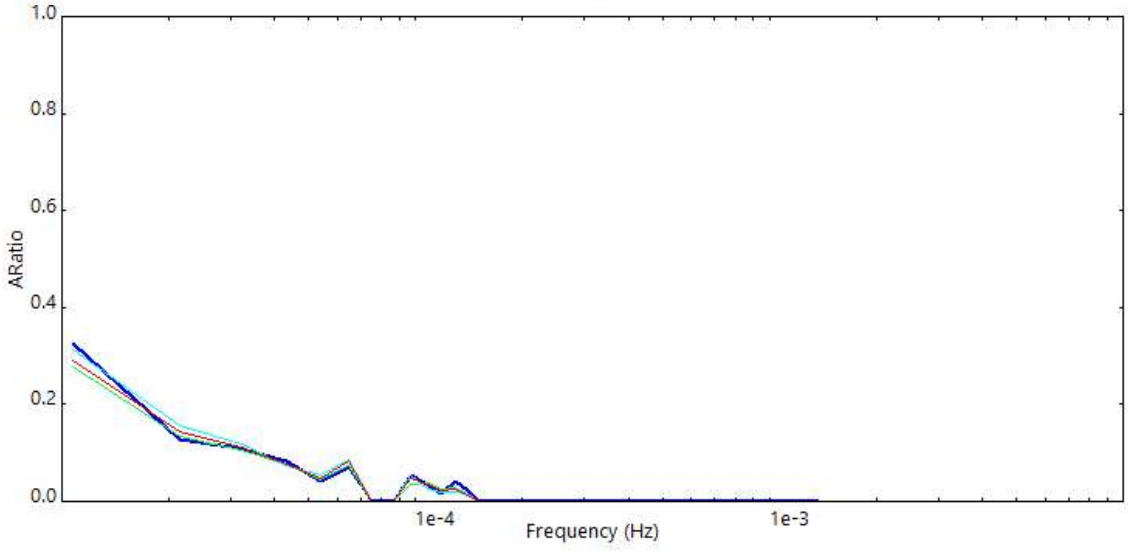

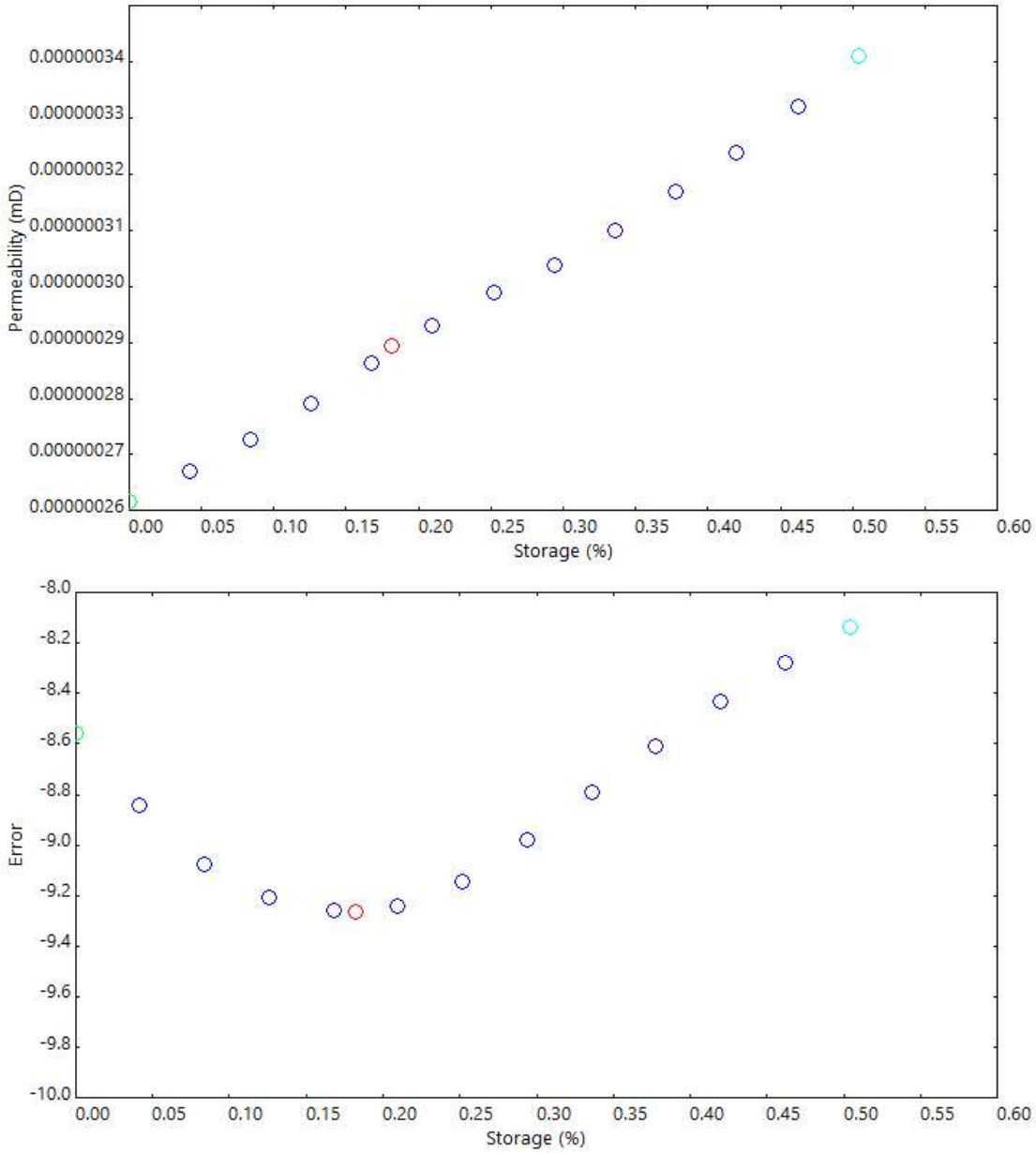

Figure B-54. Permeability results for sample LCT091014-1a

11. LCT091014-1b

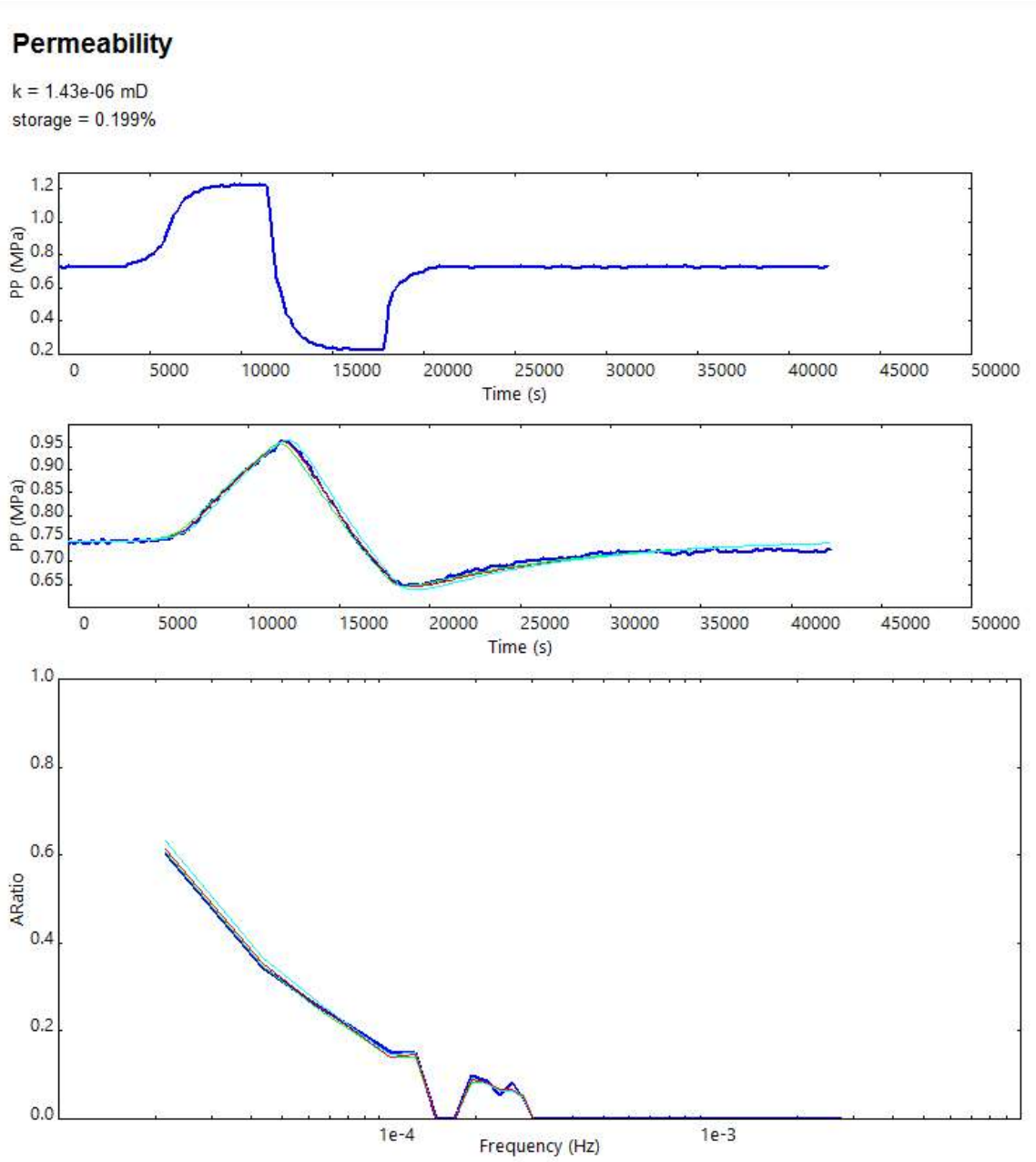

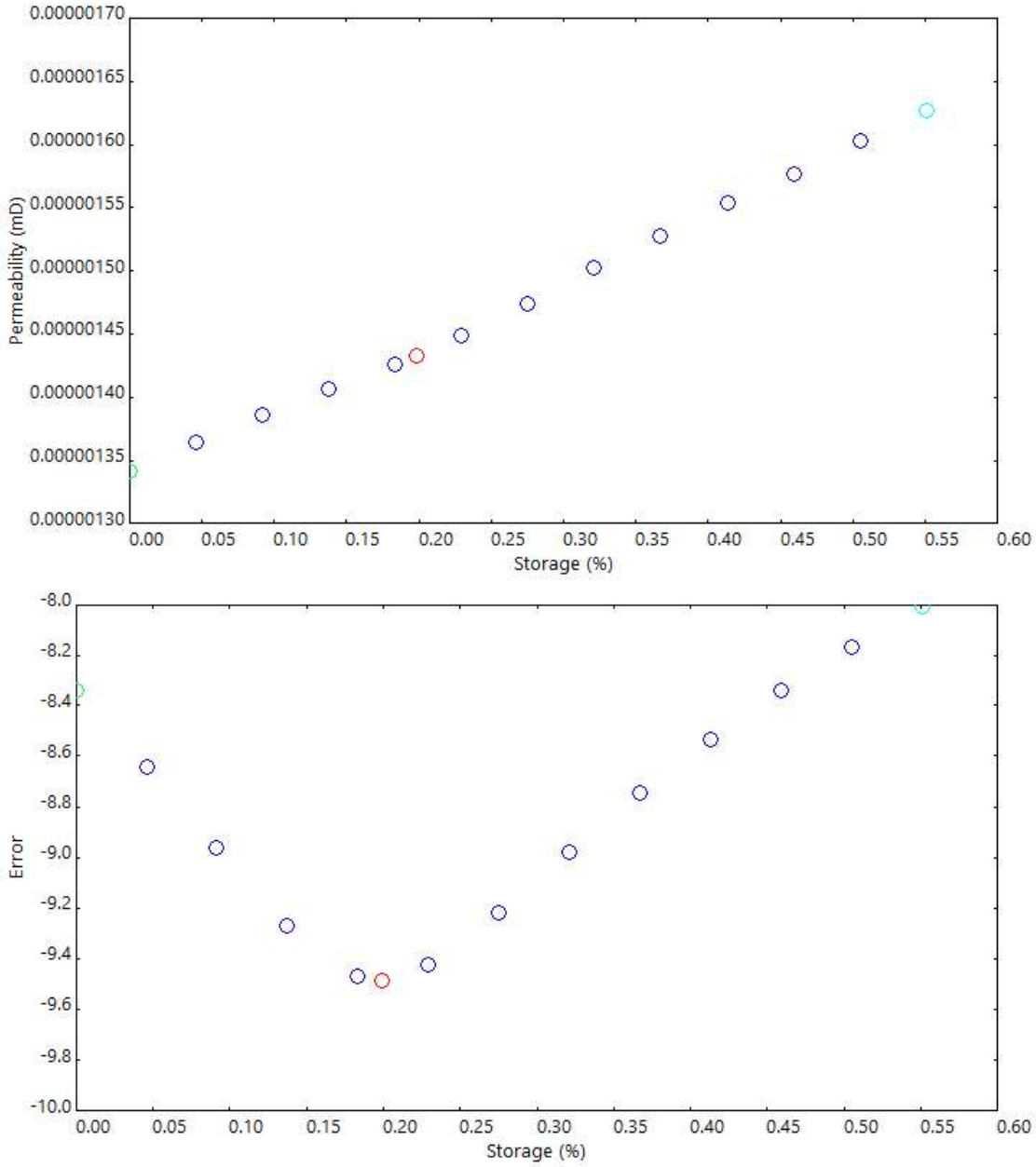

Figure B-55. Permeability results for sample LCT091014-1b

12. LCT091514-3(1)

Permeability

k = 1.36e-07 mD
storage = 0.295%

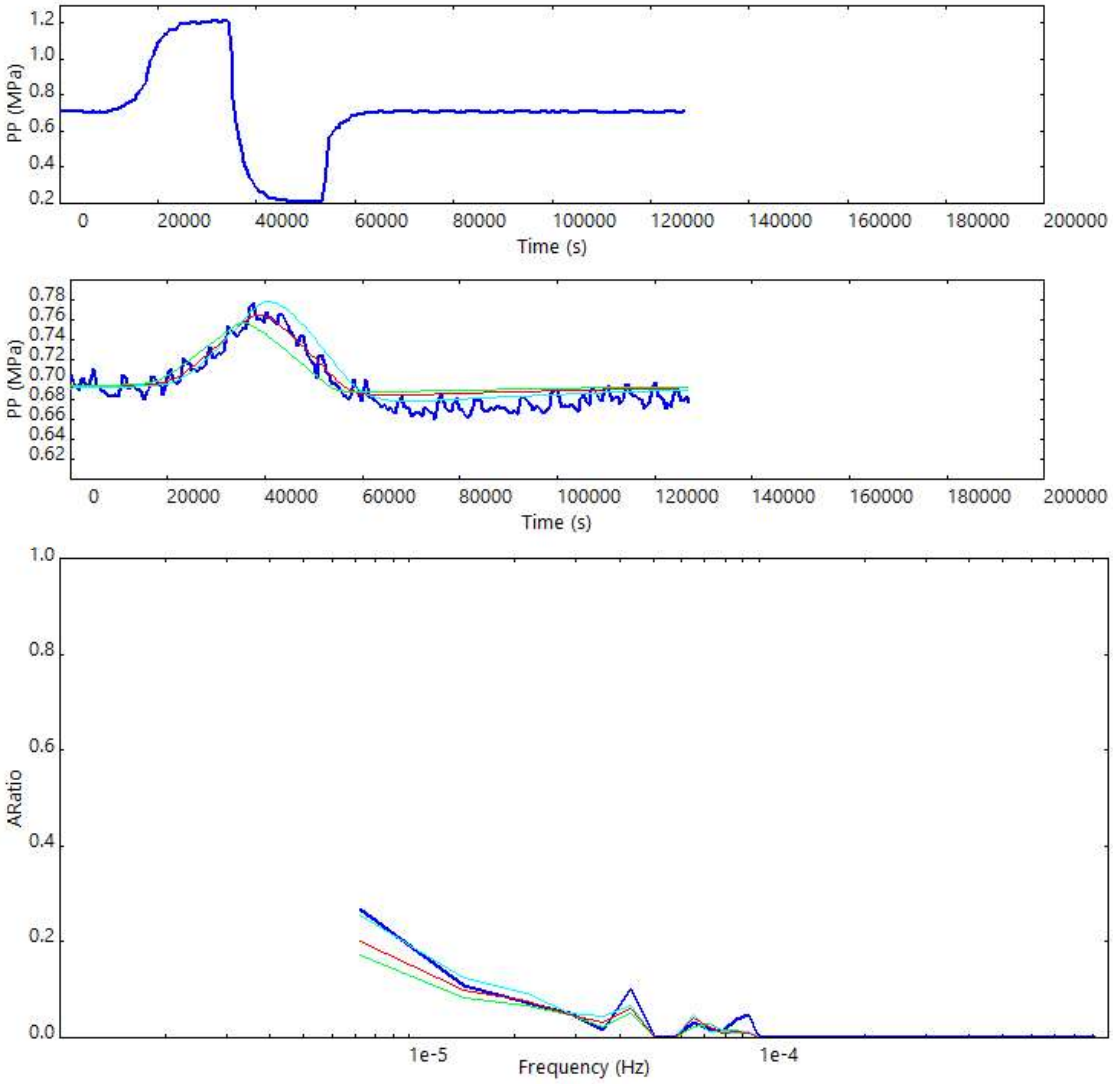

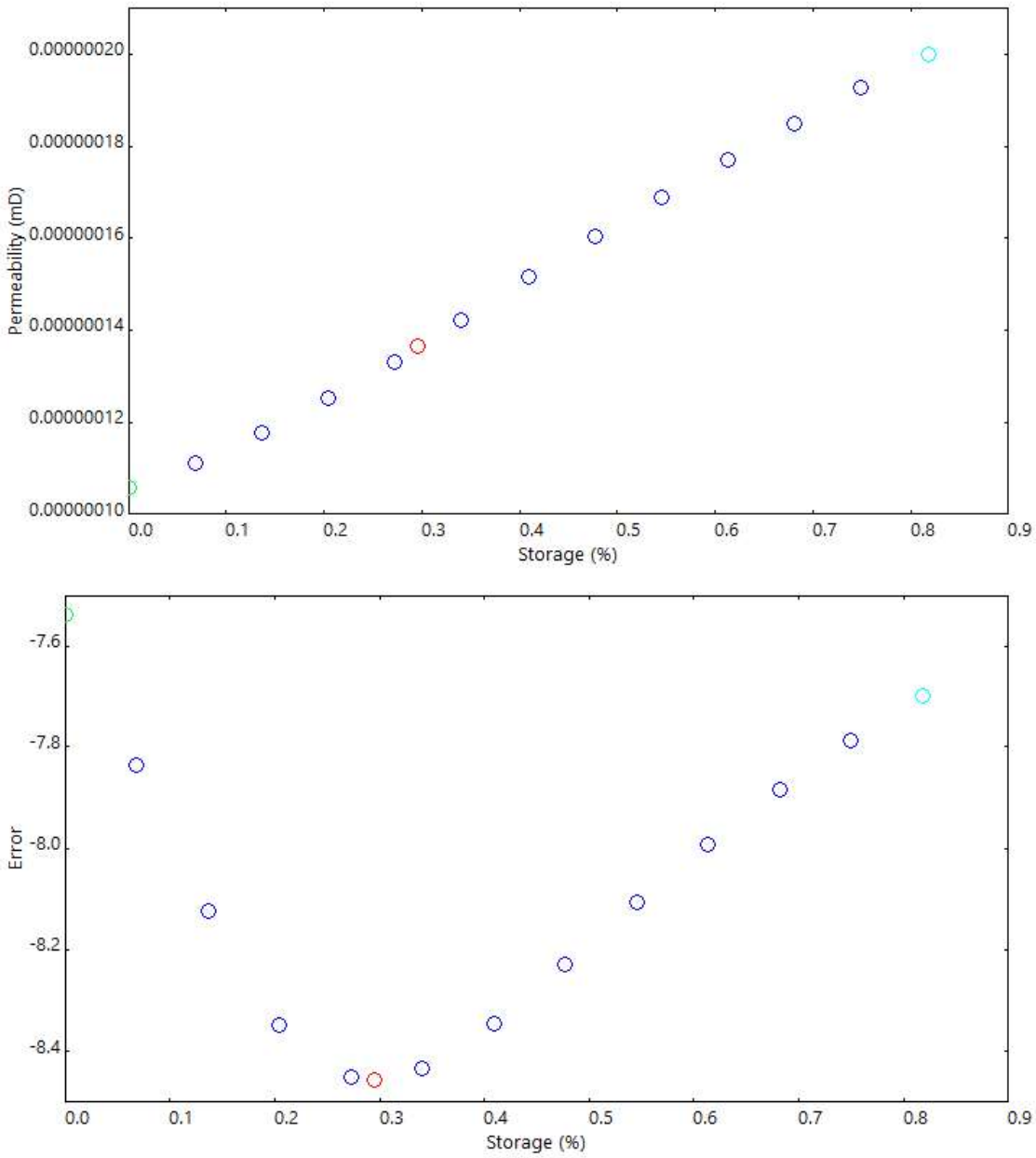

Figure B-56. Permeability results for sample LCT091514-3(1)

13. LCT091514-3(2)

Permeability

k = 4.21e-07 mD
storage = 0.943%

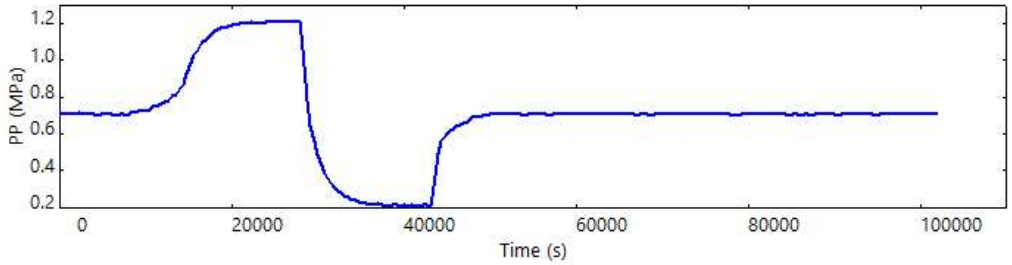

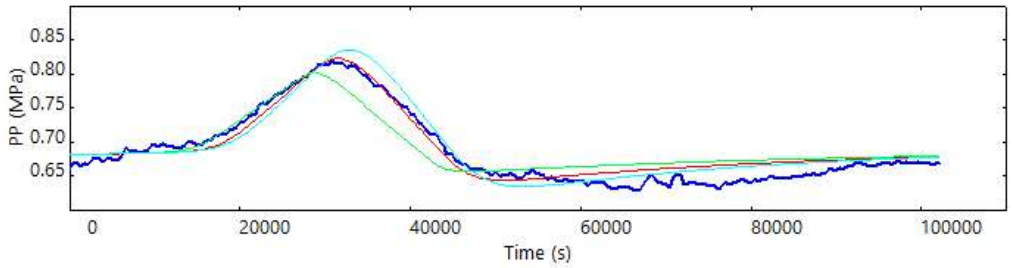

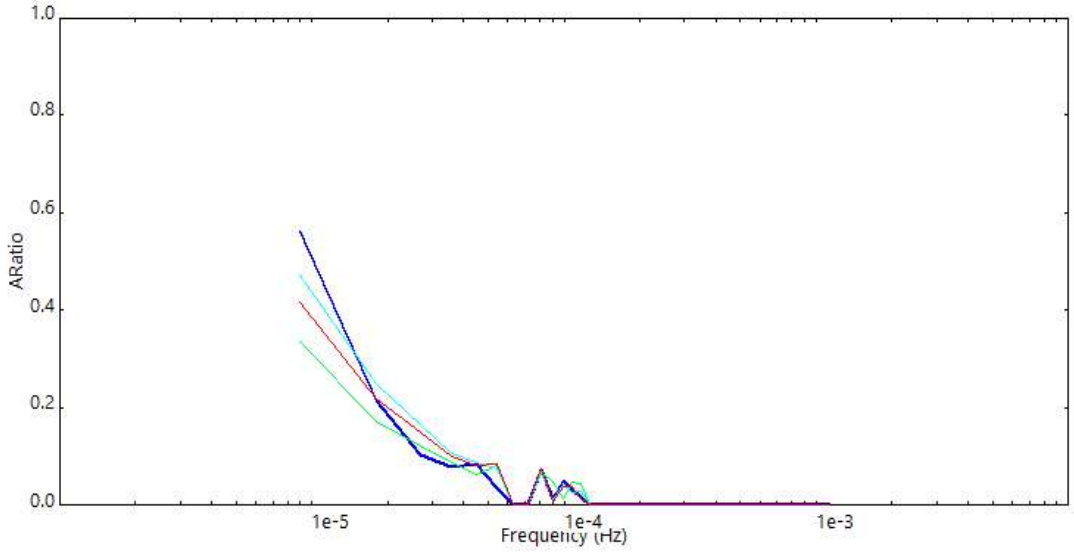

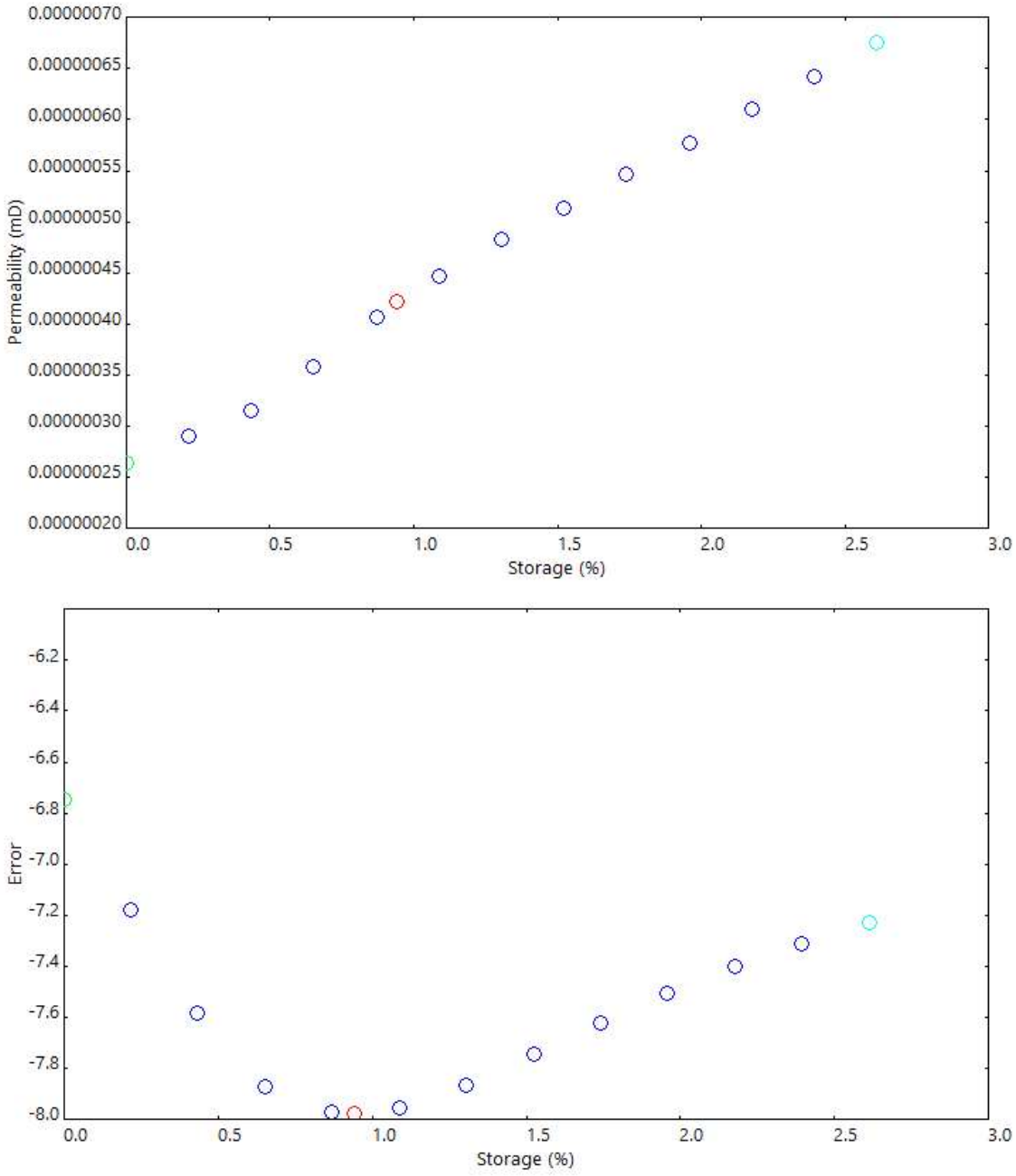

Figure B-57. Permeability results for sample LCT091514-3(2)

14. LCTBV071714-5a

Permeability

k = 2.59e-07 mD
storage = 0.120%

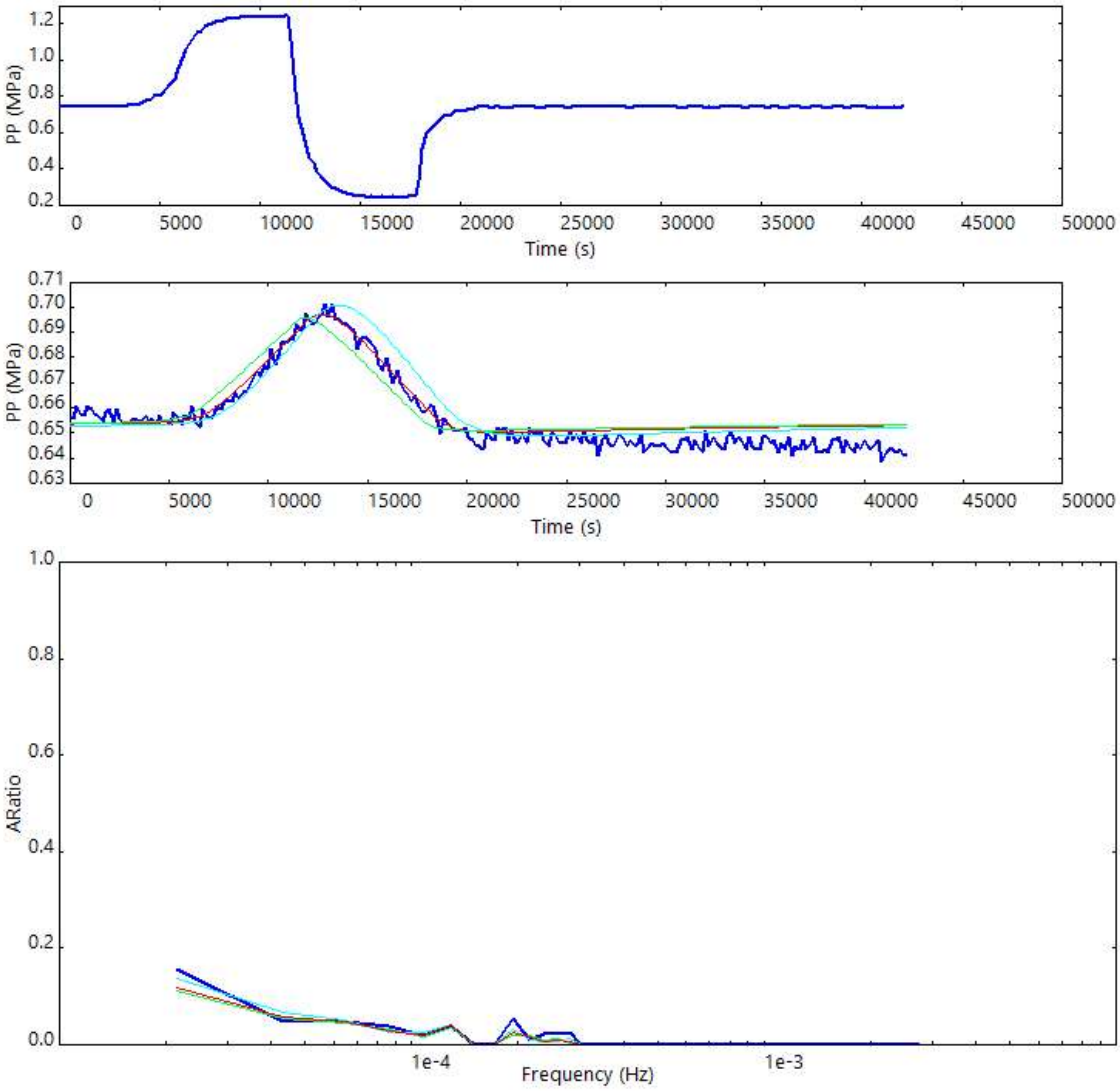

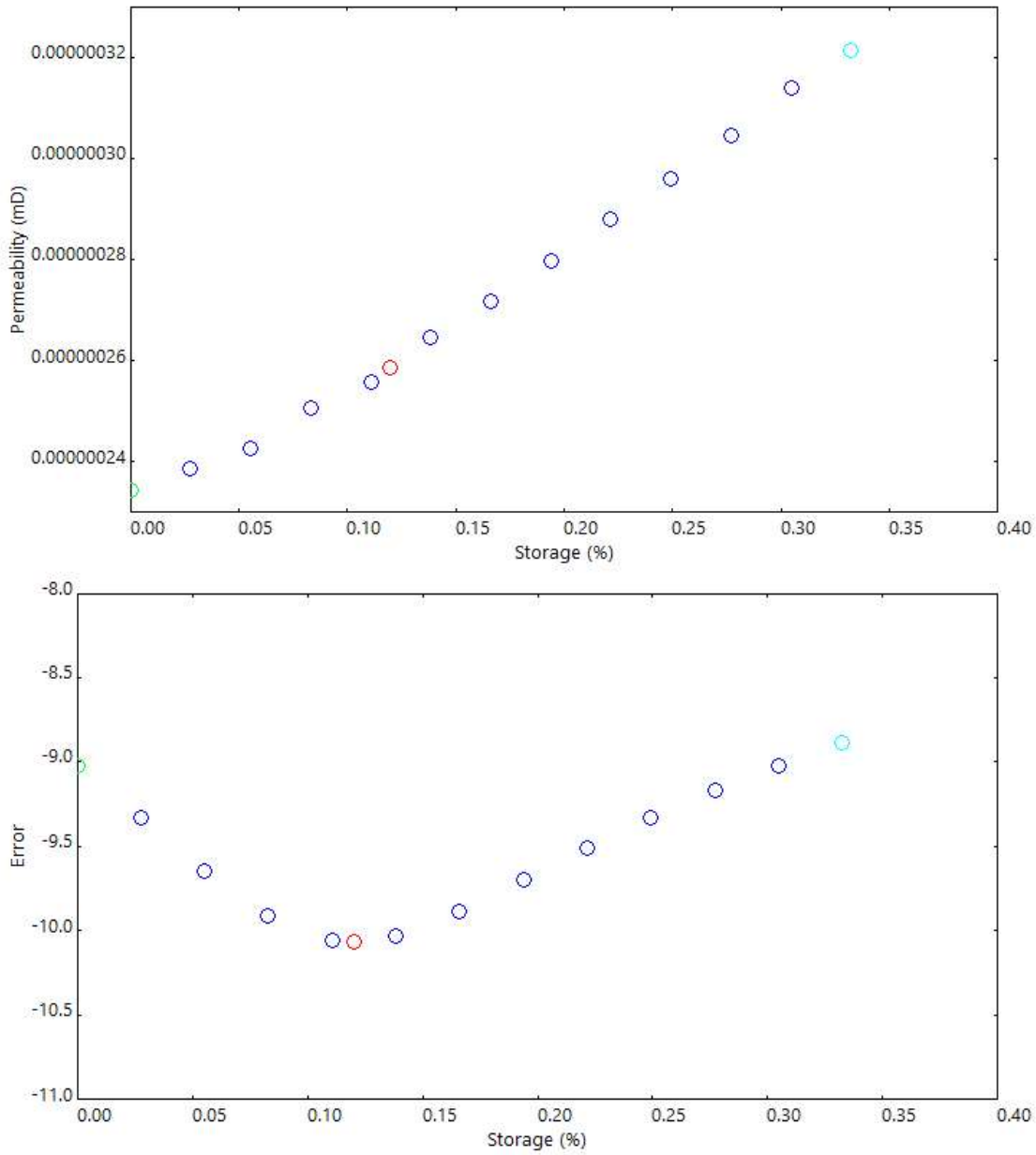

Figure B-58. Permeability results for sample LCTBV071714-5a

15. LCTV091314-4a

Permeability

k = 9.96e-07 mD
storage = 0.199%

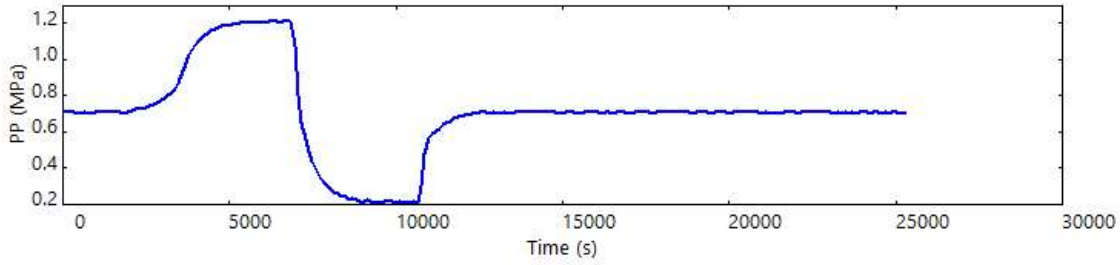

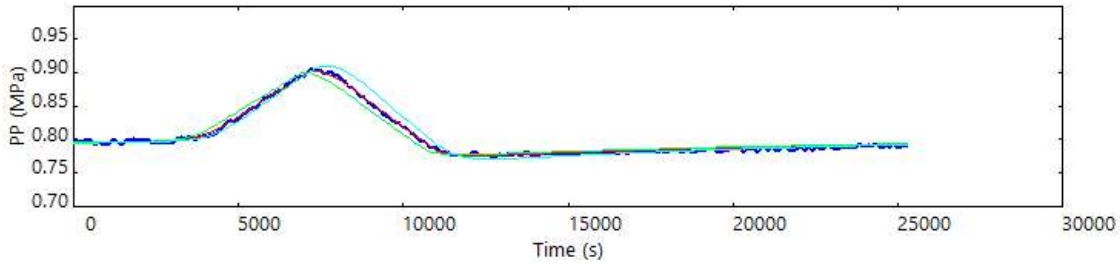

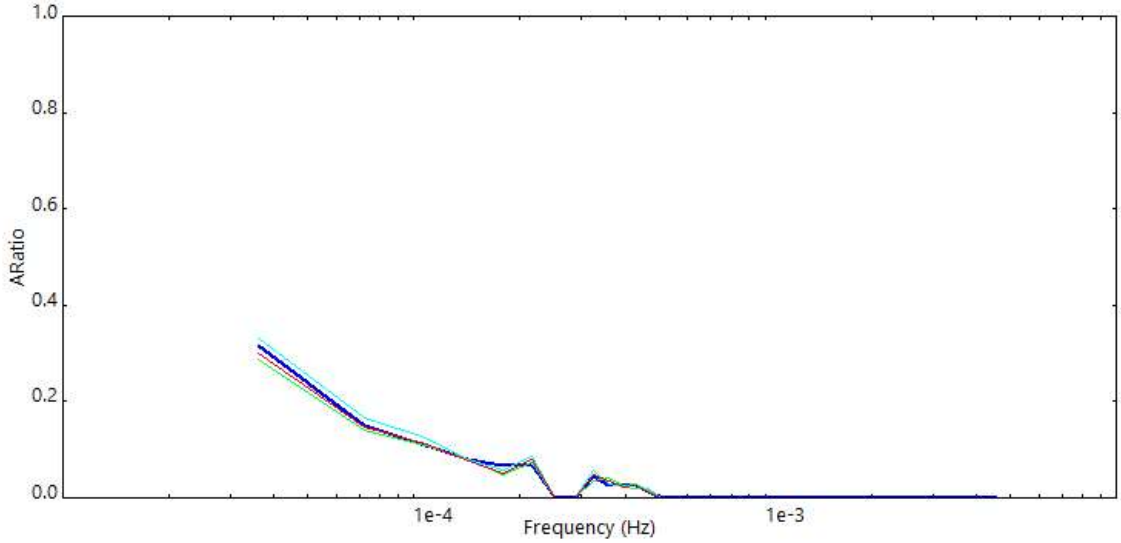

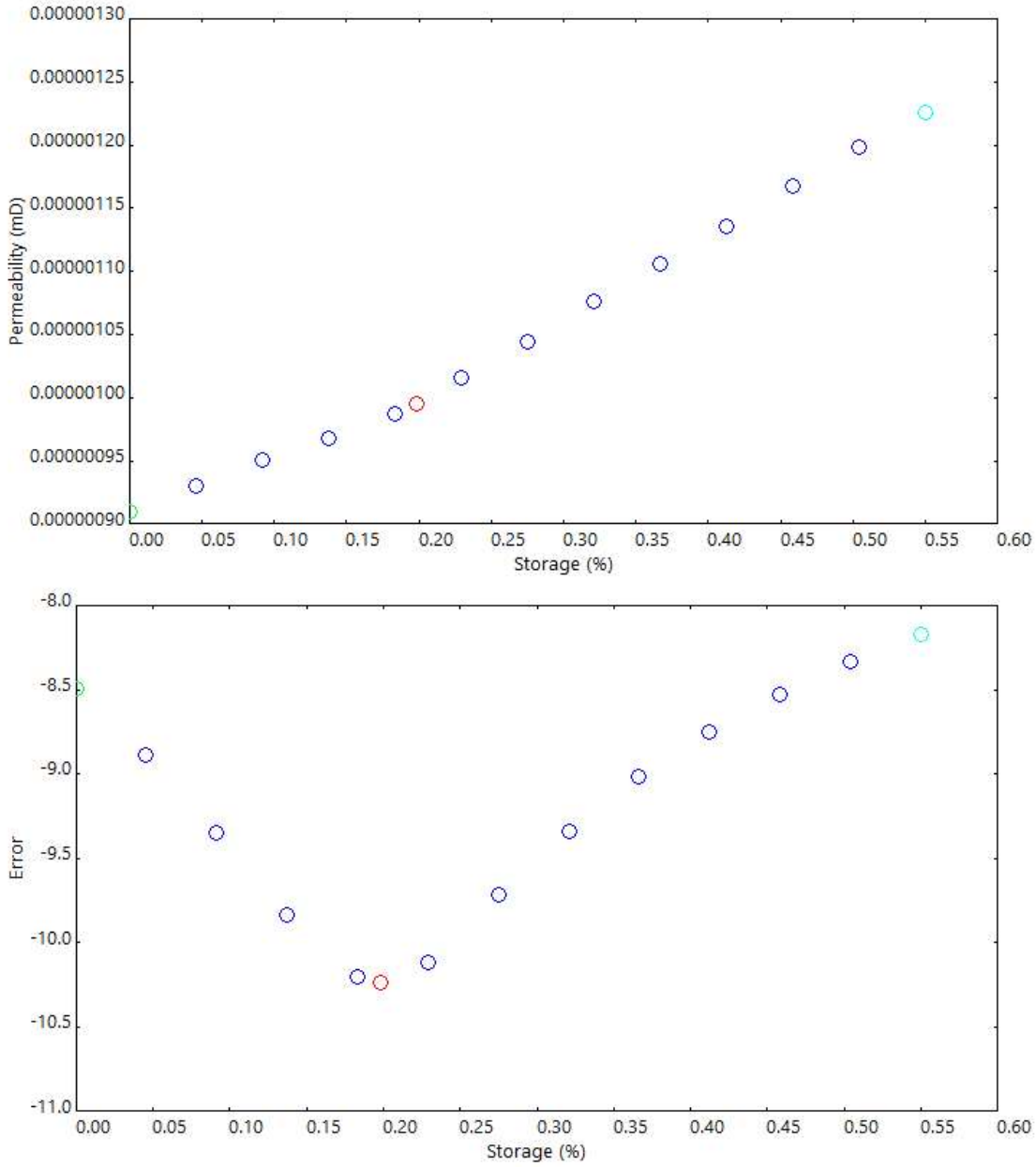

Figure B-59. Permeability results for sample LCTV090314-4a

16. LCTV091014-1c

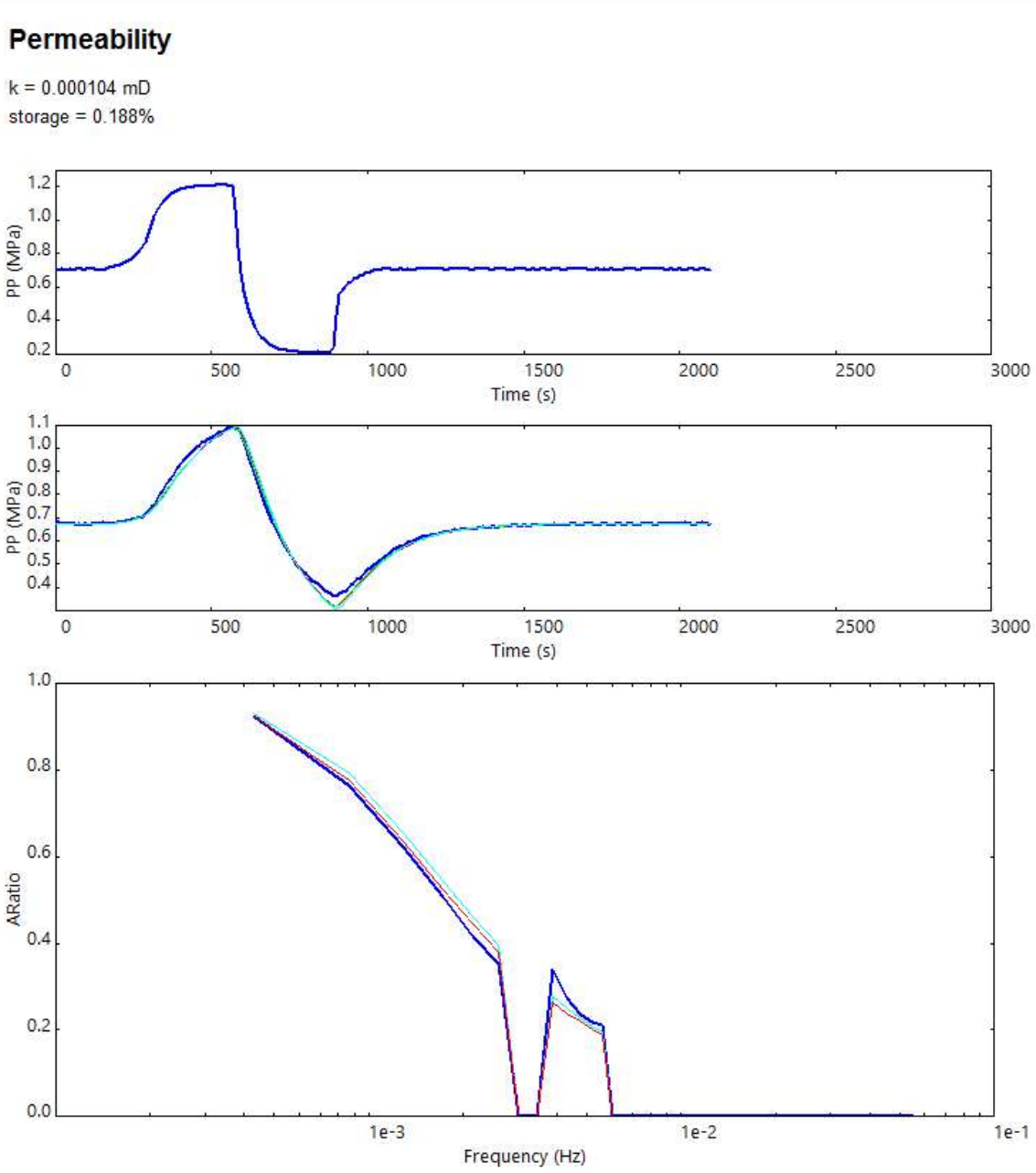

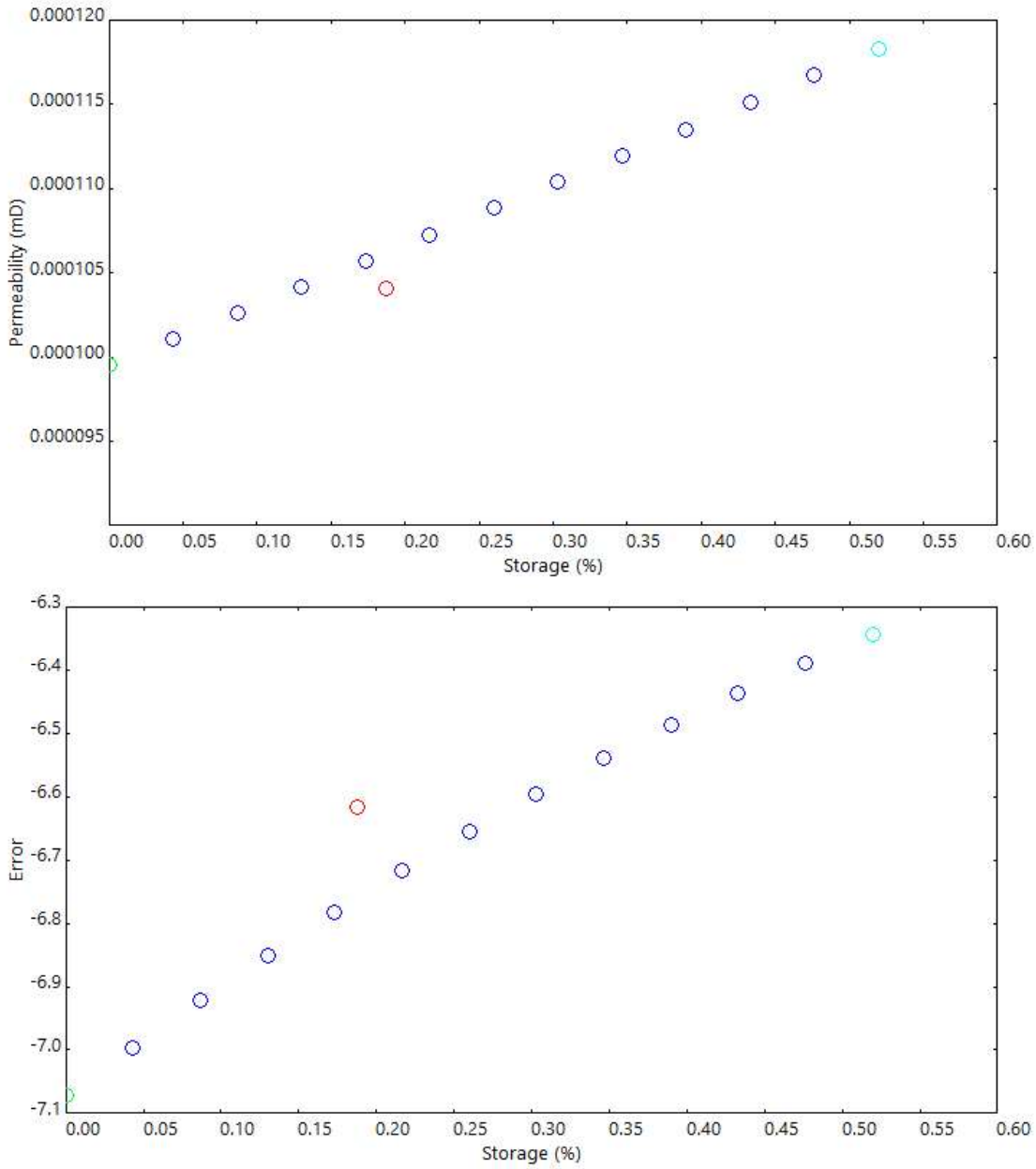

Figure B-60. Permeability results for sample LCTV091014-1c

17. LCTV091014-1d

Permeability

k = 5.63e-06 mD
storage = 0.590%

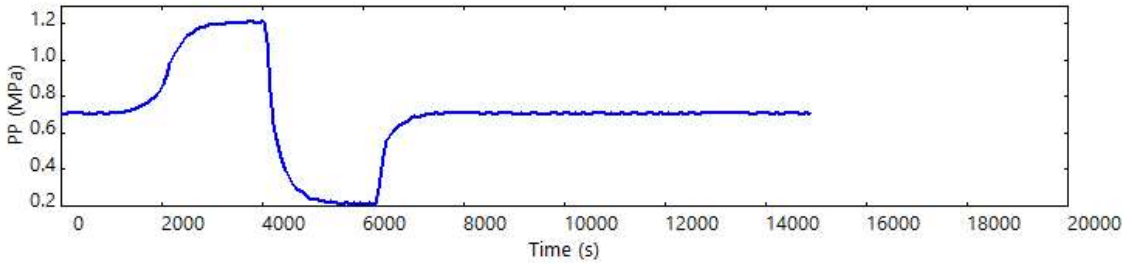

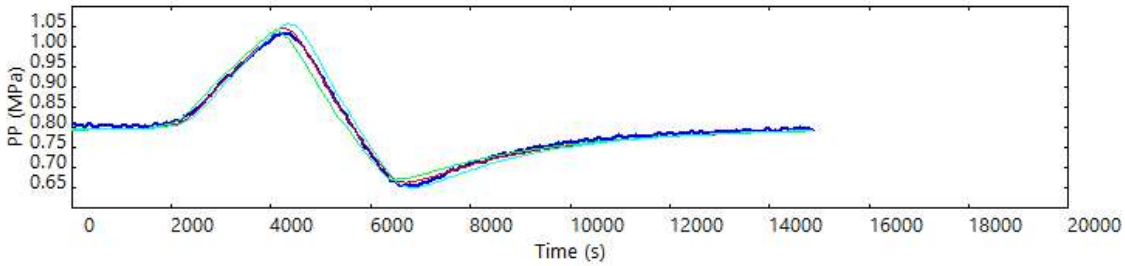

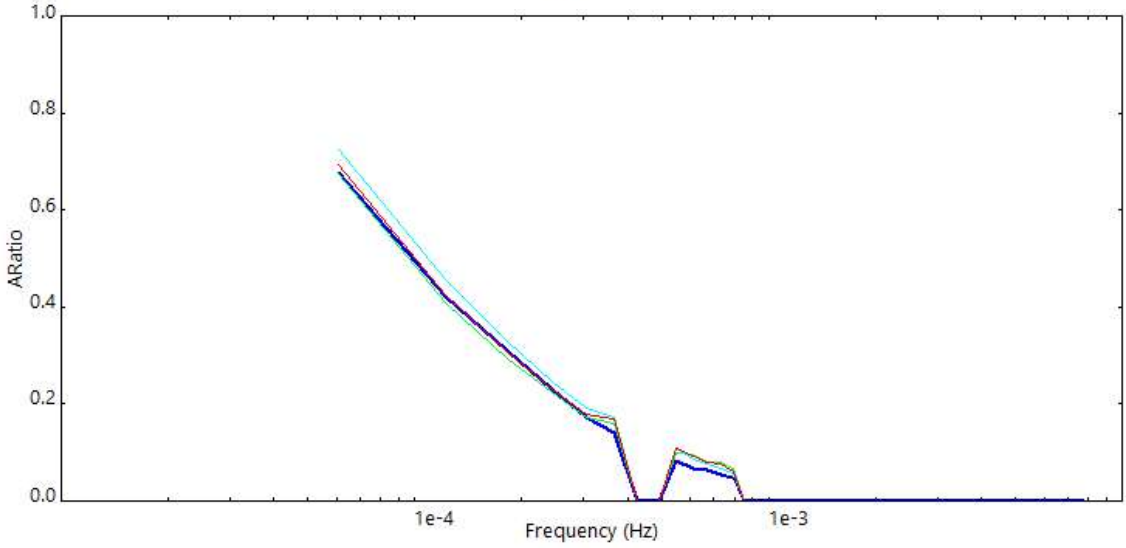

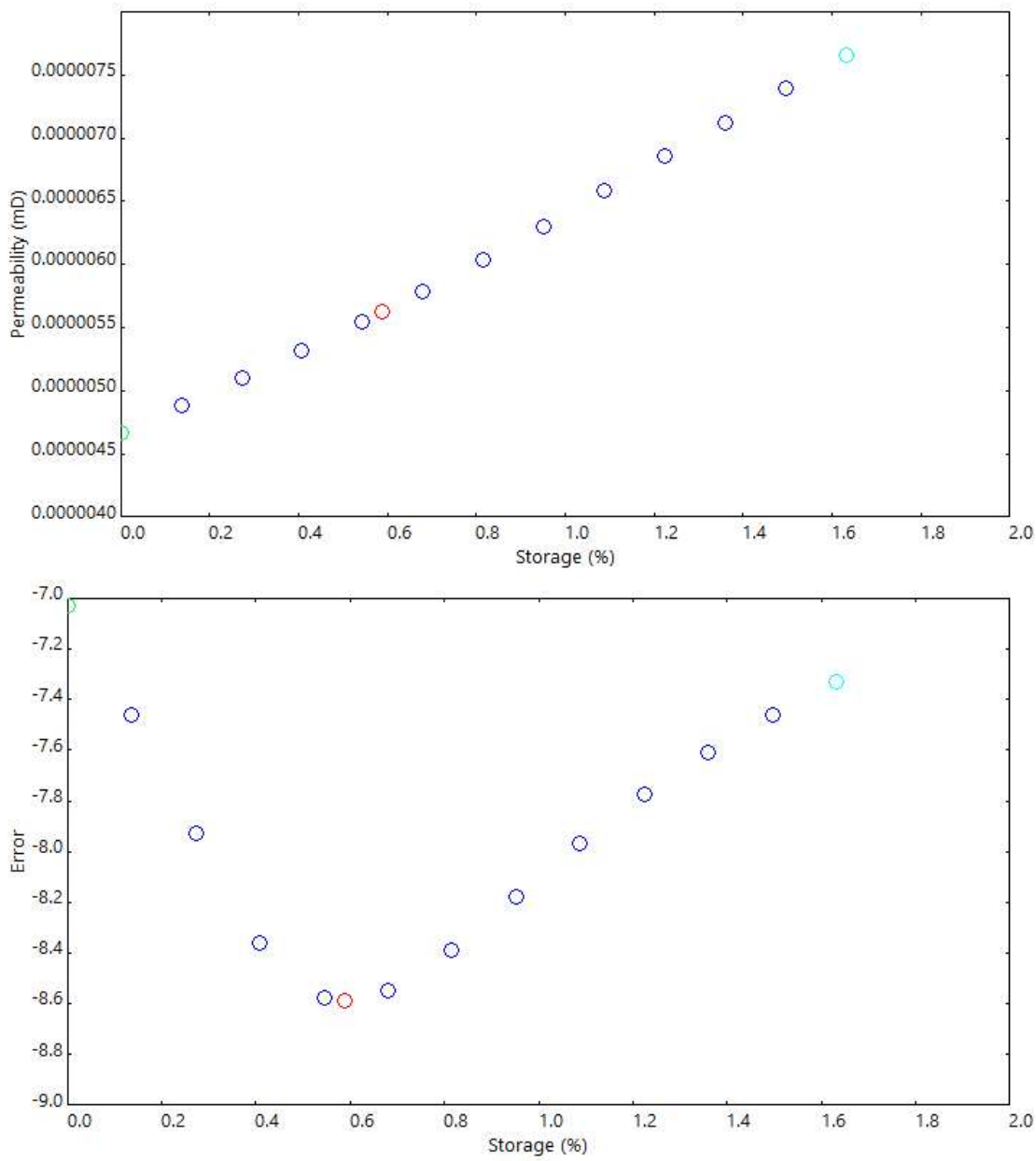

Figure B-61. Permeability results for sample LCTV091014-1d

B.7 Porosity Data

B.7.1 Telaga Bodas Samples

Table B-33. Wax measurement data for the Telaga Bodas samples

Sample	Dry Weight (W) (g)	Weight with Wax (P) (g)	Suspended Weight (Swax) (g)	Total Volume (Vsw) (cm3)	Volume of Wax (Vwax) (cm3)	Volume (V) (cm3)	Bulk Density (GB) (g/cm3)
K33_0191_00	52.26	54.63	30.15	24.48	2.59	21.89	2.39
K33_0191_03	51.31	53.33	30.28	23.05	2.21	20.84	2.46
K33_0192_1276	55.92	58.52	33.47	25.05	2.84	22.21	2.52
K33_0192_1277.75	53.14	55.37	30.64	24.73	2.44	22.29	2.38
K33_0364_1752	55.71	57.89	34.3	23.59	2.38	21.21	2.63
K33_0364_1753	52.66	55.47	30.98	24.49	3.07	21.42	2.46
K33_0393_1833.2	59.6	62.21	37.17	25.04	2.85	22.19	2.69
K33_0393_1834	59.23	61.59	37.16	24.43	2.58	21.85	2.71
K33_0423_1916.3	56.24	58.96	34.35	24.61	2.97	21.64	2.60
K33_0423_1919	52.86	55.95	30.66	25.29	3.38	21.91	2.41
T2_0117_00	57.87	60.1	35.57	24.53	2.44	22.09	2.62
T2_0117_03	56.56	59.14	35.04	24.1	2.82	21.28	2.66
T2_0156_03	54.98	57.62	32.73	24.89	2.89	22.00	2.50

Table B-34. Pycnometer measurements for the Telaga Bodas sub-samples used to calculate porosity

Sample	Sub-sample	Dry Weight (g)	Av. density (g/cm3)	Volume (cm3)	Av. Particle Density (g/cm3)
0191_00	A	3.130	2.8402	1.1020	2.8567
	B	2.570	2.8723	0.8948	
	C	2.612	2.8512	0.9161	
	F	3.147	2.8629	1.0992	
0191_03	A	5.539	2.7840	1.9896	2.8224
	B	5.254	2.8011	1.8757	
	C	3.066	2.8527	1.0748	
	D	3.443	2.8518	1.2073	
1276	A	4.338	2.7798	1.5605	2.7304
	B	6.377	2.6757	2.3833	
	C	6.623	2.7023	2.4509	
	D	4.638	2.7638	1.6781	
1277.75	A	5.157	2.7700	1.8617	2.7819
	B	4.280	2.7516	1.5555	
	C	5.203	2.7462	1.8946	
	D	6.822	2.8043	2.4327	
	E	3.449	2.8376	1.2155	
1752m	A	5.033	2.8684	1.7546	2.9518
	B	3.465	2.9905	1.1587	
	C	2.766	2.9004	0.9537	
	D	3.084	3.0477	1.0119	
1753	A	5.512	2.9781	1.8508	3.0018
	B	4.364	3.0430	1.4341	
	C	3.787	3.0259	1.2515	
	D	6.904	2.9601	2.3324	
1833.2	A	5.616	2.8089	1.9994	2.8074
	B	5.574	2.8092	1.9842	
	C	5.411	2.8077	1.9272	
	D	6.806	2.8038	2.4274	
1834	A	5.109	2.8401	1.7989	2.8434
	B	6.360	2.8310	2.2466	
	C	4.775	2.8471	1.6771	

	D	3.489	2.8555	1.2219	
1916.3	A	9.003	2.8661	3.1412	2.9191
	B	6.859	2.9073	2.3592	
	C	7.363	3.0005	2.4539	
	D	3.749	2.9023	1.2917	
1919	A	6.263	2.8219	2.2194	2.8382
	B	7.236	2.8434	2.5448	
	C	4.992	2.8593	1.7459	
	D	5.796	2.8281	2.0494	
0117_00	A	6.837	2.8549	2.3948	2.8518
	B	7.693	2.7993	2.7482	
	C	5.604	2.7914	2.0076	
	D	4.114	2.9617	1.3891	
0117_03	A	3.513	2.8637	1.2267	2.9107
	B	4.714	2.9616	1.5917	
	C	2.755	2.9069	0.9477	
0156_03	A	7.149	2.6817	2.6658	2.7270
	B	7.123	2.7198	2.6189	
	C	7.522	2.7442	2.7411	
	D	2.872	2.7621	1.0398	

B.7.2 Lake City Samples

Table B-35. Wax measurement data for the Lake City samples

Sample	Dry Weight (W) (g)	Weight with Wax (P) (g)	Suspended Weight (Swax) (g)	Total Volume (Vsw) (cm3)	Volume of Wax (Vwax) (cm3)	Volume (V) (cm3)	Bulk Density (GB) (g/cm3)
LCB090314-1b	57.98	60.43	36.03	24.4	2.68	21.72	2.67
LCB090314-5	55.43	57.69	33.73	23.96	2.47	21.49	2.58
LCB091414-2	55.96	58.61	33.97	24.64	2.90	21.74	2.57
LCDLA082913-1	41.79	44.63	20.12	24.51	3.10	21.41	1.95
LCDLA082913-2	42.71	45.47	21.93	23.54	3.02	20.52	2.08
LCG090714-2c	56.22	58.97	33.62	25.35	3.01	22.34	2.52
LCG090714-3a	53.28	56.44	31.51	24.93	3.45	21.48	2.48
LCG090714-3b	55.55	58.13	34.32	23.81	2.82	20.99	2.65
LCG091314-1b	54.52	56.7	32.95	23.75	2.38	21.37	2.55
LCT091014-1a	51.2	53.74	29.62	24.12	2.78	21.34	2.40
LCT091014-1b	51.69	53.98	29.64	24.34	2.50	21.84	2.37
LCT091514-3(1)	53.5	56.02	31.1	24.92	2.75	22.17	2.41
LCT091514-3(2)	52.65	54.92	30.83	24.09	2.48	21.61	2.44
LCTBV071714-5a	55.76	57.94	33.71	24.23	2.38	21.85	2.55
LCTV090314-4a	54.99	58.03	33.17	24.86	3.32	21.54	2.55
LCTV091014-1c	55.08	57.61	33.47	24.14	2.77	21.37	2.58
LCTV091014-1d	54.54	58.18	32.18	26	3.98	22.02	2.48

Table B-36. Pycnometer measurements for the Lake City sub-samples used to calculate porosity

Sample	Sub-sample	Dry Weight (g)	Av. density (g/cm3)	Volume (cm3)	Av. Particle Density (g/cm3)
B-1b	A	5.315	2.7910	1.9043	2.7866
	B	4.967	2.7949	1.7772	
	C	3.921	2.8128	1.3940	
	D	7.759	2.7475	2.8240	
B-5	A	10.858	2.6993	4.0225	2.6890
	B	11.827	2.6409	4.4784	
	C	13.018	2.7087	4.8060	
	D	13.710	2.7069	5.0648	
B-2	A	7.188	2.7507	2.6132	2.7911
	B	5.500	2.8071	1.9593	
	C	4.600	2.7906	1.6484	
	D	4.207	2.8343	1.4843	
	E	5.422	2.7729	1.9554	
DLA-1	A	7.379	2.4905	2.9629	2.4882
	B	9.997	2.4865	4.0205	
	C	9.755	2.4840	3.9271	
	D	9.699	2.4918	3.8924	
DLA-2	A	6.435	2.5692	2.5047	2.5645
	B	7.039	2.5605	2.7491	
	C	6.429	2.5679	2.5036	
	D	7.596	2.5604	2.9667	
G-2c	A	9.882	2.6766	3.6920	2.6723
	B	9.102	2.6735	3.4045	
	C	10.997	2.6696	4.1193	
	D	12.166	2.6694	4.5576	
G-3a	A	7.217	2.6848	2.6881	2.6832
	B	7.955	2.6773	2.9713	
	C	6.689	2.6875	2.4889	
	D	7.537	2.6831	2.8091	
G-3b	A	9.005	2.6915	3.3457	2.7022
	B	8.944	2.7155	3.2937	
	C	11.176	2.6950	4.1469	

	D	9.767	2.7066	3.6086	
G-1b	A	7.195	2.7074	2.6575	2.6814
	B	10.841	2.6609	4.0742	
	C	7.739	2.6958	2.8708	
	D	9.547	2.6613	3.5873	
T-1a	A	6.552	2.7052	2.4220	2.7136
	B	5.693	2.7068	2.1032	
	C	4.525	2.7247	1.6607	
	D	4.409	2.7176	1.6224	
T-1b	A	9.066	2.6685	3.3974	2.6580
	B	8.893	2.6477	3.3588	
	C	8.074	2.6467	3.0506	
	D	9.567	2.6690	3.5845	
T-3	A	10.457	2.6014	4.0198	2.5911
	B	8.134	2.5900	3.1405	
	C	7.425	2.5820	2.8757	
TBV-5a	A	6.189	2.6409	2.3435	2.6737
	B	4.907	2.6546	1.8485	
	C	3.710	2.6779	1.3854	
	D	3.542	2.7212	1.3016	
TV-4a	A	5.756	2.6815	2.1466	2.6756
	B	6.899	2.6696	2.5843	
	C	6.652	2.6802	2.4819	
	D	6.789	2.6615	2.5508	
	E	4.875	2.6880	1.8136	
	F	6.609	2.6728	2.4727	
TV-1c	B	5.618	2.6766	2.0989	2.6715
	C	3.924	2.6664	1.4716	
TV-1d	A	8.646	2.6617	3.2483	2.6987
	B	6.506	2.6845	2.4235	
	C	4.602	2.6788	1.7179	
	D	6.588	2.7096	2.4314	
	E	4.994	2.7450	1.8193	
	F	2.918	2.7125	1.0758	

B.8 UCS Data and Post-Failure Core Photographs

B.8.1 Telaga Bodas Samples

1. K33_0191_00

Figure B-62. UCS data and post-failure photographs for sample K33_0191_00

2. K33_0191_03

Figure B-63. UCS data and post-failure photographs for sample K33_0191_03

3. K33_0192_1276

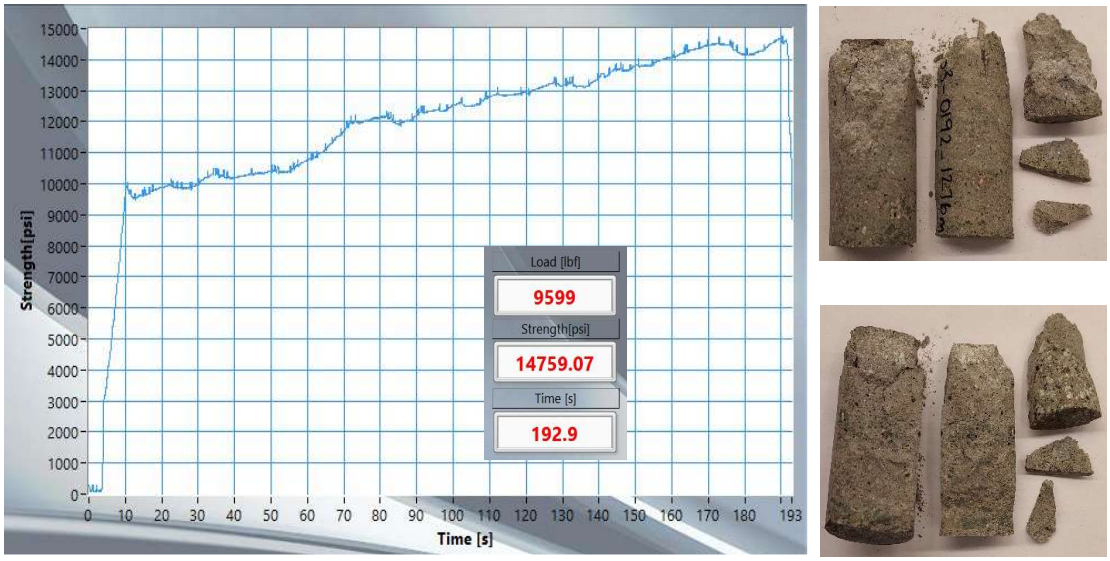

Figure B-64. UCS data and post-failure photographs for sample K33_0192_1276

4. K33_0191_1277.75

Figure B-65. UCS data and post-failure photographs for sample K33_0192_1277.75

5. K33_0364_1752

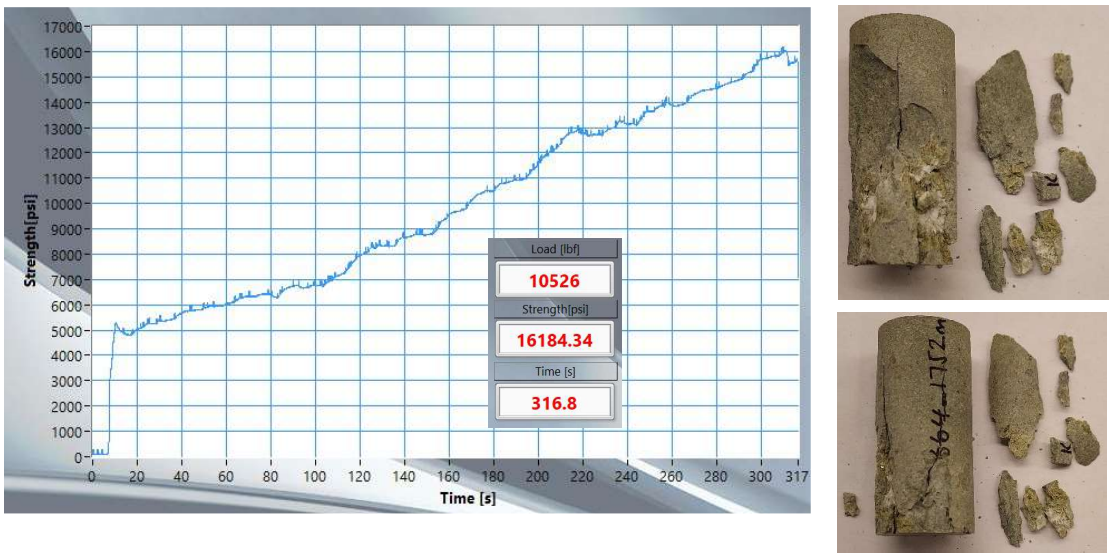

Figure B-66. UCS data and post-failure photographs for sample K33_0364_1752

6. K33_0364_1753

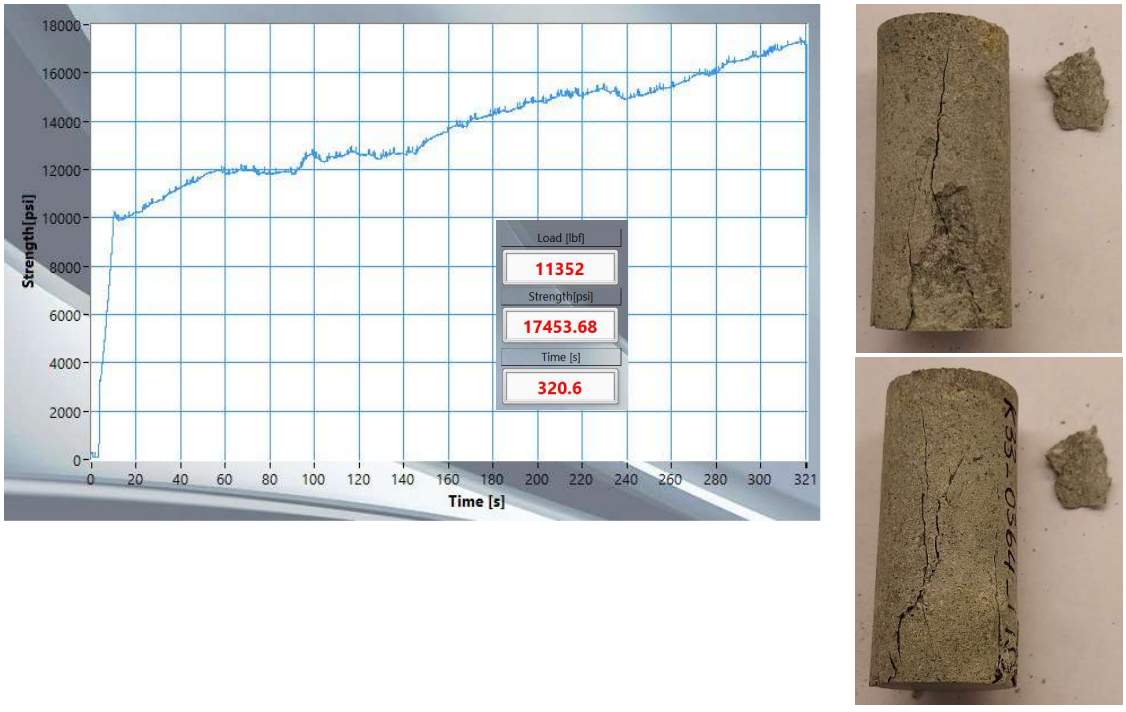

Figure B-67. UCS data and post-failure photographs for sample K33_0364_1753

7. K33_0393_1833.2

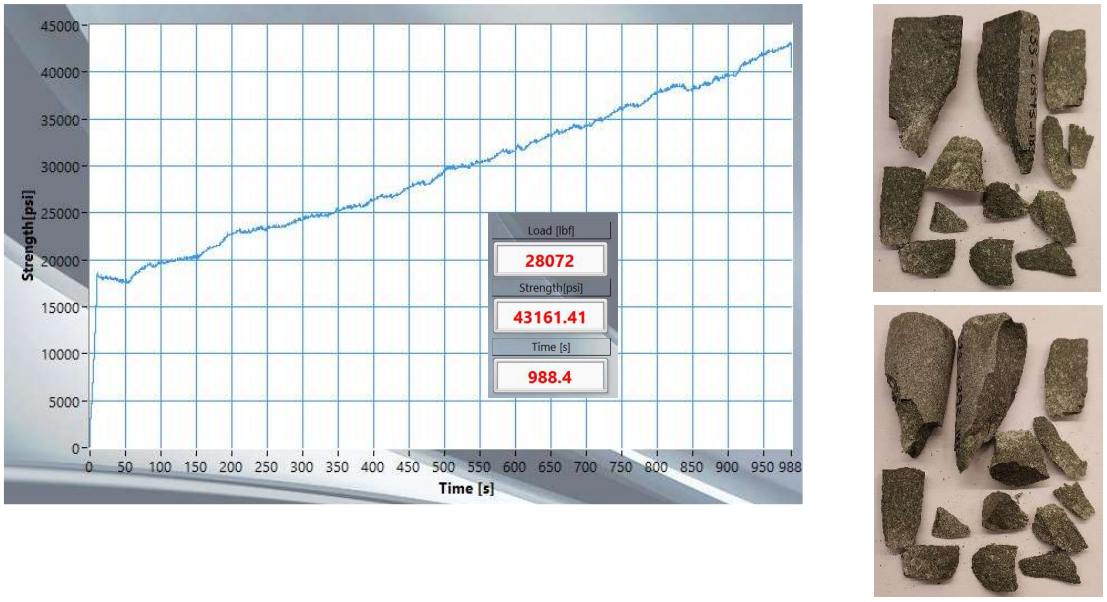

Figure B-68. UCS data and post-failure photographs for sample K33_0393_1833.2

8. K33_0393_1834

Figure B-69. UCS data and post-failure photographs for sample K33_0393_1834

9. K33_0423_1916.3

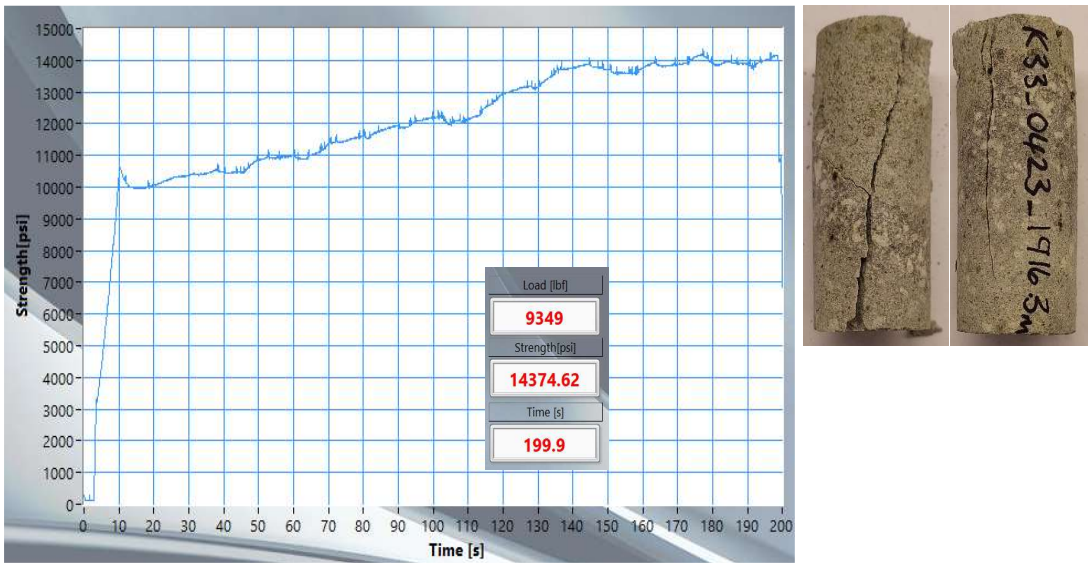

Figure B-70. UCS data and post-failure photographs for sample K33_0423_1916.3

10. K33_0423_1919

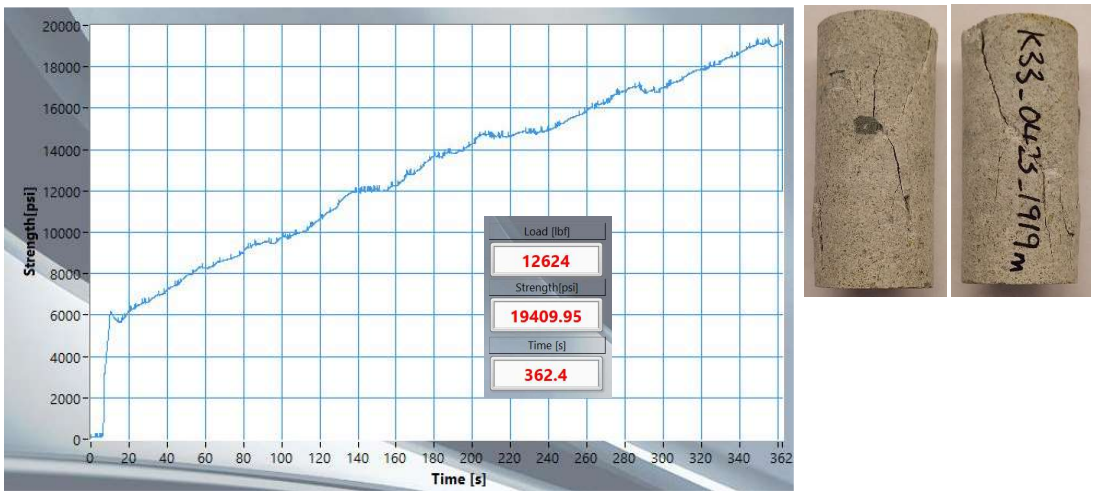

Figure B-71. UCS data and post-failure photographs for sample K33_0423_1919

11. T2_0156_03

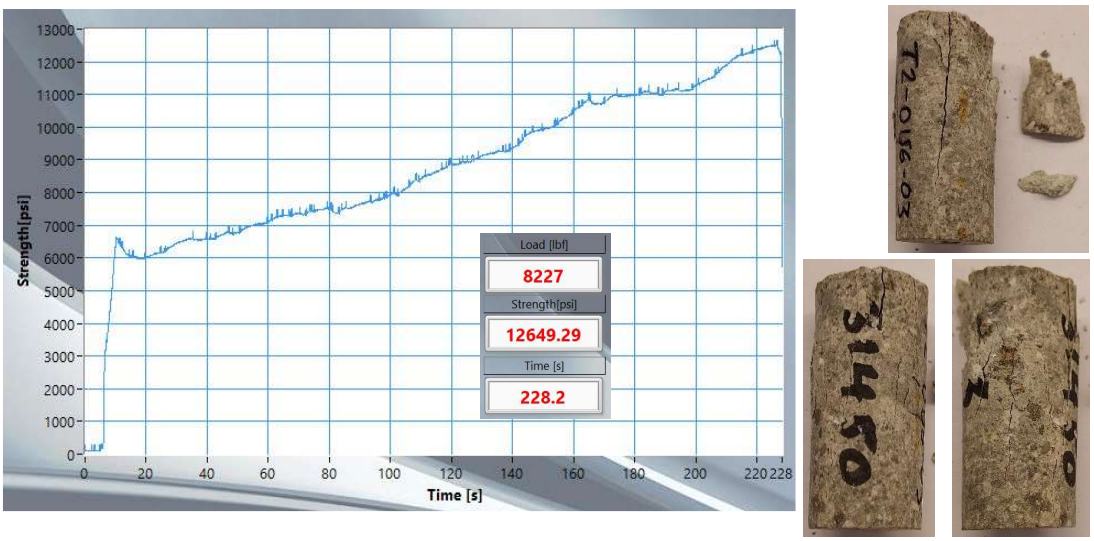

Figure B-72. UCS data and post-failure photographs for sample T2_0156_03

12. T2_0117_00

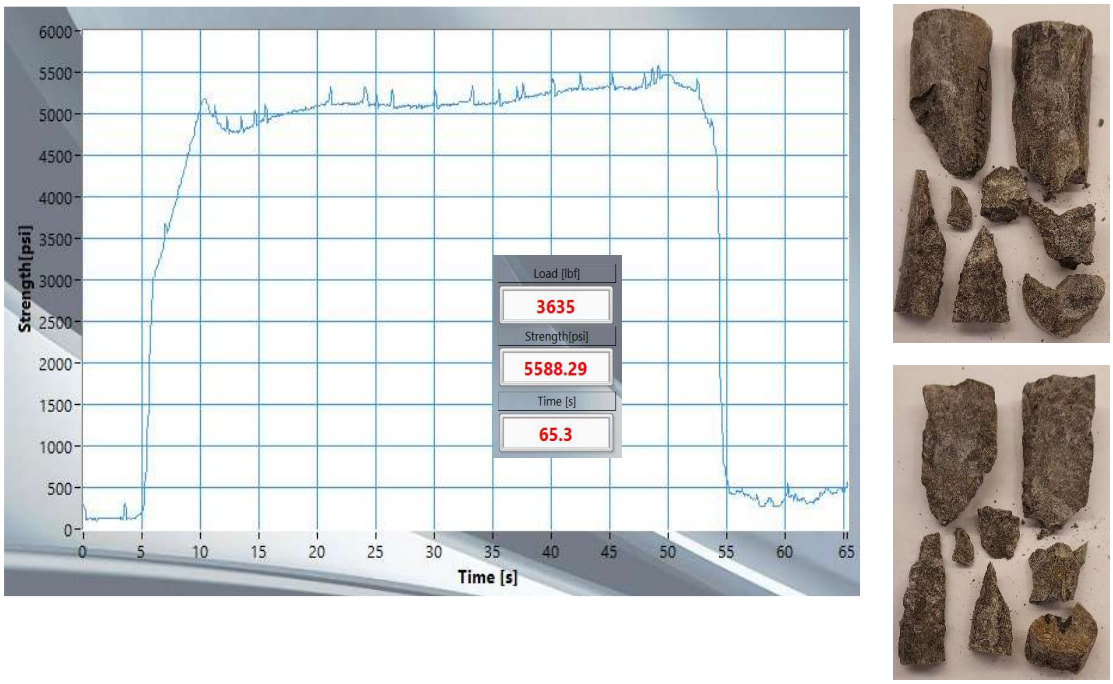

Figure B-73. UCS data and post-failure photographs for sample T2_0117_00

13. T2_0117_03

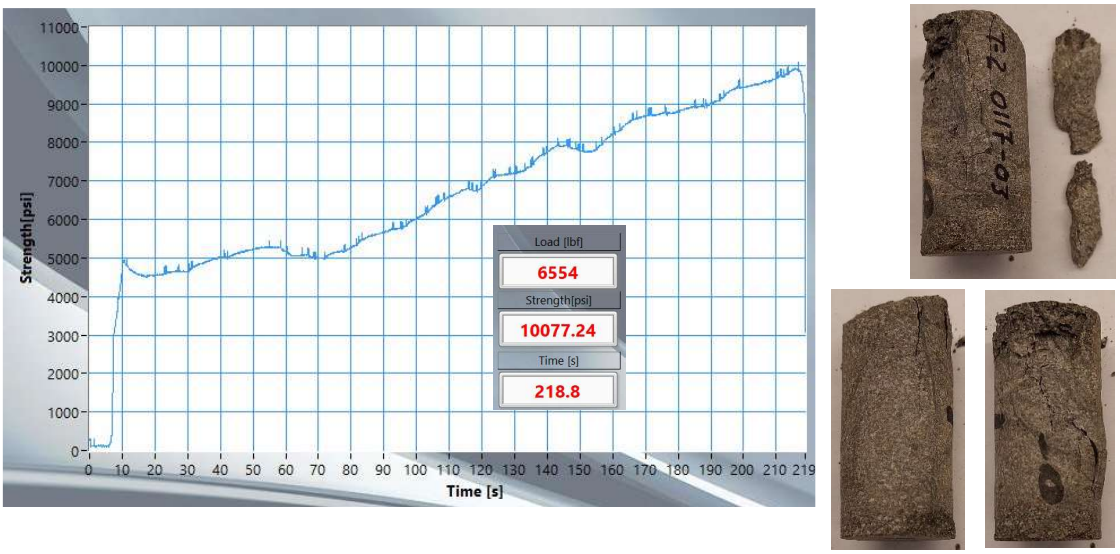

Figure B-74. UCS data and post-failure photographs for sample T2_0117_03

B.8.2 Lake City Samples

1. LCB090314-1b

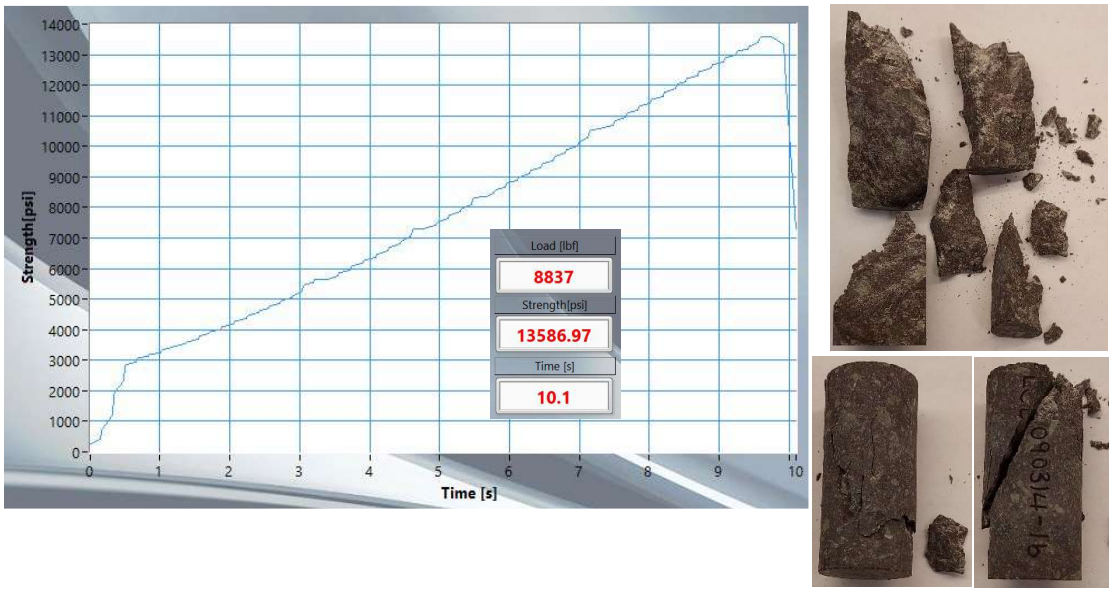

Figure B-75. UCS data and post-failure photographs for sample LCB090314-1b

2. LCB090314-5

Figure B-76. UCS data and post-failure photographs for sample LCB090314-5

3. LCB091414-2

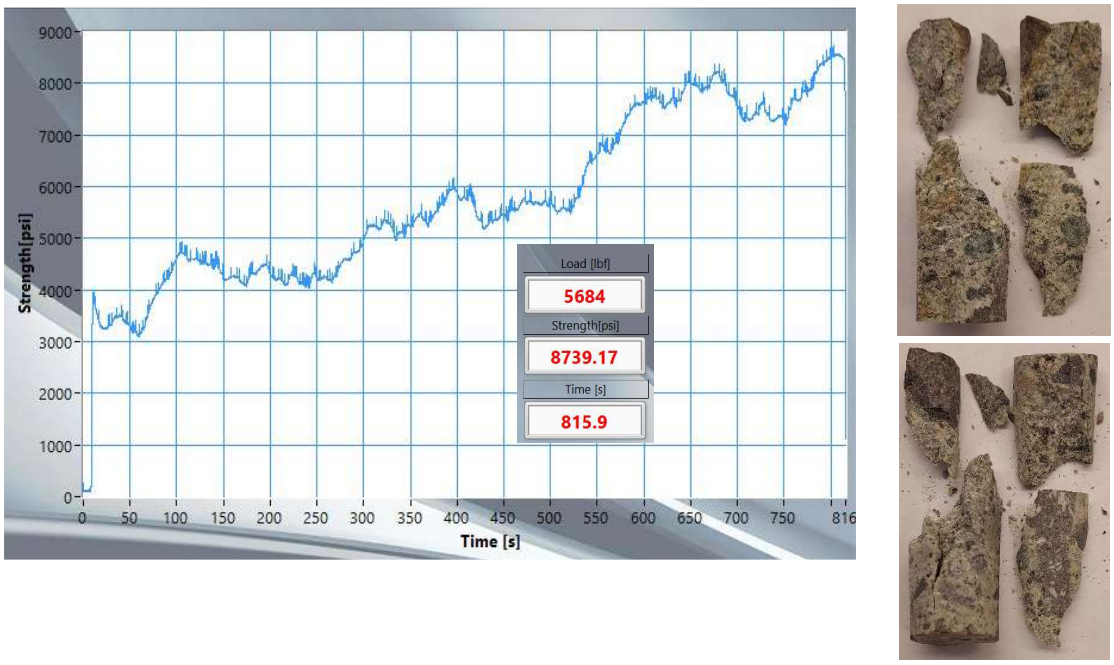

Figure B-77. UCS data and post-failure photographs for sample LCB091414-2

4. LCDLA082913-1

Figure B-78. UCS data and post-failure photographs for sample LCDLA082913-1

5. LCDLA032912-2

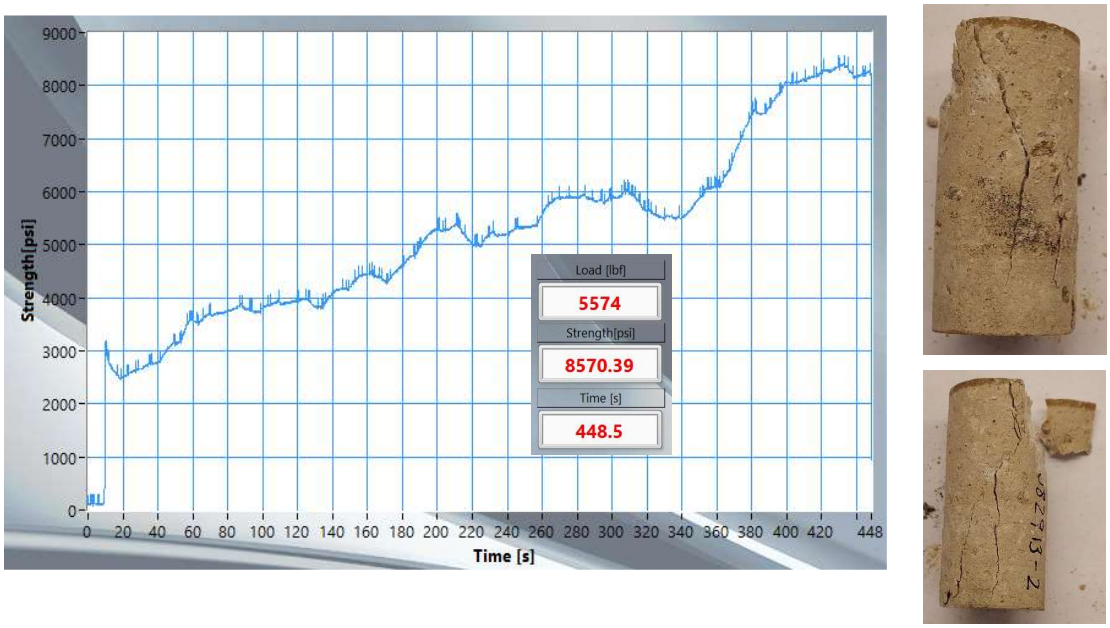

Figure B-79. UCS data and post-failure photographs for sample LCDLA082913-2

6. LCG090714-2c

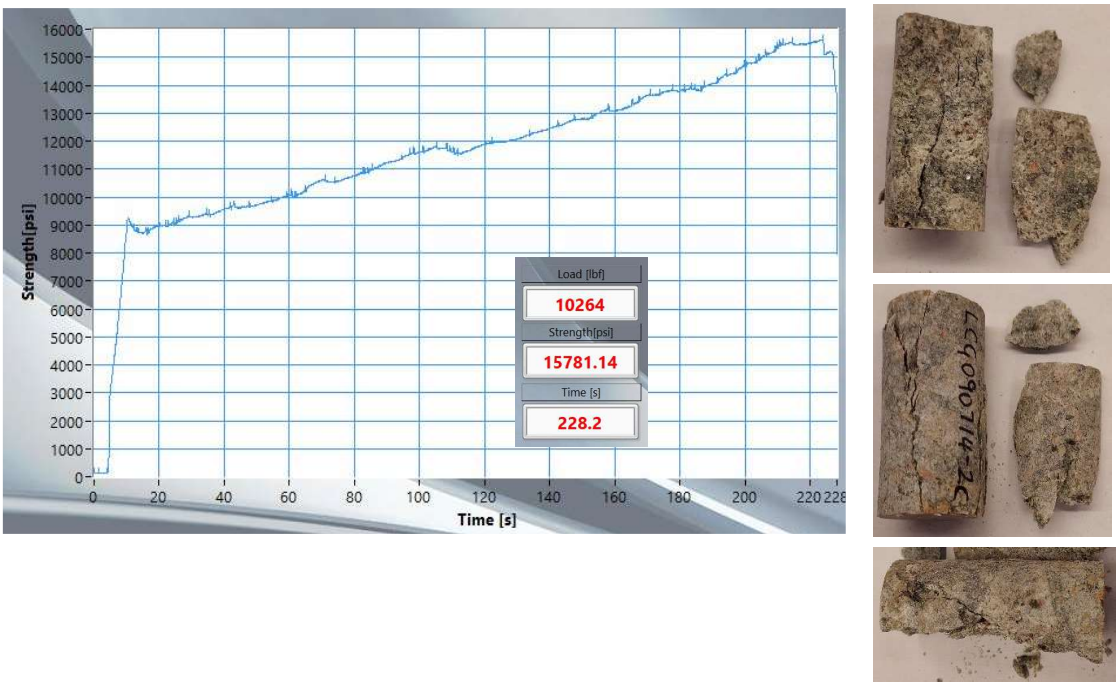

Figure B-80. UCS data and post-failure photographs for sample LCG090714-2c

7. LCG090714-3a

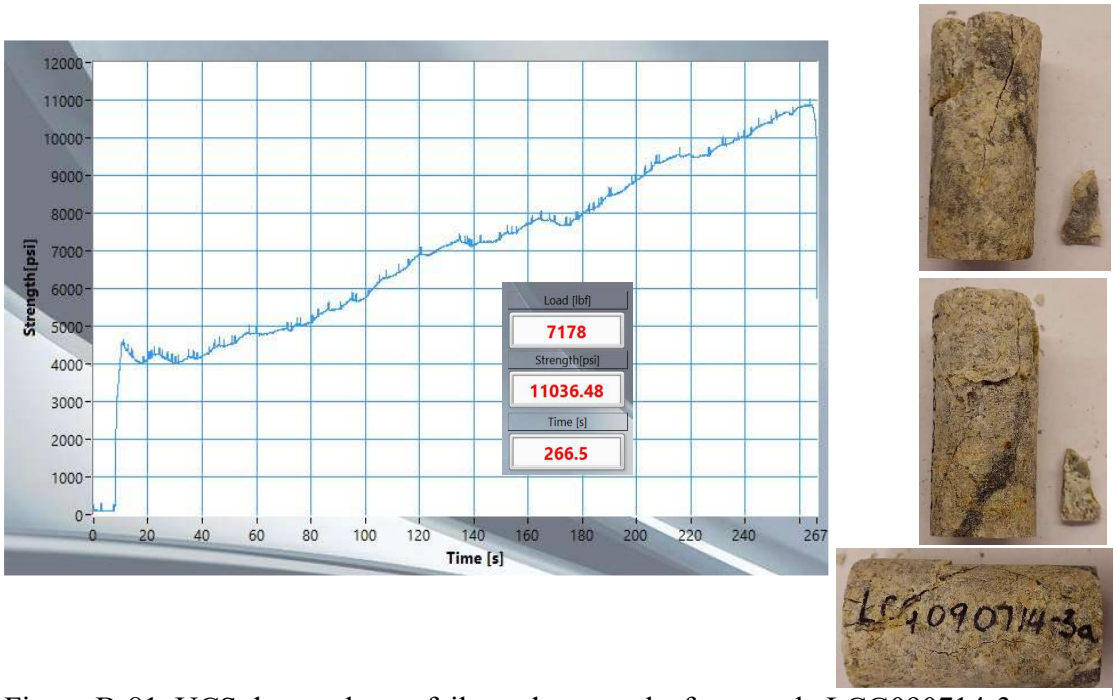

Figure B-81. UCS data and post-failure photographs for sample LCG090714-3a

8. LCG090714-3b

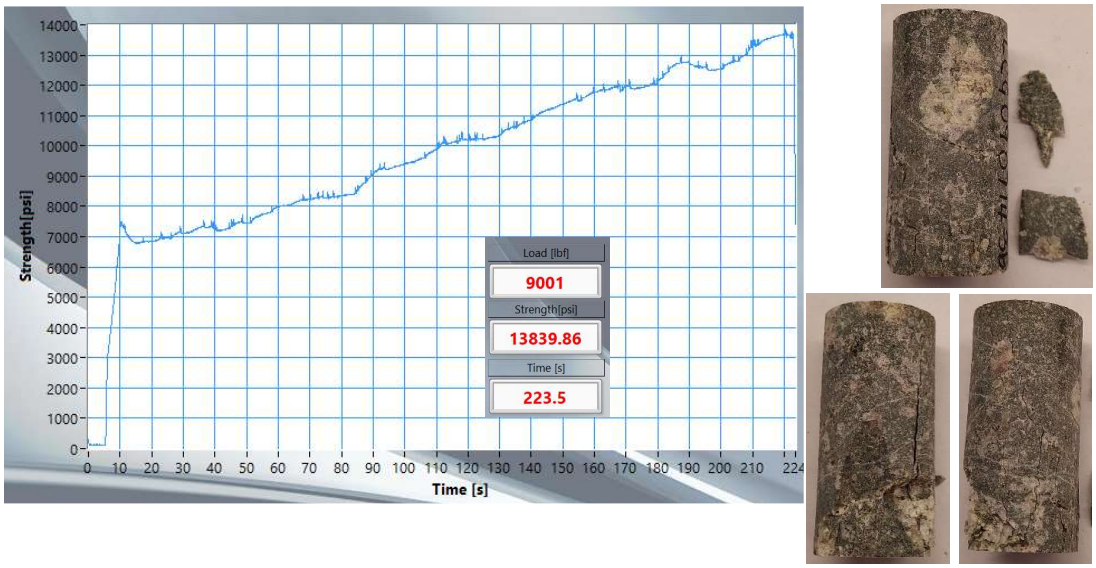

Figure B-82. UCS data and post-failure photographs for sample LCG090714-3b

9. LCG091314-1b

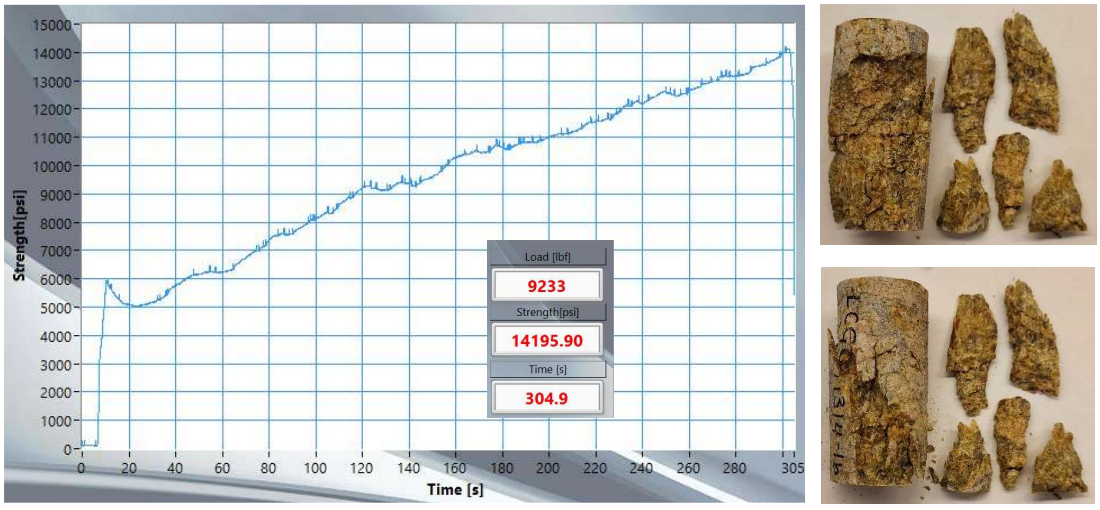

Figure B-83. UCS data and post-failure photographs for sample LCG091314-1b

10. LCT091014-1a

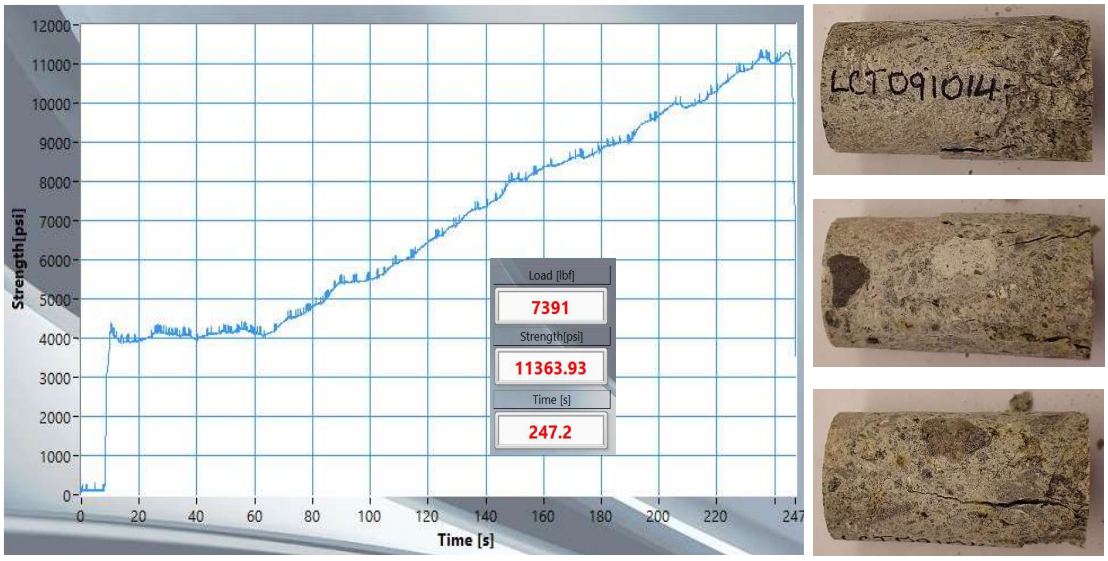

Figure B-84. UCS data and post-failure photographs for sample LCG091014-1a

11. LCT091014-1b

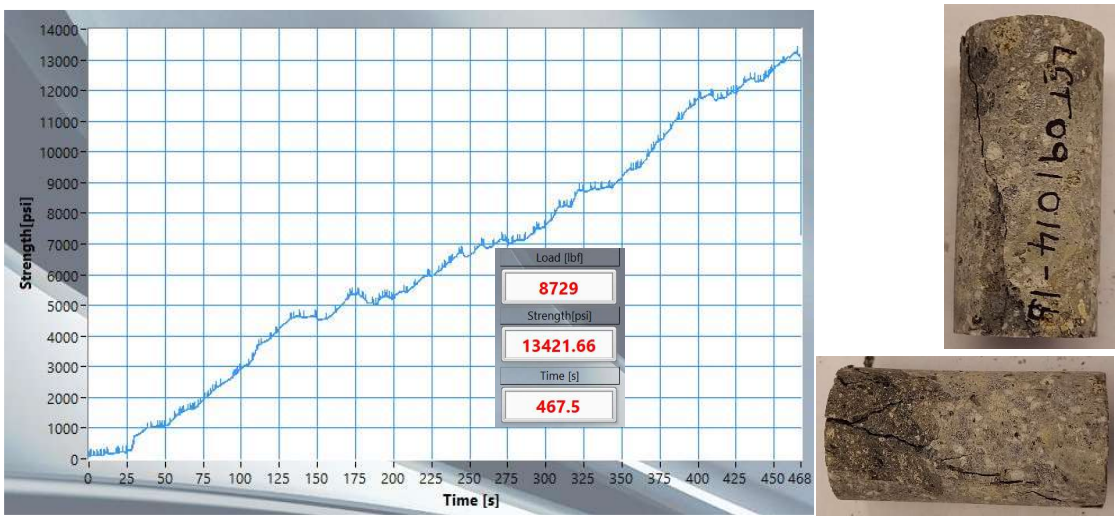

Figure B-85. UCS data and post-failure photographs for sample LCG091014-1b

12. LCT091514-3(1)

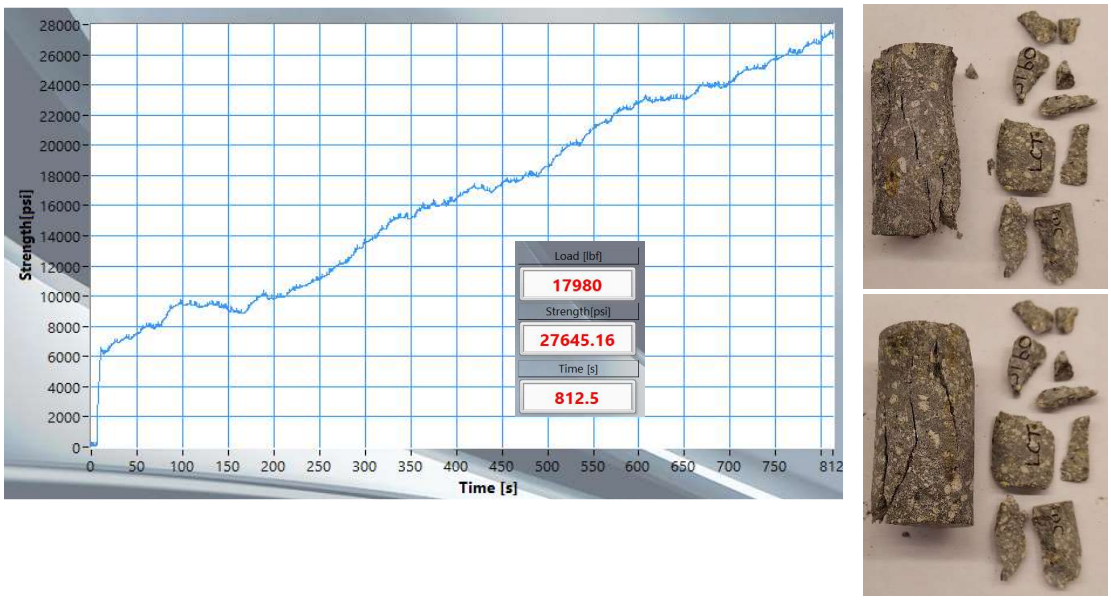

Figure B-86. UCS data and post-failure photographs for sample LCG091514-3(1)

13. LCT091514-3(2)

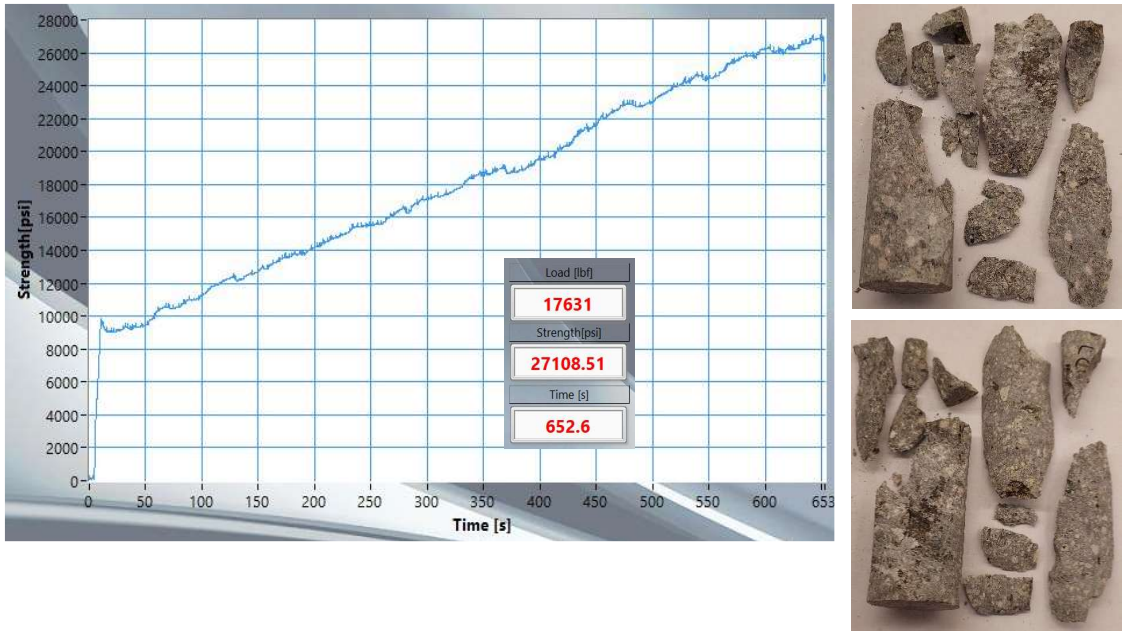

Figure B-87. UCS data and post-failure photographs for sample LCG091514-3(2)

14. LCTBV071714-5a

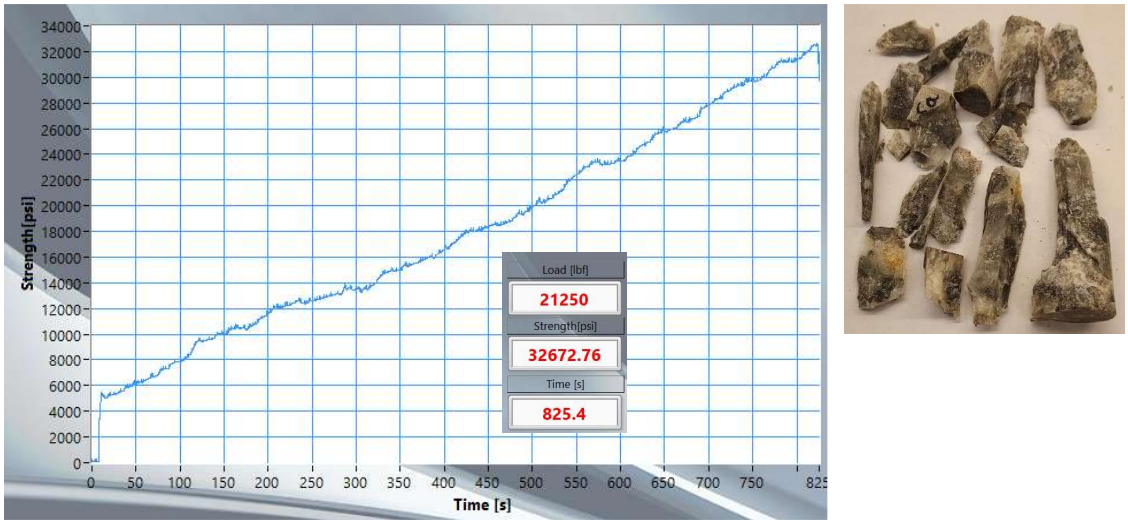

Figure B-88. UCS data and post-failure photographs for sample LCTBV071714-5a

15. LCTV090314-4a

Figure B-89. UCS data and post-failure photographs for sample LCTV090314-4a

16. LCTV091014-1c

Figure B-90. UCS data and post-failure photographs for sample LCTV091014-1c

17. LCTV091014-1d

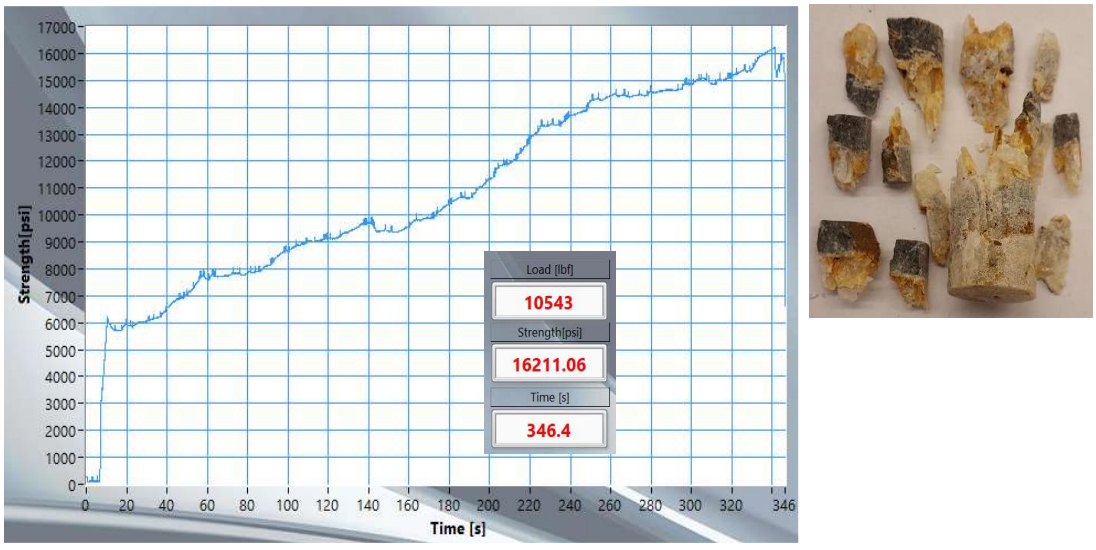

Figure B-91. UCS data and post-failure photographs for sample LCTV091014-1d

C Copyright documentation

C.1 Permission for use of material from Wyering et al., 2015

ELSEVIER LICENSE TERMS AND CONDITIONS

May 14, 2022

This Agreement between Michigan Technological Univsersity-- Rachel Hetherington ("You") and Elsevier ("Elsevier") consists of your license details and the terms and conditions provided by Elsevier and Copyright Clearance Center.

License Number	5307751409001
License date	May 14, 2022
Licensed Content Publisher	Elsevier
Licensed Content Publication	Engineering Geology
Licensed Content Title	The development and application of the alteration strength index equation
Licensed Content Author	L.D. Wyering,M.C. Villeneuve,I.C. Wallis,P.A. Siratovich,B.M. Kennedy,D.M. Gravley
Licensed Content Date	Dec 14, 2015
Licensed Content Volume	199
Licensed Content Issue	n/a
Licensed Content Pages	14
Start Page	48
End Page	61
Type of Use	reuse in a thesis/dissertation
Portion	figures/tables/illustrations
Number of figures/tables/illustrations	4
Format	electronic

Are you the author of this Elsevier article?	No
Will you be translating?	No
Title	A Hyperspectral Approach to the Alteration Strength Index
Institution name	Michigan Technological University
Expected presentation date	May 2022
Portions	Tables 1, 2, 3, and 5 (parameter details).
Requestor Location	Michigan Technological University 1400 Townsend Drive HOUGHTON, MI 49931 United States Attn: Michigan Technological University
Publisher Tax ID	98-0397604
Total	0.00USD

Terms and Conditions

INTRODUCTION

1. The publisher for this copyrighted material is Elsevier. By clicking "accept" in connection with completing this licensing transaction, you agree that the following terms and conditions apply to this transaction (along with the Billing and Payment terms and conditions established by Copyright Clearance Center, Inc. ("CCC"), at the time that you opened your Rightslink account and that are available at any time at http://myaccount.copyright.com).

GENERAL TERMS

2. Elsevier hereby grants you permission to reproduce the aforementioned material subject to the terms and conditions indicated.

3. Acknowledgement: If any part of the material to be used (for example, figures) has appeared in our publication with credit or acknowledgement to another source, permission must also be sought from that source. If such permission is not obtained then that material may not be included in your publication/copies. Suitable acknowledgement to the source must be made, either as a footnote or in a reference list at the end of your publication, as follows:

"Reprinted from Publication title, Vol /edition number, Author(s), Title of article/ title of chapter, Pages No., Copyright (Year), with permission from Elsevier [OR APPLICABLE SOCIETY COPYRIGHT OWNER]." Also Lancet special credit - "Reprinted from The Lancet, Vol. number, Author(s), Title of article, Pages No., Copyright (Year), with permission from Elsevier."

4. Reproduction of this material is confined to the purpose and/or media for which permission is hereby given.

5. Altering/Modifying Material: Not Permitted. However figures and illustrations may be altered/adapted minimally to serve your work. Any other abbreviations, additions, deletions and/or any other alterations shall be made only with prior written authorization of Elsevier Ltd. (Please contact Elsevier's permissions helpdesk here). No modifications can be made to any Lancet figures/tables and they must be reproduced in full.

6. If the permission fee for the requested use of our material is waived in this instance, please be advised that your future requests for Elsevier materials may attract a fee.

7. Reservation of Rights: Publisher reserves all rights not specifically granted in the combination of (i) the license details provided by you and accepted in the course of this licensing transaction, (ii) these terms and conditions and (iii) CCC's Billing and Payment terms and conditions.

8. License Contingent Upon Payment: While you may exercise the rights licensed immediately upon issuance of the license at the end of the licensing process for the transaction, provided that you have disclosed complete and accurate details of your proposed use, no license is finally effective unless and until full payment is received from you (either by publisher or by CCC) as provided in CCC's Billing and Payment terms and conditions. If full payment is not received on a timely basis, then any license preliminarily granted shall be deemed automatically revoked and shall be void as if never granted. Further, in the event that you breach any of these terms and conditions or any of CCC's Billing and Payment terms and conditions, the license is automatically revoked and shall be void as if never granted. Use of materials as described in a revoked license, as well as any use of the materials beyond the scope of an unrevoked license, may constitute copyright infringement and publisher reserves the right to take any and all action to protect its copyright in the materials.

9. Warranties: Publisher makes no representations or warranties with respect to the licensed material.

10. Indemnity: You hereby indemnify and agree to hold harmless publisher and CCC, and their respective officers, directors, employees and agents, from and against any and all claims arising out of your use of the licensed material other than as specifically authorized pursuant to this license.

11. No Transfer of License: This license is personal to you and may not be sublicensed, assigned, or transferred by you to any other person without publisher's written permission.

12. No Amendment Except in Writing: This license may not be amended except in a writing signed by both parties (or, in the case of publisher, by CCC on publisher's behalf).

13. Objection to Contrary Terms: Publisher hereby objects to any terms contained in any purchase order, acknowledgment, check endorsement or other writing prepared by you, which terms are inconsistent with these terms and conditions or CCC's Billing and Payment terms and conditions. These terms and conditions, together with CCC's Billing and Payment terms and conditions (which are incorporated herein), comprise the entire agreement between you and publisher (and CCC) concerning this licensing transaction. In the event of any conflict between your obligations established by these terms and conditions and those established by CCC's Billing and Payment terms and conditions, these terms and conditions shall control.

14. Revocation: Elsevier or Copyright Clearance Center may deny the permissions described in this License at their sole discretion, for any reason or no reason, with a full refund payable to you. Notice of such denial will be made using the contact information provided by you. Failure to receive such notice will not alter or invalidate the denial. In no event will Elsevier or Copyright Clearance Center be responsible or liable for any costs, expenses or damage incurred by you as a result of a denial of your permission request, other than a refund of the amount(s) paid by you to Elsevier and/or Copyright Clearance Center for denied perm1ss10ns.

LIMITED LICENSE

The following terms and conditions apply only to specific license types:

15. Translation: This permission is granted for non-exclusive world English rights only unless your license was granted for translation rights. If you licensed translation rights you may only translate this content into the languages you requested. A professional translator must perform all translations and reproduce the content word for word preserving the integrity of the article.

16. Posting licensed content on any Website: The following terms and conditions apply as follows: Licensing material from an Elsevier journal: All content posted to the web site must maintain the copyright information line on the bottom of each image; A hyper-text must be included to the Homepage of the journal from which you are licensing at http://www.sciencedirect.com/science/joumal/xxxxx or the Elsevier homepage for books at http://www.elsevier.com; Central Storage: This license does not include permission for a scanned version of the material to be stored in a central repository such as that provided by Heron/XanEdu.

Licensing material from an Elsevier book: A hyper-text link must be included to the Elsevier homepage at http://www.elsevier.com. All content posted to the web site must maintain the copyright information line on the bottom of each image.

Posting licensed content on Electronic reserve: In addition to the above the following clauses are applicable: The web site must be password-protected and made available only to bona fide students registered on a relevant course. This permission is granted for 1 year only. You may obtain a new license for future website posting.

17. For journal authors: the following clauses are applicable in addition to the above:

Preprints:

A preprint is an author's own write-up of research results and analysis, it has not been peer- reviewed, nor has it had any other value added to it by a publisher (such as formatting, copyright, technical enhancement etc.).

Authors can share their preprints anywhere at any time. Preprints should not be added to or enhanced in any way in order to appear more like, or to substitute for, the final versions of articles however authors can update their preprints on arXiv or RePEc with their Accepted Author Manuscript (see below).

If accepted for publication, we encourage authors to link from the preprint to their formal publication via its DOI. Millions of researchers have access to the formal publications on ScienceDirect, and so links will help users to find, access, cite and use the best available version. Please note that Cell Press, The Lancet and some society-owned have different preprint policies. Information on these policies is available on the journal homepage.

Accepted Author Manuscripts: An accepted author manuscript is the manuscript of an article that has been accepted for publication and which typically includes author-incorporated changes suggested during submission, peer review and editor-author communications.

Authors can share their accepted author manuscript:

- immediately
  - via their non-commercial person homepage or blog
  - by updating a preprint in arXiv or RePEc with the accepted manuscript
  - via their research institute or institutional repository for internal institutional uses or as part of an invitation-only research collaboration work-group
  - directly by providing copies to their students or to research collaborators for their personal use
  - for private scholarly sharing as part of an invitation-only work group on commercial sites with which Elsevier has an agreement
- After the embargo period
  - via non-commercial hosting platforms such as their institutional repository
  - via commercial sites with which Elsevier has an agreement

In all cases accepted manuscripts should:

- link to the formal publication via its DOI
- bear a CC-BY-NC-ND license - this is easy to do
- if aggregated with other manuscripts, for example in a repository or other site, be shared in alignment with our hosting policy not be added to or enhanced in any way to appear more like, or to substitute for, the published journal article.

Published journal article (JPA): A published journal article (PJA) is the definitive final record of published research that appears or will appear in the journal and embodies all value-adding publishing activities including peer review co-ordination, copy-editing, formatting, (ifrelevant) pagination and online enrichment.

Policies for sharing publishing journal articles differ for subscription and gold open access articles:

Subscription Articles: If you are an author, please share a link to your article rather than the full-text. Millions of researchers have access to the formal publications on ScienceDirect, and so links will help your users to find, access, cite, and use the best available version.

Theses and dissertations which contain embedded PJAs as part of the formal submission can be posted publicly by the awarding institution with DOI links back to the formal publications on ScienceDirect.

If you are affiliated with a library that subscribes to ScienceDirect you have additional private sharing rights for others' research accessed under that agreement. This includes use for classroom teaching and internal training at the institution (including use in course packs and courseware programs), and inclusion of the article for grant funding purposes.

Gold Open Access Articles: May be shared according to the author-selected end-user license and should contain a CrossMark logo, the end user license, and a DOI link to the formal publication on ScienceDirect.

Please refer to Elsevier's posting policy for further information.

18. For book authors the following clauses are applicable in addition to the above: Authors are permitted to place a brief summary of their work online only. You are not allowed to download and post the published electronic version of your chapter, nor may you scan the printed edition to create an electronic version. Posting to a repository: Authors are permitted to post a summary of their chapter only in their institution's repository.

19. Thesis/Dissertation: If your license is for use in a thesis/dissertation your thesis may be submitted to your institution in either print or electronic form. Should your thesis be published commercially, please reapply for permission. These requirements include permission for the Library and Archives of Canada to supply single copies, on demand, of the complete thesis and include permission for Proquest/UMI to supply single copies,

on demand, of the complete thesis. Should your thesis be published commercially, please reapply for permission. Theses and dissertations which contain embedded PJAs as part of the formal submission can be posted publicly by the awarding institution with DOI links back to the formal publications on ScienceDirect.

Elsevier Open Access Terms and Conditions

You can publish open access with Elsevier in hundreds of open access journals or in nearly 2000 established subscription journals that support open access publishing. Permitted third party re-use of these open access articles is defined by the author's choice of Creative Commons user license. See our open access license policy for more information.

Terms & Conditions applicable to all Open Access articles published with Elsevier:

Any reuse of the article must not represent the author as endorsing the adaptation of the article nor should the article be modified in such a way as to damage the author's honour or reputation. If any changes have been made, such changes must be clearly indicated.

The author(s) must be appropriately credited and we ask that you include the end user license and a DOI link to the formal publication on ScienceDirect.

If any part of the material to be used (for example, figures) has appeared in our publication with credit or acknowledgement to another source it is the responsibility of the user to ensure their reuse complies with the terms and conditions determined by the rights holder.

Additional Terms & Conditions applicable to each Creative Commons user license:

CC BY: The CC-BY license allows users to copy, to create extracts, abstracts and new works from the Article, to alter and revise the Article and to make commercial use of the Article (including reuse and/or resale of the Article by commercial entities), provided the user gives appropriate credit (with a link to the formal publication through the relevant DOI), provides a link to the license, indicates if changes were made and the licensor is not represented as endorsing the use made of the work. The full details of the license are available at http://creativecommons.org/licenses/by/4.0.

CC BY NC SA: The CC BY-NC-SA license allows users to copy, to create extracts, abstracts and new works from the Article, to alter and revise the Article, provided this is not done for commercial purposes, and that the user gives appropriate credit (with a link to the formal publication through the relevant DOI), provides a link to the license, indicates if changes were made and the licensor is not represented as endorsing the use made of the work. Further, any new works must be made available on the same conditions. The full details of the license are available at http://creativecommons.org/licenses/by-nc-sa/4.0.